ROLE OF THIOLS IN MICROBIAL METAL REDUCTION AND IMPORTANCE OF ORGANIC-FE(III) COMPLEXES ON THE BENTHIC FLUX OF IRON FROM CONTINENTAL MARGIN SEDIMENTS

A Dissertation
Presented to
The Academic Faculty

by

Eryn M. Eitel

In Partial Fulfillment
of the Requirements for the Degree
Doctor of Philosophy in the
School of Earth and Atmospheric Science

Georgia Institute of Technology
December 2018

ROLE OF THIOLS IN MICROBIAL METAL REDUCTION AND IMPORTANCE OF ORGANIC-FE(III) COMPLEXES ON THE BENTHIC FLUX OF IRON FROM CONTINENTAL MARGIN SEDIMENTS

Approved by:

Dr. Martial Taillefert, Advisor
School of Earth and Atmospheric Sciences
Georgia Institute of Technology

Dr. Frank Stewart
School of Biology
Georgia Institute of Technology

Dr. Thomas DiChristina
School of Biology
Georgia Institute of Technology

Dr. Christophe Rabouille
Laboratoire des Sciences du Climat et de l'Environnement, LSCE/IPSL
CEA-CNRS-UVSQ-Université de Paris Saclay, France

Dr. Yuanzhi Tang
School of Earth and Atmospheric Sciences
Georgia Institute of Technology

Date Approved: [July 26, 2018]

ACKNOWLEDGEMENTS

I would like to thank my advisor, Dr. Martial Taillefert, for giving me a chance to explore my own research interests and participate in a lot of field work in awesome locations. Thank you for reminding me that writing is supposed to be fun and being patient with me when I want to question everything. Sometimes it was a challenge, but it's been a good one and it has helped me become the scientist I am today. I would like to thank my committee for all their support and the research opportunities they have given me over the years. Dr. Tom DiChristina, thank you for all your microbiology help over the years and getting me on the thiol path. Dr. Christophe Rabouille, thank you for letting me see what a French research cruise is like and helping with the most revisions of a paper ever. Dr. Yuanzhi Tang, thank you for your encouraging words, optimism, and help with solid phase analysis. Dr. Frank Stewart, thank you for letting me come on two research cruises and for inspiring exploration of the omics world.

I would also like to thank Don Nuzzio for his help with numerous analytical systems, David Bostwick for helping me with ESI-MS, and all the captains and crew members of the research vessels I have been on.

Thank you to all the past and present members of both the Taillefert and DiChristina lab groups and everyone who's assisted on research cruises over the years. Ben, Tony, Keaton, Joel, Jens, Liz, Laura, Laurie, and Olivia: cruises would have been so much harder and porting wouldn't have been nearly as fun without all of you. Shannon, I don't think I would have survived a few of those cruises and the electrode demand without you, thank you for your unending patience. Anna, thank you for making electrochemistry fun from the

beginning and letting me visit you all over the world. Nadia, thank you for always being a shoulder to lean on.

I would also like to thank Emily Saad for always being there for me, Shelby and Annika for making the end of grad school more fun, and Amanda for always being ready to swap dog stories. I am also grateful for my amazing friends Amy, Mia, Maria, and Michele; you all made living in Atlanta so much fun. Also to Sid who basically deserves a degree too since he's come to school with me just about every day. I am especially grateful to Nathan, even writing this thesis wasn't too terrible with you by my side and I hope I can be even half as helpful when you write yours. Finally, I would like to thank my mom and dad who have supported me so much and have driven such long distances just to pick up Sid or see me for the weekend.

TABLE OF CONTENTS

LIST OF TABLES

LIST OF FIGURES

LIST OF SYMBOLS AND ABBREVIATIONS

3-MPA	3-Mercaptopropanoic Acid
ACN	Acetonitrile
CA	Cysteamine
CAAC	Cystamine
CS	Cysteine
CSSC	Cystine
DFOB	Deferoxamine-B
DMR	Dissimilatory Metal Reduction
DMSP	Dimethylsulfoniopropionate
EDTA	EthyleneDiamineTetracetic Acid
EEC	Extracellular Electron Conduit
EIC	Extracted Ion Chromatogram
ESI-MS	ElectroSpray Ionization-Mass Spectrometry
EXAFS	Extended X-ray Absorption Fine Structure
GS	Reduced Glutathione
GSSG	Oxidized Gluathione
HILIC	Hydrophilic Interaction Liquid Interface Chromatography
HNLC	High-Nutrient Low Chlorophyll
HS	Homocysteine
HSSH	Homocystine
IDA	IminoDiacetic Acid
IMAC	Immobilized Metal Affinity Chromatography

LC	Liquid Chromatography
M	Molecular ion in MS (eg. $[M+H]^+$)
MS	Mass Spectrometry
MSR	Microbial Sulfate Reduction
OM	Outer Membrane
OPD	Oxygen Penetration Depth
PEEK	PolyEtherEtherKetone
PMT	PhotoMultiplier Tube
RPLC	Reverse Phase Liquid Chromatography
SPE	Solid Phase Extraction
SSA	Specific Surface Area
SWI	Sediment-Water Interface
TA	Total Alkalinity
TEA	Terminal Electron Acceptor
TIC	Total Ion Chromatogram
XANES	X-ray Absorption Near Edge Structure
XAS	X-ray Absorption Spectroscopy
XRD	X-Ray Diffraction

SUMMARY

Both Fe(III) and Mn(III,IV) oxides are ubiquitous in aquatic sediments and represent favorable terminal electron acceptors for microbial respiration. As a result, the dissimilatory reduction of Fe(III) and Mn(III,IV) contributes to the cycling of carbon in both marine and freshwater sediments and impacts a variety of other important biogeochemical and environmental processes, including the oxygen, nitrogen, phosphorus, and sulfur cycles, and the mobilization of organic and inorganic contaminants. Despite the potential impact of these processes, the microbial mechanism of metal reduction remains under debate as the organism must transfer electrons to a solid electron acceptor, a unique physiological problem in microbiology. The redox cycling of soluble electron shuttles, by which an efficient reductant of Fe(III) and Mn(III,IV) oxides is microbially recycled, has emerged as a potential solution to this problem. Indeed, addition of exogenous electron shuttles such as hydroquinones and thiols increases the rate and extent of Fe(III) and Mn(IV) oxides reduction in pure cultures of model Mn(III,IV)- and Fe(III)-reducing bacteria. In this dissertation, the ability for thiols to act as electron shuttles during dissimilatory reduction of Fe(III) and Mn(III,IV) oxides was assessed through the development of a novel voltammetric technique that simultaneously quantifies thiol and disulfide species *in situ*. This method was employed to investigate the kinetics and mechanism of the abiotic reaction of four low molecular weight thiols with both ferrihydrite and common Mn(III,IV) oxides at environmentally relevant concentrations and pH. To investigate the role of thiols as potential electron shuttles in the reduction of Fe(III) and Mn(IV) in sediments, depth profiles of thiols in the pore waters from a variety of

locations, including subalpine freshwater wetlands in Colorado, a salt marsh in Georgia, the Rhone River delta, and the continental margins off North Carolina and Louisiana were determined along with the main redox processes in these sediments. Thiols were detected at all locations, and depth profiles demonstrated significant correlations between thiols and reduced iron (Fe^{2+}). Sediment slurry incubations and cultures of model Fe(III)-reduction bacteria *Shewanella oneidensis* MR-1 confirmed endogenous production of thiols during iron reduction. Overall, these results demonstrate that thiols may be efficient electron shuttles in microbial metal reduction and could be used as tracers to differentiate dissimilatory Fe(III) reduction from the chemical reduction by dissolved sulfides in sediments, a notoriously difficult problem in marine biogeochemistry.

Reduction of Fe(III) oxides in marine sediments may have important implications in chemical oceanography as it may allow dissolved iron to diffuse across the sediment water interface and the benthic iron flux may stimulate primary productivity in the water column of iron-limited high nutrient low chlorophyll (HNLC) zones. Although aeolian deposition as well as inputs from rivers, hydrothermal vents, icebergs and continental margin sediments represent significant sources of iron to the ocean, the contribution of sediments to the iron supply to the water column is not well constrained. The benthic iron flux has mostly been determined from continental shelf sediments in upwelling zones or areas exposed to large riverine inputs, overlooking slope sediments and passive continental margins. In this dissertation, the sedimentary flux of dissolved iron was determined along a transect across the North Carolina continental margin, which does not experience major upwelling or is not exposed to large riverine inputs. This study demonstrated that slope sediments produce more bioavailable iron than shelf sediments, as continental slopes are

depocenters for both organic matter and terrigenous material. The upward flux of dissolved iron to the overlying waters may be suppressed and replaced by the burial of iron under the form of FeS or pyrite in sediments receiving a large flux of organic carbon that are typically dominated by sulfate reduction. In the highly active sediments of the Rhône River prodelta, complete reduction of sulfate titrated Fe^{2+} and increased burial of FeS. The burial of FeS resulted in the decoupling of anaerobic and aerobic processes, which allowed alkalinity to flux across the sediment water interface and potentially contribute to the buffering capacity of the waters overlying those sediments. Finally, as the stabilization of dissolved Fe(III) under the form of organic-Fe(III) complexes may be required to maintain a significant iron flux across the sediment-water interface and as these complexes are observed in most sediments not dominated by sulfate reduction, a new technique was developed to isolate the ligands responsible for stabilizing Fe(III) in solution in marine sediments. Immobilized metal affinity chromatography (IMAC) with Fe(III) successfully retained known Fe(III)-binding ligands for detection by mass spectrometry (MS), and preliminary results demonstrated the method could be used to isolate Fe(III)-ligands from both natural samples and incubations of model Fe(III)-reducing bacteria. Overall, the findings of this dissertation help redefine the mechanism of dissimilatory iron reduction, provide new chemical proxies to distinguish between microbial and chemical Fe(III) reduction in marine sediments, and provide insight into the importance of Fe(III) reduction in continental margin sediments and the biogeochemical processes controlling the release of dissolved iron from sediments.

CHAPTER 1. INTRODUCTION

1.1 Iron and Manganese Chemistry in Aqueous Environments

Iron (Fe) and manganese (Mn) are the fourth and fifth most abundant metals in the Earth's crust. Both are ubiquitous in natural sediments and as the elemental cycles of Mn and Fe in aqueous sediments are closely coupled, their transformations not only impact the cycling of each other (Postma and Appelo, 2000; Schippers and Jorgensen, 2001), but also a number of other biogeochemical cycles including carbon (Kostka et al., 2002; Meiggs and Taillefert, 2011; Thamdrup et al., 1994; Van Cappellen and Wang, 1996), oxygen (Burns et al., 2010), nitrogen (Luther et al., 1997; Vancleemput and Baert, 1983), phosphorus (Rozan et al., 2002; White et al., 2008), and sulfur (ΣH_2S) (Pyzik and Sommer, 1981; Schippers and Jorgensen, 2001).Additionally, the dissolution of solid Fe (Borch et al., 2010; DiChristina et al., 2005; Lovley, 1991; Lovley et al., 1989) and Mn (Feng et al., 2007; Jenne, 1968; Nelson and Lion, 2003; Oscarson et al., 1981; Remucal and Ginder-Vogel, 2014; Weaver and Hochella, 2003) oxides may result in the release of adsorbed organic and inorganic contaminants. Thus, due to their reactivity and prevalence in natural environments, it is important to investigate the factors contributing to and affected by their transformations.

In nature, iron exists mainly in the +II (ferrous) or +III (ferric) oxidation states. Whereas Fe^{2+} is highly soluble over a large range of pH and ionic strength values, Fe^{3+} is only soluble at extreme pH or when complexed by organic ligands. When uncomplexed, Fe^{3+} hydrolyzes extremely rapidly to form solid (oxy)hydroxides near circumnetural pH (Stumm and Morgan, 1996). Despite the increased solubility of Fe^{2+}, this form of iron is

short lived with a half-life of ~5 minutes in many aquatic environments due to the rapid oxidation and precipitation as Fe(III) oxides in fully oxygenated waters (Davison, 1993; Millero et al., 1995). In oxic aqueous systems, the metastable amorphous ferrihydrite is formed initially and slowly transforms to lepidocrocite (γ-FeOOH), goethite (α-FeOOH), or hematite (α-Fe_2O_3) depending on pH and solution composition (Schwertmann and Murad, 1983; Schwertmann et al., 2004). Increased concentrations of Fe^{2+} may results in mixed Fe(II)/Fe(III) minerals such as green rusts and magnetite depending on the environmental conditions (Hansel et al., 2003; Rickard and Luther, 2007). In the absence of sulfide, siderite ($FeCO_3$) is the main Fe(II)-dominant phase in marine sediments (Garrels and Thompson, 1960). In the presence of sulfide, Fe(II) may be buried as either FeS or pyrite (FeS_2) (Rickard, 1989).

Although Mn may theoretically exist in oxidation states ranging between 0 to +VII, it is primarily observed in the +II, +III, and +IV oxidation states in natural environments. Unlike the reduced form of iron, Mn^{2+} exists in aerobic environments as its reaction with oxygen is quite slow at circumneutral pH (Emerson et al., 1982; Kessick and Morgan, 1975). However, microbial oxidation of Mn^{2+} is several orders of magnitude more rapid than oxidation by O_2 and results in the precipitation of Mn(III,IV) oxyhydroxide phases such as MnOOH or MnO_2 (Nealson et al., 1988; Tebo et al., 2004; Tebo et al., 1997). In addition, microbial production of reactive oxygen species may greatly contribute to Mn^{2+} oxidation in the environment (Learman et al., 2011a). Soluble Mn(III) may exist in both oxic and anoxic environments through complexation with organic ligands (Madison et al., 2013; Oldham et al., 2015), however without these stabilizing ligands, soluble Mn^{3+} disproportionates in acidic conditions or precipitates as Mn(III) oxides at pH > 7 (Davison,

1993). Ligands capable of complexing Mn(IV) have yet to be observed in natural environments (Morgan, 2000), therefore Mn(IV) occurs in the solid phase only. In most environments layered phylomanganates such as birnessite are the most abundant solid phases (Post, 1999), however, reaction with Mn^{2+} results in the reductive transformation to other phases such as hausmannite or manganite (Elzinga, 2011; Lefkowitz et al., 2013). Additionally, tunnel structured phase hollandites are commonly observed in weathered sediments (Ostwald, 1992).

1.2 Microbial Respiration on Solid Terminal Electron Acceptors

Due to the importance of Fe(III) and Mn(III,IV) oxides in most aquatic environments it is critical to understand how microorganisms extract energy from these compounds. As oxygen is rapidly depleted in sedimentary environments, organisms are forced to couple the oxidation of organic carbon or H_2 with the reduction of a terminal electron acceptors (TEAs). Generally, the amount of energy an organism can receive from a redox couple is determined by the difference in oxidation potential of the electron donor and the reduction potential of the electron acceptor. Therefore, as the TEA reduction potential decreases, the amount of energy gained by reaction with the same electron donor also decreases (Jin and Bethke, 2002). In sediments, the reduction potential of TEAs decreases in the sequential order O_2 > NO_3^- > Mn(III,IV) and Fe(III) oxides > SO_4^{2-} >> CO_2 (Froelich et al., 1979). Reduction of soluble TEA such as molecular oxygen, NO_3^-, and SO_4^{2-} occurs intracellularly via reductases on the inner membrane or within the periplasmic space (Brittain et al., 1992; Ingledew and Poole, 1984; Peck and LeGall, 1982). However, the low solubility of Fe(III) and Mn(III,IV)-oxides at circumneutral pH poses a physiological problem as solid TEAs are not able to diffuse through the cell membrane to reach the

localized electron transport systems utilized during respiration of soluble electron acceptors. To overcome this physiological challenge, metal-reducing microorganisms have developed a variety of strategies to transfer electrons to solid Fe(III) and Mn(III,IV). The metal reduction mechanism has been extensively studied in model Fe(III)- and Mn(III,IV)-reducing bacteria *Shewanella* and *Geobacter* (Cooper et al., 2016; Lovley et al., 2004). Although bacteria capable of reducing either Fe(III) or Mn(III,IV) are generally capable of reducing the other species as well, most studies have focused on the mechanism of Fe(III) reduction. Four pathways involving the direct contact between the organism and the mineral, nanowires to transfer electrons, solubilization of Fe(III) prior to reduction, and electron shuttles have been proposed to explain how dissimilatory iron reduction (DIR) proceeds: (Figure 1-1).

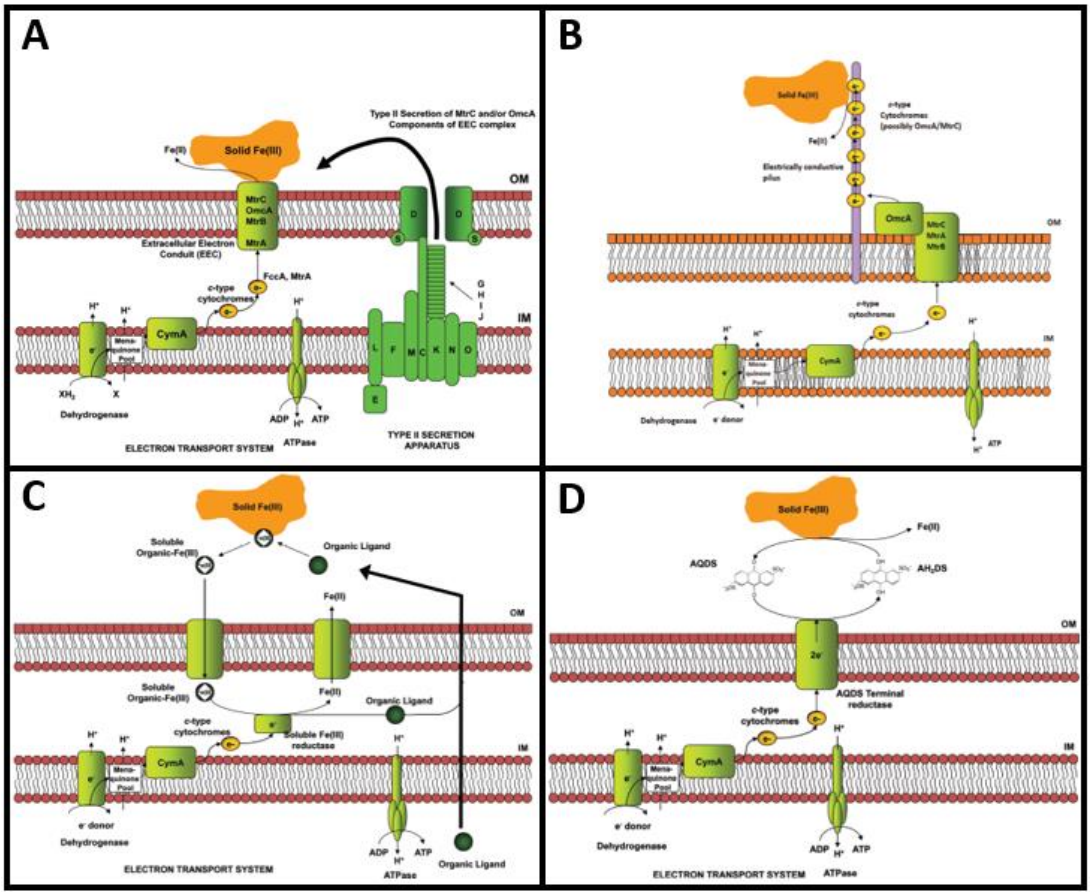

Figure 1-1 . Proposed mechanisms for electron transfer from *Shewanella* sp. to solid Fe(III) oxides include A) direct contact between cells and OM proteins, B) direct contact between cells and extracellular appendages (i.e. "nanowires"), C) solubilization of Fe(III) prior to reduction of the organic-Fe(III) complex, and D) electron shuttling via redox active molecules (AQDS shown as example) (Figure modified with permission from Cooper et al, 2017).

In the direct contact mechanism, electrons are transferred from outer membrane (OM) reductases in direct contact, or less than 15 angstroms away, with the solid TEA (Myers and Myers, 2002). In *Shewanella oneidensis*, a Type II protein secretion system is required for solid Fe(III) reduction (DiChristina et al., 2002). The Type II protein secretion system places c-type cytrochromes MtrC and OmcA on the outside of the OM where they can then form a lipid-embedded extracellular electron conduit (EEC) with other c-type cytochromes MtrB and MtrA (Figure 1-1A). The inner membrane electron transport system

can then transfer electrons from a menaquinol-oxidizing c-type cytochrome, CymA, to the EEC, then to external electron acceptors. This mechanism may be preferred by metal reducing bacteria in environments where electron shuttles or Fe(III)-chelating ligands are limited or production is energetically costly (Richter et al., 2012). However, physical separation of the cells and Fe(III) oxides demonstrates that direct contact is not required for reduction of solid TEA (Jacobson, 1994).

Extracellular electrically conductive appendages, referred to as nanowires, are also produced by metal reducing bacteria to reach solid TEA at a distance (El-Naggar et al., 2010; Gorby et al., 2006). Nanowires can transport electrons over several microns through self-assembled conjugated polymers with two-dimensional extended aromatic systems (Briseno et al., 2008). As c-type cytochromes MtrC and OmcA are required for Fe(III)-reducing activity in *S. oneidensis*, nanowires are thought to depend on associations between these cytochromes and not intrinsic characteristics of the pilus (El-Naggar et al., 2010; Gorby et al., 2006; Lovley, 2008) (Figure 1-1B). Although a Type IV pilus is also necessary for the reduction of insoluble Fe(III) oxides by *Geobacter sulfurreduces* and *S. oneidensis* contains genes encoding a variety of pili, the production of nanowires for Fe(III) reduction in nature remains under debate (Gorby et al., 2006; Lovley, 2008; Reguera et al., 2005).

Rather than directly contacting solid TEA through either OM bound cytochromes or nanowires, an alternate strategy involves the non-reductive solubilization of Fe(III) oxides to allow Fe(III) to be brought inside the cell prior to reduction. Soluble organic-Fe(III) complexes are produced during dissimilatory iron reduction by *S. oneidensis* (Jones et al., 2010; Taillefert et al., 2007a) and do not involve known siderophore ligands (Fennessey et al., 2010). After formation, it is hypothesized that the soluble organic-Fe(III)

complexes are brought either to the OM or across the cell membrane for reduction. The organic ligand is then released and recycled multiple times (Figure 1-1C). Dissolution prior to reduction may increase the reduction potential of iron (Zinder et al., 1986) and lower the activation energy required for iron reduction (Taillefert et al., 2007a; Wang et al., 2008), thus increasing the energy gained by the organism during respiration.

Finally, microorganisms may utilize either endogenous or exogenous electron shuttles to transfer electrons to solid TEA outside of the cell. After reduction of the TEA, the oxidized electron shuttle may be microbially reduced by either inner or outer membrane c-type cytochromes and recycled for further iron reduction (Figure 1-1D). *S. oneidensis* mutants lacking to OM c-type cytochromes MtrC and OmcA are unable to reduce Fe(III), suggesting that the oxidized form of the electron shuttles is reduced outside of the cell (Roden et al., 2010). Proposed electron shuttles include humic acids (Kappler et al., 2004) and their quinone analog AQDS (Bond and Lovley, 2005), flavins (Marsili et al., 2008), and thiols (Doong and Schink, 2002).

Both archaea and bacteria are capable of dissimilatory metal reduction (DMR), suggesting that microbial respiration on metals may have been among the first to evolve on the early Earth (Lonergan et al., 1996; Vargas et al., 1998). Depending on the environmental conditions and available resources, metal-reducing microorganisms may rely on any of the four mechanisms described above to respire on Fe(III) or Mn(III,IV) oxides, or even combined mechanisms. For example, microorganisms could initially solubilize Fe(III) with an organic ligand, then reduce this complex by an endogenously produced electron shuttle, such as a thiol (Figure 1-2).

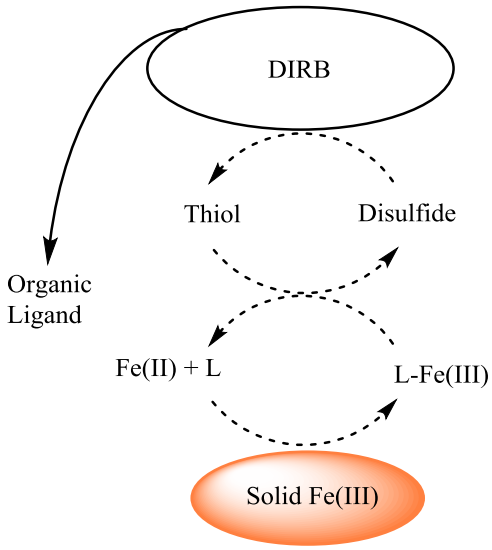

Figure 1-2. Combination of two proposed mechanisms for respiration on solid Fe(III) by dissimilatory iron reducting bacteria (DIRB). Production of an organic ligand may non-reductively dissolve solid Fe(III), followed by extracellular reduction of the organic-Fe(III) complex by a soluble electron shuttle, such as a thiol. The microorganism then reduces the oxidized electron shuttle, allowing both the electron shuttle and organic ligand to be continously recycled.

1.3 Chemical Proxies of Dissimilatory Metal Reduction Zones in Sediments

Whereas functional genes for reduction of other major anaerobic TEAs, such as nitrate and sulfate, are well known and allow identification of microbes capable of these processes in natural environments, the functional genes required for DMR display high sequence divergence (Kappler and Bryce, 2017). As a result, the application of molecular biomarkers to examine the fundamental ecological principles of Fe(III) and Mn(III,IV) reduction remains limited and it is difficult to differentiate between DMR and abiotic reduction of Fe(III) and Mn(III,IV) oxides in sediments. Identification of unique compounds utilized during DMR, such as the organic ligands involved in the solubilization

pathway or endogenous electron-shuttling mediators, may provide a way to differentiate between microbial and chemical metal reduction in sediments.

1.3.1 Soluble Organic-Fe(III) Complexes as Proxies for Dissimilatory Iron Reduction in Sediments

In the early 1990s, observations of soluble Fe(III) in sediment pore waters was attributed to complexation by organic ligands, and electrochemical measurements confirmed the existence of soluble organic-Fe(III) complexes in a variety of sedimentary environments (Brendel and Luther, 1995; Liang et al., 1993; Luther et al., 1996; von Gunten and Schneider, 1991). These soluble complexes, thereafter designated 'org-Fe(III)' have been detected in a number of freshwater (Chow and Taillefert, 2009; Ma et al., 2008), harbor (Brendel and Luther, 1995), salt marsh (Bull and Taillefert, 2001; Luther et al., 1996; Taillefert et al., 2007b; Taillefert et al., 2002b), estuarine (Beckler et al., 2015; Meiggs and Taillefert, 2011; Taillefert et al., 2002a), and continental shelf (Beckler et al., 2016; Taillefert et al., 2017; Taillefert et al., 2000b) sediments. Formation of org-Fe(III) has been attributed to either oxidation of Fe^{2+} by O_2 or aerobic Fe-oxidizing bacteria in the presence of organic ligands (Roden et al., 2004; Sobolev and Roden, 2001; Taillefert et al., 2000a), oxidation of complexed Fe(II) by Fe(III) (Beckler et al., 2015; Luther et al., 1992), or production during DIR (Beckler et al., 2015; Fennessey et al., 2010; Jones et al., 2010; Nevin and Lovley, 2002; Taillefert et al., 2007a). Although the source of org-Fe(III) in sediments may vary, spatial consideration of inorganic species, such as O_2, Fe^{2+}, $\sum H_2S$, and FeS_{aq}, with sediment depth may provide insight into the mechanism of org-Fe(III) formation. In this way, org-Fe(III) provides an additional tool to aid in differentiating between chemical and microbial Fe(III) reduction in natural environments. As the org-

Fe(III) ligands remain currently unknown and the organic ligands produced endogenously during DIR are likely different from exogenously produced org-Fe(III), identification of theses ligands would greatly aid in determining the source of org-Fe(III) signals in natural sediments.

1.3.2 Electron Shuttling Thiols as Proxies for Dissimilatory Metal Reduction in Sediments

Thiols represent good chemical reductants of Fe(III) oxides (Amirbahman et al., 1997; Eitel and Taillefert, 2017; Jameson et al., 1988; Sisley and Jordan, 1995), Fe(III) in clays (Morrison et al., 2013), MnO_2 nanoparticles (Altaf and Jaganyi, 2014; Andrabi and Khan, 2007; Herszage et al., 2003), and Mn(III) nanoparticles (Salamon et al., 2004). Thiols likely represent good chemical reductants of solid Mn(III,IV) oxides as well although this reaction has not previously examined. Amendments of thiols to pure cultures of Fe(III)-reducing bacteria have resulted in elevated Fe^{2+} production, demonstrating that thiols may be utilized as electron shuttles during DIR (Doong and Schink, 2002; Liu et al., 2014). Thiols have been detected in both marine (Kiene, 1991; Kiene and Taylor, 1988b; Luther et al., 1986; MacCrehan and Shea, 1995; Shea and MacCrehan, 1988) and freshwater sediments (Zhang et al., 2004), although they have not been related to iron concentrations. Given the rapid reduction of metal oxides by thiols and the ability of model Fe(III)-reducing bacteria to utilize thiols as electron shuttles, it is likely that natural microbial populations do the same. Thus, detection of thiols in a variety of sediments may provide evidence for DIR and allow differentiation between microbial and chemical Fe^{2+} production.

1.4 Sediments as an Important Source of Iron for Primary Production in the Surface Ocean

As an essential nutrient, iron exerts a substantial control on ocean productivity and export of organic matter to the deep ocean. Indeed, vast areas of the ocean are abundant in macronutrients such as nitrate, phosphate, and silica, but phytoplankton activity remains low. Such locations, termed high-nutrient low chlorophyll (HNLC) zones, are suspected to result from iron limitations (Coale et al., 1996; Kolber et al., 1994; Martin and Fitzwater, 1988). Such iron limitations may result from rapid oxidation of Fe^{2+} in fully oxygenated waters (Millero et al., 1995) and low solubility of Fe(III) at circumneutral pH (Liu and Millero, 2002). Significant sources of iron to the ocean include aeolian deposition (Fung et al., 2000; Jickells, 2001) as well as inputs from rivers (Martin and Meybeck, 1979; Poulton and Raiswell, 2002), hydrothermal vents (Tagliabue et al., 2010), icebergs (Bhatia et al., 2013; Raiswell et al., 2008), and continental margin sediments (Chase et al., 2005; Johnson et al., 1999) though contributions from these sediments are not well constrained. Interestingly, the iron flux from continental margin sediments has mostly been determined in upwelling zones (Berelson et al., 2003; Elrod et al., 2004; Esch et al., 2013; Lam and Bishop, 2008) or areas exposed to large riverine inputs and seasonal hypoxia (Friedl et al., 1998; Friedrich et al., 2002; Lohan and Bruland, 2008; Noffke et al., 2012; Severmann et al., 2010). Although upwelling may promote resuspension of particulate iron and advective transport of Fe^{2+} across the sediment-water interface (SWI) (Bruland et al., 2001; Bruland et al., 2005; Chase et al., 2005), once Fe^{2+} reaches oxic waters rapid oxidation and precipitation of Fe(III) oxides may decrease overall iron transport to the water column (Figure 1-3A). In addition, upwelling generates a shear stress across the sediment-water

interface that likely injects oxygenated waters and maintains suboxic conditions into the top few centimeters of sediments (Huettel et al., 1998; Taillefert et al., 2007b). In these conditions, sulfate reduction is likely limited and may eventually promote reductive dissolution of Fe(III) oxides to dissolved Fe^{2+} only.

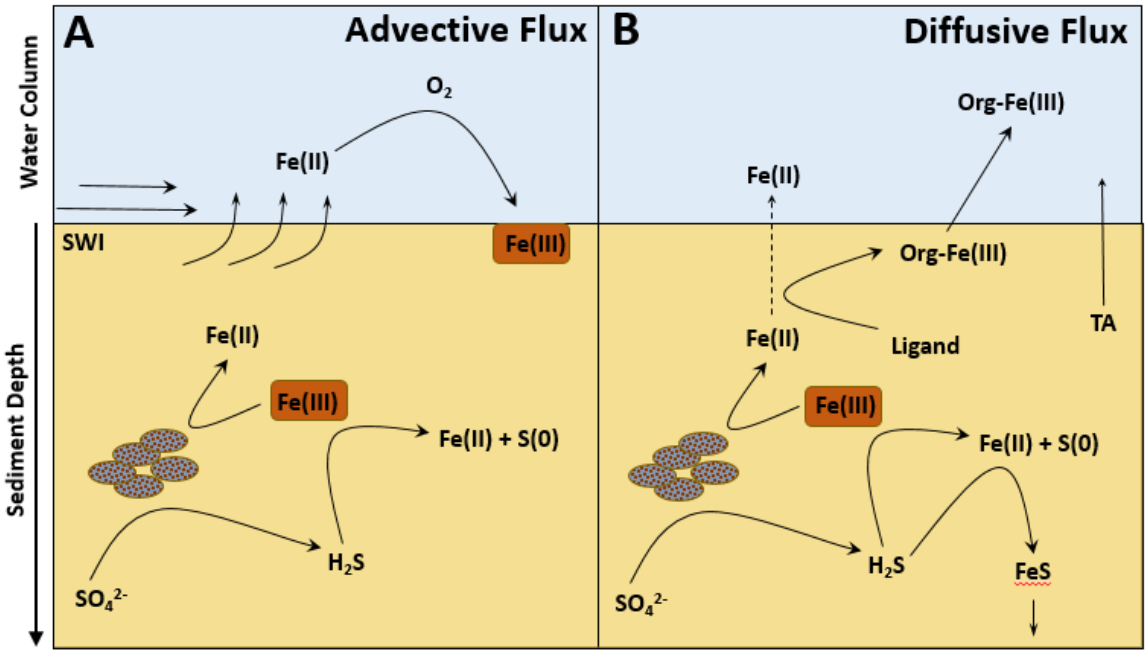

Figure 1-3. Two scenarios controlling the flux of iron across the sediment-water interface (SWI). A) Strong advective flux in upwelling zones may increase the transport of Fe(II) across the SWI and limit sulfate reduction. However, rapid Fe(II) oxidation and subsequent precipitation of Fe(III) oxides may dampen the overall contribution of these high Fe(II) fluxes to the bioavailable fraction in the water column. B) The diffusive flux prevalent in most continental margin sediments allows for Fe(II) oxidation and complexation of Fe(III) by natural organic ligands in the sediment, which may stabilize dissolved iron diffusing to the water column. Sediments receiving large inputs of natural organic matter, however, may be dominated by sulfate reduction, therefore promoting abiotic reduction of Fe(III) oxides and precipitation of FeS and suppressing the flux of Fe(III) across the SWI. As these reduced metabolites are buried rather than reoxidized near the SWI, the total alkalinity (TA) produced during microbial respiration is not consumed, resulting in

an upward TA flux which may buffer the overlying waters and mitigate ocean acidification of the water column.

In non-upwelling zones, advective forcing is decreased and molecular transport is primarily diffusion controlled. The slower diffusive transport of Fe^{2+} across the SWI allows time for complexation by natural organic ligands during Fe^{2+} oxidation in the sediment (Beckler et al., 2015; Luther et al., 1992; Roden et al., 2004; Taillefert et al., 2000a), which may increase iron stability and bioavailability in the overlying waters (Buck et al., 2007; Chase et al., 2005) (Figure 1-3B). In turn, the flux of iron across the SWI in non-upwelling zones may be suppressed by rapid formation and precipitation of FeS (Rickard and Luther, 2007) if the sediments are dominated by sulfate reduction. Thus, it is important to investigate both the flux and speciation of iron from marine sediments which do not experience strong advective forcing to evaluate their potential as a source of bioavailable iron to the ocean.

1.5 Hypotheses and Objectives of This Dissertation

The microbial mechanism of dissimilatory iron reduction may proceed through a number of pathways, resulting in a lack of genetic markers to identify this process. As a result, there is currently no good way to differentiate between microbial and chemical reduction of Fe(III) oxides. To overcome this problem, the possible use of chemical proxies of dissimilatory iron reduction, such as organic-Fe(III) complexes and small thiols, as electron shuttling compounds was investigated in well-defined conditions with pure cultures of an iron-reducing microorganism and in a variety of natural environments. Evidence suggests that thiols are good chemical reductants of metal oxides and may be utilized as electron shuttles by Fe(III)-reducing bacteria, resulting in the following hypothesis:

1.5.1 *Hypothesis 1: Small thiols are important electron shuttling compounds in dissimilatory metal reduction and may be used as chemical proxies to identify zones of dissimilatory metal reduction in sedimentary environments.*

In this dissertation, this hypothesis was tested by studying the abiotic reaction of thiols with Fe(III) and Mn(III,IV) oxides in environmentally relevant conditions and the prevalence of thiols in natural sediments in relation to Fe reduction.

Iron is a limiting nutrient in much of the ocean, however the source of iron is not well constrained. In particular, continental margin sediments may represent an important iron source to surface waters. Interestingly, however most studies have focused on upwelling zones and neglected passive margins even though they cover the majority of the oceans. Additionally, as complexation of Fe(III) may increase bioavailability and transport into oxic waters, it is important to consider speciation when assessing benthic iron production. Given these knowledge gaps, the following hypothesis was tested:

1.5.2 *Hypothesis 2: The formation of organic-Fe(III) complexes in low-energy sedimentary environments may provide a significant benthic iron flux to the overlying waters*

This hypothesis was tested by determining the diffusive flux and speciation of iron in a continental margin with limited upwelling and no major riverine input. The results of this study were compared to another study in continental margin sediments receiving significant inputs of organic matter and terrigenous material from a large river.

Although organic-Fe(III) complexes have been previously detected in a number of sediments and may originate from different processes in nature, pure culture incubations of model Fe(III)-reducing bacteria demonstrate that these species are produced during dissimilatory iron reduction. It is therefore hypothesized that:

1.5.3 Hypothesis 3: A unique class of Fe(III)-complexing organic ligands is generated by iron-reducing microorganisms to solubilize Fe(III) oxides.

Currently, the organic-Fe(III) ligands have not been identified in either pure cultures or sediments. In this dissertation, a method was optimized to isolate and identify standard Fe(III)-binding ligands and tested with Fe(III) binding ligands from pure culture incubations and natural sediment pore waters.

1.6 Organization of This Dissertation

After this introduction, Chapter 2 includes a collection of the analytical techniques employed throughout this work. Specific focus is placed the voltammetric techniques used to determine depth profiles of the main redox species in sediments and pure culture incubations. Additionally, a technique to measure trace level concentrations of Fe^{2+} by chemiluminesence was optimized for future analysis of samples collected autonomously by benthic chambers.

Chapter 3, published in *Geochimica et Cosmochimica Acta* (Eitel and Taillefert, 2017), presents an in-depth investigation of the chemical reduction of ferrihydrite by four common low molecular weight thiols (cysteamine, cysteine, homocysteine, reduced glutathione) at environmentally relevant concentrations and pH. A kinetic rate law was

determined and the molecular mechanism was investigated using a network of coupled elementary reactions in a kinetic model. The structure of the intermediate surface species formed with cysteamine, homocysteine, and glutathione is discussed in the context of the reaction.

Chapter 4, presently under review for *Environmental Science & Technology*, investigated the chemical reduction of fresh and aged Mn oxides with varied structures by the same thiols previously investigated with ferrihydrite (cysteamine, cysteine, homocysteine, reduced glutathione). As the rate of this chemical reaction is extremely fast, previous studies were not able to analyze thiol and disulfide concentrations *in situ* or with a high temporal resolution. This chapter represents the first study to investigate the reduction of solid Mn(III,IV) oxides by thiols.

Chapter 5, to be submitted for publication in *Limnology and Oceanography*, investigated the presence of thiols in relation to iron reduction in natural sediments. Sediments from five distinct locations were investigated including a freshwater bog located in the Frasier Experimental Forest in Colorado, a salt marsh from coastal Georgia, the Rhone river delta, the Gulf of Mexico near the Mississippi river delta, and a deep sea shelf break off the coast of North Carolina. Incubations of the model iron reducing bacterium *S. oneidensis* as well as marine sediments with and without amendments of molybdate to inhibit dissimilatory sulfate reduction investigated how the production of thiols was influenced by microbial respiration processes.

Evidence for the formation of soluble organic-Fe(III) in marine sediments raises the possibility that these complexes may be stable enough to persist in oxygenated waters and

that the flux of ferric iron at the sediment-water interface may be underestimated in continental margin sediments. Chapter 6, to be submitted for publication in *Marine Chemistry*, investigates the benthic flux and speciation iron in the continental margin off Cape Lookout, North Carolina. This continental margin does not experience major upwelling or input or large riverine inputs.

Chapter 7, currently under final revisions for *Marine Chemistry*, investigated early diagenesis in the Rhone River delta in collaboration with colleagues in France to determine the effect of sulfate reduction on iron speciation and benthic iron production.

Chapter 8 presents a new immobilized metal affinity chromatography (IMAC) procedure developed to isolate and identify the natural ligands involved in the solubilization of Fe(III) oxides. The method was optimized with model hydrophobic biogenic iron binding ligands riboflavin and desferroxamine-B through IMAC coupled with solid phase extraction (SPE), reverse phase liquid chromatography (LC), and electrospray ionization mass spectrometry (ESI-MS).

Finally, Chapter 9 synthesizes the main findings and conclusions of this dissertation and provide a suite of recommendations for future work.

CHAPTER 2. ANALYTICAL TECHNIQUES

2.1 Voltammetry

Voltammetry allows for rapid and non-disruptive measurement of multiple dissolved, redox active species simultaneously. In voltammetry the electrochemical potential between the working and reference electrode is varied as a function of time and the resulting current is recorded at the counter electrode. Voltammetry conducted with solid-state Au microelectrode amalgamated with Hg provides a unique method for *in situ* detection of redox active compounds in natural samples (Brendel and Luther, 1995). For this method, the three-electrode configuration consisted of the Au/Hg working electrodes, a Ag/AgCl reference electrodes, and Pt counter electrode for detection of dissolved O_2, Fe^{2+}, Mn^{2+}, ΣH_2S ($H_2S + HS^- + S^0 + S_x^{2-}$), FeS_{aq}, $S_2O_3^{-2}$, and org-Fe(III) (Brendel and Luther, 1995; Nuzzio et al., 2000; Taillefert et al., 2000a; Theberge et al., 1997). Dissolved O_2 is commonly determined by linear sweep voltammetry (LSV) between -0.1 and -1.75 V at a scan rate of 200 mV/s with an initial conditioning step of 10 s at -0.1 V and calibration *in situ* using temperature and salinity of the overlying water assuming oxygen was at saturation (Luther et al., 2008) (Figure 2-1A). All other species are typically determined by square-wave voltammetry, a pulsed voltammetric technique consisting of a square wave function superimposed onto a stair step potential sweep resulting in both forward and reverse potential scans (Osteryoung and Osteryoung, 1985). In cathodic square wave voltammetry (CSWV) (Figure 2-1B-E), scans are performed from positive to negative potentials, typically from between -0.1 and -1.75 V at a rate of 200 mV/s with a conditioning step of 10 s at -0.1 V (Brendel and Luther, 1995). When org-Fe(III) or $\sum H_2S$

are detected, an additional conditioning step of 10 s at -0.9 V is included prior the above procedure to clean the electrode (Taillefert et al., 2000b). For the detection of high $\sum H_2S$ concentrations anodic square wave voltammetry (ASWV) is conducted with scans from negative to positive potentials to prevent formation of cinnabar at the electrode surface, which passivates the electrode and decreases sensitivity (Davison et al., 1988). ASWV is typically conducted from -1.6 and -0.1 V at a rate of 200 mV/s (Figure 2-1F). Just before use, electrodes are calibrated for Mn^{2+} by CSWV with $MnCl_2$, and Mn^{2+} sensitivities are used to quantify species according to the pilot ion method (Brendel and Luther 1995). As org-Fe(III) and FeS_{aq} are not quantifiable, normalized current intensities to the sensitivity of a reference Au/Hg microelectrode are reported to compare results between electrodes (Tercier-Waeber and Taillefert, 2008). For these analyses, DLK-60,100,70 potentiostats (AIS, Inc.) were utilized along with a DLK-MAN-60 micromanipulator or a cell stand (AIS. Inc.). All voltammetric data were integrated using VOLTINT, a semiautomated Matlab script with peak recognition software (Bristow and Taillefert, 2008).

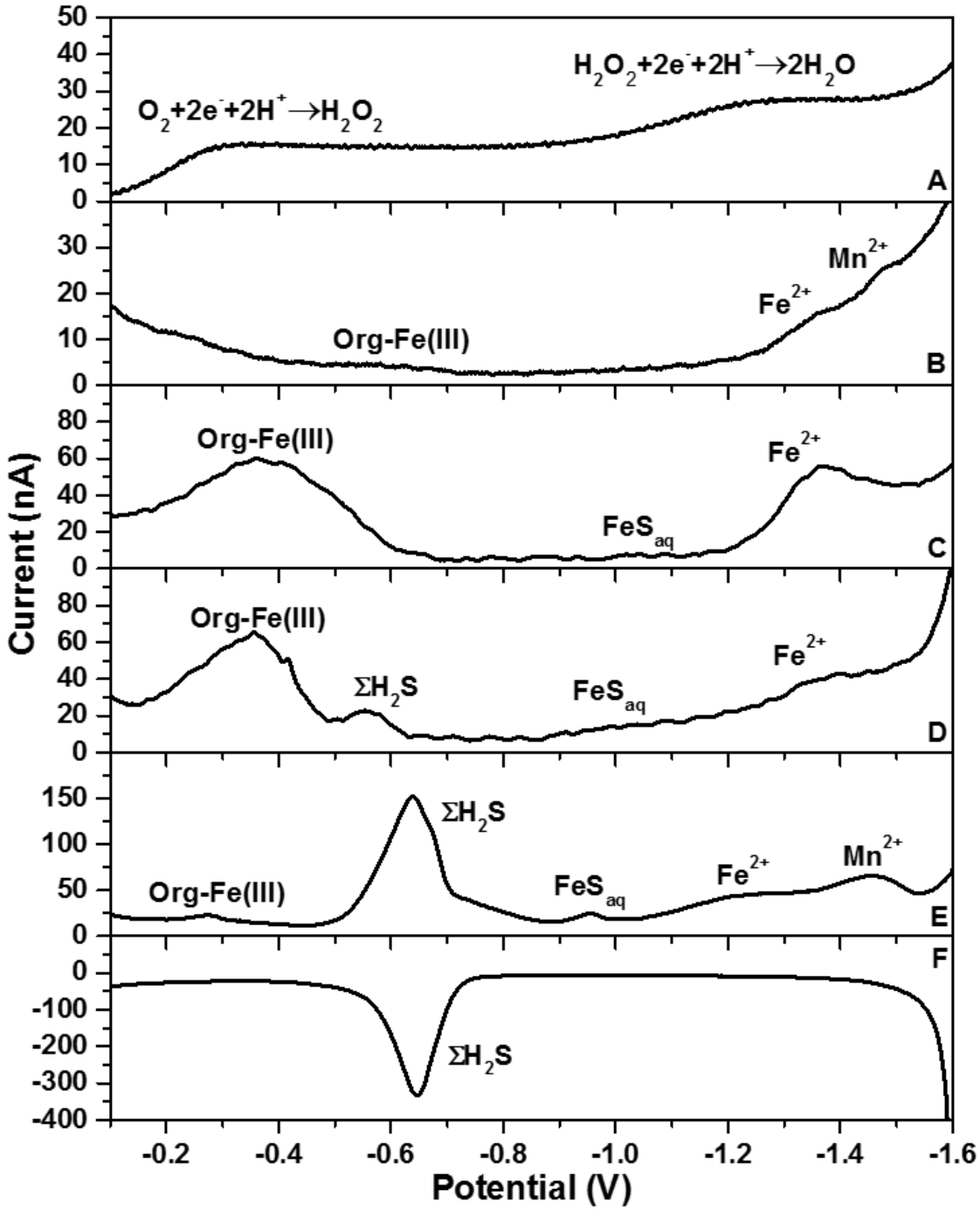

Figure 2-1 Examples of voltammograms obtained with Au/Hg microelectrodes in marine pore waters of A) LSV, B-E) CSWV, and F) ASWV.

2.2 Chemiluminescence

Luminol (5-amino-2,3 dihydro-1,4-phthalazinedione) has been previously used to detect trace Fe^{2+} in natural samples (Emmenegger et al., 1998; Hansard and Landing, 2009; King et al., 1995; O'Sullivan et al., 1995; Rose and Waite, 2001). The following method was developed for the detection of Fe^{2+} in benthic chamber samples collected in the Gulf of Mexico during a cruise on the R/V Savannah in July 2017.

Luminol reagent comprised of 0.001 M luminol in 1 M NH_4OH is prepared in opaque HMPE containers. After mixure of the reagent, the pH is adjusted to 10.3 with concentrated HCl (~5 mL) and heated for ~ 15 hours at 60ºC to enhance sensitivity (Hansard and Landing, 2009). The solution is cooled before use and may be kept for up to 1 week, although sensitivity decreases with time. Weekly Fe^{2+} stocks are made with 4 mM ferrous ammonium sulfate in 0.2 M HCl. Daily stocks are diluted to 2 mM Fe^{2+} in 0.3 mM HCl, which is acidified enough to prevent rapid oxidation but does not significantly alter the pH when added to seawater. Standards are prepared by addition of the daily stock to seawater that has been bubbled with air for at least one day to allow for complete oxidation of any trace Fe^{2+}. Sulfite maybe used as reductant of Fe(III) for the detection of total dissolved iron (O'Sullivan et al., 1995). For this purpose, a 0.04 M sulfite stock solution is prepared by addition of Na_2SO_3 in 15 mL of water and 5 mL of 0.4 M ammonium acetate at pH 5.5. To each 1 mL sample, 2.5 µL of the sulfite stock should be added.

For analysis, the AIS, Inc. chemiluminescence detector prototype containing the photomultiplier (Hamamatsu PMT H11462-011) must be kept completely in the dark as even traces of light will affect the photomultiplier (PMT). With great care, a baseline signal

close to 0 au (arbitrary units) can be reached. The signal is saturated at -9.166 au. Samples (or standards) and the luminol reagent must me mixed directly before the photomultiplier due to the rapid reaction between luminol and Fe^{2+}. As a result, these two solutions are injected at equal flow rates using peristaltic pump (Ismatec®) and mixed with a Y-junction directly before the PMT window. The protorype flow cell consists of coiled Tygon tubing taped directly to the face of the detector, however a serpentine flow cell would be ideal to ensure consistent mixing of the luminol reagent and sample (Terry et al., 2008). To increase mixing and allow detection of the luminescence produced during the rapid reaction between Luminol and Fe^{2+} of the sample or standard, a fast flow speed (~ 4 mL/min) is necessary. Even if both sample and luminol are pumped at equal rates, in a low pressure system equal mixing is difficult to achieve. Increased mixing can be achieved with a backpressure valve positioned at the output of the PMT to better control the flow, however calibrations immediately before sample analysis are recommended without powering off the pump to avoid variations in flow rates which generate fluctuations in chemiluminescence response.

Samples were measured from benthic chamber incubations during a research cruise in the Gulf of Mexico during July 2017 on the R/V Savannah. Immediately upon retrieval of the lander, benthic chamber samples were filtered using 0.2 µm Puradisc polyethersulfone (PES) syringe filters (Whatman) under a N_2 atmosphere to prevent oxidation of Fe^{2+}. To each 10 mL sample collected, 10 µL 6 M HCl was added to slightly acidify samples and decrease oxidation. Calibrations between 20 pM and 3 nM Fe^{2+} were run (Figure 2-2) as samples were filtered by someone else such that samples could be immediately analyzed after removal from the N_2 atmosphere. Benthic chamber samples

from six stations during the cruise were analyzed (Figure 2-3). Although the success of the benthic chamber incubations is unclear, these results demonstrate the potential for this method to detect trace Fe^{2+} in natural samples.

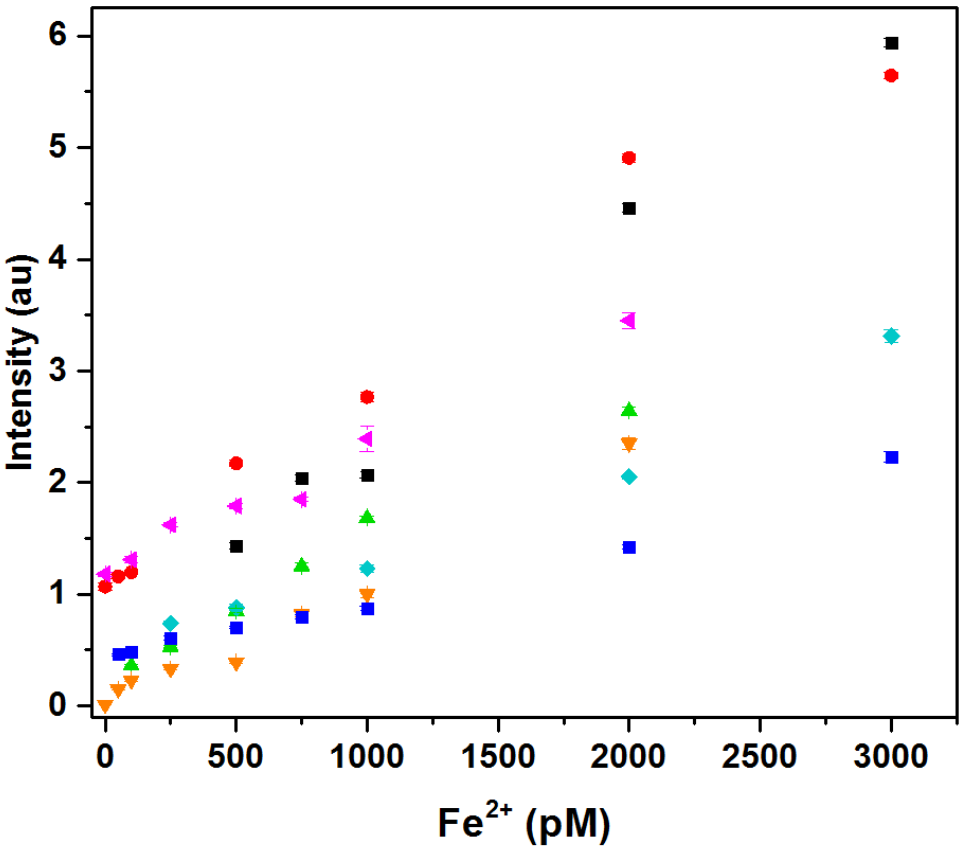

Figure 2-2 Calibration curves collected on the R/V Savannah in July 2017.

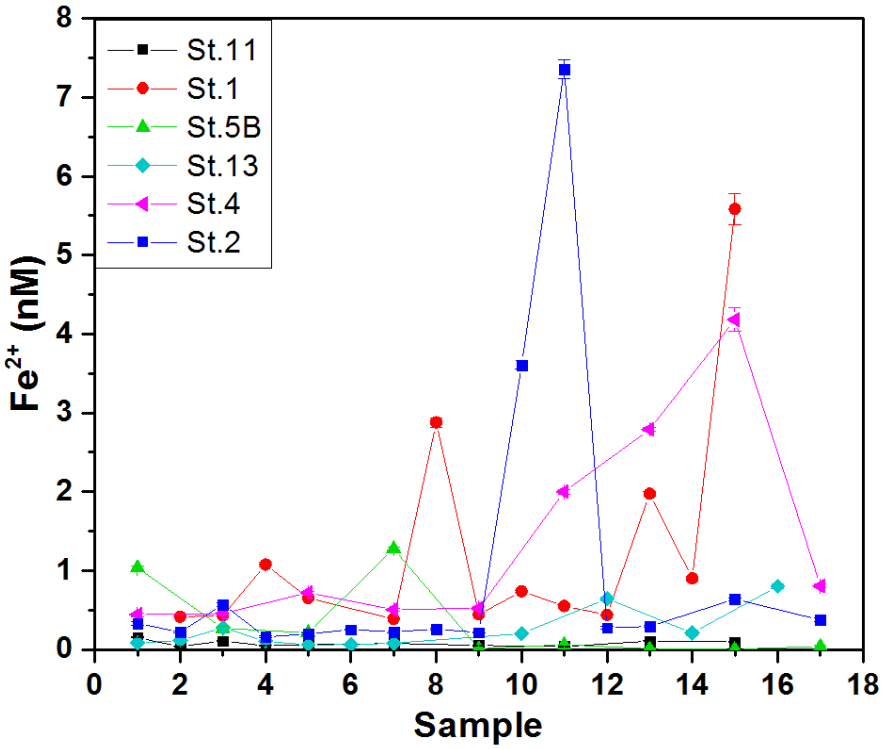

Figure 2-3 Analysis of Fe^{2+} in benthic chamber samples collected in the Gulf of Mexico in July 2017.

CHAPTER 3. MECHANISTIC INVESTIGATION OF FE(III) REDUCTION BY LOW MOLECULAR WEIGHT ORGANIC SULFUR SPECIES

This is the reprint of an article published in *Geochimica et Cosmochimica Acta*, authored by Eryn Eitel and Martial Taillefert entitled "Mechanistic Investigation of Fe(III) reduction by low molecular weight organic sulfur species".

3.1 Abstract

Low molecular weight organic sulfur species, often referred to as thiols, are known to be ubiquitous in aquatic environments and represent important chemical reductants of Fe(III) oxides. Thiols are excellent electron shuttles used during dissimilatory iron reduction, and in this capacity could indirectly affect the redox state of sediments, release adsorbed contaminants via reductive dissolution, and influence the carbon cycle through alteration of bacterial respiration processes. Interestingly, the reduction of Fe(III) oxides by thiols has not been previously investigated in environmentally relevant conditions, likely due to analytical limitations associated with the detection of thiols and their oxidized products. In this study, a novel electrochemical method was developed to simultaneously determine thiol/disulfide pair concentrations *in situ* during the reduction of Fe(III) oxides. First order rate laws with respect to initial thiol concentration were confirmed for Fe(III) oxide reduction by four common thiols: cysteine, homocysteine, cysteamine, and glutathione. Zero order was determined for both Fe(III) oxide and proton concentration at circumneutral pH. A kinetic model detailing the molecular mechanism of the reaction was optimized with proposed intermediate surface structures. Although metal oxide overall reduction rate constants were inversely proportional to the complexity of the thiol structure,

the extent of metal reduction increased with structure complexity, indicating that surface complexes play a significant role in the ability of these thiols to reduce iron. Taken together, these results demonstrate the importance of considering the molecular reaction mechanism at the iron oxide surface when investigating the potential for thiols to act as electron shuttles during dissimilatory iron reduction in natural environments.

3.2 Introduction

Iron transformations greatly impact a variety of biogeochemical processes in the environment. First, Fe(III) oxides are good scavengers of inorganic and organic contaminants, and their dissolution in reducing conditions may lead to the release of these adsorbed contaminants (Borch et al., 2010; DiChristina et al., 2005; Lovley, 1991; Lovley et al., 1989). Second, reduction of Fe(III) oxides by dissolved sulfides produced by dissimilatory sulfate reduction can lead to the formation of $FeS_{(s)}$ (Pyzik and Sommer, 1981) and pyrite (Rickard, 1997) which may buffer the redox state of reducing environments. Third, dissimilatory reduction of Fe(III) oxides may significantly contribute to the cycling of organic carbon in the absence of dissimilatory sulfate reduction (Kostka et al., 2002; Meiggs and Taillefert, 2011; Thamdrup et al., 1994). Finally, Fe(II) produced by the reductive dissolution of Fe(III) oxides abiotically interacts with a variety of other biogeochemically important species, including $O_{2(aq)}$ (Burns et al., 2010), NO_2^- (Vancleemput and Baert, 1983), Fe(III) oxides (Hansel et al., 2005; Latta et al., 2012), Mn(IV) oxides (Postma and Appelo, 2000), and dissolved sulfides (ΣH_2S) (Pyzik and Sommer, 1981). Thus, the product of the reduction of Fe(III) oxides may have an indirect effect on biogeochemical processes by removing significant oxidants of natural organic matter (i.e. $O_{2(aq)}$, NO_2^-, Mn(IV) oxides), reducing organic contaminants (i.e.

nitroaromatics, chlorinated solvents, pesticides), and sequestering reductants in the solid phase (i.e. ΣH_2S).

Although not often recognized as playing a large role in the cycling of iron, thiols are known to be good chemical reductants of Fe(III) oxides (Amirbahman et al., 1997; Jameson et al., 1988; Sisley and Jordan, 1995) as well as Fe(III) in clays (Morrison et al., 2013). The overall reduction of Fe(III) by thiols, represented as RSH in Eq. 3-1, produces two moles of Fe(II) and one disulfide species (RSSR) per two moles of thiol reactant.

$$2\,Fe(OH)_3 + 2\,RSH + 4H^+ \leftrightarrow RSSR + 2\,Fe^{2+} + 6H_2O \qquad (3\text{-}1)$$

The mechanism of the reaction has been proposed to proceed via adsorption of the electron transferring sulfhydryl group of the thiol onto the Fe-oxide surface to form either a neutral or a negatively charged species, depending on the possible deprotonation of functional groups on the thiol ligand, and a water molecule (Amirbahman et al., 1997) (Eq. 3-2).

$$\equiv FeOH + RS^- + nH^+ \leftrightarrow \equiv FeRS^{n-1} + H_2O \qquad (3\text{-}2)$$

Where *n* represents the number of protons exchanged with the solution during the surface complexation reaction (*n* = 1 for a neutral surface species or *n* = 0 for negatively charged surface species).

The surface species formed proceeds through a series of reactions (Amirbahman et al., 1997) characterized primarily by the electron transfer reaction (Eq. 3-3) followed by rapid dissolution of the thiol radical (Eq. 3-4), dissolution of Fe(II), and regeneration of the

oxide surface (Eq. 3-5). In solution the thiol radical immediately dimerizes to form the stable disulfide product (Eq. 3-6).

$$\equiv FeRS^{n-1} \xrightarrow{e^- transfer} \equiv Fe(II)RS^{\cdot} + (n-1)H^+ \quad (3\text{-}3)$$

$$\equiv Fe(II)RS^{\cdot} + H_2O \xrightarrow{fast} \equiv Fe(II)OH_2 + RS^{\cdot} \quad (3\text{-}4)$$

$$\equiv Fe(II)OH_2 + 2H^+ \xrightarrow{fast} \equiv Fe(III)OH + Fe(II) \quad (3\text{-}5)$$

$$2RS^{\cdot} \xrightarrow{fast} RSSR \quad (3\text{-}6)$$

Naturally occurring thiols have been detected in a variety of aquatic environments. Glutathione has been observed in concentrations ranging from 225 nM to 2.4 µM in marine sediments (Kiene and Taylor, 1988a; Luther et al., 1986), up to 300 nM in marine waters (Legall and Van Den Berg, 1993), and reaching intracellular concentrations as high as 12 mM in plant and microbial cells (Giovanelli, 1987; Meister and Anderson, 1983). Cysteine has been reported in even larger concentrations (i.e. ~10 µM) in marine pore waters (Shea and Maccrehan, 1988). Although homocysteine and cysteamine contribute to the production of cellular glutathione (Meier and Issels, 1995) and cysteamine, in particular, is thought to have been prevalent in early Earth (Miller and Schlesinger, 1993), the source of these thiols in aquatic environments remains under debate. The concentration of thiols in both fresh and marine waters has been correlated to chlorophyll levels and, therefore, attributed to phytoplankton production (Al-Farawati and Van Den Berg, 2001; Hu et al., 2006; Matrai and Vetter, 1988a), whereas microbial production of thiols has been attributed to the detoxification of toxins such as Cu, Hg, and, Zn by complexation in both marine

waters and sediments (Chapman et al., 2009; Kawakami and Achterberg, 2012; Legall and Van Den Berg, 1993; Park and Butcher, 2010; Shea and Maccrehan, 1988; Zhang et al., 2004b). Thiols may also be produced in natural environments as a result of microbial deamination of amino acids (Kiene et al., 1990) as well as microbial degradation of plant material (Kiene and Taylor, 1988a; Kiene and Taylor, 1988b; Sorensen, 1988). Finally, thiols may be produced from the reaction of dissolved sulfides with natural organic matter (Luther et al., 1986; Vairavamurthy and Mopper, 1987).

Regardless of their source, thiols represent excellent potential electron shuttles during dissimilatory iron reduction. In this process, the reduced electron shuttle delivers electrons to the Fe(III) oxides at distance through an abiotic process resulting in the formation of the oxidized form of the shuttle. The oxidized shuttle is then reduced microbially to complete the catalytic cycle which can be repeated numerous times. Using this approach, the production of millimolar Fe(II) may result from the cycling of just nanomolar concentration of electron shuttle. Model iron reducing bacteria, *Geobacter sulfurreducens* and three different strains of *Shewanella*, demonstrated the ability to reduce cystine to cysteine (Doong and Schink, 2002; Kaden et al., 2002; Liu et al., 2014). Amendment of both the thiol and disulfide forms to incubations of *Shewanella algae* on smectites increased the initial rate and extent of Fe(II) production by around 19% (Liu et al., 2014), whereas experiments with *G. sulfurreducens* and ferrihydrite showed a 5 fold increase in Fe(II) production when amended with 0.5 mM cysteine and a 2.5 fold increase when amended with 0.5 mM cystine (Doong and Schink, 2002). Both studies observed a linear increase in the initial rate of Fe(II) production as a function of the concentration of thiol added to the incubations. These pure culture experiments confirm that microorganisms

capable of dissimilatory Fe(III) reduction are able to utilize thiols as electron shuttles and imply that the same process could be significant in natural environments.

As multiple thiols are present in natural environments, the reactivity of these thiols with Fe(III) oxides likely controls the rate of iron reduction, and the electron shuttle with the lowest redox potential is expected to represent the most favorable electron donor. Thus, glutathione should reduce Fe(III) oxides at a greater rate and extent than cysteine due to its slightly more negative standard redox potential (E^0 = -0.24 V for gluthathione versus E^0 ranging from -0.21 V to -0.23 V for cysteine) (Jocelyn, 1967). However, the addition of anthraquinone-2,6-disulfonate (AQDS), a commonly studied electron shuttle with a standard redox potential of -0.184 V, to cultures resulted in higher microbial Fe(III) rates and extent than similar incubations with cysteine (O'Loughlin, 2008), despite the lower reduction potential of the cysteine/cystine couple. Although differences in enzyme specificity and binding affinity may explain this behavior, electron shuttle structure is likely to play an important role in both the abiotic and biotic aspects of this cyclic process (Liu et al., 2014). In such case, a mechanistic understanding of the reaction is required to determine the potential role of low molecular weight organic sulfur species as electron shuttles in the cycling of iron in natural environments.

Although previous studies have investigated the reduction of Fe(III) oxides and clays by cysteine, rate laws of these reactions and their mechanisms remain poorly defined for a variety of reasons. First, previous experiments have been conducted at extreme pH which is unlikely to occur in natural environments. Second, these investigations have primarily been carried out in excess thiols, mainly because of issues with the detection limit of analytical techniques. As the presence of excess thiols may affect rates due to the alteration

of the mole fraction of active sites to total sites on the Fe(III) oxides during the course of the reaction (Stumm, 1992) , these kinetic parameters may not be relevant in natural environments. Finally, these studies have focused solely on the oxidation of cysteine while ignoring other environmentally relevant thiols. As a result, a study investigating the mechanistic reduction of Fe(III) oxides by thiols at both environmentally relevant concentrations and circumneutral pH has yet to be reported. The objective of this study was to determine a kinetic rate law and the step by step mechanism of reduction of Fe(III) oxides by four common low molecular weight thiols in natural environments: cysteamine (CA), cysteine (CS), homocysteine (HS), and glutathione (GS). Investigation of a variety of thiols will not only fill gaps necessary to understand their role in natural settings, it will also provide new information on the influence of the thiol structure on their reactivity and the rate determining step in the reaction.

3.3 Methods

3.3.1 Experimental Setup

Thiol and disulfide stocks were prepared weekly (Sigma-Aldrich, Inc: L-Cysteine ≥ 98%, L-Cystine ≥98%, Cysteamine ≥98%, Cystamine dihydrochloride ≥98%, DL-Homocysteine ≥95%, DL-Homocystine, L-Glutathione reduced ≥98%, L-Glutathione oxidized ≥98%) and stored at 4˚C. Two-line ferrihydrite was prepared by titration of $FeCl_3$ solution by 10 mM NaOH to pH 7 as described previously (Schwertmann, 2000). Fe(III) oxides were washed with milliQ-water three times prior to use, and experiments were performed in 100 mL sealed PEEK^{TM} batch reactors specifically fabricated for *in situ* detection of voltammetrically active redox species with gold/mercury amalgam (Au/Hg)

microelectrodes (Taillefert et al., 2007a). Reactors were amended with Fe(III) oxides, and degassed for 2 h with ultra-high purity (UHP) N_2 previously passed through a copper oxide column heated at 350 °C to remove traces of oxygen. Thiols were injected with a syringe through the sample port at time zero, and the slurries were stirred constantly during the experiments, except during the voltammetric analyses, using a magnetic stir bar. All experiments were conducted in at least duplicate in solution composed of inorganic salts (mainly $(NH_4)_2SO_4$) buffered at pH 7.0 with 5.7 mM K_2HPO_4/ 3.3 mM KH_2PO_4 (0.09 M ionic strength) unless otherwise noted (Myers and Nealson, 1988). A suite of experiments was also conducted over a range of pH between 6 and 8 to determine the order of the reaction with respect to the proton concentration. In these experiments, the same phosphate buffer was used but the pH was initially adjusted with 10 M HCl or NaOH.

3.3.2 In Situ Electrochemical Detection of Thiols and Their Disulfide Species

Voltammetric measurements were performed with a three electrode system consisting of a 100 µm diameter Au/Hg microelectrode as working electrode, a 500 Pt µm diameter counter electrode, and a 500 µm diameter Ag/AgCl reference electrode all encased in 3 mm diameter PEEK™ (polyethyletherketone) tubing as previously described (Luther et al., 2008). All the potentials reported below are therefore relative to the standard potential of the saturated Ag/AgCl system. The Au/Hg microelectrode was prepared by polishing the gold wire with 15, 6, 1, and 0.25 µm diamond pastes (Buehler) followed by plating with Hg at -0.1 V in a $Hg(NO_3)_2$ solution and polarization at -9.0 V for 90 s to stabilize the amalgam (Brendel and Luther, 1995). Voltammetric measurements were carried out with a computer-operated DLK-100A potentiostat (Analytical Instrument Systems, Inc.), and data was integrated using VOLTINT a semi-automated Matlab™ script

(Bristow and Taillefert, 2008). To confirm electrode quality, electrodes were calibrated for Mn^{2+} in degassed solution by cathodic square wave voltammetry (CSWV) from -0.1 to -1.75 V at 200 mV/s with a preconditioning step at -0.1 V for 10 seconds. Electrodes were then calibrated for thiol and disulfide species in degassed solution based on previous observations of cysteine and cystine at the hanging Hg drop electrode (Stankovich and Bard, 1977). CSWV was performed solely for the detection of disulfide species at -1.1 V (Figure 3-1A).

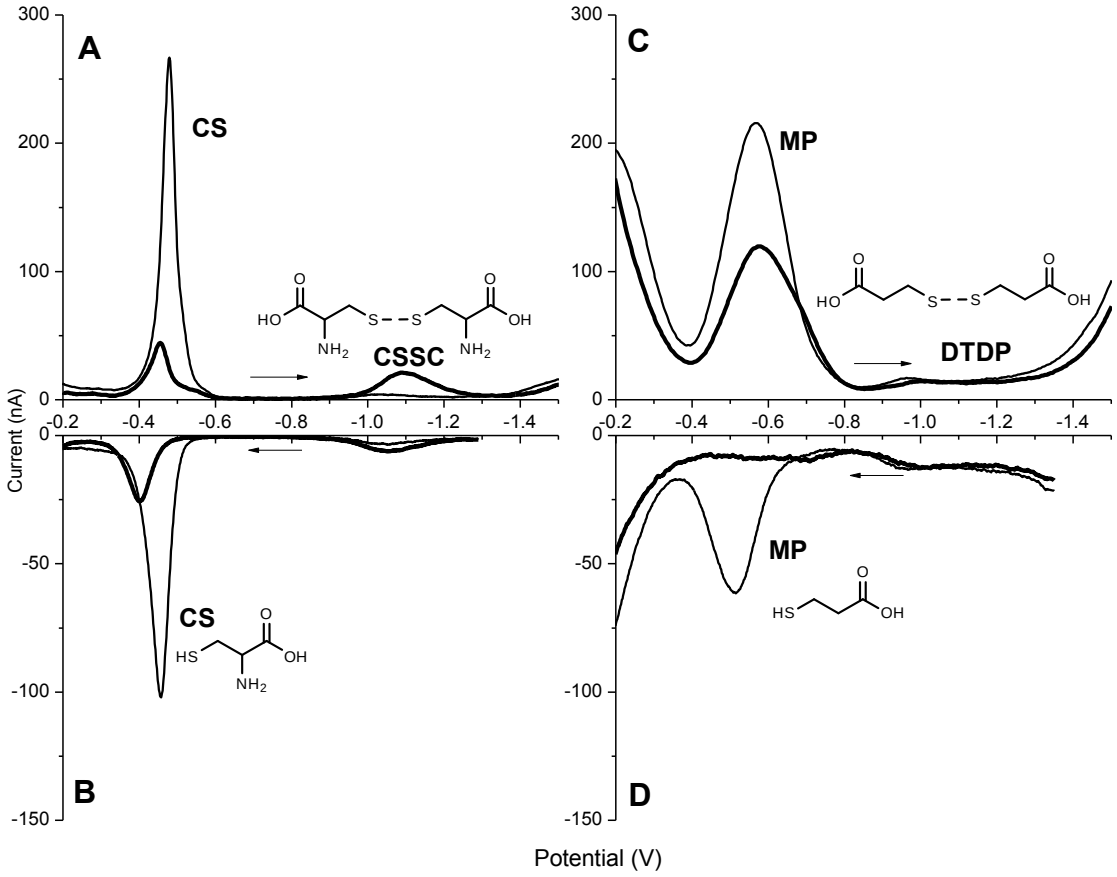

Figure 3-1 A) Cathodic square wave (CSW) and B) anodic square wave (ASW) voltammetry scans obtained with 200 µM cysteine (CS, thin line) and cystine (CSSC, bold line). C) CSW and D) ASW voltammetry scans obtained with 200 µM mercaptopropanoic acid (MP, thin line) and dithiodipropanoic acid (DTDP, bold line). Concentrations of disulfide species were quantified from their cathodic peak at -1.1 V. Although thiols produce a clear cathodic voltammetry signal at ca -0.47 V, the anodic voltammetry peak at ca. -0.45 V was preferentially used to quantify thiols, as it does not suffer from double film formation of cinnabar-like species at the mercury electrode. When needed, the disulfide concentrations measured cathodically were substracted from the concentrations obtained anodically to quantify the thiol signals accurately. Cathodic voltammetry peak near -1.1 V and anodic voltammetry peak near -0.45 V were not observed for disulfide species lacking amine groups (e.g. dithiopropanoic acid) such that only their reduced thiol form could be quantified accurately at ca. -0.5 V using ASW.

At this potential disulfide species in solution are reductively cleaved to their individual thiols:

$$(RSSR)_{soln} + 2H^+ + 2e^- \rightarrow 2(RSH)_{soln} \quad (3\text{-}7)$$

Scans were run from -0.1 to -1.75 V at a rate of 200 mV/s. A preconditioning step of 10 seconds at -0.8 V was added to clean the electrode surface between measurements and reduce adsorption of disulfide species to the electrode surface. Although another clear peak observed at -0.47 V by CSWV receives contributions from both species (Figure 3-1A) and could be used along with the peak at -1.1 V to determine the concentration of thiols by difference, it suffers from possible interference caused by the formation of double films of cinnabar like complexes on the electrode surface (Davison et al., 1988). Anodic square wave voltammetry (ASWV) often provides cleaner results with thiol species by preventing the formation of these interfering complexes and was primarily used in this work. ASWV scans were run from -1.45 to -0.1 V at a rate of 200 mV/s with a preconcentration step at -1.45 V for 10 seconds to detect a combined signal at -0.44 V (Figure 3-1B) resulting from the reductive cleavage of the Hg-adsorbed disulfide species (Eq. 3-8):

$$[Hg(RSSR)]_{ads} + 2H^+ + 2e^- \rightarrow 2(RSH)_{soln} + Hg \quad (3\text{-}8)$$

as well as the oxidation of any thiol present on the electrode surface to a mercuric thiolate species (Eq. 3-9):

$$2(RSH)_{soln} + Hg \leftrightarrow [Hg(RS)_2]_{ads} + 2H^+ + 2e^- \quad (3\text{-}9)$$

As a result, the concentration of the disulfide species quantified cathodically was substracted from the concentration of total thiol quantified anodically to correct for the potential interference of the disulfide species on the anodic signal. Optimization of the method for simultaneous thiol/disulfide detection of a variety of compounds indicated that disulfides lacking an amine functional group (e.g dithiodiglycolic acid, dithiodipropanoic acid, and oxidized Ellman's reagent) did not produce consistent cathodic voltammetric signals at -1.1 V (Figure 3-1C) or anodic signals (Figure 3-1D), although thiols lacking an amine still produced voltammetric signals cathodically at -0.59 V and anodically -0.45 V (Figure 3-1C, D). Thus, the concentration of disulfide species for these compounds could not be determined experimentally *in situ* and their kinetics of transformation was not investigated further.

3.3.3 Determination of Thiols and Disulfide by HPLC

The in situ voltammetric detection of thiol and disulfide species was confirmed by high pressure liquid chromatography (HPLC) after fluorescent derivation based on a previously developed method (Isokawa et al., 2013) using a ZIC-HILIC column (150 mm x 2.1 mm i.d., 5 mm, Merck, Germany). The reducing agent tris(2-carboxylethyl)phosphine (TCEP) was omitted for detection of the thiol species, and disulfide concentrations were obtained by subtraction of the thiol species quantified without TCEP from the total sulfur species obtained after reduction with TCEP. The separation was conducted in the isocratic mode at a flow rate of 0.4 mL/min with a Waters 1525 binary high-pressure pump and a mobile phase consisting of 75/25% (v/v) acetonitrile and 10 mM ammonium formate buffer (pH 3.0). In line detection of dissolved sulfur species was achieved by excitation at 375 nm and emission at 510 nm using a Waters 2475 fluorescence detector.

3.3.4 Modeling Thiol Transformation Using a Mechanistic Approach

A kinetic model based on a series of reversible and irreversible elementary reactions was developed and implemented in Matlab^{TM} to diagnose our understanding of the reaction mechanism. The model was based on a standard transition state theory formulation that includes the reversible adsorption of thiols onto Fe(III) oxides to form a transition state complex which further react in an electron-transfer reaction to form the products. The adsorption reaction was supplemented with the irreversible removal of the thiol compound to reproduce observations. In each case, the suite of coupled ordinary differential equations was integrated using the Runge-Kutta-(4,5)-based Matlab^{R} solver, *ode45*, and elementary rate constants were optimized to both the thiol and disulfide species over time with the nonlinear least squares Matlab^{R} solver, *lsqcurvefit*. For cysteine, triplicate reactions were optimized independently, and individual rate constants averaged to determine the final values. Given the good reproducibility of the reactions, only duplicate experiments were conducted with cysteamine, homocysteine, and glutathione.

3.4 Results

3.4.1 Kinetics of Fe(III) Oxyhydroxides Reduction by Thiols

The voltammetric detection of thiol and disulfide species was confirmed by comparison with HPLC results during the reduction of Fe(III) oxides by homocysteine. In these experiments, disulfide species as a function of time were within 95.5 (±0.4) % of the concentrations obtained by HPLC (not shown). The iron reaction product, Fe(II), remained mostly below detection limit during each of these reactions, likely due to their re-adsorption onto the excess Fe(III) oxide. All four thiols investigated were rapidly

consumed, and the resulting disulfide species were released into solution, though differences in reactivity between the various thiols was observed (Figure 3-2).

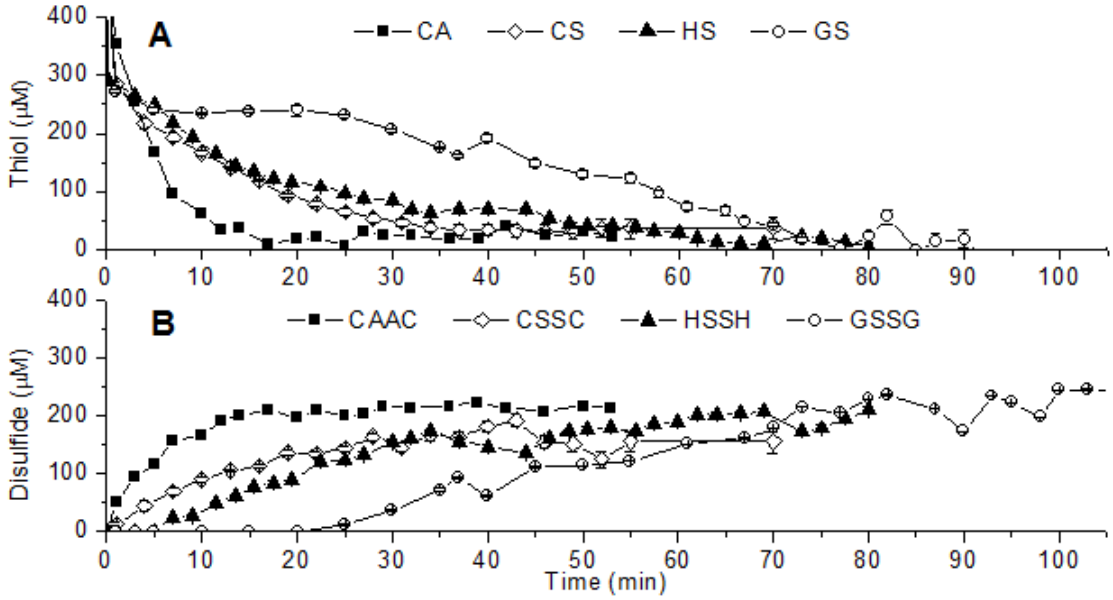

Figure 3-2 Time evolution of A) the thiols cysteamine (CA), cysteine (CS), homocysteine (HS), and reduced glutathione (GS) and B) their disulfide products cystamine (CAAC), cystine (CSSC), homocysteine (HSSH), and oxidized glutathione (GSSG) in solution during the reaction of 500 µM thiol with 40 mM Fe(III) oxide at pH 7.0. Standard deviations represent the average of at least triplicate measurements at each time point and are often smaller than the symbols.

Cysteamine reacted the fastest and was below detection limit (~10 µM) after 17 minutes. Similarly, cysteine, homocysteine, and glutathione were completely removed from solution in 37, 68, and 77 minutes respectively (Figure 3-2A). Although both cystamine and cystine were produced immediately after the addition of thiol to the Fe(III) oxide suspension (half-life of 5.5 and 15 minutes), homocystine (half-life of 32 minutes), and oxidized glutathione (half-life of 61 minutes) lagged in their production and did not initially appear until 5 and 25 minutes respectively (Figure 3-2B). According to the stoichiometry of the reaction (Eq. 3-1), 250 µM disulfide should be produced at steady-state by reaction of 500 µM thiol with

an excess Fe(III) oxides. These theoretical yields, however, were not reached with any of the thiols as the reaction extent (calculated as experimental disulfide yields ÷ theoretical yield x 100) as only 90.6 % of cysteamine, 58.7% of cysteine, 69.2% of homocysteine, and 97.9% of glutathione were found as cystamine, cystine, homocystine, and oxidized glutathione, respectively (Table 3-1).

Table 3-1 Measured Compared to Modeled Overall First Order Rate Constants (k) as well as Reaction Extent for the Reduction of Ferrihydrite by each Thiol at pH 7.0. Measured Overall First Order Rate constants were Calculated from the Experimental Data, Whereas Modeled Overall First Order Rate constants were Obtained from the Optimized set of Kinetic Rate Laws. The Reaction Extent of the Oxidation of Each Thiol by Ferrihydrite was Calculated from the Experimental Disulfide Yield.

Thiols	Measured k [min^{-1}]	Modeled k [min^{-1}]	Reaction Extent
Cysteamine	0.10 ± 0.05	$0.10 \pm 1x10^{-3}$	90.6%
Cysteine	0.035 ± 0.003	$0.034 \pm 2x10^{-5}$	58.7%
Homocysteine	0.016 ± 0.008	$0.017 \pm 2x10^{-5}$	69.2%
Glutathione	0.011 ± 0.002	$0.011 \pm 7x10^{-5}$	97.9%

Although the fraction of adsorbed species that reacts to form the disulfide products cannot be experimentally differentiated from the fraction of adsorbed species that does not contribute to the formation of disulfides, the total adsorbed fraction ($[FeRS]$) can be determined by mass balance as:

$$[FeRS] = [RS^-]_0 - [RS^-] - 2[RSSR] \quad (3\text{-}10)$$

where $[RS^-]_0$ is the initial concentration of thiol, $[RS^-]$ is the concentration of thiol, and $[RSSR]$ is the concentration of disulfide in solution measured during the course of the reaction. Not surprisingly, mass balance performed at each time step indicated the total adsorbed fraction reacted differently depending on the thiol investigated (Figure 3-3).

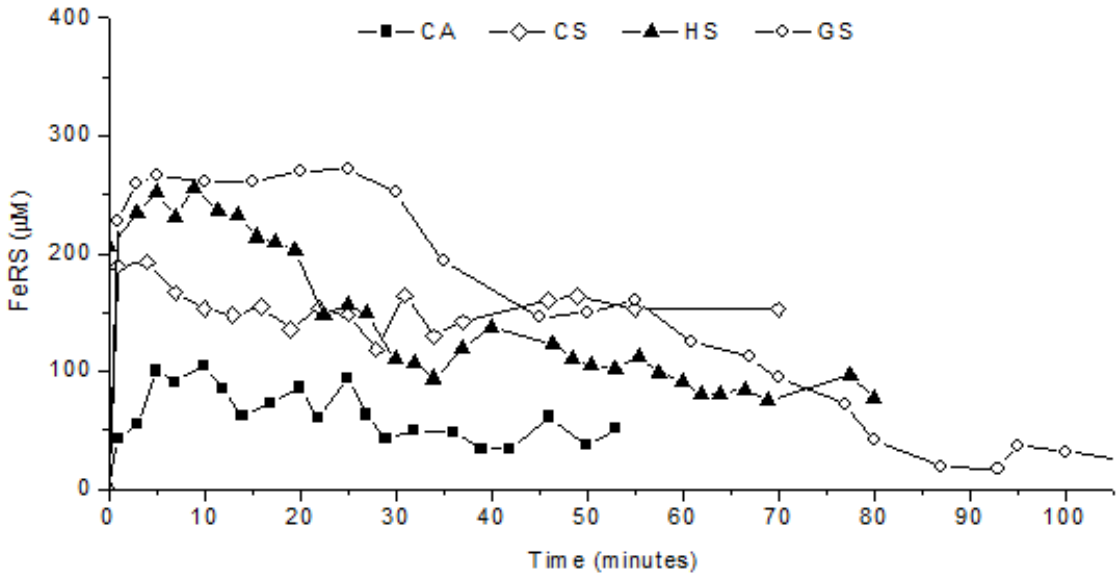

Figure 3-3 Time evolution of the total adsorbed surface species ($FeRS$) calculated from mass balance for thiols cysteamine (CA), cysteine (CS), homocysteine (HS), and reduced glutathione (GS) during the reaction of 500 µM thiol with 40 mM Fe(III) oxide at pH 7.0.

Although the fraction of each adsorbed thiol reached a maximum concentration within 10 minutes, then decreased as the reduction of Fe(III) oxides proceeded, adsorbed cysteine and cysteamine reached steady-state within 20 and 30 minutes, while adsorbed homocysteine and glutathione reached steady-state after 60 and 90 minutes. In addition, the concentration of adsorbed but unreacted thiol at the end of the experiment decreased in

the order cysteine (CS) > homocysteine (HS) > cysteamine (CA) > reduced glutathione (GS).

3.4.2 Overall Rate Law for the Reduction of Fe(III) Oxides by Cysteine

The rate of disulfide production (R) depends on the thiol and Fe(III) oxide concentrations as well as the pH resulting in an experimental rate law that can be generally expressed as:

$$R = \frac{d\,[RSSR]}{dt} = k\,[RS^-]_{reactive}{}^{a}[Fe(III)oxide]^b[H^+]^c \qquad (3\text{-}11)$$

where k is the overall rate constant and a, b, and c represent the order of the reaction with respect to each constituent. $[RS^-]_{reactive}$ is $2 * [RSSR]_{SS} - 2 * [RSSR]$ where $[RSSR]_{SS}$ is the concentration of disulfide produced at steady state and $[RSSR]$ is the concentration of disulfide produced as the reaction proceeds. At constant pH and in excess metal oxide, the rate of disulfide production is proportional to the thiol concentration only, allowing the rate law to be rewritten as:

$$RR = \frac{d\,[RSSR]}{dt} = k_{obs}\,[RS^-]_{reactive}{}^{a} \qquad (3\text{-}12)$$

where:

$$k_{obs} = k[Fe(III)oxide]^b[H^+]^c \qquad (3\text{-}13)$$

is the apparent pseudo-order rate constant. The order of the reaction with respect to the thiol species can therefore be determined as the slope of the linear regression that fits the

log of the initial rate of disulfide production as a function of the initial concentration of thiol (Eq. 3-14).

$$\log(R_i) = \log(k_{obs}) + a \log([RS^-]_{reactive_i}) \quad (3\text{-}14)$$

Using the change in concentration of disulfide species as a function of time during the first 10-15% of the reaction extent to calculate initial rates, a slope of 0.92 ± 0.07 was determined from experiments conducted with varying initial cysteine concentrations at pH 7.0 and in the presence of excess Fe(III) oxides (Figure 3-4A), demonstrating first order kinetics with respect to cysteine.

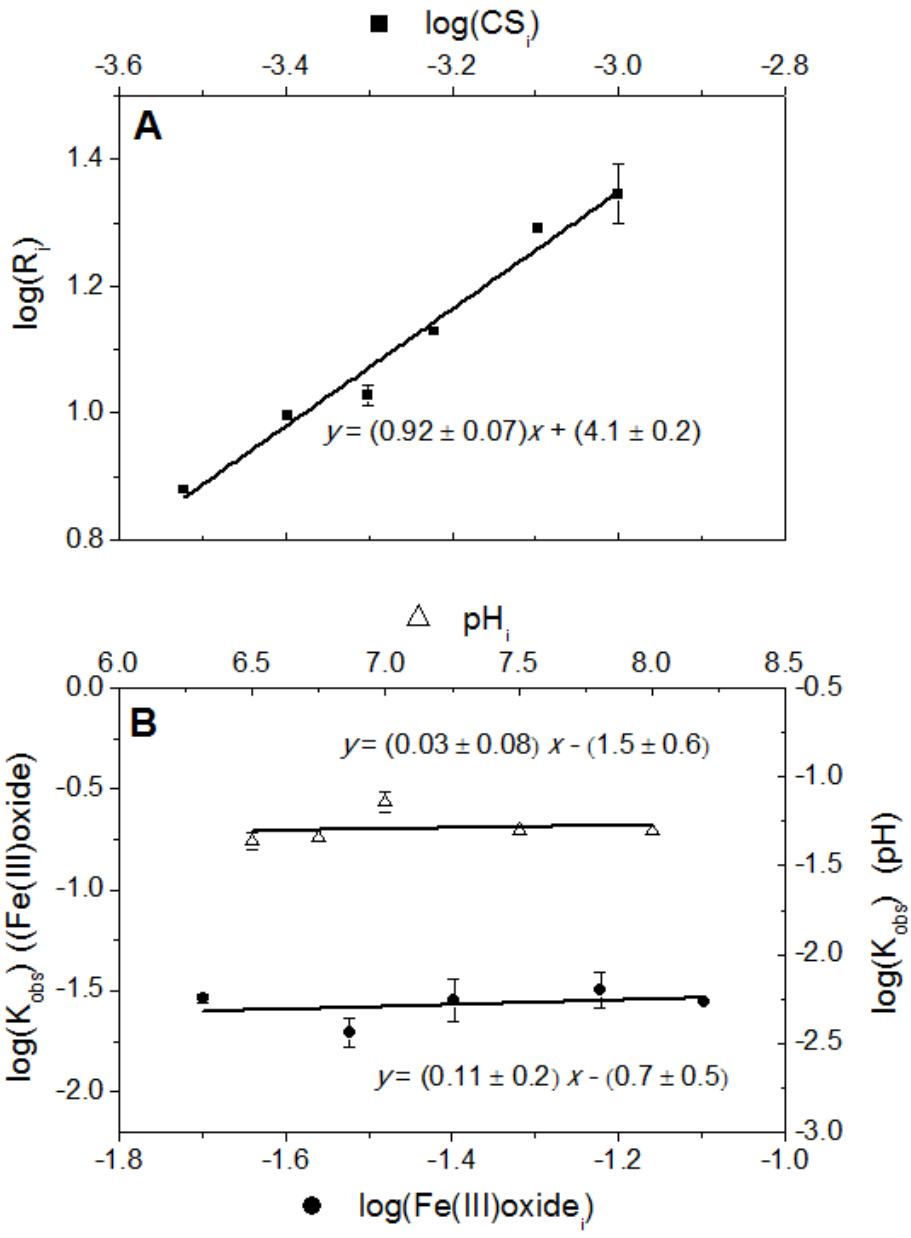

Figure 3-4 Experimental determination of the reaction order with respect to A) cysteine using the isolation method in the presence of 40 mM Fe(III) oxide at pH 7.0, and B) Fe(III) oxide and pH using the isolation and pseudo-order method. To determine the order with respect to Fe(III) oxide, the initial metal oxide concentration was varied in a suite of experiments conducted with 500 µM cysteine at pH 7.0

(circles). To determine the order with respect to pH, the pH was varied in a suite of experiments conducted with 500 µM cysteine and 40 mM Fe(III) oxide (triangles).

Cysteine and cystine were also monitored during experiments conducted in the presence of the same concentration of cysteine (500 µM) but different concentrations of excess Fe(III) oxides (ranging from 20 to 80 mM), and these data were used to determine k_{obs} at each concentration of Fe(III) oxides after integration of Eq. 3-12 (with a = 1) by representing the natural log of the reactive cysteine concentration ($[RS^-]_{reactive}$) as a function of time (Eq. 3-15).

$$\ln([RS^-]_{reactive}) = -2k_{obs}t + \ln(2 * [RSSR]_{SS}) \quad (3\text{-}15)$$

The order of the reaction with respect to the Fe(III) oxide (b) was then determined from the slope of the linear regression of the log of the k_{obs} as a function of the log of the concentration of Fe(III) oxides (Eq. 3-16 derived from the log of Eq. 3-13) at the same constant pH:

$$\log(k_{obs}) = \log(k) - c\ pH + b \log([Fe(III)\ oxide]_i) \quad (3\text{-}16)$$

Using this approach, a slope of 0.11 ± 0.18 was determined (Figure 3-4B), indicating a zero order rate law with respect to Fe(III) oxides, as anticipated due to the oxide surface site concentration being in great excess to the thiols. The same approach was used for the order of the reaction with respect to the proton concentration over a range of pHs commonly observed in most natural environments. Experiments were conducted at different pH between 6 and 8 in the presence of a fixed initial concentration of cysteine (500 µM) and Fe(III) oxides (40 mM). Dependence of the log of the k_{obs} on environmentally relevant pH

generated a slope of 0.022 ± 0.083 (Figure 3-4B) pointing towards zero order with respect to pH in that pH range. Overall, the kinetic rate law for disulfide produced by reduction of Fe(III) oxides by cysteine in the presence of excess Fe(III) oxides at circumneutral pH can therefore be written as the following overall first order rate law:

$$R = k[RS^-]_{reactive} \quad (3\text{-}17)$$

Finally, the experimental rate constant of the reaction can be calculated, after integration of the overall first order rate law (Eq. 3-17), from the slope of the natural log of the thiol concentration as a function of time normalized to its initial concentration (Eq. 3-18) (Table 3-1).

$$Ln(\frac{[RS^-]_{reactive}}{[RS^-]_0}) = -k * t \quad (3\text{-}18)$$

The rate constant (k) for the reaction of each thiol with Fe(III) oxides was determined from the slope of the integrated rate law (Eq. 3-18), assuming the rate law derived from experiments with cysteine is the same for all thiols (Figure 3-5).

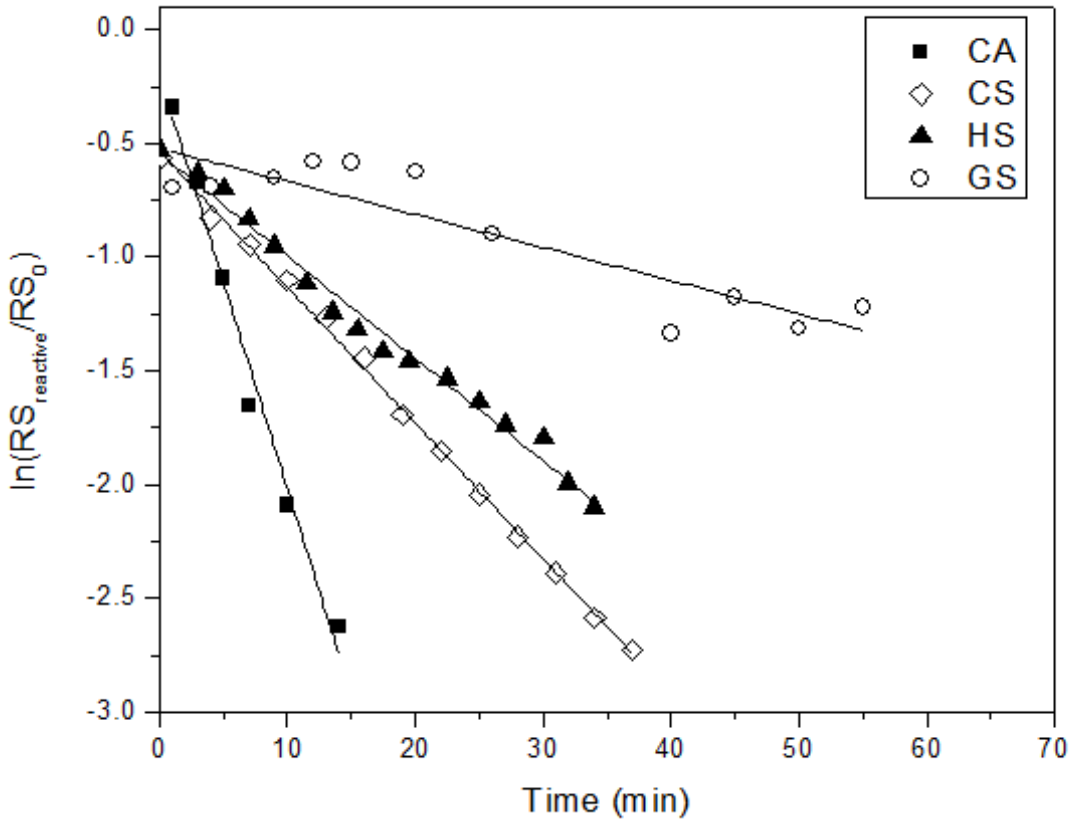

Figure 3-5 Evolution of natural logarithmic of the concentration of cysteamine, cysteine, homocysteine, and glutathione normalized to their initial concentration as a function of time during the reaction of oxidation of each thiol by 40 mM Fe(III) oxides at pH 7.0. The slope of each linear curve was used to calculate the overall rate constant of the reaction.

Although reduced glutathione displayed high variability, the representation of the integrated rate law confirmed an overall first order with respect to each thiol. Rate constants decreased as the chemical structure of the reductant became more complex in the order: CA > CS > HS > GS (Table 3-1).

3.5 Discussion

As low molecular weight thiols represent excellent electron shuttling compounds for dissimilatory iron reduction and a variety of low molecular weight thiols are pervasive in sediments, a more fundamental understanding of the abiotic redox reaction between thiols and Fe(III) oxides is required to evaluate their potential importance in the redox cycle of iron. In this study, a novel voltammetric method was developed and validated to simultaneously monitor each thiol and their oxidized disulfide product as a function of time *in situ* and investigate the reaction mechanism of several common organic sulfur species with 2-L ferrihydrite to mimic the type of conditions encountered in most sedimentary environments. These experiments revealed that the oxidation of each thiol in the presence of excess ferrihydrite follows first order kinetics with respect to the thiol species and zero order with respect to Fe(III) oxides and pH. The significant differences between the experimental rate constants for the oxidation of cysteamine, cysteine, homocysteine, and glutathione by Fe(III) oxides, in otherwise identical conditions (Table 3-3), and between the fraction of thiol adsorbed onto Fe(III) oxides but recalcitrant to oxidation (Figure 3-3) suggest small differences in the mechanism that need to be addressed.

3.5.1 Development of a Kinetic Model to Determine the Mechanism of Fe(III) Oxyhydroxide Reduction by Various Thiols

To identify the mechanistic differences that could result in the variations in the overall first order rate constants of the oxidation of each thiol with Fe(III) oxides, the formation and reaction of intermediate surface complexes can be introduced in a molecular kinetic model and their elementary rate constants optimized to study their kinetic of

transformation. A representation of the mechanism determined in this work is depicted in Figure 3-6 with cysteine as example.

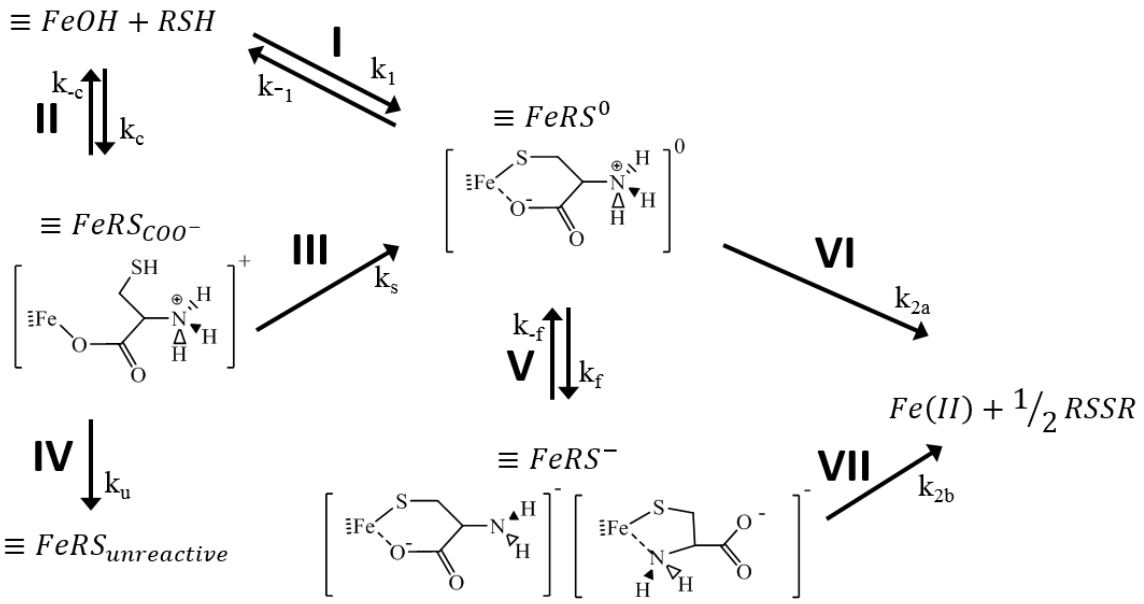

Figure 3-6 Reaction pathway for the reduction of Fe(III) oxide by cysteine, including possible intermediate structures and rate constants. The model described for cysteine is also valid for the other thiols, except that only the neutral intermediate surface complex can be formed with cysteamine as a result of the absence of carboxylate group in this thiol.

3.5.1.1 Formation of Intermediate Surface Species

Describing the possible intermediate reactive surface species ($\equiv FeRS^{n-1}$) at the molecular level provides insight into the mechanism of electron transfer and dissolution. The structure of both neutral and negative surface species have been previously proposed for cysteine with both ferrihydrite (Amirbahman et al., 1997) and polymeric MnO_2 (Herszage et al., 2003), where X represents either Fe(III) or Mn(IV).

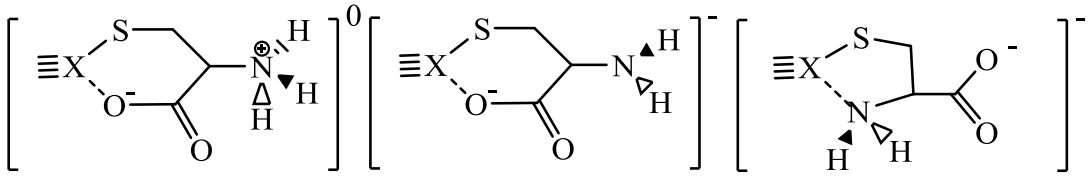

(I) (II) (III)

Initially the thiol (RS) adsorbs to the Fe(III) oxide surface through the sulfhydryl group resulting in the formation of a net neutral species and water (Eq. 3-2 with n = 1 for cysteine, Figure 3-6I):

$$\equiv FeOH + RSH \underset{k_{-1}}{\overset{k_1}{\rightleftarrows}} \equiv FeRS^0 + H_2O \tag{3-19}$$

Simultaneously, coordination may occur between the metal center and the carboxylic group of cysteine to form a bidentate six membered ring that stabilizes the neutral intermediate species (Species I). A negative intermediate complex (Species II) may then form directly by deprotonation of the amine on the six-member ring complex. Alternately, adsorption of the sulfhydryl group to the metal center may be followed by coordination of the amine with simultaneous release of a proton to form the bidentate five membered ring species that is negatively charged (Species III). In both cases, deprotonation of the primary amine groups of the thiol forms a negative intermediate complex (Eq. 3-20, Figure 3-6V).

$$\equiv FeRS^0 \underset{k_{-f}}{\overset{k_f}{\rightleftarrows}} \equiv FeRS^- + H^+ \tag{3-20}$$

Similar to the case with cysteine, homocysteine surface complexes can be postulated for both Mn(IV) or Fe(III) by inserting an additional carbon resulting in a neutral seven

membered ring complex (Species IV), and two negatively charged species (Species V and VI), with six and seven membered rings depending on the type of coordination (carboxylic or amine) involved with the metal center.

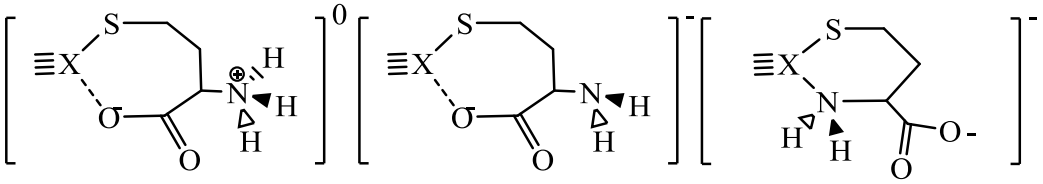

(IV) (V) (VI)

In turn, numerous surfaces species may exist for glutathione due to the possible protonation of multiple functional groups and coordination to multiple metal center allowed by its large structure. Among these structures, however, two can be proposed for the coordination of the sulfhydryl group and neighboring carboxylic groups to a single metal center resulting in six (Species VII) and seven (Species VIII) membered ring intermediates. In addition, negative surface species could be formed with the deprotonation of the primary amine groups.

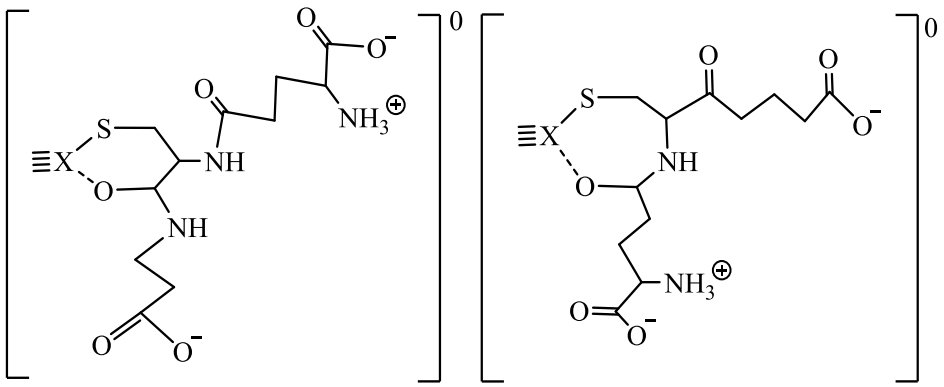

(VII) (VIII)

Finally, the surface species possible for cysteamine are limited by its small structure and lack of carboxylic acid functional groups. Thus, a neutral, five membered ring may form only through complexation of both the sulfhydryl and amine functional groups to the same metal center (Species IX). As the amine group must initially be deprotonated to form the neutral species (n = 1 in Eq. 3-2 or Eq. 3-19), additional deprotonation is extremely unlikely, and no negative species is proposed. Lack of negative surface species greatly simplifies the proposed reaction mechanism.

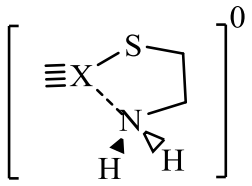

(IX)

3.5.1.2 Initial Adsorption Through Alternate Functional Groups

Except for cysteamine which lacks alternate functional groups, initial adsorption of cysteine, homocysteine, and glutathione may also occur via their carboxylic group independently of the sulfhydryl group (Eq. 3-21, Figure 3-6II). In turn, primary adsorption through the amine group is unlikely as it carries a positive local charge at circumneutral pH (pK_a of 10.78, 10.87, and 9.65 for cysteine, homocysteine, and glutathione) (Dawson, 1959; Edsall and Wyman, 1958; Lide, 2003) which is repulsed from the oxide surface.

$$\equiv FeOH + RSH \underset{k_{-c}}{\overset{k_c}{\rightleftarrows}} \equiv FeRS^{+}_{COO^-} + H_2O \qquad (3\text{-}21)$$

Following complexation of the carboxylic group to the oxide surface, rearrangement may occur to allow covalent bonding through the sulfhydryl group (Eq. 3-22, Figure 3-6III) and form the neutral intermediate complex (Species I for cysteine, Species IV for homocysteine, and Species VII or VIII for glutathione). Alternately, the species may remain adsorbed, but unreactive (Eq. 3-23, Figure 3-6IV), accounting for the disparity between the theoretical and actual yield of disulfide product observed in these experiments (Table 3-1).

$$\equiv FeRS^{+}_{COO^-} \overset{k_s}{\rightarrow} \equiv FeRS^{0} \tag{3-22}$$

$$\equiv FeRS^{+}_{COO^-} \overset{k_u}{\rightarrow} FeRS_{unreactive} \tag{3-23}$$

With cysteamine, a small fraction of adsorbed but unreactive species may form directly upon initial adsorption (Eq. 3-24), possibly via bidentate binding with two metal centers.

$$\equiv FeOH + RSH \overset{k_u}{\rightarrow} FeRS_{unreactive} \tag{3-24}$$

3.5.1.3 Electron Transfer and Formation of Products

Both neutral and negative surface species proceed through a series of reactions characterized by initial electron transfer (Eq. 3-3) followed by rapid dissolution of the thiol radical (Eq. 3-4), dissolution of Fe(II), regeneration of the oxide surface (Eq. 3-5), and dimerization of the thiol radical to its disulfide product (Eq. 3-6) as previously described (Amirbahman et al., 1997). For the modeling exercise these reactions are combined to form the overall reaction of the protonated (Eq. 3-25, Figure 3-6VI) and deprotonated (Eq.

3-26, Figure 3-6VII) surface intermediates to the reduced metal and disulfide product in solution.

$$\equiv FeRS^0 \xrightarrow{k_{2a}} Fe(II) + {}^1/_2\, RSSR \tag{3-25}$$

$$\equiv FeRS^- \xrightarrow{k_{2b}} Fe(II) + {}^1/_2\, RSSR \tag{3-26}$$

3.5.2 Optimization of Elementary Rate Constants

The elementary reactions (Eq. 3-19 to 3-26) combined in Figure 3-6 represent the case of cysteine, but should be valid for homocysteine and glutathione given these thiols carry the same functional groups. The model includes eight species: the free thiol in solution, the Fe(III) oxide, three reactive surface intermediate species ($\equiv FeRS^0, \equiv FeRS^-, \equiv FeRS^-_{COO^-}$), the unreactive fraction ($FeRS_{unreactive}$), the Fe(II) released in solution, and the disulfide product. Accordingly, a suite of eight ordinary differential equations, representing the reversible and irreversible rate of formation and transformation of each individual component involved in the reaction scheme was built assuming first order kinetics with respect to each component of these elementary reactions (Table 3-2). For cysteamine, only one reactive intermediate surface species is formed ($\equiv FeRS^0$), and thus only six ordinary differential equations, representing the rate of formation and disappearance of each component, were needed. The individual rate constants of Eq. 3-19 to 3-26 were optimized for each set of replicate experiment with each thiol, then averaged for the discussion (Table 3-3).

Table 3-2 Overall rate law for each species described by the reaction network of Eq. 3-19 to 3-26. Reactions with cysteine, homocysteine, and glutathione follow the same pathway and produce three possible intermediate surface complexes. In turn, reactions with cysteamine only produce one possible intermediate surface complex.

Species	Reaction Equations	
	Cysteine, Homocysteine, Glutathione	Cysteamine
$\partial[RSH]/\partial t$	$-k_1[RSH][\equiv FeOH] + k_{-1}[\equiv FeRS^0] - k_c[RSH][\equiv FeOH] + k_{-c}[\equiv FeRS^-_{COO^-}]$	$-k_1[RSH][\equiv FeOH] + k_{-1}[\equiv FeRS^0] - k_u[RSH][\equiv FeOH]$
$\partial[FeOH]/\partial t$	$-k_1[RSH][\equiv FeOH] + k_{-1}[\equiv FeRS^0] - k_c[RSH][\equiv FeOH] + k_{-c}[\equiv FeRS^-_{COO^-}]$	$-k_1[RSH][\equiv FeOH] + k_{-1}[\equiv FeRS^0] - k_u[RSH][\equiv FeOH]$
$\partial[\equiv FeRS^0]/\partial t$	$k_1[RSH][\equiv FeOH] - k_{-1}[\equiv FeRS^0] + k_s[\equiv FeRS^-_{COO^-}] - k_f[\equiv FeRS^0] + k_{-f}[\equiv FeRS^-][H^+] - k_{2a}[\equiv FeRS^0]$	$k_1[RSH][\equiv FeOH] - k_{-1}[\equiv FeRS^0] - k_{2a}[\equiv FeRS^0]$
$\partial[\equiv FeRS^-]/\partial t$	$k_f[\equiv FeRS^0] - k_{-f}[\equiv FeRS^-][H^+] - k_{2b}[\equiv FeRS^-]$	
$\partial[\equiv FeRS^-_{COO^-}]/\partial t$	$k_c[RSH][\equiv FeOH] - k_{-c}[\equiv FeRS^-_{COO^-}] - k_s[\equiv FeRS^-_{COO^-}] - k_u[\equiv FeRS^-_{COO^-}]$	
$\partial[FeRS_{unreactive}]/\partial t$	$k_u[\equiv FeRS^-_{COO^-}]$	$k_u[RSH][\equiv FeOH]$
$\partial[Fe(II)]/\partial t$	$k_{2a}[\equiv FeRS^0] + k_{2b}[\equiv FeRS^-]$	$k_{2a}[\equiv FeRS^0]$
$\partial[RSSR]/\partial t$	$1/2\,(k_{2a}[\equiv FeRS^0] + k_{2b}[\equiv FeRS^-])$	$1/2\,k_{2a}[\equiv FeRS^0]$

Table 3-3 Optimized Molecular Rate Constants of Each Elementary Step Involved in the Proposed Mechanistic Model (Eq. 3-19 to 3-26) of Oxidation of Cysteamine, Cysteine, Homocysteine, and Reduced Glutathione by Ferrihydrite. Rate Constants Represent the Average and Standard Deviation of the Rate Constants Optimized With Each set of Replicate Experiments Conducted With a Particular Thiol.

	Cysteamine	Cysteine	Homocysteine	Glutathione
k_1 **($min^{-1}M^{-1}$)**	10.6±0.4	19.9±1.1	1.82±0.83	$5.9±4.9x10^{-2}$
k_1*FeOH_i **(min^{-1})**	0.424	0.796	$7.28x10^{-2}$	$2.36x10^{-3}$
k_{-1} **(min^{-1})**	0.64±0.46	1.92±0.35	0.14±0.07	$3.0±0.6x10^{-14}$
k_{2a} **(min^{-1})**	0.93±0.13	0.14±0.03	$9.7±1x10^{-2}$	$7±2x10^{-2}$
k_{2b} **(min^{-1})**		6.54±1.8	9.02±0.10	0.26±0.006
k_c **($min^{-1}M^{-1}$)**		9.35±0.9	12.3±1.10	52.09±0.28
k_c*FeOH_i **(min^{-1})**		0.374	0.492	2.08
k_{-c} **(min^{-1})**		0.85±0.2	0.75±0.24	4.2±0.38
k_s **(min^{-1})**		1.27±0.9	0.126±0.10	$7.3±0.9x10^{-2}$
k_f **(min^{-1})**		$3.2±5.5x10^{-4}$	$1.5±1.4x10^{-6}$	$1.8±0.3\ x10^{-7}$
k_u **(min^{-1})**	1.6±1.0	0.16±0.08	$1.7±0.6x10^{-2}$	$4.0±0.7x10^{-14}$

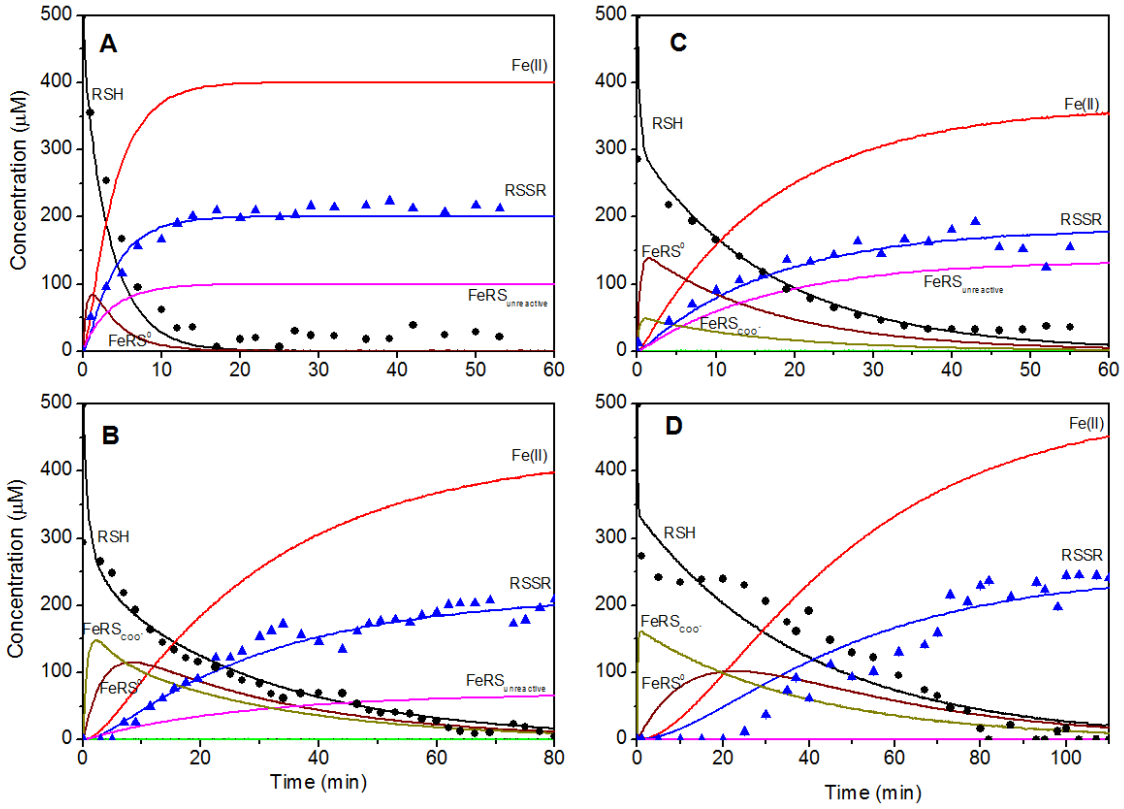

Figure 3-7 Modeled time evolution of the reactants, intermediate species, and products of the reduction of 40 mM HFO by 500 μM of A) cysteamine; B) homocysteine; C) cysteine; and D) glutathione at pH 7.0 using average rate constants optimized from all experiments compared to the measured thiols and their disulfide product of one replicate experiment. The scattered points represent experimental data and lines represent the optimized kinetic model.

The resulting kinetic model using the average of the optimized rate constants appears to be in good agreement with the data of a random replicate experiment (Figure 3-7), suggesting the approach is self-consistent. As these rate constants were optimized based on independent experiments conducted in duplicates or triplicates, large standard deviations from some of the average rate constants were not unexpected. Although optimized rate constants likely represent one outcome to a set of numerous solutions to this complex reaction scheme, the integrity of the optimization technique allows comparison of

each rate constant between thiols to examine variations in the mechanism of thiol oxidation by Fe(III) oxides in response to the structure of the intermediate surface species.

The rate constant for the binding of the sulfhydryl group to the Fe(III) oxide (k_1) to form the neutral intermediate species (Figure 3-6I) decreases in the order: cysteine (CS) > cysteamine (CA) > homocysteine (HS) > glutathione (GS) (Table 3-3). In the case of cysteamine, only one structure of the intermediate surface complex is possible (Species IX), and although the amine group of cysteamine is easily deprotonated without interference from any carboxylic group, the necessary deprotonation probably slows the rate of formation of the intermediate. Comparatively, formation of the neutral intermediate surface complex with cysteine and homocysteine does not require amine deprotonation but experiences increased steric hindrance from their carboxylic groups. However, coordination of the carboxylic group and covalent bonding of the sulfhydryl group to the metal center generates a six-membered ring cysteine intermediate (Species I) that likely adds stability and reduces the activation energy of the complex, thus increasing its rate of formation compared to cysteamine. On the other hand, the additional carbon of homocysteine results in the formation of the less stable seven-membered neutral intermediate (Species IV) which likely decreases its rate of formation, whereas the extra functional groups in glutathione increase steric hindrance such that the rate of formation of the neutral intermediate surface complex through sulfhydryl bonding (Species VII and VIII) is slow. Desorption of the neutral species (k_{-1}) follows the same trend for thiols with carboxylic groups (CS > HS >> GS) and results in an equilibrium constant for the formation of the neutral surface complex from solution ($K_1 = k_1 / k_{-1}$) that increases from 10.4 for cysteine to 12.7 for homocysteine and 2.2×10^{12} for glutathione. Although close equilibrium

constants for cysteine and homocysteine are expected, the high value for glutathione can be explained when taking into account that the electron transfer from the neutral species to the products is much more rapid than the desorption of glutathione from the Fe(III) oxide ($k_{2a} >> k_{-1}$).

The rate constants for the binding of the carboxylic group of cysteine, homocysteine, and glutathione on Fe(III) oxides (k_c) decrease in the order: GS >> HS > CS (Table 3-3). The large rate constant for glutathione is likely due to its numerous functional groups, whereas the rate constants of homocysteine and cysteine are lower and closer in value as they both contain only one carboxylic and one amine group. Simultaneously, the rate constant for the desorption of these carboxylate-bound surface species (k_{-c}) decreases according to the order: GS > CS > HS. The large desorption of GS can be explained by the important steric hindrance of its different complexes (Species VII and VIII). In turn, the larger k_{-c} value for cysteine compared to homocysteine is likely related to the higher stability of the bidentate neutral intermediate surface species with cysteine (Species I) compared to homocysteine (Species IV). Indeed, the rate constant for the rearrangement of the carboxyl-bound species to the bidentate neutral intermediate species (k_s) increases in the order GS < HS < CS due to the large steric hindrance of the six-member ring bidentate neutral intermediate complex with glutathione (Species VII) and the increasing stability of the six-member ring complex with cysteine (Species I) compared to the seven-member ring complex with homocysteine (Species IV).

As the pK_a for the deprotonation of the amine group of each neutral sulfhydryl surface complex represents the ratio of the rate constant for the formation of the negatively charged sulfhydryl complex (k_f) to that of its reversible reaction (k_{-f}), only one of the two

rate constants involved in the transformation of the neutrally-charged into the negatively-charged sulfhydryl complex has to be optimized if the pK_a of the sulfhydryl surface complex is known. Although most of these pK_as are unknown, the pK_a of the amine group of the cysteine surface complex was estimated to be 7.5 (Amirbahman et al., 1997), or 0.35 pH units below the lowest value of the amine group in cystine (Table 3-4).

Table 3-4 Acid-base Equilibrium Constants (pK_as) of the Different Functional Groups of Each Thiol and Disulfide Product Observed in this Study.

Species	Amine	Carboxylic	Sulfhydryl	Reference
Cysteamine	10.81		8.35	(Lide, 2003)
Cystamine	9.3/9.91			
Cysteine	10.78	1.71	8.33	(Dawson, 1959)
Cystine	7.85/9.85	1.65/2.26		(Dawson, 1959)
Homocysteine	10.87	2.22	8.87	(Lide, 2003)
Homocystine	8.52/9.44	1.59/2.54		(Lide, 2003)
Red. Glutathione	9.65	2.12/3.59	8.75	(Edsall and Wyman, 1958)
Ox. Glutathione	8.57/9.54	3.14/4.03		(Bjerrum, 1958)

Using this reference point, the pK_as of the other surface complexes were estimated by examining their chemical structure relative to that of cysteine and the pK_as of the oxidized product. Insertion of the additional carbon in the homocysteine surface complex diminishes both the field and inductive effects of the electron withdrawing metal center further, making deprotonation of the amine group less favorable. As the pK_as of the amine groups in homocystine are 8.52 and 9.44 (Table 3-4), the pK_a of the homocysteine surface intermediate was postulated to be slightly lower by around 0.2 pH unit (pK_a = 8.32).

Similarly, as disulfide bonding in oxidized glutathione does not seem to have a significant effect on the pK_a of the amine groups, complexation to a metal center does likely not result in any large changes to the acidity of the primary amine group. As a result, the pK_a of the primary amine of the coordinated surface species (Species VII and VIII) was postulated to be around 8.47, only 0.1 units below the lowest pK_a of the amine group of the oxidized form. Given the uncertainty in the different pK_as of the different surface complexes, the rate constants for the formation of the negatively charged sulfhydryl surface complexes (k_f) should be considered carefully. Nonetheless, their optimized values are orders of magnitude lower than the other rate constants (Table 3-3), indicating that these species likely only play a large role at more alkaline pH.

The rate constant for the formation of the unreactive species (k_u) decreases according to the order: CA > CS > HS > GS (Table 3-3) and, as expected, is inversely correlated to the increase in reaction extent for the thiols carrying a carboxylic group (Table 3-1). In turn, the rate constant for the formation of the unreactive species is larger for cysteamine, likely due to the absence of intermediate species during its formation. Despite the large rate constant for the formation of the unreactive cysteamine complex, the extent of the reaction is relatively high (Table 3-1) due to the rapid formation of the reactive surface species.

Finally, the rate constant for the transformation of the bidentate neutral intermediate surface species to the final disulfide products (k_{2a}) decreases according to the order: CA > CS > HS > GS, demonstrating that the increase in complexity of the thiol has a large influence on the rate of the reaction. For cysteamine the simple structure of the bidentate neutral surface complex (Species IX) and lack of carboxylic groups accelerate the rate of

reaction to the product. The high stability of the six-ring bidentate neutral surface complex for cysteine (Species I) compared to the seven-membered complex for homocysteine (Specie IV) should favor electron transfer from cysteine over homocysteine to Fe(III) oxides, as increasing the stability of the intermediate complex lessens the structural rearrangement necessary for electron transfer to occur (Stone, 1983), therefore decreasing the activation energy necessary for Fe(III) reduction by cysteine below that of homocysteine. Indeed, formation of the neutral surface complex (k_1) appears faster with cysteine than homocysteine (Table 3-3). Glutathione, however, is a large molecule with added steric hindrance to destabilize the bidentate neutral surface species as well as alternate functional groups that could interact with other metal centers and decrease the electron transfer rate. Interestingly, the rate constant for the transformation of the negative intermediate surface complex (k_{2b}) is greater than that for the neutral intermediate (k_{2a}) with all thiols, as already observed with cysteine (Amirbahman et al., 1997). The increase in k_{2b} from cysteine to homocysteine (Table 3-3) can also be explained by the structure of the negative intermediate surface complexes. As the negative intermediate complex with homocysteine coordinated through the amine is stabilized by the formation a six-membered ring (Species VI), deprotonation of the seven-ring neutral intermediate complex (Species IV) should preferentially rearrange to the amine form compared to the five-membered negative surface species formed for cysteine (Species III). This increase in stability should increase the concentration of the negative intermediate complex over the neutral intermediate complex and, thus, increase the rate of the reaction, according to the transition state theory. Comparison of these two rate constants (k_{2a} and k_{2b}) also demonstrates that reduction of Fe(III) oxides by thiols should be enhanced above circumneutral pH.

3.5.3 Rate-Determining Step at Circumneutral pH

As both the detachment of the reduced metal from the surface and the dimerization of the thiol radicals to form the disulfide product should have similar kinetics regardless of the type of thiol involved, the variation in reactivity of the different thiols with the same Fe(III) oxides in otherwise identical conditions suggests the rate of the reaction is controlled either by the electron transfer step or the adsorption and rearrangement of the surface species. The rates of oxidation of cysteamine, cysteine, and homocysteine can be compared in relation to their intermediate complex structures to determine whether the rate limiting step is the electron transfer as determined previously in excess ligand concentrations or surface complex formation, as hypothesized in low ligand concentrations (Amirbahman et al., 1997). As only one intermediate species is formed with cysteamine and formation of this species requires deprotonation of the amine group, the rate limiting step of this sequential reaction must be the initial adsorption step. Indeed, the rate of formation of the product (k_{2a}) is higher than the desorption of the complex (k_{-1}) and the rate of formation of the surface complex (k_1 x $[Fe(III)]_i$) is lower than the formation of the product, indicating that the adsorption of cysteamine onto the Fe(III) oxide surface is the rate limiting step, as expected since removal of the proton necessary for amine coordination would decrease the adsorption rate.

For cysteine, homocysteine, and glutathione, however, multiple rearrangements on the Fe(III) oxides surface and formation of the disulfide products from two intermediate species must also be considered when determining the rate limiting step. First, the electron transfer step in the formation of the disulfide product through the negative intermediate species is always faster than the protonation of the negative surface species ($k_{2b} >> k_{-f}$ x

$[H^+]$ at pH 7.0), as the pK_a for the deprotonation of the neutral complex is high and k_f is low for all thiols (Table 3-3). Simultaneously, the rate of reduction of the negative surface complex is higher than the rate of deprotonation of the surface complex ($k_{2b} >> k_f$) such that the rate limiting step in the reaction of formation of the disulfide complex via the negative surface complex is the formation of the complex. However, as the rate of the parallel reaction of formation of the product via the intermediate neutral complex is always greater than the rate of formation of the deprotonated species ($k_{2a} >> k_f$), formation of the disulfide product through the negative surface species does not appear to be favorable for any of the thiols at pH 7.0. Second, the rate of formation of the disulfide product via the intermediate neutral complex is smaller than the dissociation of the intermediate neutral complex into the reactants ($k_{2a} << k_{-1}$) for cysteine and homocysteine, suggesting that the formation of the neutral surface complex may require initial carboxylate binding. As the rate constant for the dissociation of the carboxylated complex is smaller than the rearrangement of the carboxylated complex for cysteine ($k_{-c} < k_s$), the formation of the neutral intermediate species through initial adsorption of the carboxylic group is dependent on the sequential reactions of the adsorption of cysteine (k_c) and rearrangement of the complex (k_s). As the rate of carboxylate binding by cysteine is greater than the rearrangement of the intermediate carboxylated complex (k_c x $[Fe(III)]_i > k_s$), the rate limiting step in this pathway is the rearrangement of the intermediate carboxylated complex (Figure 3-6III). Simultaneously, the rate of formation of the sulfhydryl surface complex for cysteine is faster than the rate of adsorption of cysteine via the carboxylated complex ($k_1 > k_c$), indicating that the rate limiting step for the formation of the neutral surface complex with cysteine is the direct adsorption via sulfhydryl binding. For homocysteine, the

desorption of the carboxylated complex is faster than its rearrangement ($k_{-c} >> k_s$) and its formation ($k_{-c} > k_c \times [Fe(III)]_i$), indicating that the formation of the carboxylated surface complex controls formation of the neutral surface species via the carboxylic pathway. As the rate of formation of the carboxylic complex is greater than that of the sulfhydryl complex ($k_c >> k_1$) for homocysteine, the reaction proceeds mainly through adsorption of the carboxylic group and rearrangement into the neutral surface species. For glutathione, the rate of electron transfer for the reaction of the intermediate neutral species is much larger than the rate of dissociation of the neutral species ($k_{2a} >> k_{-1}$) and the rate of the formation of the neutral surface complex ($k_{2a} >> k_1 \times [Fe(III)]_i$), suggesting that the rate limiting step for glutathione could be the formation of the neutral surface complex. As the intermediate neutral complex is also formed via rearrangement of the carboxylated complex (Figure 3-6II and III), however, it may be possible that the rate limiting step is the formation of the surface complex via the carboxylated pathway. Indeed, the rate of dissociation of the carboxylated intermediate complex to the reactants is much faster than its rearrangement ($k_{-c} >> k_s$) and faster than its rate of formation ($k_{-c} > k_c \times [Fe(III)]_i$), indicating the formation of the carboxylated complex is the rate limiting step in the formation of the neutral surface complex via the carboxylated pathway. As the formation of the carboxylated complex is faster than that the direct sulfhydryl binding ($k_c >> k_1$) for glutathione, the formation of the neutral surface complex should depend mainly on the carboxylated pathway. This analysis is indeed verified by the model as the $\equiv FeRS^{+}_{COO^-}$ complex is the dominant intermediate for glutathione and homocysteine while the $\equiv FeRS^{0}$ complex is dominant for cysteine (Figure 3-7). Finally, the overall rate limiting step can be determined by comparing the rates that control formation of the neutral intermediate

species via direct sulfhydryl bonding for cysteine (k_1 x $[Fe(III)]_i$) or carboxylate bonding for homocysteine and glutathione (k_c x $[Fe(III)]_i$) to the sequential reaction of electron transfer (k_{2a}). As k_{2a} is smaller for all three thiols (Table 3-1), the reaction is limited by the electron transfer step at pH 7.0, in contrast to what was predicted at low cysteine concentrations (Amirbahman et al., 1997).

3.5.4 Comparison of the Experimental and Modeled Overall Rate Constants

To determine a modeled overall first order rate constant for the oxidation of each thiol by Fe(III) oxides that could be compared to the experimentally-derived overall rate constant, the optimized rate constants of each elementary step involved in the reaction of each individual thiol (Eq. 3-19 to 3-26) were used to calculate the initial rate of production of each disulfide from the slope of its concentration as a function of time using less than 5% of the reaction progress. This calculation was repeated at different initial thiol concentration, and the slope of the linear regression of the initial rate of disulfide production represented against the initial thiol concentration was used to determine the overall first order rate constant of oxidation of each individual thiol. The rate constant of the overall reaction derived from the mechanistic model for all four thiols was in good agreement with the measured rate constant (Table 3-1) confirming that the experimental rate law inferred from the reaction between Fe(III) oxides and cysteine can be used for the other thiols as expected based on the results for both cysteine and glutathione with MnO_2 (Herszage and Afonso, 2003). Both the experimental and optimized rate constants do not follow the trend expected from reported redox potentials although extent of reaction does, providing additionally support for the importance of thiol structure in these reactions.

3.5.5 Environmental Importance

The mechanistic aspect of this study demonstrates the importance of the thiol structure on their reactivity and recovery of the disulfide product. In natural environments it is plausible that multiple electron shuttles may be used by iron-reducing microorganisms, depending on their availability, the crystallinity of the Fe(III) oxide, as well as energy constraints. Although a more complex thiol such as glutathione should be efficiently reoxidized at the Fe(III) oxide surface, the rate of the reaction may be too slow, especially with more crystalline Fe(III) oxides, to represent a good electron sink for iron-reducing bacteria. On the other end of the spectrum, a thiol such as cysteine may be able to react much faster with Fe(III) oxides, though a significant fraction may be immobilized on the Fe(III) oxides as unreacted species. In such conditions, a high concentration of electron shuttle may be required to act as electron sink for iron-reducing bacteria. Direct comparison between rates determined in this study and those of thiol-mediated microbial iron reduction may be challenging as the rate of disulfide reduction to thiol appears to vary widely between *G. sulfurreducens* and three different strains of *Shewanella* (Doong and Schink, 2002; Liu et al., 2014), and initial rates of dissimilatory iron reduction vary over a wide range (Jones et al., 1983; Kostka and Nealson, 1995; Roden and Zachara, 1996). This study sets the stage for future investigations to rely not only on published redox potentials, but to also consider ligand structure, reaction rates, and reaction extent when determining the potential use of electron shuttles in dissimilatory iron reduction.

3.6 Conclusion

In this study, a kinetic rate law for the oxidation of four environmentally relevant thiols (i.e. cysteamine, cysteine, homocysteine, and glutathione) by excess Fe(III) oxides was determined at circumneutral pH. The rate law is first order with respect to the thiol species and zero order with respect to the proton concentration in the pH range of most environments (pH 6-9). The rate law is also zero order with respect to the Fe(III) oxides concentrations, as expected given the generally small concentration of thiols in natural sediments compared to Fe(III) oxides. The overall first-order rate constant revealed that the reactivity of the thiols decreases in the order cysteamine > cysteine > homocysteine > glutathione, suggesting that the structure of the thiol surface species affects the rate of the reaction. Simultaneously, these kinetic experiments demonstrated that a fraction of thiol is immobilized on the solid surface as an unreactive species. Except for cysteamine, which was only partially retained on the mineral surface, the extent of the reaction increased with the complexity of the thiol molecule despite a concurrent decrease in the rate of thiol oxidation. These findings indicate that while thiols with simpler structures may react more rapidly, larger molecules with an increasing number of alternate functional groups significantly increase the extent of thiol oxidation by Fe(III) oxides. A multi-component kinetic model was built based on the reversible adsorption, rearrangement, and irreversible oxidation of the thiols to their disulfide products, and kinetic rate constants from elementary reactions optimized mathematically to investigate the differences in mechanism that could result in these variations in reactivity. Although rate constants optimized with the model indicate that the formation of the surface species appears rate limiting with cysteamine due to the necessary amine coordination of the neutral surface

species, the electron transfer step is the rate limiting step with thiols carrying carboxylic groups. These findings may have important ramifications in the cycling of iron in sediments, as dissimilatory iron-reducing bacteria supplemented with small concentrations of thiols have been demonstrated to significantly enhance the rate of iron reduction by recycling the disulfide product back to its thiol reactant during growth. Although iron-reducing bacteria may preferentially use simple thiols such as cysteamine for rapid electron transfer, the release of larger, more complex thiols such as glutathione are returned most efficiently from the iron surface and may increase the extent of iron reduction over time.

3.7 Acknowledgments

We would like to thank George W. Luther III for some stimulating discussion on the mechanism of electron transfer with thiols. This work was supported by the National Science Foundation (grant numbers MCB-1021735 and DEB-1542596).

CHAPTER 4. EFFECT OF MANGANESE OXIDE AGING ON THE KINETICS OF THIOL OXIDATION

This manuscript, authored by Eryn M. Eitel, Shiliang Zhao, Yuanzhi Tang, and Martial Taillefert[1] entitled "Effect of manganese oxide aging on the kinetics of thiol oxidation" is under review for publication in Environmental Science and Technology

[1]School of Earth and Atmospheric Sciences, Georgia Institute of Technology, Atlanta, GA 30332

4.1 Abstract

The kinetics and mechanism of thiol oxidation by Mn oxides undergoing aging and transformation under environmentally relevant conditions remain poorly understood. In this study, thiol/disulfide pair concentrations were simultaneously determined during the interaction of four common thiols (cysteine, homocysteine, cysteamine, and glutathione) with fresh and aged δ-MnO_2 at pH 7.0. The reaction kinetics was first order with respect to thiol and zero order with respect to Mn oxides. A transient intermediate sulfur surface species observed during the reaction provides evidence for a mechanism involving two successive one-electron transfer steps. The reaction kinetics of fresh and aged δ-MnO_2 was investigated with cysteine and compared to that of manganite, a Mn(III) oxyhydroxide phase. The reactivity of aged δ-MnO_2 decreased as a result of structural transformation to cryptomelane but remained higher than that of manganite, suggesting the potential roles of transient Mn(III) surface intermediate in promoting the reduction of Mn(IV) in δ-MnO_2 and cryptomelane (compared to Mn(III) in manganite). This study demonstrates the importance of correlating Mn oxide mineral structure and redox reactivity and extends the

potential for thiols commonly found in sedimentary environments to be utilized as electron shuttles during dissimilatory Mn reduction.

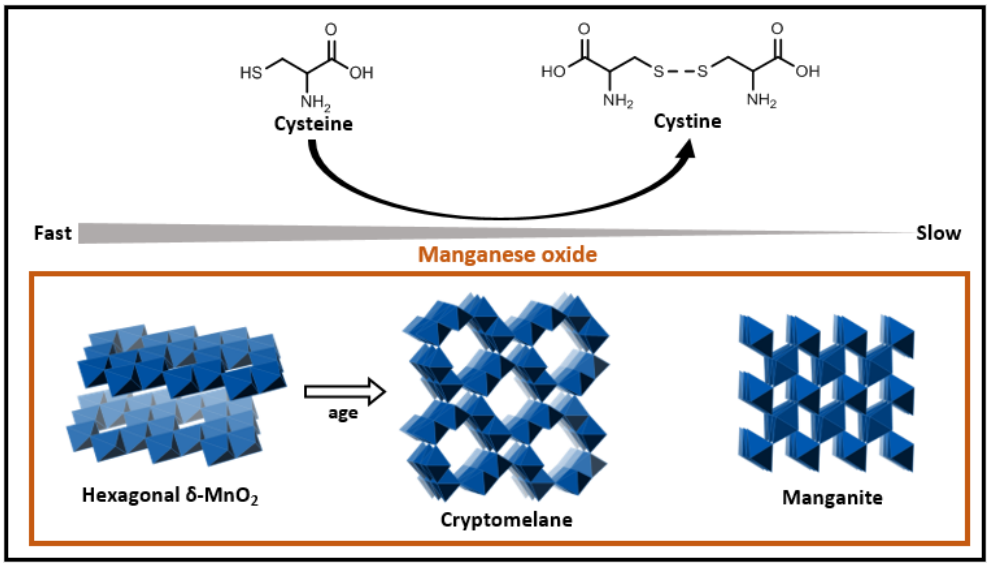

Abstract Art 4-1

4.2 Introduction

Manganese (Mn) is the second most prevalent transition metal in Earth's crust after iron (Fe) and plays important roles in the biogeochemical cycling of carbon, nitrogen, phosphorus, sulfur, and iron in sediments (Burdige and Nealson, 1986; Luther et al., 1997; Neretin et al., 2003; Schippers and Jorgensen, 2001; Tebo et al., 2004; White et al., 2008). The transformation of Mn(III,IV) (oxyhydr)oxides (hereafter referred to as Mn oxides) also influences the transport and fate of inorganic (e.g. (Feng et al., 2007; Jenne, 1968; Nelson and Lion, 2003; Oscarson et al., 1981; Weaver and Hochella, 2003)) and organic (Remucal and Ginder-Vogel, 2014) contaminants. Both layered and tunnel structured Mn oxides are commonly found in natural environments (Bilinski et al., 2002; Taylor et al., 1964). Fresh biogenic Mn oxides are typically highly reactive layered hexagonal phyllomanganates that

are structurally similar to δ-MnO_2 (vernadite) and birnessite, and have high surface area and a large number of vacancy sites (Post, 1999; Tebo et al., 2004; Webb et al., 2005). Although layered phyllomanganates are typically more abundant (Post, 1999), 2×2 tunnel structured hollandite type Mn oxides (such as cryptomelane) represent the major phases detected in the supergene oxidation zones of Mn deposits and lateritic weathered profiles (Faria et al., 2013; Lu and Li, 2015; Ostwald, 1992; Parc et al., 1989). In marine sediments, aged Mn(III,IV) oxides with higher structure order and lower reactivity as well as Mn(III) oxyhydroxides (such as manganite with 1×1 tunnel structure) dominate the oxic layers closest to the sediment-water interface (Anschutz et al., 2005; van der Zee and van Raaphorst, 2004). Indeed, dissolved Mn(II) is known to react with structural Mn(IV) in Mn(III,IV) oxides to produce Mn(III) and result in phase transformations. Low Mn(II) concentrations may favor the transformation of birnessite layer symmetry from hexagonal to triclinic (e.g. (Bargar et al., 2005; Zhao et al., 2016; Zhu et al., 2010). At higher Mn(II) concentration and under anoxic conditions, such reductive transformation can lead to the formation of manganite (γ-$Mn^{III}OOH$) at pH 7.0–8.0 and hausmannite ($Mn^{II}Mn^{III}_2O_4$) at pH 8.0–8.5 (Elzinga, 2011; Lefkowitz et al., 2013). Under oxic conditions, reaction of concentrated Mn(II) and hexagonal birnessite generates cryptomelane ($K_{1.3-1.5}Mn^{III,IV}_8O_{16}$) at pH 4.0, groutite (α-MnOOH) at pH 6.0, and manganite at pH 7–7.5 (Mandernack et al., 1995; Tu et al., 1994). Wet-dry cycling has been reported to facilitate the conversion of birnessite into tunneled Mn oxides in freshwater sediments (Bargar et al., 2009).

As a result of the variety of processes affecting Mn oxide formation, structure, and transformation, the redox reactivity of Mn oxides in natural sediments varies widely (van der Zee and van Raaphorst, 2004). Both the chemical (Remucal and Ginder-Vogel, 2014)

and microbial (Burdige et al., 1992b) reduction of disordered low crystallinity Mn oxides, which have higher surface area and include more reactive vacancy sites, are faster than the higher crystallinity phases. As microorganisms may recycle electron shuttling compounds to reduce solid metal oxides (Coates et al., 2002; Coates et al., 1998; Lovley et al., 1996), the abiotic oxidation of these electron shuttles may be similarly affected by differences in mineralogy. Thiols represent excellent electron shuttles for the dissimilatory reduction of Fe(III)-containing minerals such as poorly crystalline Fe(III) oxides (Doong and Schink, 2002) and smectite (Liu et al., 2014) and are likely to be utilized during dissimilatory Mn reduction. The overall reduction of Mn(IV) by thiols (RSH), produces one mole of Mn(II) and disulfide species (RSSR) per two moles of thiol reactant (Eq. 4-1):

$$MnO_2 + 2\,RSH + 2H^+ \leftrightarrow RSSR + Mn^{2+} + 2H_2O \qquad (4\text{-}1)$$

Although the kinetics of Fe oxide reduction by different thiols has been extensively studied (Amirbahman et al., 1997; Eitel and Taillefert, 2017), investigations of the reaction of thiols with solid Mn oxides have been limited and require analytical techniques that are capable of probing the fast reaction kinetics and related structural aspects (Altaf and Jaganyi, 2014; Andrabi and Khan, 2007; Herszage et al., 2003; Salamon et al., 2004).

The reaction between Mn oxides and thiols is of interest as it likely influences Mn redox cycling, the mobilization and redox transformation of inorganic and organic contaminants, and a number of biogeochemical processes affected by Mn transformations. This study systematically investigated the reaction kinetics of four low molecular weight thiols (cysteamine, cysteine, homocysteine, and reduced glutathione) with environmentally common Mn oxide phases, including δ-MnO_2 of different ages and manganite, to examine

the effects of aging and phase transformation on reaction kinetics. To the best of our knowledge, this is the first study that determines the kinetic of solid Mn oxide reaction with thiols under environmentally relevant conditions.

4.3 Methods

4.3.1 Materials and Solid Phase Characterization

Unless otherwise stated, all chemicals were at least ACS grade reagents and obtained from Sigma-Aldrich, Inc. Stock solutions of thiol and disulfide were prepared weekly and stored at 4 ˚C. δ-MnO_2 was prepared by the oxidation of Mn(II) by permanganate following a previous procedure (Murray, 1974). Aging and low temperature transformation of δ-MnO_2 was allowed to occur in the original synthesis solution containing excess K^+ (Deguzman et al., 1994). At varied time points (1 month to 6 years), aliquots of the aging suspension were removed, repeatedly rinsed, and resuspended in the reaction medium. These samples are labeled as δMnO_2_aging time (e.g. δMnO_2_1m and δMnO_2_2yr indicates δ-MnO_2 samples aged for 1 month and 2 years). Cryptomelane was prepared by the addition of heated potassium permanganate solution to manganese sulfate solution (Inman et al., 2001; Moore et al., 1950). Manganite was synthesized by reacting 36 mM Mn(II) with 1 g/L δ-MnO_2 under anoxic conditions for 3 months at pH 7 (Lefkowitz and Elzinga, 2015). A portion of the synthesized solid phases were freeze-dried and characterized by X-ray diffraction (XRD) using a Panalytical Empyrean diffractometer with Cu Kα radiation (λ = 0.15406 nm) and by Mn K-edge X-ray absorption spectroscopy (XAS) (details in Supporting Information; SI). Surface area of the Mn oxides were

determined by nitrogen physiosorption at 77 K using the BET method on a Micromeritics TriStar 2030 after vacuum drying for 12 h at room temperature.

4.3.2 Experimental Set Up

Experiments were performed in a DLK Cell Stand (Analytical Instruments System Inc.) specifically fabricated for use with gold/mercury amalgam (Au/Hg) voltammetric microelectrodes. Reactor cells were amended with Mn oxide suspensions and degassed for 10 min using ultra-high purity (UHP) N_2. Thiols were injected to initiate the reaction, and the suspension was constantly stirred during the experiments, except during the voltammetric analyses (< 20 sec). All experiments were conducted in at least duplicate in solution composed of inorganic salts (mainly $(NH_4)_2SO_4$) buffered at pH 7.0 with 5.7 mM K_2HPO_4/ 3.3 mM KH_2PO_4 (0.09 M ionic strength) (Myers and Nealson, 1988). In independent experiments, cysteine and homocysteine concentrations were varied between 300 and 1000 μM in the presence of 10 mM δ-MnO_2 aged for 1.5 or 2.5 years, whereas concentrations of δ-MnO_2 aged for 1.5 years were varied between 5 and 15 mM in the presence of 500 μM cysteine to determine the reaction order with respect to each species.

4.3.3 In Situ Electrochemical Thiol and Disulfide Measurements

In situ voltammetric measurements of thiol and disulfide species in the thiol-Mn oxide reaction suspension were performed according to previous procedures (Eitel and Taillefert, 2017) with a three electrode system consisting of a 100 μm diameter Au/Hg microelectrode as working electrode, a 500 Pt μm diameter counter electrode, and a 500 μm diameter Ag/AgCl reference electrode all encased in 3 mm diameter PEEK™ (polyethyletherketone) tubing as previously described (Luther et al., 2008). All the

potentials reported in this study are therefore relative to the standard potential of the saturated Ag/AgCl system. The Au/Hg microelectrode was prepared by polishing the gold wire with 15, 6, 1, and 0.25 μm diamond pastes (Buehler) followed by plating with Hg at -0.1 V in a $Hg(NO_3)_2$ solution for 4 min and polarization at -9.0 V for 90 sec to stabilize the amalgam (Brendel and Luther, 1995). Voltammetric measurements were carried out with a computer-operated DLK-100 potentiostat (Analytical Instrument Systems, Inc.), and data was integrated using VOLTINT a semi-automated Matlab™ script (Bristow and Taillefert, 2008). To confirm electrode quality, linear sweep voltammograms of dissolved oxygen and Mn(II) calibrations were obtained (Luther et al., 2008). The electrodes were then calibrated for thiols and disulfide species in degassed solution.

4.4 Results and Discussion

4.4.1 Effect of Aging on the Structural Transformation of δ-MnO_2

Long term aging of fresh δ-MnO_2 led to the formation of cryptomelane as a final product, as evident in the XRD patterns of fresh and aged δ-MnO_2 (Figure 4-1). Similar transformations have been previously observed with aging of birnessite at room temperature (Villalobos et al., 2003). XRD data of the fresh δ-MnO_2 is consistent with previous studies, with two broad peaks at ~37° (11,20) and ~66° (31,02). The weak peak at ~25° (002) indicates limited layer stacking along the c axis. Upon aging, three peaks at ~23°, 38°, and 56° first increased, then decreased, and eventually disappeared. These peaks indicate the formation of phyllomanganate phase/sheets with orthogonal (triclinic) symmetry (Hinkle et al., 2016; Lanson et al., 2002; Lanson et al., 2000), which is a common transformation product upon Mn oxide interaction with low concentrations of dissolved

Mn(II) (Hinkle et al., 2016; Learman et al., 2011a; Learman et al., 2011b; Tang et al., 2014; Zhao et al., 2016; Zhu et al., 2010). In addition, XRD peaks (at ~18°, 29°, 37°, 42°, 51°) corresponding to cryptomelane (a 2×2 tunnel structured tectomanganate phase) continuously increased after ~1 month of the aging process, and cryptomelane was the only phase observed after 6 years aging time (sample δMnO_2_6year in Figure 4-1), suggesting that the triclinic phyllomanganate phase served as an intermediate during the transformation from δ-MnO_2 to cryptomelane. Presence of intermediate triclinic phyllomanagnates were also observed in previous studies during Mn oxide transformation from layered to tunneled structure (Cui et al., 2010; Feng et al., 2010). Mn(III) in triclinic vernadite sheets is thought to generate a Jahn-Teller effect that promotes the transition from layered to tunneled structure (Li et al., 2016).

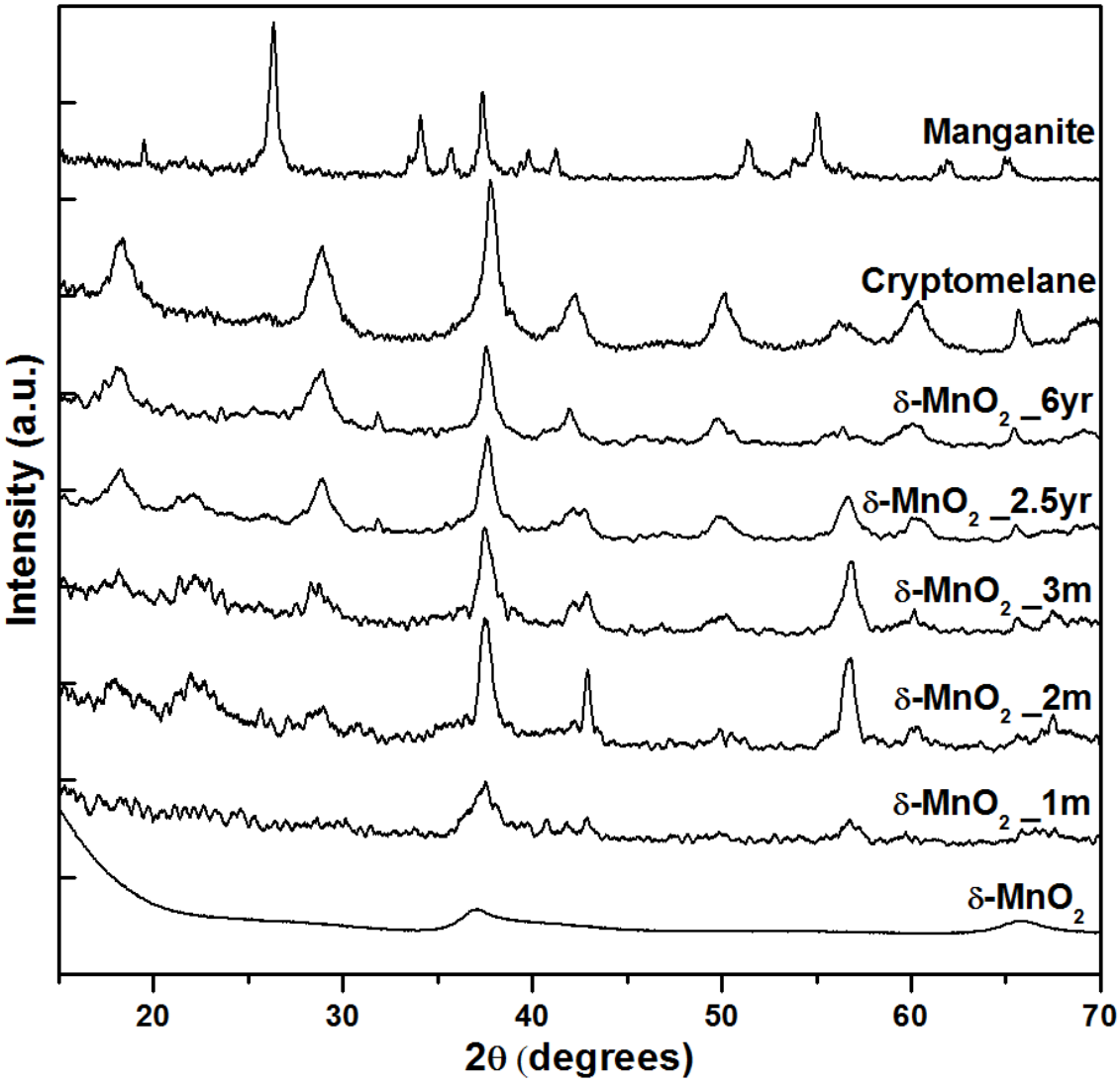

Figure 4-1 XRD patterns of manganite, cryptomelane, fresh δ-MnO_2, and δ-MnO_2 aged for 1 month, 2 months, 3 months, 2.5 years, and 6 years.

Figure A 1 (Appendix A) shows the k3-weighted Mn K-edge extended X-ray absorption fine structure (EXAFS) data of fresh and aged δ-MnO_2, as well as cryptomelane and triclinic birnessite. The gradual transformation from δ-MnO_2 to cryptomelane is clearly observed from the changes in the ~7.5–10 $Å^{-1}$ indicator region. Linear combination fitting (LCF) using fresh δ-MnO_2, cryptomelane, and triclinic birnessite as end members (Table A 1) indicates the presence of ~51% δ-MnO_2, ~9% triclinic birnessite, and ~41% cryptomelane in the 2-month-old sample (δ-MnO_2_1m), and almost complete transformation to cryptomelane after 2.5 years (samples δ-MnO_2_2.5yr and δ-MnO_2_6yr). Interestingly, the LCF obtained fraction of triclinic birnessite was lower than expected, whereas that of cryptomelane was higher than expected from XRD data (Figure 4-1). These differences may be due to analytical biases of these two spectroscopic techniques. XRD detects the long range structural order, therefore better ordered (i.e. higher crystallinity) phases display more distinctive peaks (in this case triclinic birnessite and cryptomelane) than poorly ordered (i.e. low crystallinity) phases (in this case the broad peaks corresponding to hexagonal δ-MnO_2). In comparison, XAS is an element specific technique that probes local coordination environment around the central atom (in this case Mn) but does not discriminate phases of varying crystallinity. Despite variations in the relative abundance of the different Mn phases obtained from XRD and XAS analysis, the overall trend in the aging system is consistent with the gradual disappearance of hexagonal δ-MnO_2, formation of a triclinic birnessite intermediate phase, and the ultimate conversion to cryptomelane. The above mentioned changes in Mn-containing phase and crystallinity is also consistent with the gradual decrease of BET specific surface area observed with age (Table A 2).

4.4.2 Effect of Thiol Structure on Thiol Oxidation Kinetics

To examine the relative reactivity of different thiols, cysteamine, cysteine, homocysteine, and reduced glutathione were reacted with 1.5-year-old δ-MnO_2 (δ-MnO_2_1.5yr). All thiols were rapidly oxidized and the resulting disulfide product was simultaneously released into solution (Figure 4-2A, B). However, clear differences in the reaction kinetics were observed between the thiols: Cysteamine reacted the fastest and was completely removed from solution within the first minute (half-life < 10 seconds), followed by cysteine, homocysteine, and reduced glutathione, which were removed with half-lives of 1.75, 2, and 4.5 min, respectively. The formation kinetics of the disulfide product followed the order of disappearance of their corresponding thiol: Cystamine reached equilibrium concentrations after 2.5 min, followed by cystine (4 min), homocystine (12.5 min), and oxidized glutathione (16 min). In general, the reaction rates of thiols with Mn oxides were significantly higher than the previously reported reaction rates of thiols with ferrihydrite under identical conditions (Eitel and Taillefert, 2017). This finding is consistent with the differences in reactivity of Fe(III) and Mn(IV) molecular orbitals with dissolved sulfide (Luther, 1990) and the lower redox potential of Fe(III) oxides (Stumm and Morgan, 1996). Similar results have been observed with birnessite, cryptomelane, and Fe(III) oxides during the oxidation of phenolic compounds (Shindo and Huang, 1984). The reactivity of the different thiols followed the same trend as observed with ferrihydrite (Eitel and Taillefert, 2017) and agreed with results obtained with MnO_2 nanoparticles (Herszage et al., 2003). In contrast to the ferrihydrite system (Eitel and Taillefert, 2017), however, the conversion of thiols to their respective disulfide product was complete as theoretical concentrations of disulfide were always reached at steady state (Figure 4-2B).

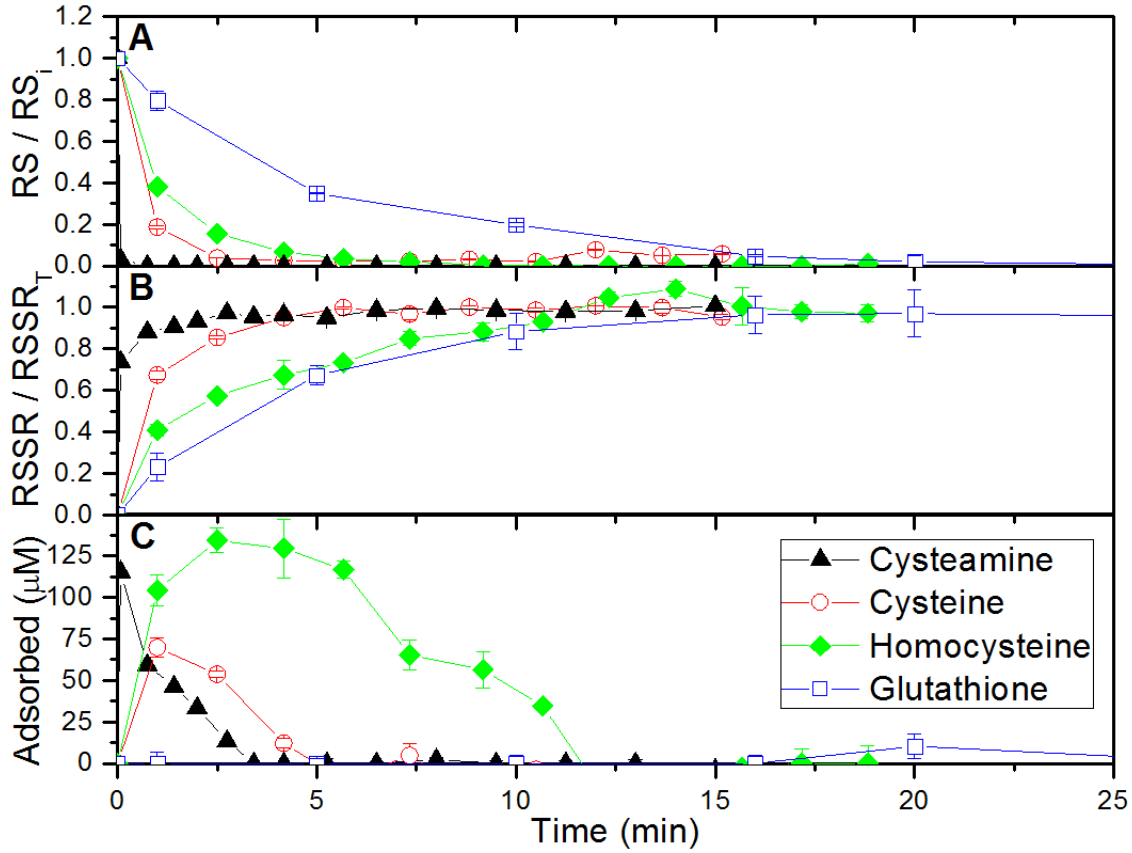

Figure 4-2 Temporal evolution of the molar ratio of: (A) the thiols cysteamine (CA), cysteine (CS), homocysteine (HS), and reduced glutathione (GS); (B) their disulfide products cystamine (CAAC), cystine (CSSC), homocystine (HSSH), and oxidized glutathione (GSSG); and (C) the intermediate sulfur surface species calculated from mass balance during the reaction of 500 µM thiol with 10 mM δ-MnO_2 aged for 1.5 years at pH 7.0. Standard deviations represent the average of at least triplicate measurements at each time point and are often smaller than the symbols.

The simultaneous analysis of both the thiol reactant and disulfide product in solution by voltammetric microelectrodes over such a short time scale is unique and allows to close mass balance on the sulfur species. Mass balance calculations (Eq. 4-2) can be used to identify any intermediate sulfur surface species (MnRS) formed during the reaction.

$$[MnRS] = [RS^-]_0 - [RS^-] - 2[RSSR] \quad (4\text{-}2)$$

where $[RS^-]_0$ is the initial concentration of thiol, and $[RS^-]$ and $[RSSR]$ represent the concentrations of dissolved thiol and disulfide measured as a function of time, respectively (Figure 4-2A,B). Although differentiation between surface species cannot be accounted for electrochemically, these calculations indicate that the lifetime of the intermediate sulfur surface complex depends on the thiol structure, as the rate of formation and transformation of the intermediate sulfur complexes with the different thiols decreased in the order of cysteamine > cysteine > homocysteine and was below detection limit over the course of the reaction with glutathione (Figure 4-2C). The absence of surface-bound glutathione was not unexpected based on its numerous negatively charged functional groups and the increased steric hindrance resulting from the large structure of glutathione compared to the other smaller thiols. Lack of permanently adsorbed glutathione was also observed during reactions with Fe(III) oxides in contrast to similar experiments with cysteamine, cysteine, and homocysteine (Eitel and Taillefert, 2017). The desorption of glutathione here was likely rapid due to the lower point of zero charge (PZC) of Mn(IV) oxides compared to Fe(III) oxides, which decreases the interaction between the negatively charged carboxylic functional groups of the thiol reactant with the negatively charged Mn oxide surface and thus promotes desorption of the product of the reaction once it is formed. In contrast, the high reactivity of cysteamine can be explained by its small size and lack of carboxylic group to interfere with the negative surface charges of the Mn oxide.

4.4.3 Effect of Mn Oxide Aging on Thiol Oxidation Kinetics

The reaction between cysteine and fresh δ-MnO_2 was extremely fast and complete almost immediately (Figure 4-3A), including production of cystine to equilibrium concentrations within the first 15 sec (half-life of < 6 sec, Figure 4-3B). The

reaction rate decreased progressively with δ-MnO_2 that was aged for 1 and 2 months (half-lives of 15 and 18 sec, respectively), whereas the rate of cysteine oxidation with δ-MnO_2 aged for 2 months, 3 months, and 1.5 years showed no significant difference. With more aged δ-MnO_2 (2.5 and 6 years old), the rate of cysteine oxidation decreased progressively (Figure 4-3A), likely due to the increased fraction of tunnel structured cryptomelane as identified by XRD and XAS (Figure 4-1 and Figure A 1). Meanwhile, the rate of cystine production declined concomitantly, and cystine concentration reached equilibrium within 1, 3, 3.5, 4.25, 7, and 10 min as the age of δ-MnO_2 increased from 1 month to 6 years (Figure 4-3B). The lowest reaction rates were observed with manganite, which did not reach equilibrium until 14 min (half-life of 5.75 min). For all aged δ-MnO_2 as well as manganite, the concentration of the intermediate sulfur surface complex calculated from mass balance (Eq. 4-2) confirmed complete transformation of the thiol to its disulfide product within 15 min. The concentration of the intermediate surface complex with most of the aged δ-MnO_2 reached a maximum within a minute, except for 6-year-old δ-MnO_2 which reached a maximum between 4–5 min (Figure 4-3C). These results demonstrate that the transformation from layered δ-MnO_2 to tunneled cryptomelane significantly slowed down the reaction.

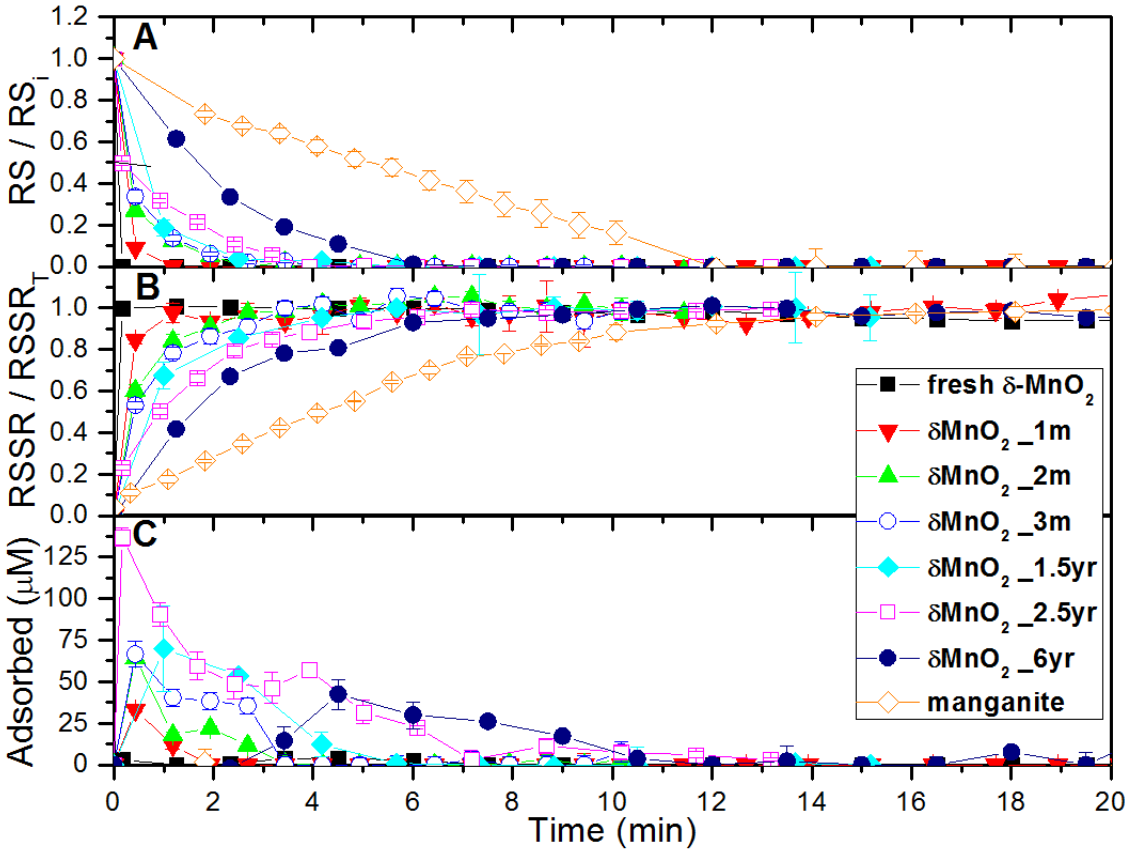

Figure 4-3 Temporal evolution of the molar ratio of: (A) the cysteine (CS) reactant, (B) the cystine product (CSSC), and (C) the intermediate sulfur surface species calculated from mass balance in solution during the reaction of 500 µM cysteine with 10 mM δ-MnO_2 of different age or 10 mM manganite at pH 7.0. Standard deviations represent the average of at least triplicate measurements at each time point and are often smaller than the symbols.

4.4.4 Evidence for the Reaction Mechanism

The mechanism of the reaction has been proposed to proceed via initial adsorption of the electron transferring sulfhydryl group of the thiol onto the Mn(IV)-oxide surface to form a neutral species and a water molecule (Herszage et al., 2003) (Eq. 4-3).

$$\equiv Mn(IV)OH + RSH \leftrightarrow \equiv Mn(IV)SR + H_2O \qquad (4\text{-}3)$$

The surface species undergoes a series of reactions characterized primarily by a single electron transfer between the sulfur and Mn(IV) center (Eq. 4-4) followed by rapid dissolution of the thiol radical (Eq. 4-5), adsorption of a second thiol to the surface-bound Mn(III) (Eq. 4-6), a second electron transfer (Eq. 4-7), and release of the second thiol radical and generation of a surface-bound Mn(II) (Eq. 4-8) that is eventually released in solution (Eq. 4-9). In solution the thiol radical immediately dimerizes to form the stable disulfide product (Eq. 4-10).

$$\equiv Mn(IV)SR \xrightarrow{e^- transfer} \equiv Mn(III)SR \tag{4-4}$$

$$\equiv Mn(III)SR + H_2O \xrightarrow{fast} \equiv Mn(III)OH + RS^{\cdot} + H^+ \tag{4-5}$$

$$\equiv Mn(III)OH + RSH \xrightarrow{fast} \equiv Mn(III)SR + H_2O \tag{4-6}$$

$$\equiv Mn(III)SR \xrightarrow{e^- transfer} \equiv Mn(II)SR \tag{4-7}$$

$$\equiv Mn(II)SR + H_2O \xrightarrow{fast} \equiv Mn(II)OH_2^+ + RS^{\cdot} \tag{4-8}$$

$$\equiv Mn(II)OH_2^+ \xrightarrow{fast} \equiv Mn(IV)OH + Mn(II)_{aq} + H^+ \tag{4-9}$$

$$2RS^{\cdot} \xrightarrow{fast} RSSR \tag{4-10}$$

Based on molecular orbital theory, two separate one electron transfers and formation of an Mn(III) intermediate is the most probable pathway for reduction of Mn(IV) to Mn(II) (Luther, 2005). Indeed, adsorbed Mn(III) has been identified as intermediate species during the reaction between birnessite and inorganic reductants such as arsenite,

Cr(III), and selenite (Banerjee and Nesbitt, 1999; Banerjee and Nesbitt, 2000; Nesbitt et al., 1998), and the microbial reduction of Mn(IV) oxides generates Mn(III) complexes in solution (Lin et al., 2012). The reduction of Mn(III) by thiols is not inhibited by common Mn(III) stabilizers, such as pyrophosphate (Kostka et al., 1995), and the reaction proceeds extremely rapidly (data not shown). As a result, direct detection of a Mn(III) intermediate during thiol oxidation has thus far not been possible (Herszage et al., 2003). Although electrochemical data cannot identify the intermediate sulfur surface species, mass balance calculations (Eq. 4-2) provides novel insights into the reaction mechanism. With cysteamine, homocysteine, and possibly cysteine, a secondary maximum in the concentration of the intermediate sulfur surface species was observed during reaction with the 1.5 year-old δ-MnO_2 (Figure 4-2C). This secondary maximum in the sulfur intermediate was clearly observed during reaction between cysteine and all δ-MnO_2 aged for more than 1 month (Figure 4-3C). The presence of the two local maxima in intermediate sulfur surface species suggests that the transformation from layered δ-MnO_2 to tunneled cryptomelane slows down the reaction enough to identify the intermediate sulfur surface species as the Mn(IV) (Eq. 4-3) and the Mn(III) (Eq. 4-6) thiol complexes formed prior to each electron transfer step. These findings therefore provide evidence for the proposed two steps of one electron transfer from Mn(IV) to Mn(III), and from Mn(III) to Mn(II). As formation of Mn(III) at the surface of the Mn(IV) oxides during the reaction (Eq. 4-6) may result in Jahn-Teller distortion which promotes the subsequent reduction of Mn(III) sites (Nico and Zasoski, 2000), it is likely that the two thiol oxidation reactions proceed at a single site rather than different Mn(IV) centers in these minerals.

4.4.5 Overall Rate Law

From Eq. 4-1, the rate of disulfide production at constant pH depends on the concentrations of thiol and Mn oxide, resulting in an experimental rate law that can be generally expressed as:

$$R = \frac{d\,[RSSR]}{dt} = -\frac{1}{2}\frac{d\,[RS^-]}{dt} = k\,[RS^-]^a[Mn\ oxide]^b \tag{4-11}$$

where k is the overall rate constant and a and b represent the order of the reaction with respect to each constituent. In the presence of excess Mn oxide, the rate of disulfide production is simplified into a pseudo-order kinetic model as:

$$R_i = k_{obs}\,[RS^-]^a \tag{4-12}$$

where

$$k_{obs} = k[Mn\ oxide]^b \tag{4-13}$$

is the apparent rate constant. From Eq. 4-12, the order of the reaction with respect to the thiol species can be determined as the slope of the linear regression that fits the log of the initial rate of disulfide production as a function of the log of the initial concentration of thiol. By calculating initial rates using the change in disulfide concentration as a function of time during the first 10-15% of the reaction extent, a slope of 0.96 ± 0.07 was determined for the reaction between cysteine and 1,5-year-old δ-MnO_2 (Figure 4-4), demonstrating first order kinetics with respect to thiol. First order kinetics with respect to thiol was also confirmed for homocysteine reaction with 1,5-year-old δ-MnO_2 (slope = 0.91 ± 0.21) and for cysteine reaction with 2,5-year-old δ-MnO_2 (slope = 0.93 ± 0.08) (Figure 4-4).

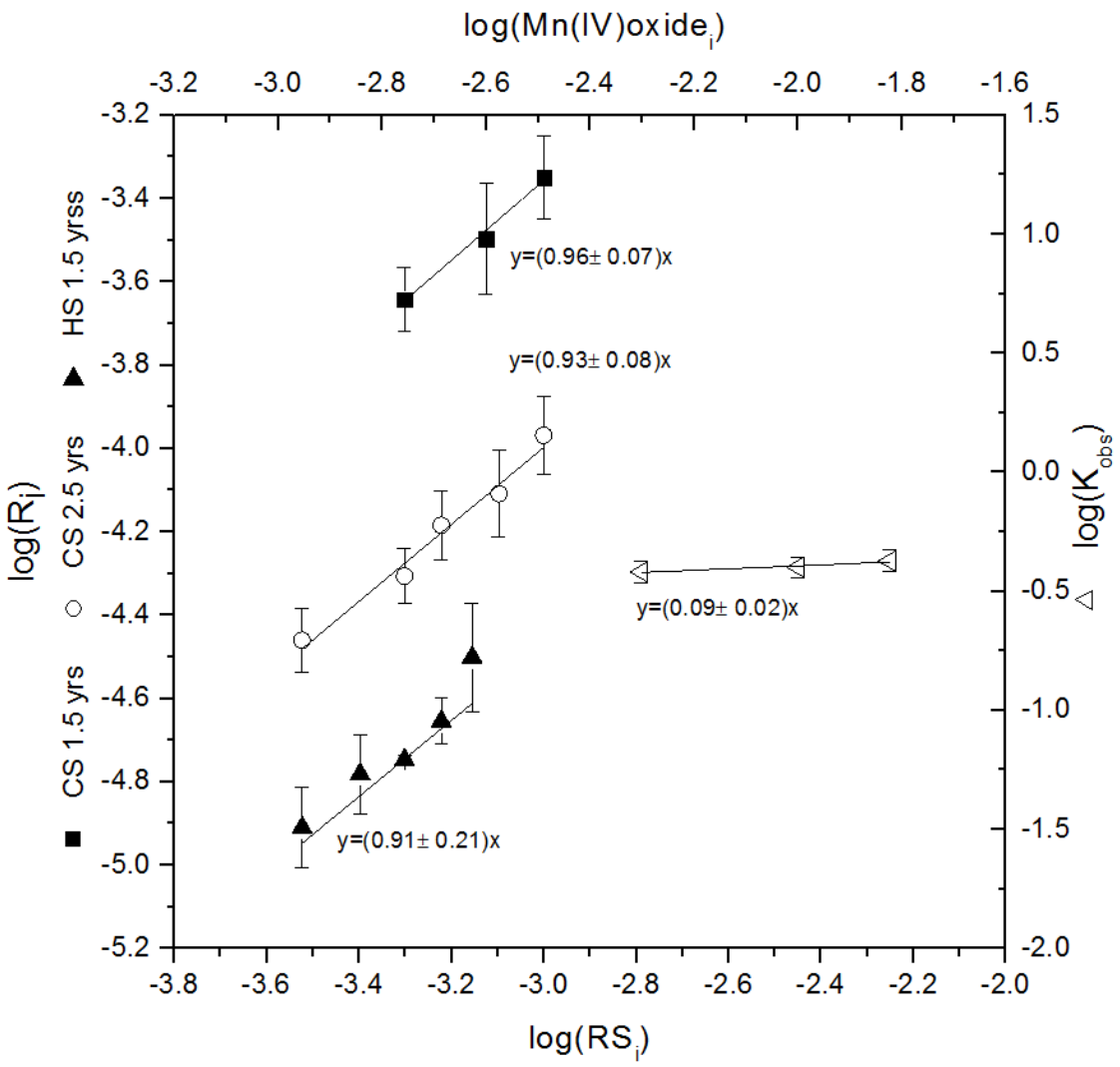

Figure 4-4 Experimental determination of the reaction order with respect to: (left axis) cysteine (CS) and homocysteine (HS) using the isolation method in the presence of 10 mM δ-MnO_2 aged for 1.5 and 2.5 years at pH 7; and (right axis) Mn oxide using the isolation and pseudo-order methods. To determine the order with respect to the Mn oxide, the initial concentration of a suspension of δ-MnO_2 aged for 1.5 years was varied between 5 and 15 mM in a suite of experiments conducted with 500 µM cysteine at pH 7.0.

Experiments were also conducted with constant cysteine concentrations and varied concentrations of 1,5-year-old δ-MnO_2 to determine k_{obs} at each Mn oxide concentration after integration of Eq. 4-12 (with a = 1) by representing the natural log of the cysteine concentration ($[RS^-]$) as a function of time (Eq. 4-14).

$$\ln([RS^-]) = -2k_{obs}t + \ln([RS^-]_0) \quad (4\text{-}14)$$

The order of the reaction with respect to Mn oxide (b) was then determined from the slope of the linear regression of the log of k_{obs} as a function of the log of Mn oxide concentration (Eq. 4-13). A slope of 0.09 ± 0.02 was determined (Figure 4-4), indicating a zero order rate law with respect to Mn oxide concentration, as observed previously for the reaction of cysteine with excess MnO_2 nanoparticles (Altaf and Jaganyi, 2014) and excess Fe(III) oxides (Eitel and Taillefert, 2017).

As a result, the overall kinetic rate law of cysteine oxidation by Mn oxides in environmentally relevant conditions at pH 7 and in the presence of excess Mn oxides can be written as the following first order rate law:

$$R = k[RS^-] \quad (4\text{-}15)$$

Assuming the rate law derived from experiments with cysteine, homocysteine, and two different aged δ-MnO_2 is the same for all thiols and all Mn oxides in this study, the experimental rate constant (k) can be obtained after integration of the overall first order rate law (Eq. 4-15) from the slope of the natural log of the thiol concentration as a function of time normalized to its initial concentration (Eq. 4-16) and represented graphically (Figure 4-5).

$$Ln(\frac{[RS^-]}{[RS^-]_0}) = -2k * t \quad (4\text{-}16)$$

The good linearity of the integrated rate law with all thiols (Figure 4-5A) and the different minerals (Figure 4-5B) confirms that the overall rate law is accurate. As previously observed with Fe(III) oxides (Eitel and Taillefert, 2017), rate constants decreased in the order of cysteamine > cysteine > homocysteine > glutatione (Figure 4-6A) as the chemical structure of the reductant becomes more complex. In addition, rate constants decreased with increasing age of δ-MnO_2 (Figure 4-6B). This decrease was drastic within the first two months of aging then gradual between 3 months and 6 years, even after normalizing the rate constant by the specific surface area. As rate constants are independent of reactant concentrations and these experiments were conducted in excess of surface sites compared to thiol reactant, the change in mineral structure during aging must be responsible for the observed differences in reactivity with the thiols. These findings indicate that the synthesis of manganese mineral phases plays an important role in reduction kinetics and that great care should be taken to synthesize minerals of appropriate age. Finally, among all the Mn oxides tested, manganite displayed the lowest rate of cysteine oxidation (Figure 4-6B) as observed for Cr(III) oxidation by manganite relative to cryptomelane and birnessite (Weaver and Hochella, 2003) and for the oxidation of a number of organic contaminants by Mn oxides of different structure (Remucal and Ginder-Vogel, 2014). Despite the higher redox potential of manganite compared to δ-MnO_2 (Bricker, 1965), slower reaction is likely due to the increased crystallinity as well as the thermodynamic stability of Mn(III) within the MnOOH structure. Indeed, shorter bond lengths with increased orbital overlap are observed between surface Mn(IV) sites of birnessite with inorganic reductants such as

arsenite compared to surface Mn(III) sites of manganite (Zhu et al., 2009). Shorter bond lengths between Mn(IV) and the surface-bound reactant may increase electron transfer and further support increased reduction rates of δ-MnO_2 and even cryptomelane compared to manganite. Disruption of the mineral structure by formation of surface Mn(III) (Nico and Zasoski, 2000) in the first electron transfer step during Mn(IV) reduction likely decreased the energy necessary for the second electron transfer and increased the rate of thiol oxidation by δ-MnO_2 and cryptomelane compared to manganite.

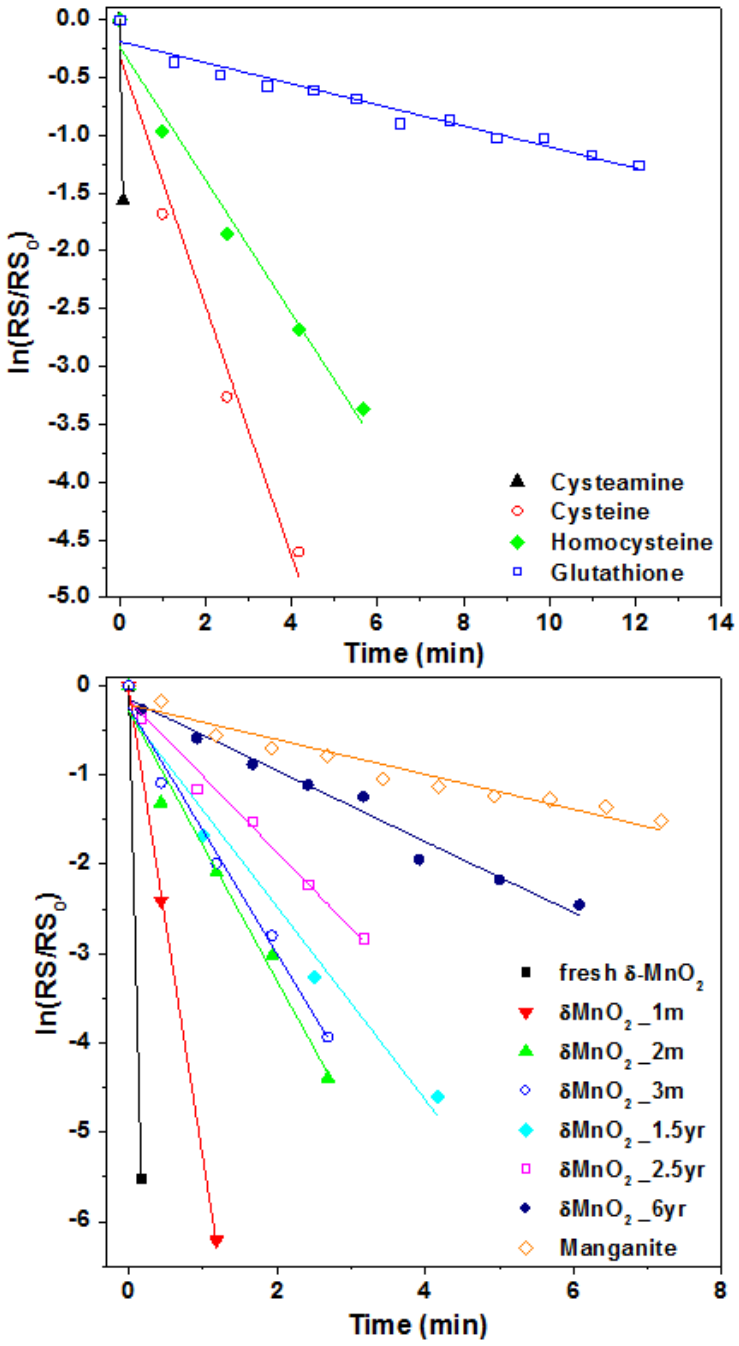

Figure 4-5 Temporal evolution of the natural logarithmic of the concentration of: (A) cysteamine, cysteine, homocysteine, and glutathione normalized to their initial concentration during the reaction of each thiol with 10 mM δ-MnO_2 aged for 1.5 year at pH 7.0; and (B) cysteine normalized to its initial concentration during its oxidation

by different age δ-MnO_2 and manganite. The slope of duplicate linear curves was averaged and used to calculate the overall rate constant of the reaction.

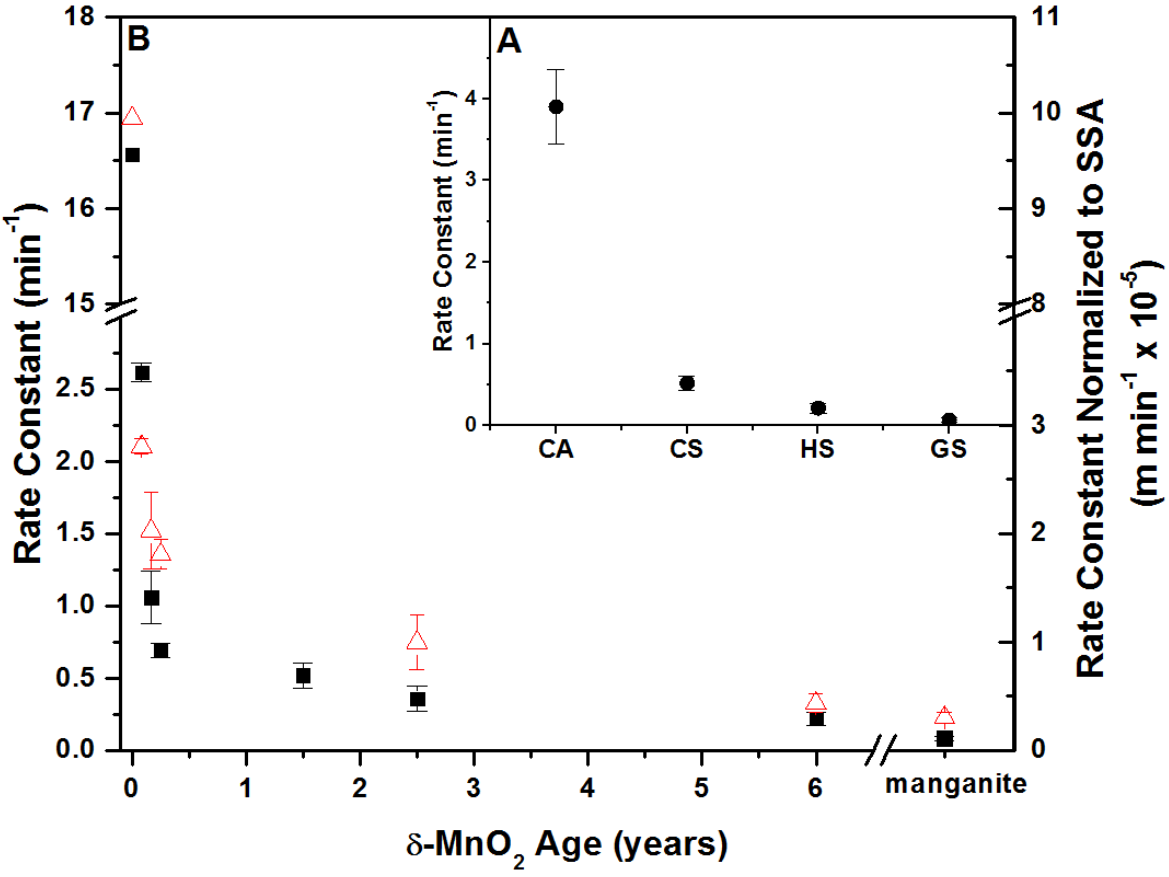

Figure 4-6 Overall first order rate constants for (A) the reaction of cysteamine (CA), cysteine (CS), homocysteine (HS), and reduced glutathione (GS) with δ-MnO_2 aged for 1.5 years, and (B) the reaction of cysteine with δ-MnO_2 of different age and manganite (left axis, closed black squares) and normalized to BET specific surface area (SSA) (right axis, open red triangles).

4.5 Environmental Implications

The findings of this study have important environmental implications. The rapid reduction of an efficient adsorbent and oxidant of inorganic (Feng et al., 2007; Jenne, 1968; Nelson and Lion, 2003; Oscarson et al., 1981; Weaver and Hochella, 2003) and organic (Remucal and Ginder-Vogel, 2014) contaminants may have important implications on the

remediation of environments where thiol production is significant. The differences in reactivity of cysteine with Mn oxides of different structure (i.e. δ-MnO_2 of different age and manganite) also demonstrate the importance of correlating solid phase structure and reactivity when dealing with the redox properties of Mn oxides. In this context, the reaction kinetics of Mn oxides with inorganic and organic reductants should be determined with various δ-MnO_2 transformation products to accurately predict the environmentally-relevant biogeochemical significance of Mn oxides in sedimentary environments.

Thiols have been detected in both freshwater (Zhang et al., 2004a) and marine (Kiene, 1991; Kiene and Taylor, 1988b; Luther et al., 1986; MacCrehan and Shea, 1995) sediments, and previous studies have demonstrated the importance of cysteine as an electron shuttle during microbial Fe reduction (Doong and Schink, 2002; Liu et al., 2014) and confirmed the reduction of cystine by model metal-reducing bacteria (Doong and Schink, 2002; Kaden et al., 2002; Liu et al., 2014). The increased abiotic reaction rate between thiols and Mn oxides and the complete conversion of the thiols to their disulfide product compared to the Fe(III) oxide system (Eitel and Taillefert, 2017) suggests that thiols may act as electron shuttles during dissimilatory Mn reduction to an even greater extent than during dissimilatory Fe reduction. Thus, if thiols are microbially recycled, even small thiol concentrations may result in significant reduction of Mn oxides in sedimentary environments. The reduction of Mn oxides by thiols may therefore have a significant impact on inorganic (Feng et al., 2007; Jenne, 1968; Nelson and Lion, 2003; Oscarson et al., 1981; Weaver and Hochella, 2003) and organic (Remucal and Ginder-Vogel, 2014) contaminant degradation and indirectly influence the biogeochemical cycling of carbon, nitrogen, phosphorus, sulfur, and iron in sediments (Burdige and Nealson, 1986; Luther et

al., 1997; Neretin et al., 2003; Schippers and Jorgensen, 2001; Tebo et al., 2004; White et al., 2008).

4.6 Acknowledgments

This work was supported by the National Science Foundation (Grant numbers DEB-1542596 to MT and EE and CHE-1710285 to YT and SZ). We thank Dr. Nadia Szeinbaum for synthesis of some Mn oxides, Nan Xie for help with XRD analysis, Biao Wan and Pan Liu for help with EXAFS analyses, and Nathan Ellebracht for BET analysis. We also appreciate the support from beamline scientists Qing Ma (APS 5BM) and Ryan Davis (SSRL 4-1). Portions of this research were conducted at the Advanced Photon Source (APS) and Stanford Synchrotron Radiation Lightsource (SSRL). APS is a U.S. Department of Energy (DOE) Office of Science User Facility operated for the DOE Office of Science by Argonne National Laboratory under Contract No. DE-AC02-06CH11357. Use of SSRL, SLAC National Accelerator Laboratory, is supported by DOE Office of Science, Office of Basic Energy Sciences under Contract No. DE-AC02-76SF00515.

CHAPTER 5. THIOLS AS ELECTRON SHUTTLES DURING DISSIMILATORY IRON REDUCTION IN NATURAL SEDIMENTS

5.1 Abstract

Although dissimilatory reduction of iron oxides potentially represents a significant carbon remineralization process, the importance of this process in marine sediments may be underestimated due to the difficulty in differentiating between the microbial and chemical production of Fe(II). Small thiols rapidly reduce iron oxides and various metal-reducing bacteria are able to reduce disulfides and recycle thiols to increase iron reduction rates. Although small thiols from a variety of sources have been previously detected in both freshwater and marine sediments, the relationship between thiols and iron in sediments has not been thoroughly investigated. In this study, sediments from four marine and one freshwater locations were investigated for the co-existence of thiols and iron reduction by-products. Depth profiles of cysteine, glutathione, and cysteamine reached maximum concentrations in zones of iron reduction, whereas 3-mercaptopropanoic acid (3-MPA) was only produced in the sulfidic zone of sediments. The good correlation between pore water thiols and Fe^{2+} as well as organic-Fe(III) complexes, proposed to be produced as intermediates during microbial iron reduction, provides evidence for thiol electron-shuttling during dissimilatory iron reduction in natural sediments. These findings are supported by sediment incubations conducted under either metal- or sulfate-reducing conditions as well as incubations conducted with pure cultures of the model Fe(III)-reducing bacteria *Shewanella oneidensis* MR-1. Together these results not only provide insight into the mechanism of dissimilatory iron reduction in marine sediments, but also

suggest that thiols may be used as a proxy to differentiate between microbial and chemical iron reduction in sediments.

5.2 Introduction

It has long been accepted that organic sulfur comprises a significant fraction of the total sulfur pool in both freshwater and marine sediments (Ferdelman et al., 1991; Urban et al., 1999). In fact, the quantitative significance of organic sulfur to reduced sulfur is second only to pyrite in sedimentary environments (Anderson and Pratt, 1995; Berner and Raiswell, 1983; Garrels and Lerman, 1984; Vairavamurthy et al., 1995). Although the majority of organosulfur compounds may be attributed to sulfur incorporation into oil and kerogen deposits (Aizenshtat et al., 1995; Orr, 1986; van Dongen et al., 2003), as many as 20 organic compounds containing sulfhydryl groups, referred to as thiols, have been observed in aquatic environments (Vairavamurthy and Mopper, 1987). Detection of thiols in shallow sediments has been attributed to a number of processes including the abiotic reaction of dissolved sulfide with organic matter (Luther et al., 1986; Vairavamurthy and Mopper, 1987), microbial deamination of amino acids (Kiene et al., 1990), as well as microbial degradation of plant material (Kiene and Taylor, 1988a; Kiene and Taylor, 1988b; Sorensen, 1988). In both fresh and marine waters, thiol concentrations have been correlated to chlorophyll levels and, therefore, attributed to phytoplankton production (Al-Farawati and Van Den Berg, 2001; Hu et al., 2006; Matrai and Vetter, 1988a). Microbial production of thiols in both marine waters and sediments has also been attributed to the detoxification of toxins such as Cu, Hg, and, Zn by complexation (Chapman et al., 2009; Kawakami and Achterberg, 2012; Legall and Van Den Berg, 1993; Park and Butcher, 2010; Shea and Maccrehan, 1988; Zhang et al., 2004b). It has even been suggested that

thiols may be microbially released in sediments to solubilize trace metal nutrients from solid phases, similar to siderophores during iron acquisition in oxic environments (MacCrehan and Shea, 1995).

The cycling of thiols in natural environments is important due to their chemical reactivity. Thiols are known to be good chemical reductants of Fe(III) oxides (Amirbahman et al., 1997; Jameson et al., 1988; Sisley and Jordan, 1995;Chapter 3 of this dissertation), Fe(III) in clays (Morrison et al., 2013), MnO_2 nanoparticles (Altaf and Jaganyi, 2014; Andrabi and Khan, 2007; Herszage et al., 2003), Mn(III) nanoparticles (Salamon et al., 2004), and Mn(III,IV) oxide minerals (Chapter 4 of this dissertation). The reduction of ferrihydrite by thiols is rapid and decreases with increasing structural complexity in the order cysteamine > cysteine > homocysteine > glutathione at circumneutral pH and concentration ratios that are representative of natural sediments (Eitel and Taillefert, 2017). In environmentally relevant conditions, thiol oxidation during reaction with fresh δ-MnO_2, aged δ-MnO_2 with gradual transformation to cryptomelane, and manganite is even more rapid than during reaction with ferrihydrite (Eitel et al., 2018; Chapter 4 of this dissertation).

As it is physiologically difficult to transfer electrons to a solid substrate, the mechanism of bacterial reduction of Mn(III,IV) and Fe(III) oxides is proposed to occur through a number of pathways including direct contact with the solid phase, electron-conducting nanowires to provide electrons at a distance, non-reductive solubilization of the solid mineral by Fe(III)-binding ligands and subsequent reduction of the organic-Fe(III) complex with recycling of the organic ligand, and electron shuttling of electrons to the metal oxides via exogenous compounds that are easily recycled microbially (Cooper et al.,

2016). The electron-shuttling mechanism has received much attention recently, as humic substances of natural sediments (Amstaetter et al., 2012; Jiang and Kappler, 2008; Kappler et al., 2004; Klüpfel et al., 2014; Lovley et al., 1996; Scott et al., 1998) or humic analogs (Bae and Lee, 2013; Burgos et al., 2003; Luijten et al., 2004; Wolf et al., 2009) accelerate the rate of microbial iron reduction, and microorganisms grown on humic substances as electron acceptor have been isolated from natural sediments (Coates et al., 2002; Coates et al., 1998). Similarly, elemental sulfur also acts as electron shuttling compound in dissimilatory iron reduction (DIR) as a variety of metal-reducing microorganisms are able to use elemental sulfur as electron acceptor (Flynn et al., 2014). Finally, addition of thiols and their oxidized disulfide forms to pure cultures of model Fe(III)-reducing bacteria in the presence of Fe(III)-clays (Liu et al., 2014) and ferrihydrite (Doong and Schink, 2002) have resulted in increased rate and extent of Fe(II) production, suggesting that microorganisms may also utilize thiols as extracellular electron shuttles to transfer electrons to solid metal oxides. In this process, the oxidized disulfide species produced during the reduction of solid metal oxides may be microbially reduced, allowing the thiol to be recycled. Indeed, metal-reducing bacteria, including multiple *Shewanella* species and *Geobacter sulfurreducens*, are capable of disulfide reduction (Doong and Schink, 2002; Kaden et al., 2002; Liu et al., 2014). Given the ability of microbes to utilize thiols as electron shuttles during DIR, it is surprising that thiols have not been linked to Fe^{2+} concentrations in natural sediments.

Although microbial reduction of Fe(III) oxides is thermodynamically more favorable than sulfate (Froelich et al., 1979), the high concentrations of sulfate in seawater results in microbial sulfate reduction (MSR) being considered the dominant anaerobic

respiration process in most marine sediments (Henrichs and Reeburgh, 1987; Jorgensen, 1982; King, 1988; Skyring, 1987). In addition, dissolved sulfide produced by MSR may chemically reduce iron oxides such that it is difficult to differentiate between the abiotic and biotic production of Fe^{2+} in sedimentary environments. In the absence of MSR, however, DIR may significantly contribute to the cycling of organic carbon in marine sediments (Kostka et al., 2002; Meiggs and Taillefert, 2011; Thamdrup et al., 1994). Soluble organic-Fe(III) complexes produced as intermediates during DIR and aqueous FeS clusters produced as intermediate during the precipitation of $FeS_{(s)}$ have been used as chemical proxies to define zones of DIR and MSR in marine sediments (Beckler et al., 2016; Taillefert et al., 2017). Thiols may thus provide a new means to differentiate microbial and chemical Fe^{2+} production in natural sediments.

Interestingly, only a few studies have detected thiols in marine sediments (Kiene, 1991; Kiene and Taylor, 1988b; Luther et al., 1986; MacCrehan and Shea, 1995; Shea and MacCrehan, 1988), and even fewer measurements have been conducted in freshwater sediments (Zhang et al., 2004a). Among these studies, glutathione and cysteine have typically been observed in the top 5-10 cm of sediment (Kiene, 1991; Kiene and Taylor, 1988b; MacCrehan and Shea, 1995), where Fe^{2+} is likely to be detected. On the other hand, 3-MPA is generally observed to increase with sediment depth and coincides with the production of dissolved sulfide (Kiene and Taylor, 1988b). In this study, sediments from four different marine environments and one freshwater location were collected to investigate the relationship between pore water thiol concentrations and the different anaerobic respiration processes taking place in these sediments. In addition, sediment slurry incubations and incubations of the model Fe(III)-reducing bacteria, *Shewanella*

oneidensis MR-1 were also conducted to determine whether thiols are recycled and produced endogenously during Fe(III) reduction.

5.3 Methods

5.3.1 Site Locations

Sediments were obtained from four marine and one freshwater environment (Figure 5-1; Figure 5-2). Continental margin sediments were collected from 7 stations near Cape Lookout, North Carolina (NC) during cruises conducted in July 2015 on the R\V Savannah (Figure 5-3). The NC sediments are characterized by low organic matter remineralization and sedimentary iron concentrations (more details in Chapter 6). Additional continental margin sediments were collected from 6 stations in the Gulf of Mexico off the Louisiana coast (LA) the during a cruise in July 2016 on the R\V Pelican (Figure 5-4). Increased Fe^{2+} concentrations have been previously detected in LA sediments compared to the NC sediments, and no indication of major MSR was observed (Beckler et al., 2016). In comparison, complete removal of sulfate with sediment depth was observed at 3 of the 6 stations investigated in the Rhône River delta (France) in the Gulf of Lions on the R\V Tethys II in September 2015 (Figure 5-5) (more details in Chapter 7). Nine sediment cores were collected from the Salt Marsh Ecosystem Research Facility (SERF) at the Skidaway Institute of Oceanography, Georgia in June 2014, March 2015, and June 2016 (Figure 5-6). The sediments collected from the creek bank were generally iron-rich, while those collected from the mud flats were dominated by MSR (Bull and Taillefert, 2001; Taillefert et al., 2007b). Finally, three sediment cores were collected at 2 sites from the subalpine freshwater wetlands of the Fraser Experimental Forest, Colorado (CO) in September 2015

courtesy of Dr. Thomas Borsh Figure 5-7). Two cores were taken from Tub 2 (site A), which is at the center of a depressional wetland and one core was taken from Spring 72 (site B), which is in the middle of a slope wetland. Water for sediment core incubation was taken from St. Louis Creek, which drains a majority of the water in the Fraser Experimental Forest.

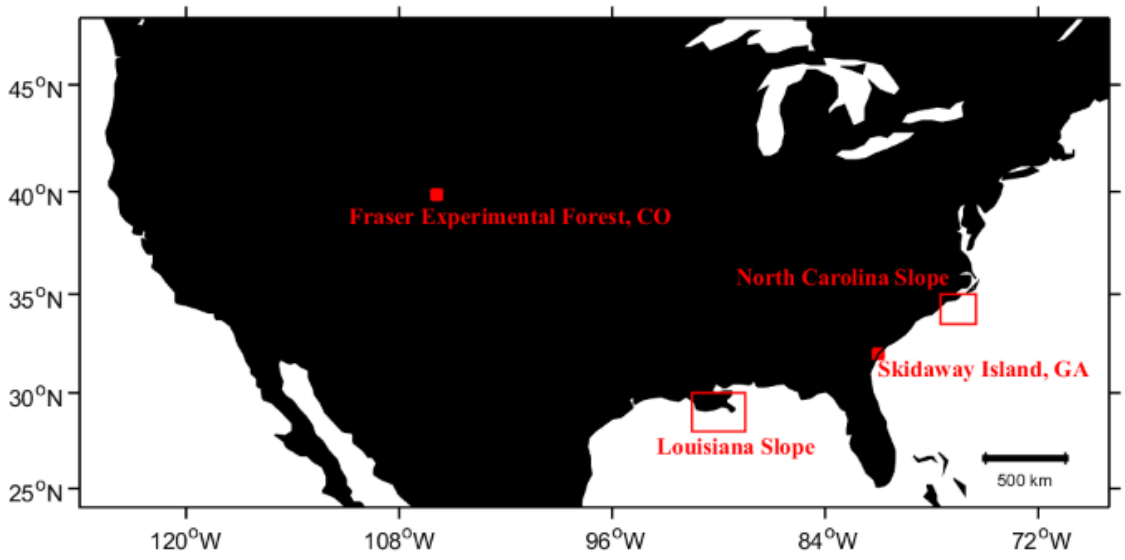

Figure 5-1 Map of North America to show the locations of three of the marine sampling locations and the freshwater location.

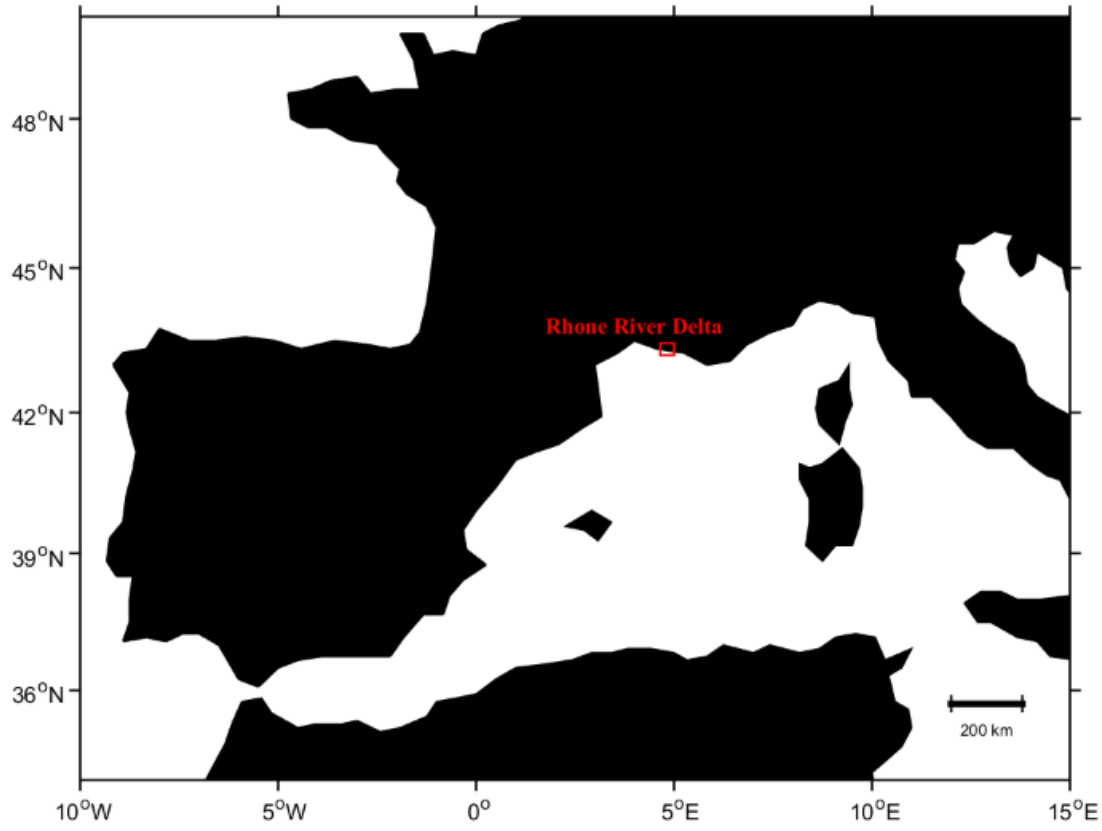

Figure 5-2 Map of Europe to show the sampling location at the Rhone River delta.

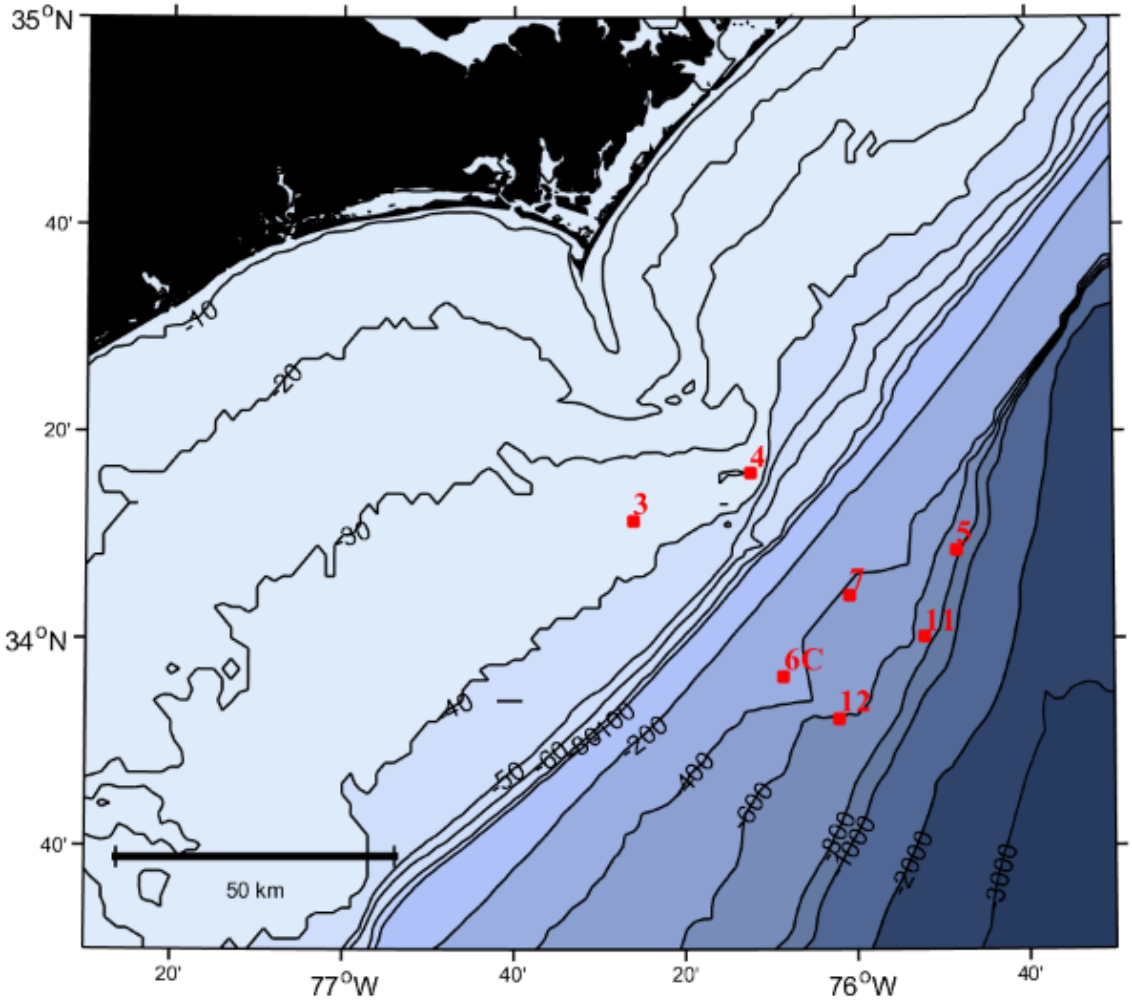

Figure 5-3 Map of sampling locations on the North Carolina continental margin off Cape Lookout.

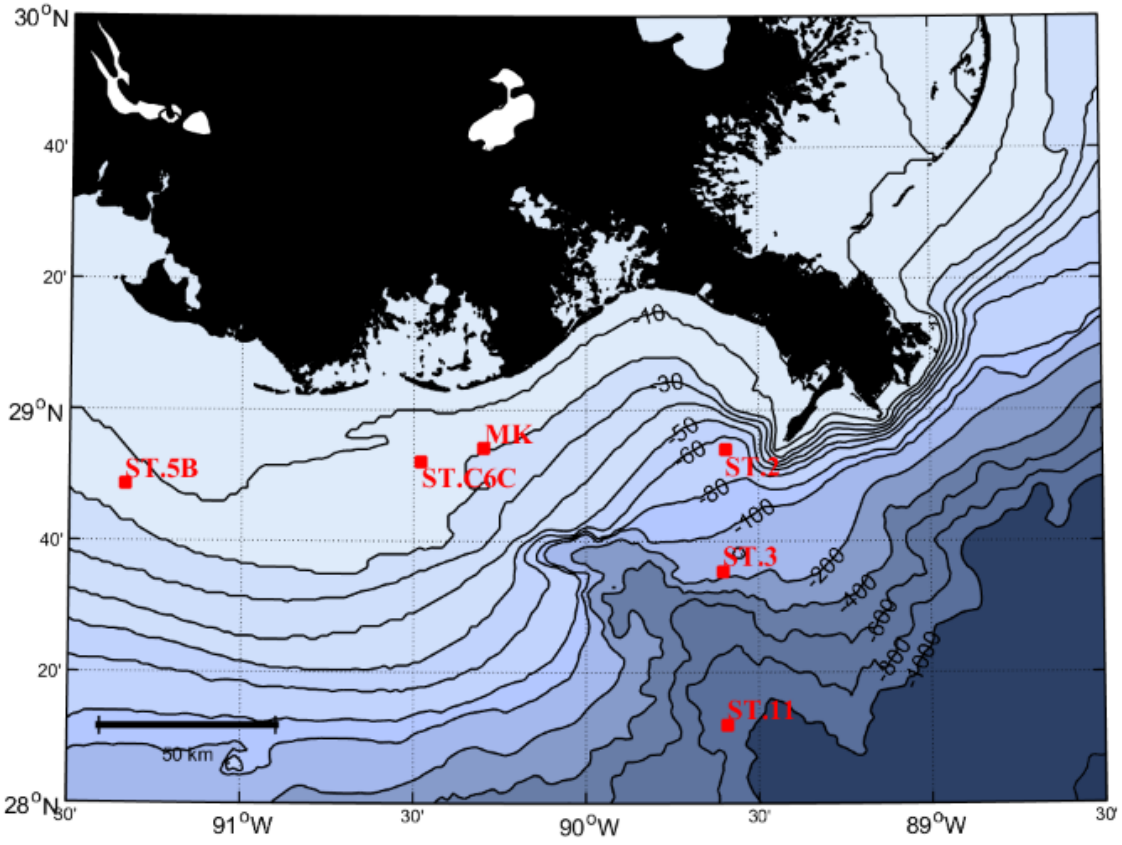

Figure 5-4 Map of sampling locations from the Louisiana continental margin near the Mississippi and Atchafalaya Rivers.

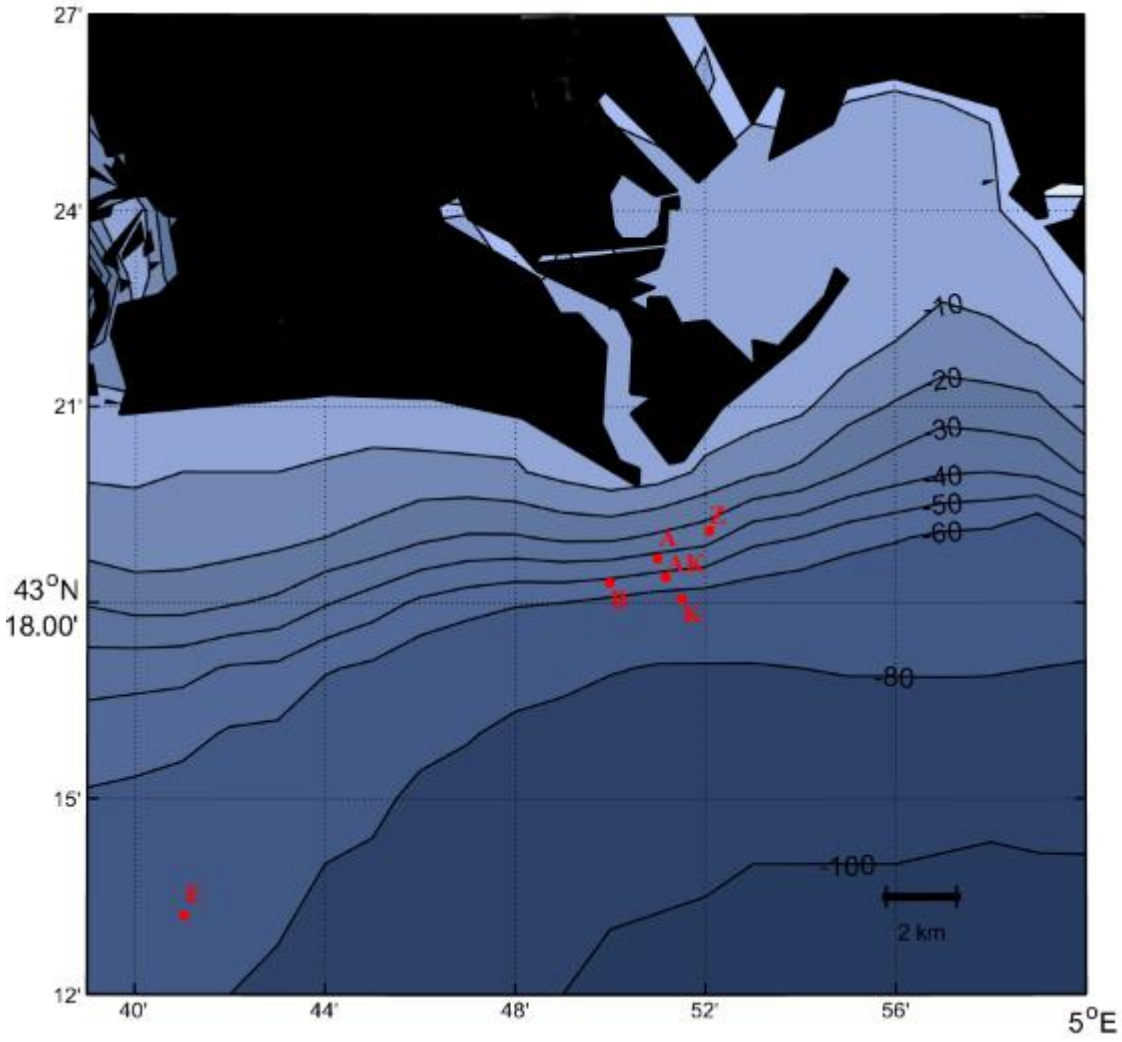

Figure 5-5 Map of sampling locations in the Rhone River prodelta of France.

Figure 5-6 Map of sampling locations off a 250 m long pier at SERF on Skidaway Island, Georgia.

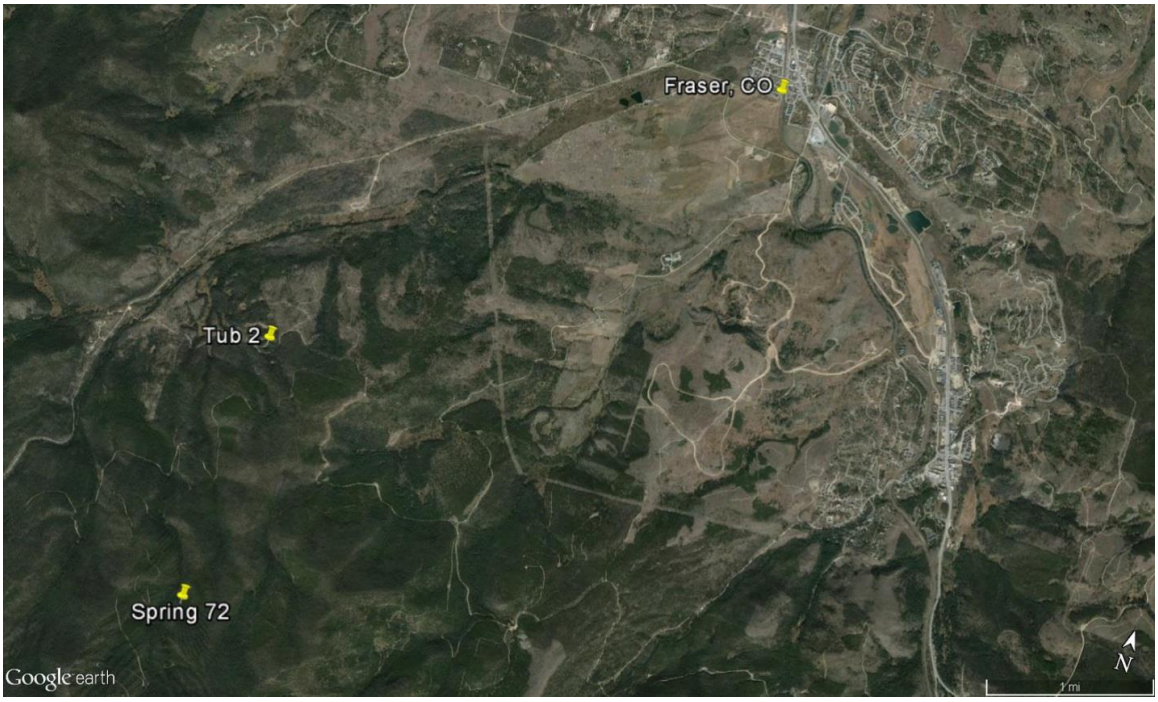

Figure 5-7 Map of sampling locations in the Fraser Experimental Forest in Colorado.

5.3.2 Experimental Reagents

Unless otherwise noted, all chemicals were of Reagent grade or higher purity and obtained from Sigma-Aldrich. Thiol and disulfide stocks were prepared weekly and stored at 4 ºC. Two-line ferrihydrite was prepared by titration of $FeCl_3$ solution by 10 mM NaOH to pH 7 as described previously (Schwertmann, 2000) and washed with miliQ-water three times prior to use. The synthesis of ferrihydrite was confirmed by X-ray diffraction (XRD).

5.3.3 Sediment Collection and Analysis

Continental margin sediments (NC and LA) were collected using either a single corer (Marinelli et al., 1998) or a MC-800 multicorer (Ocean Instruments, Inc.). Rhône sediments were collected with a single corer (UWITEC®), whereas salt marsh (SERF) and freshwater wetland (CO) samples were collected using a hand corer. Sediment cores from CO were wrapped and shipped overnight on dry ice, then incubated with water from St. Louis Creek for 5 days at 4°C to reestablish sediment characteristics. Otherwise sediments were processed within 30 minutes of collection.

Voltammetric depth profiles of dissolved O_2, Mn^{2+}, Fe^{2+}, total dissolved sulfide ($\sum H_2S = H_2S + HS^- + S(0) + S_x^{2-}$) as well as organic complexes of Fe(III) (org-Fe(III)) and iron sulfide clusters (FeS_{aq}) were obtained with mercury/gold amalgam (Hg/Au) microelectrodes in intact sediment cores. The Au solid state voltammetric microelectrodes were constructed from a 100 µm diameter Au wire immobilized with marine epoxy in a Pyrex glass tube pulled to a 0.4 mm diameter tip. The Au working electrodes were plated with mercury by electrodeposition of a $HgCl_2$ solution for 4 minutes at -0.1 V (Brendel and Luther, 1995). Voltammetric measurements were conducted in a three electrode

configuration with the Hg/Au voltammetric working microelectrode, an Ag/AgCl reference electrode, and a Pt counter electrode using a computer-controlled DLK-70 potentiostat with DLK MAN-1 micromanipulator (Analytical Instrument Systems, Inc.). Dissolved O_2 was determined by linear sweep voltammetry (LSV) between -0.1 and -1.75 V at a scan rate of 200 mV/s with an initial conditioning step of 10 s at -0.1 V and calibrated *in situ* using temperature and salinity of the overlying water assuming oxygen was at saturation (Luther et al., 2008). All other species were determined by cathodic square-wave voltammetry (CSWV), between -0.1 and -1.75 V at a scan rate of 200 mV/s with a conditioning step of 10 s at -0.1 V (Brendel and Luther, 1995). When org-Fe(III) or $\sum H_2S$ were detected, an additional conditioning step of 10 s at -0.9 V was included prior the above procedure to clean the electrode (Taillefert et al., 2000b). Electrodes were calibrated for Mn^{2+} by CSWV with $MnCl_2$, and Mn^{2+} sensitivities were used to quantify Fe^{2+} and $\sum H_2S$ according to the pilot ion method. As org-Fe(III) and FeS_{aq} are not quantifiable, normalized current intensities were reported (Tercier-Waeber and Taillefert, 2008). Cysteine and cystine were calibrated individually, and measured using both CSWV and anodic square wave voltammetry (ASWV) as previously described (Eitel and Taillefert, 2017) (Chapter 3 of this dissertation). All voltammetric data was integrated using VOLTINT, a semiautomated Matlab script with peak recognition software (Bristow and Taillefert, 2008).

Pore waters were extracted from the same sediment cores that were voltammetrically profiled, except for sediments from the Rhône River delta, where pore waters were collected from separate cores due to time limitations during the cruise. Pore waters from the Rhône sediments were extracted in 2 cm increments using rhizon filters

with an average pore size of 0.1 µm (Seeberg-Elverfeldt et al., 2005). Sediments from all other locations were sectioned in 6-10 mm sections under N_2 atmosphere. The sediment sections were centrifuged at 3000 rpm for 10 minutes and pore waters were filtered using 0.2 µm Puradisc polyethersulfone (PES) syringe filters (Whatman) under N_2 atmosphere. All pore waters were partitioned under N_2 atmosphere for immediate analyses of dissolved Fe^{2+} by the Ferrozine method (Stookey, 1970). Total dissolved iron was measured after addition of hydroxylamine, and dissolved Fe(III) was determined as the difference between total iron and Fe^{2+}. DIC was analyzed by flow injection analysis (Hall and Aller, 1992) with a conductivity meter (Fisher Scientifics, Inc.) and a computer-controlled LCC-100 Integrator (AIS, Inc.). Filtered pore waters were frozen for later HPLC analysis of SO_4^{2-} (Beckler et al., 2014) or thiols. Individual thiols were identified and quantified by high pressure liquid chromatography (HPLC) after fluorescent derivation based on a previously developed method (Isokawa et al., 2013) using a ZIC-HILIC column (150 mm x 2.1 mm i.d., 5 mm, Merck, Germany). The reducing agent tris(2-carboxylethyl)phosphine (TCEP) enabled detection of total thiol concentration. Differentiation between oxidized and reduced forms was deemed unnecessary based on preliminary results and previous studies (Mopper and Taylor, 1986). The separation was conducted in the isocratic mode at a flow rate of 0.4 mL/min (Waters 1525) and a mobile phase consisting of 75/25% (v/v) acetonitrile and 10 mM ammonium formate buffer (pH 3.0). In line detection of dissolved sulfur species was achieved by excitation at 375 nm and emission at 510 nm (Waters 2475).

5.3.4 Sediment Incubations

All sediment incubations were conducted in duplicate with sediments from SERF. Slurry incubations were conducted in 28 mL hungate tubes with 8 g of homogenized sediment from iron-rich zones of interest and 25 mL of overlying water. Hungate tubes were mixed on a rotary wheel in the dark until sampling. All sampling took place in an anaerobic glove bag and samples were measured immediately with Au/Hg microelectrodes similar to those previously described, except they were encased in PEEK^{TM} (polyethyletherketone) electrical housing rather than pyrex glass (Luther et al., 2008).

In preliminary incubations, sediment slurries were either unamended, heat killed by holding the incubations at 120ºC for 1 hour on three consecutive days (Coates et al., 1997), or amended with 50 µM NO_3^- to poise the redox potential (Carey and Taillefert, 2005), 20 mM molybdate to inhibit sulfate-reducing microorganisms (Lowe et al., 2000), or 1, 10, or 100 µM of the disulfides cystine, cystamine, and oxidized glutathione to enhance the effect of electron shuttling. Hungate tubes were sampled once after 41 days and measured electrochemically but thiols were not quantified. To investigate the kinetics of thiol transformation, separate sediment slurry incubations were conducted either with or without 20 mM molybdate. In both treatments, 100 µM of either cystine or oxidized glutathione was added. Incubations were sampled at discrete time points over 46 days. Unfiltered samples were measured electrochemically to determine dissolved Fe^{2+}, $\sum H_2S$, org-Fe(III) complexes, and FeS_{aq} clusters. Additional samples were filtered using 0.2 µm Puradisc polyethersulfone (PES) syringe filters (Whatman) for analysis of dissolved Fe^{2+} and Fe(III) by the Ferrozine method (Stookey, 1970) and frozen for analysis of thiols by HPLC as previously described.

5.3.5 Pure Culture Incubations

Pure culture incubations were performed with the model metal-reducing bacteria *Shewanella oneidensis* MR-1. All pure culture incubations were performed in either 100 mL sealed PEEK^{TM} batch reactors specifically fabricated for *in situ* detection of voltammetrically active redox species with gold/mercury amalgam (Au/Hg) microelectrodes encased in PEEK^{TM} (Taillefert et al., 2007a) or 28 mL hungate tubes mixed on a rotary wheel in the dark until sampling. Hungate tubes were only used as duplicates of ferrihydrite treatments. *S. oneidensis* MR-1 was grown anaerobically in a defined minimal salt medium (M1) (Myers and Nealson, 1988) with 15 mM lactate, 60 mM fumarate, and buffered with 9 mM phosphate at pH 7. Cells were then harvested in late lag phase and washed for batch incubations. Batch incubations were performed with initial cell concentration of approximately $1x10^7$ cell/mL (OD_{600}) in M1 medium with 15 mM lactate as electron donor, decreased phosphate concentrations (100 µM), and buffered with 9 mM PIPES at pH 7. Batch reactors were amended with either 1 mM cystine or 40 mM ferrihydrite as electron acceptor. The PEEK^{TM} reactors were mixed with a magnetic stir bar except during voltammetric analysis or sampling. Samples were collected by a syringe from the sampling port on the PEEK^{TM} reactors or through the butyl rubber stopper of the hungate tubes and filtered through 0.2 µm PES filter (Whatman) for analysis of dissolved Fe^{2+} and Fe(III) by the Ferrozine method (Stookey, 1970) and frozen for analysis of thiols by HPLC as previously described. Total Fe^{2+} was measured by the Ferrozine method after acidification of unfiltered samples with 0.5 M HCl.

5.3.6 Calculations

To compare the 30 collected sediment cores for correlation between thiols and dissolved iron, diffusive fluxes and depth-normalized whole core concentrations were compared. Depth-normalized concentrations were compared both in the whole cores collected and in the non-sulfidic zone only. The non-sulfidic zones were determined based on the absences of $\sum H_2S$ or FeS_{aq}, which are commonly indicative of sulfate reduction (Beckler et al., 2016). Diffusive fluxes were only determined in non-sulfidic zones of the sediment. Maximum diffusive fluxes of Fe^{2+}, org-Fe(III), and thiols cysteine, glutathione, and cysteamine were determined from the steepest portion of pore water gradients in concentration of each species following a modification of Fick's first law to account for tortuosity (θ) (Boudreau, 1997):

$$F_x = -\varphi \frac{D_x^0}{\theta^2} \frac{dC_x}{dz} \tag{5-1}$$

where F_x is the diffusive flux of species x, φ is the sediment porosity, D_x^0 is the ionic or molecular diffusion coefficient of species x, C_x is the concentration of species x, and z is sediment depth. The tortuosity was estimated from Archie's law ($\theta^2 = \varphi^{(1-m)}$) with m = 2 for $\varphi \leq 0.7$ and m =2.5 for φ =0.7-0.9 (Ullman and Aller, 1982). The molecular diffusion coefficient for Fe^{2+} was calculated based on temperature (*T*) of the site:

$$D_{Fe^{2+}}^0 = (m_0 + m_1 \cdot T) x 10^{-6} \tag{5-2}$$

where m_0 and m_1 are constants (Boudreau, 1997). As the composition of the org-Fe(III) complexes is unknown, the molecular diffusion coefficient was estimated from the Stokes-Einstein equation (Cornel et al., 1986), assuming spherical org-Fe^{3+} species (Eq. 5-3),

$$D^0_{Org-Fe(III)} = \frac{kT}{6\pi\mu\left(\frac{3}{4\pi}\frac{MW}{\rho N}\right)^{1/3}}\ cm^2 s^{-1} \tag{5-3}$$

where *k* is the Boltzmann constant, *T* is temperature, μ is the dynamic viscosity, ρ is density, *N* is Avogadro's number, and *MW* is the molecular weight. A model molecular weight of 1 kDa was chosen along with a density of 1.13 g cm^{-3} based on humic-like substances (Jones et al., 2011). The molecular diffusion coefficient for cysteine was determined based on temperature (*T*) of the site based on (Jin and Chen, 2000):

$$D^0_{cysteine} = kTe^{\frac{-1713}{T}} \tag{5-4}$$

where *k* is a constant. The same diffusion coefficient was used for glutathione and cysteamine as no values are available for these thiols.

Whole core depth-integrated pore water concentrations (Z) of each species (x) were calculated at each station by integrating the concentration of each species over the thickness of each core section then dividing by the total core depth length:

$$Z_x = \frac{\varphi \int_0^{z_f} C_x dz}{z_f} \tag{5-5}$$

where φ is the sediment porosity, C_x is the concentration of species x (moles/l), z is the thickness of each core section (mm), and z_f is the total length (mm) of the section of interest.

5.4 Results

5.4.1 Sediment Profiles

Representative cores from each location visually depict the relationship between org-Fe(III), Fe^{2+}, cysteine, and glutathione (Figure 5-8). Due to the differences in resolution, direct comparison of concentrations with depth is difficult, however, peaks can be detected at related depths in all cores.

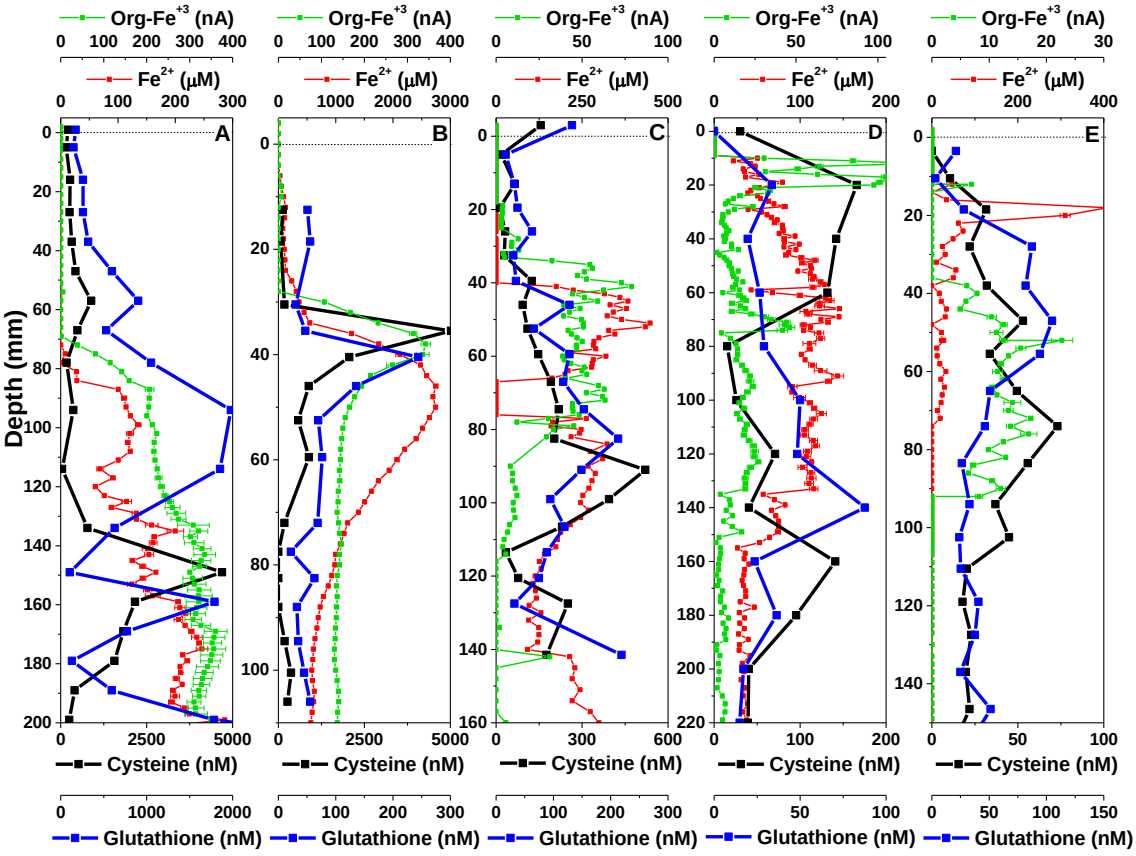

Figure 5-8 Representative cores from the five sampling locations: A) Fraser Experimental Forest, CO; B) SERF at Skidaway Island, GA; C) Rhône River delta; D) Louisiana continental margin; and E) North Carolina continental margin showing dissolved Fe^{2+}, organic-Fe(III), cysteine, and glutathione. Note the change in the depth and concentration scales between locations

To demonstrate general differences between thiols in iron-rich and sulfidic sediments, two representative cores collected from SERF are compared (Figure 5-9, Figure 5-10). In the iron rich sediment, Mn^{2+} was observed in the top 20 mm, and both Fe^{2+} and org-Fe(III) formed peaks between 20 and 40 mm, then disappeared deeper (Figure 5-9A). FeS_{aq} was detected briefly around 40 mm, but was mainly produced up to 18 nA between 60 and 90 mm then decreased slightly to 10 nA with depth. Although the presence of FeS_{aq} indicated active sulfate reduction, $\sum H_2S$ did not reach concentrations higher than 25 μM, even as deep as 180 mm in the sediment. Thiols cysteine and glutathione both formed broad

peaks around 40 mm (Figure 5-9B), slightly below the Fe^{2+} and org-Fe(III) peaks (Figure 5-9A). Cysteine reached maximum concentrations of 1741 nM at 34 mm and glutathione reached maximum concentrations of 1539 nM at 56 mm. Both cysteamine (< 65 nM) and 3-MPA (< 127 nM) remained low throughout the core. Simultaneously, sulfate decreased significantly from 29.5 to 15.5 mM and DIC increased from 2 to 5.4 Mm with depth, both suggesting that sulfate reduction was significant below (Figure 5-9C).

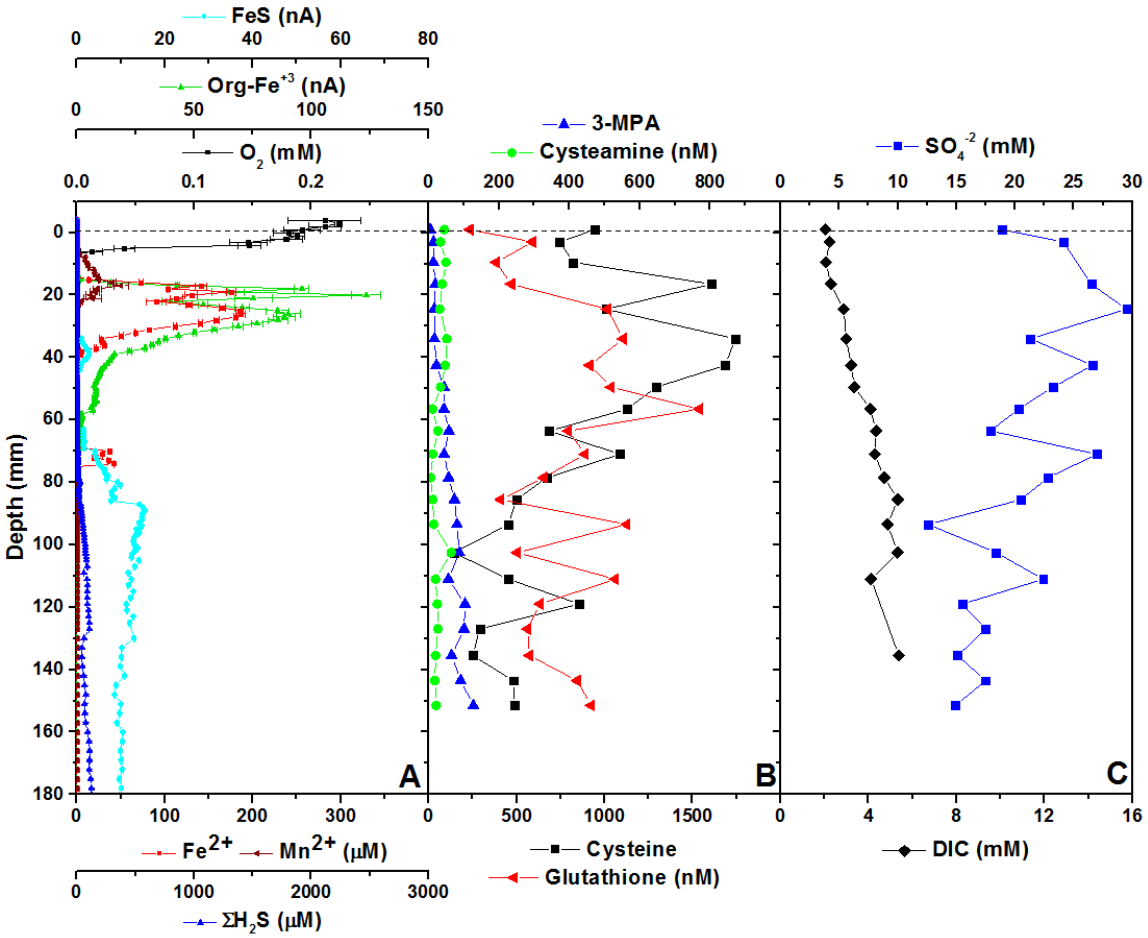

Figure 5-9 Depth profiles of A) dissolved O_2, Fe^{2+}, Mn^{2+}, $\sum H_2S$, FeS_{aq}, and organic-Fe(III); B) dissolved cysteine, glutathione, cysteamine, and 3-MPA; C) SO_4^{2-} and DIC from a less sulfidic sediment core from SERF in June 2016.

In comparison, Mn^{2+} was not detected in the sulfidic core and only low concentrations of Fe^{2+} were observed in the top 10 mm, though org-Fe(III) formed a peak around 20 mm (Figure 5-10A). FeS_{aq} increased between 30 and 37 mm, then subsided below detection by 57 mm as $\sum H_2S$ began to dominate. $\sum H_2S$ was detected as shallow as 8 mm below the sediment-water interface and gradually increased to reach maximum concentrations of 2.45 mM at 137 mm that remained constant deeper. Neither cysteine, nor glutathione reached concentrations over 550 nM although both appeared to show slight increases in concentration in the top 20 mm (Figure 5-10B). Cysteine decreased to 99 nM

at 34 mm, then increased gradually with depth to 500 nM. Cysteamine concentrations averaged around 145 nM with one peak at 75 mm. In turn, 3-MPA increased significantly from 141 nM to an average of 720 nM with depth. Simultaneously, sulfate decreased significantly from 25.5 to 6.5 mM and DIC increased from 2.4 to 15.3 mM with depth (Figure 5-10C). Sulfate, DIC, and $\sum H_2S$ profiles all suggest that microbial sulfate reduction dominated in these sediments.

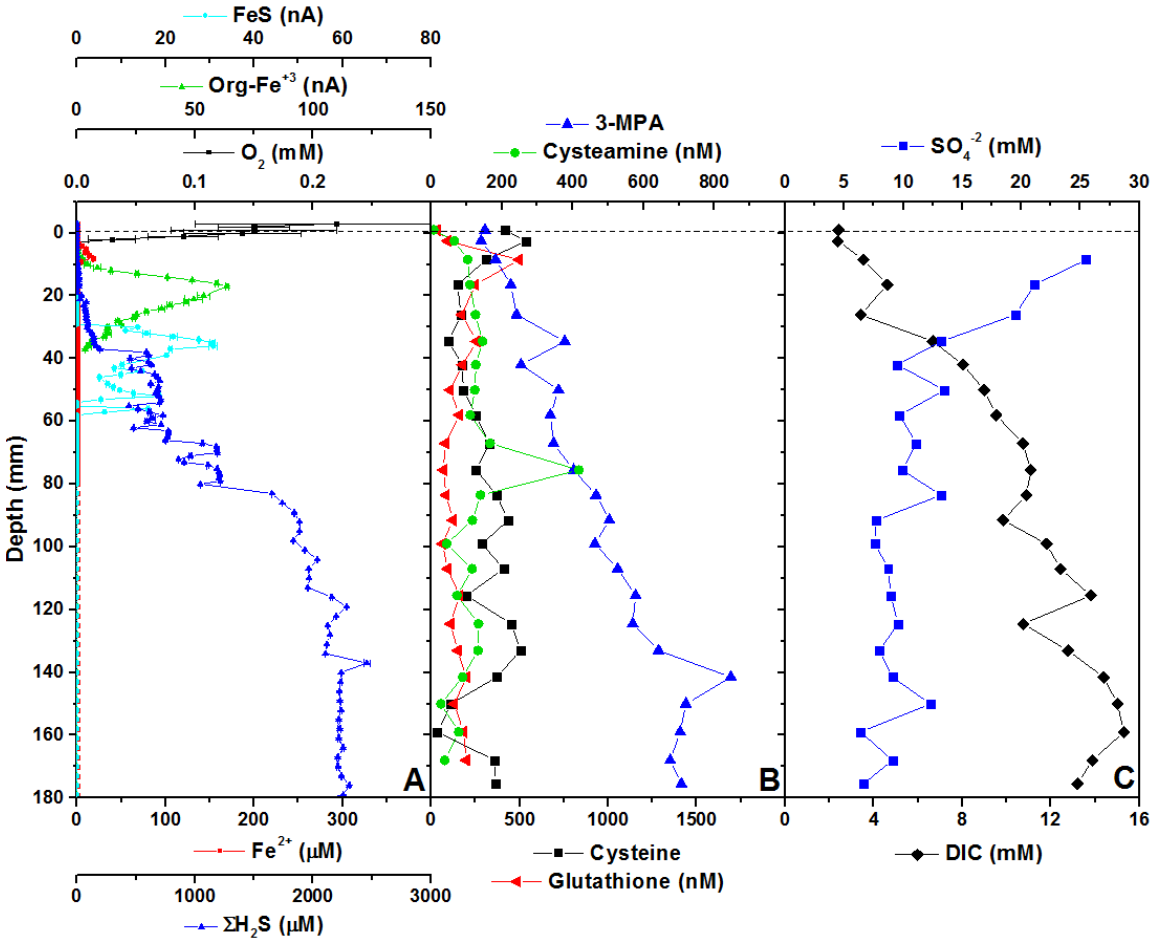

Figure 5-10 Depth profiles of A) dissolved O_2, Fe^{2+}, Mn^{2+}, H_2S, FeS_{aq}, and organic-Fe(III); B) dissolved cysteine, glutathione, cysteamine, and 3-MPA; C) SO_4^{2-} and DIC from a sulfidic sediment core from SERF in June 2016.

5.4.2 Pure Culture Incubations

To confirm reduction of disulfides by model Fe(III)-reducing bacteria, *S. oneidensis* MR-1 was incubated with 1 mM cystine as sole terminal electron acceptor (Figure 5-11). Cystine was reduced with time and was below detection after 18 hours, while cysteine was immediately produced and reached maximum concentrations of approximately 730 µM after 25 hours, then remained constant.

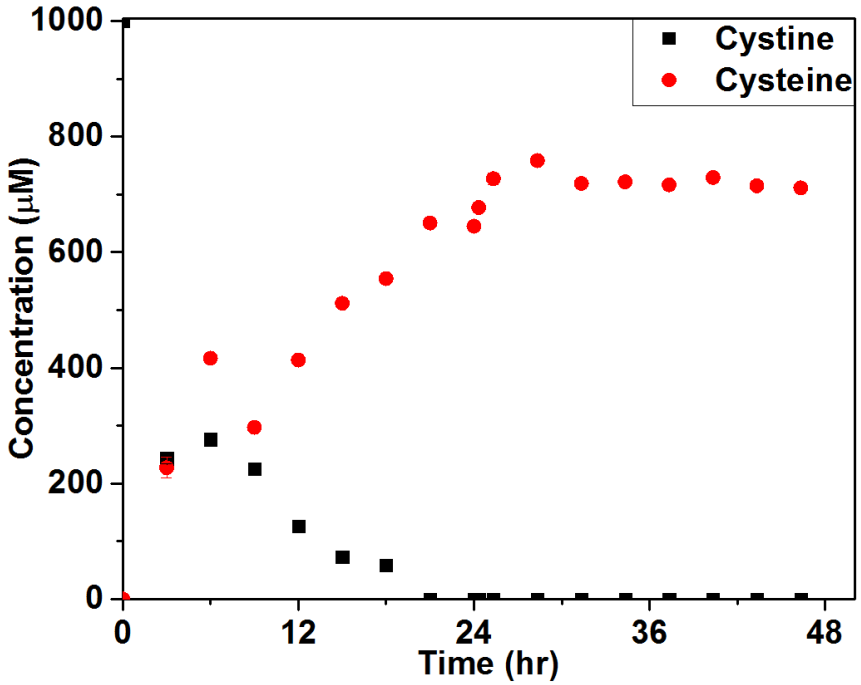

Figure 5-11 Anaerobic incubations of *S. oneidensis* MR-1 in M1 medium with 1 mM cystine as sole electron acceptor at pH 7.

To determine whether thiols are produced endogenously during DIR, *S. oneidensis* MR-1 was incubated with 40 mM ferrihydrite as sole terminal electron acceptor. Incubations were conducted in duplicate both with (Figure 5-12) and without (Figure 5-13) in situ Au/Hg microelectrodes. Similar results were observed in both incubations, although slight lag times make averaging these experiments difficult. Voltammetrically-detected Fe^{2+} increased gradually up to around 2 mM after 72 hours and remained relatively constant

after that (Figure 5-12A). In both incubations, dissolved Fe^{2+} and total Fe(II) generally increased gradually until around 35 hours, then increased at an increased rate until 83 hours when concentrations reached steady-state (Figure 5-12B, Figure 5-13A). The significant differences in concentrations of voltammetrically-detected and ferrozine-detected Fe^{2+} reflect previous findings that Fe^{2+} is complexed by a ligand that boosts voltammetric currents (Taillefert et al., 2007). Org-Fe(III) was produced gradually over the first 10 hours to 37 nA, then rapidly increased to 210 nM at 62 hours, remained above 180 nA until 75 hours, before decreasing to slightly less than 100 nA and remaining relatively constant for the remainder of the incubation (Figure 5-12A). Concentrations of Fe(III) measured by Ferrozine generally were below 100 μM until after 62 hours when concentrations rapidly increased and reached steady-state by 83 hours (Figure 5-12B, Figure 5-13A). In both incubations, cysteine increased rapidly within the first 24 hours and was the most predominant thiol detected (Figure 5-12C, Figure 5-13B). Two peaks in cysteine concentration were observed around 24 hours, and a third observed around 48 hours. Cysteine generally decreased below 100 nM around 62 hours, but rebounded and remained relatively constant throughout the remainder of the incubation. Glutathione generally increased over the first 56 hours, although to a lesser extent than cysteine, decreased at 62 hours, the rebounded afterwards. Homocysteine was detected in concentrations lower than both cysteine and glutathione, but interestingly peaked around 62 hours. Cysteamine was detected in both incubations, but did not reach concentrations above 15 nM and was close to the detection limits.

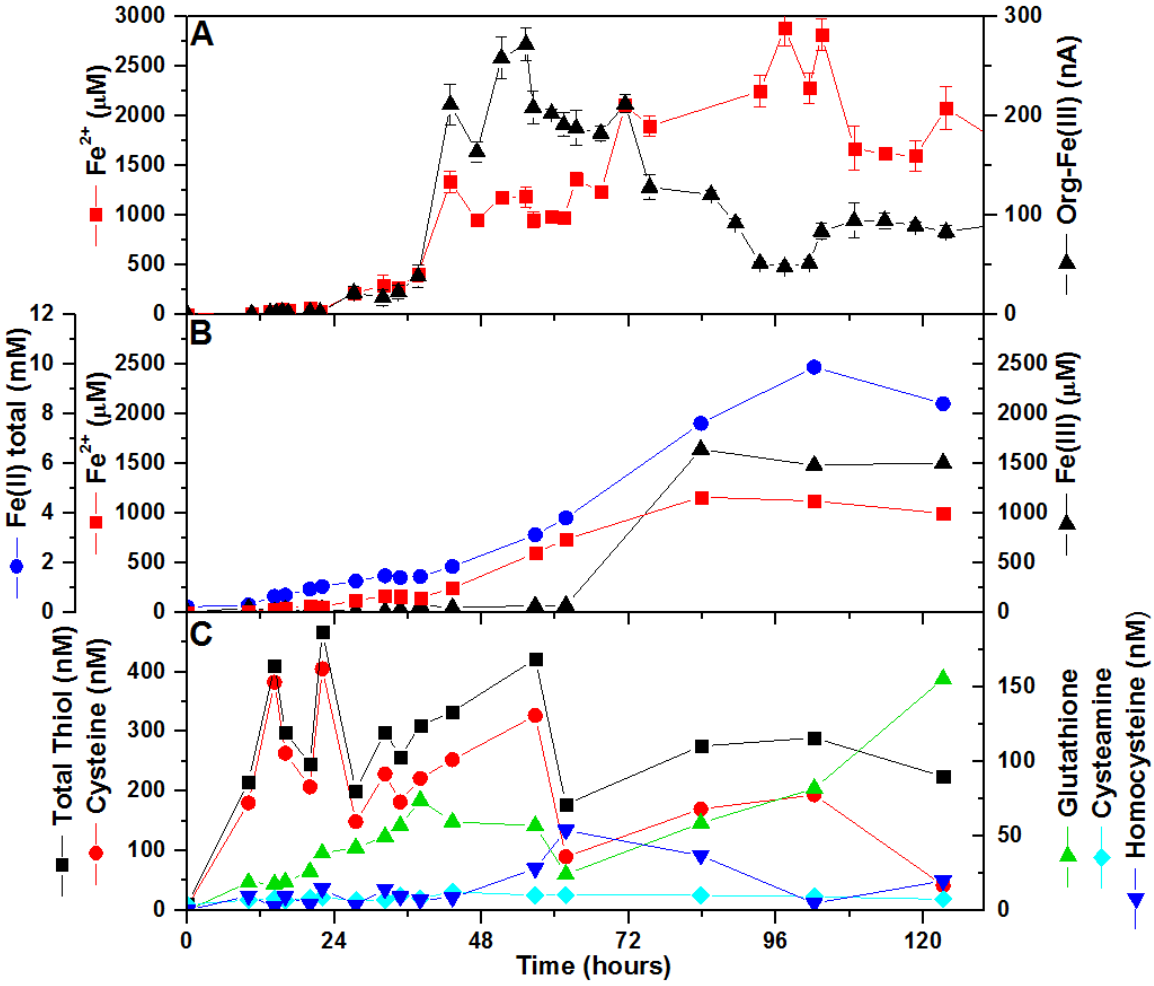

Figure 5-12 Concentration of A) dissolved Fe^{2+} and org-Fe(III) determined by electrochemistry, B) dissolved Fe^{2+}, Fe(III), and total Fe(II) determined by the Ferrozine method, and C) thiols determined by HPLC over time in incubations of *S.*

***oneidensis* MR-1 in M1 medium with 40 mM ferrihydrite buffered by 9 mM PIPES at pH 7. Total thiol concentrations were calculated as the sum of all measured thiols.**

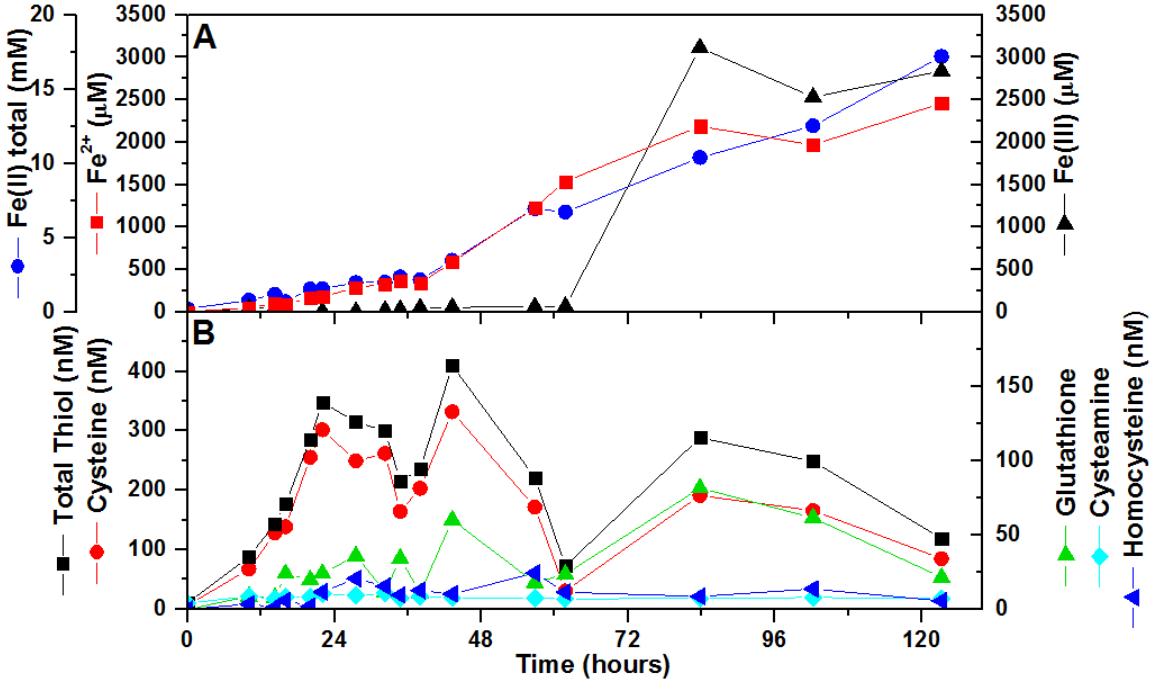

Figure 5-13 Concentrations of A) dissolved Fe^{2+}, Fe(III), and total Fe(II) determined by the Ferrozine method, and B) thiols determined by HPLC over time in secondary incubations of *S. oneidensis* MR-1 in M1 medium with 40 mM ferrihydrite buffered by 9 mM PIPES at pH 7. Total thiol concentrations were calculated as the sum of all measured thiols.

5.4.3 Sediment Incubations

5.4.3.1 Initial Incubations

Preliminary incubations conducted with sediment from iron-rich and non-sulfidic zones of a sediment core from SERF at Skidaway Island, GA showed production of Fe^{2+} in all treatments besides the heat killed control (Figure 5-14A). Increased Fe^{2+} concentrations of 529 ± 137 µM and 491 ± 143 µM were measured in molybdate and nitrate treatments compared to the 238 ± 76 µM measured in the unamended treatment, suggesting that sulfate reduction can be activated in these sediments. Although amendment of 1 and

10 µM cystamine did not result in increased Fe^{2+} production, addition of 100 µM cystamine produced similar Fe^{2+} concentrations as in the molybdate treatment. Amendment of 1, 10, and 100 µM cystine all produced Fe^{2+} at concentrations greater than the unamended samples, though the relative variations was high between treatments. In contrast, all glutathione amendments resulted in Fe^{2+} production that was not significantly different than the unamended samples.

All treatments, including the heat killed samples, produced org-Fe(III) after 41 days (Figure 5-14B). In heat killed treatments, minimal (13 ± 8 nA) org-Fe(III) was detected, whereas slightly higher signals of 31 ± 6 nA were measured in the unamended treatments. Increased org-Fe(III) was measured in the molybdate treatments (133 ± 2 nA), however nitrate amendments (53 ± 24 nA) were within error of the unamended samples. Org-Fe(III) increased with increasing concentration of cystamine in the incubations, while increasing the concentrations of both cystine and glutathione produced relatively similar org-Fe(III) signals as the molybdate treatment.

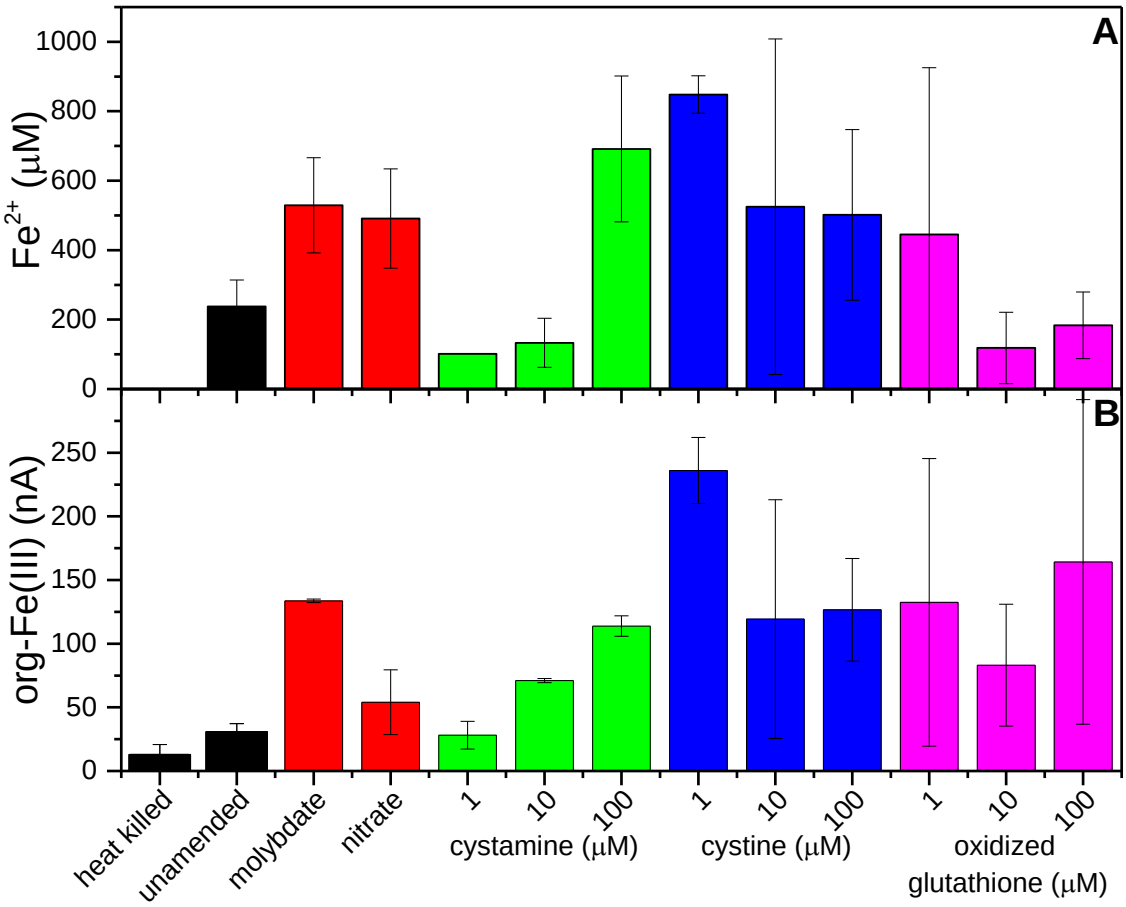

Figure 5-14 Average concentrations of A) Fe^{2+} and B) org-Fe(III) measured electrochemically in duplicate slurry incubations of sediment from SERF after 41 days. Error bars represent the variability between duplicate incubations.

5.4.3.2 Incubation Kinetics

To determine the effect of thiols on the rate of iron reduction in marine sediments, separate slurry incubations were conducted with sediment from SERF on Skidaway Island, GA. Results were primarily influenced by the presence or absence of molybdate, whereas disulfide amendment did not significantly affect incubations. Besides a few time points,

voltammetric Fe^{2+} was only produced in the incubations amended with molybdate (Figure 5-15A). Fe^{2+} was produced over the first 4 days to concentrations reaching around 400 µM depending on the molybdate treatment, but then was consumed in both disulfide-amended treatments only to reappear after 15 days and increase regularly to reach concentrations of 476 ± 388 µM and 380 ± 48 µM after 46 days in the incubations amended with cystine and glutathione. Simultaneously, voltammetric Fe^{2+} oscillated around 360 uM between day 4 and 15 in incubations amended with molybdate only and was also produced regularly after day 15 to reach concentration of 670 ± 460 µM after 46 days. In all treatments, org-Fe(III) signals of less than 200 nA were observed in the first 6 days (Figure 5-15B). Org-Fe(III) signals then increased in all samples to reach a maximum on day 15, but maximum current intensities in all treatments with molybdate averaged 635 ± 75 nA compared to 250 ± 74 nA in treatments without molybdate. After day 15, org-Fe(III) signals decreased in all treatments to below detection limit after 31 days in treatments without molybdate and to 24 ± 4 nA in incubations with molybdate after 46 days. Significant concentrations of $\sum H_2S$ were detected in the molybdate-free incubations only (Figure 5-15C). $\sum H_2S$ was produced regularly after day 20 only and in higher concentrations in disulfide-amended incubations to reach concentrations around 1 mM by day 46. Similarly to $\sum H_2S$, FeS_{aq} signals were only detected in molybdate-free incubations (Figure 5-15D). FeS_{aq} signals increased progressively after day 4 in the disulfide-amended incubations only to reach current intensities around 100 nA, while FeS_{aq} signals were only produced significantly after day 30 to reach current intensities around 40 nA by day 46.

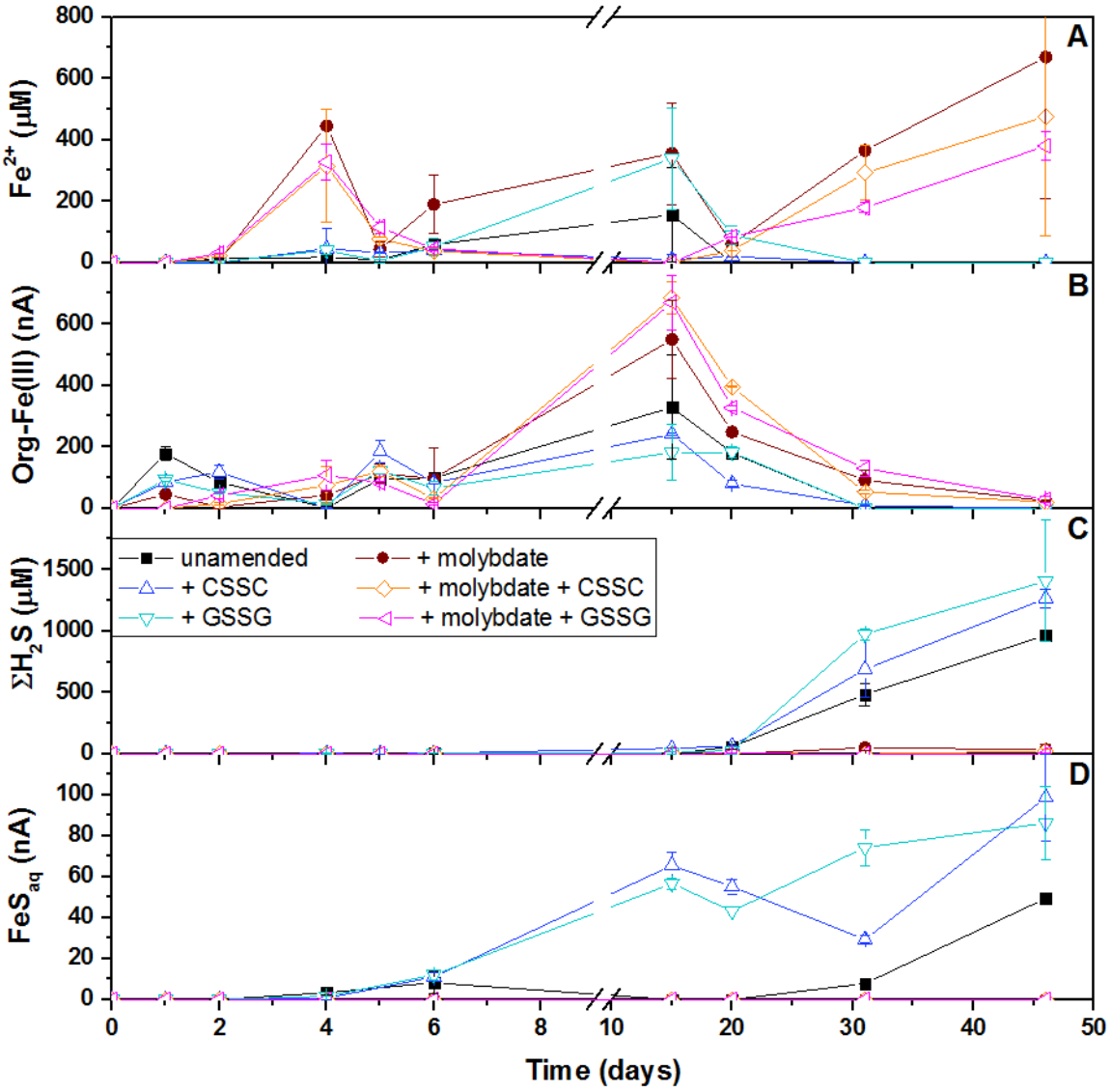

Figure 5-15 Temporal evolution of: A) Fe^{2+}; B) org-Fe(III) complexes; C) $\sum H_2S$; and D) FeS_{aq} measured by voltammetry in duplicate slurry incubations either unamended or amended with 100 µM cystine, 100 µM oxidized glutathione, molybdate only, molybdate and 100 µM cystine, or molybdate and 100 µM oxidized glutathione. Error bars represent the variability between duplicate incubations.

Analysis of the dissolved iron speciation by the Ferrozine method provides support for the electrochemical data and shows similar relationships between samples with or without molybdate and less influence of disulfide amendment (Figure 5-16). In all incubations, dissolved Fe^{2+} was produced to concentrations around 150 µM on day 6, then was consumed in all molybdate-free incubations to concentrations below 20 µM after day 15 (Figure 5-16A). In contrast, dissolved Fe^{2+} was gradually produced in molybdate-amended incubations to reach between 137 and 250 µM Fe^{2+} by day 46 depending on the treatments. Concentrations of dissolved Fe(III) varied within the first 6 days but generally increased to an average of 63 ± 16 µM Fe(III) in all treatments without molybdate and 88 ± 15 µM Fe(III) in all treatments with molybdate by day 6 (Figure 5-16B). Dissolved Fe(III) in molybdate-free incubations was consumed to below 11 µM Fe(III) after day 20 and remained low after that, while dissolved Fe(III) in molybdate-amended incubations decreased much less drastically to 7 and 13 µM on day 46 in disulfide-free and cystine treatments or remained relatively constant at 61 µM after 20 days in the presence of oxidized glutathione.

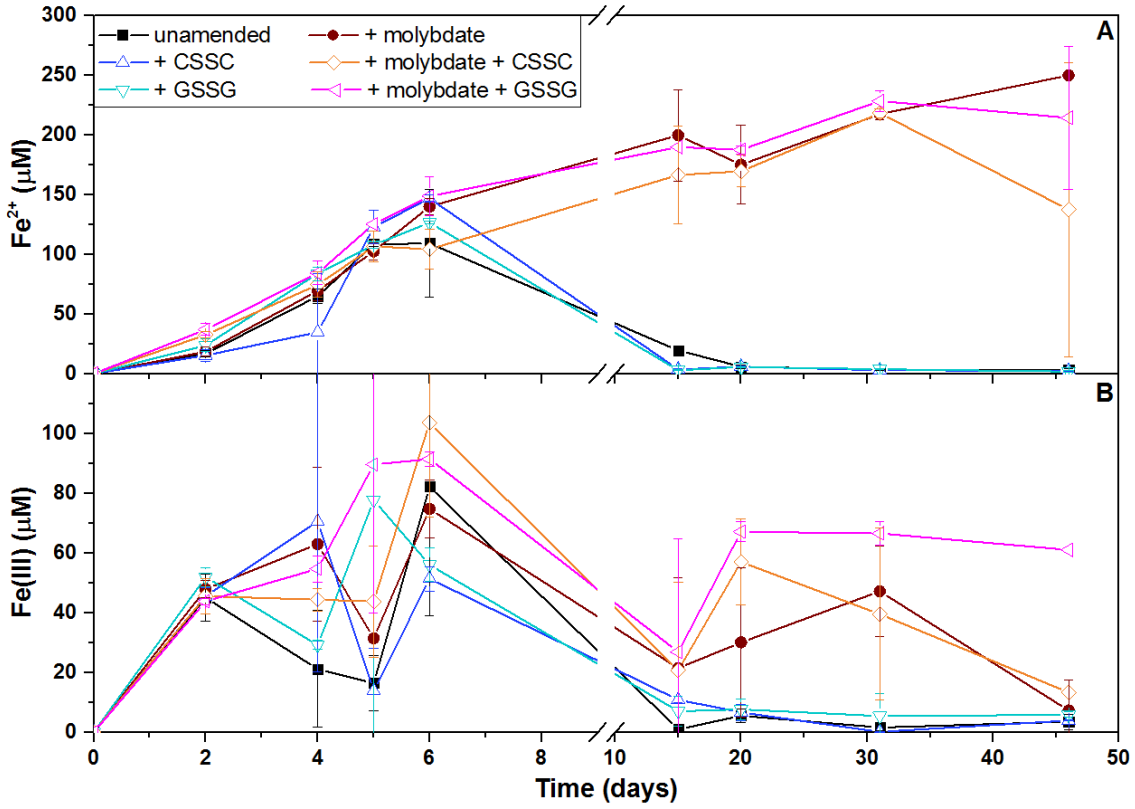

Figure 5-16 Temporal evolution of dissolved: A) Fe^{2+}; and B) Fe(III) quantified by the Ferrozine method in duplicate slurry incubations either unamended or amended with 100 µM cystine, 100 µM oxidized glutathione, molybdate only, molybdate and 100 µM cystine, or molybdate and 100 µM oxidized glutathione. Error bars represent the variability between duplicate incubations.

Thiols were quantified over time in unamended sediment slurries and slurries amended with molybdate only (Figure 5-17). The four thiols cysteine, cysteamine, glutathione, and 3-MPA were detected in both slurry incubations, albeit at different concentrations. As a result, the total concentration of thiols increased from about 100 to around 550 nM over time in the molybdate-amended incubations but only increased from 50 to around 100 nM in the unamended incubations. Although cysteamine remained below 52 nM in both treatments, cysteine, glutathione, and 3-MPA behaved differently in the presence or absence of molybdate. In incubations with molybdate, cysteine gradually increased from 51 to 417 nM over the 46 day incubation period (Figure 5-17A), while

glutathione was produced after day 5 and remained mostly constant around 100 nM for the remainder of the incubation. Glutathione, and to a lesser extent cysteine, behaved inversely to 3-MPA, which remained below 40 nM for most the incubations (Figure 5-17A). In samples without molybdate, cysteine and glutathione concentrations remained below 80 nM and 35 nM for most of the incubation (Figure 5-17B). In turn, concentrations of 3-MPA increased up to 292 nM on day 6, decreased slightly to 180 ± 36 nM on day 15, and remained constant for the rest of the incubations (Figure 5-17B).

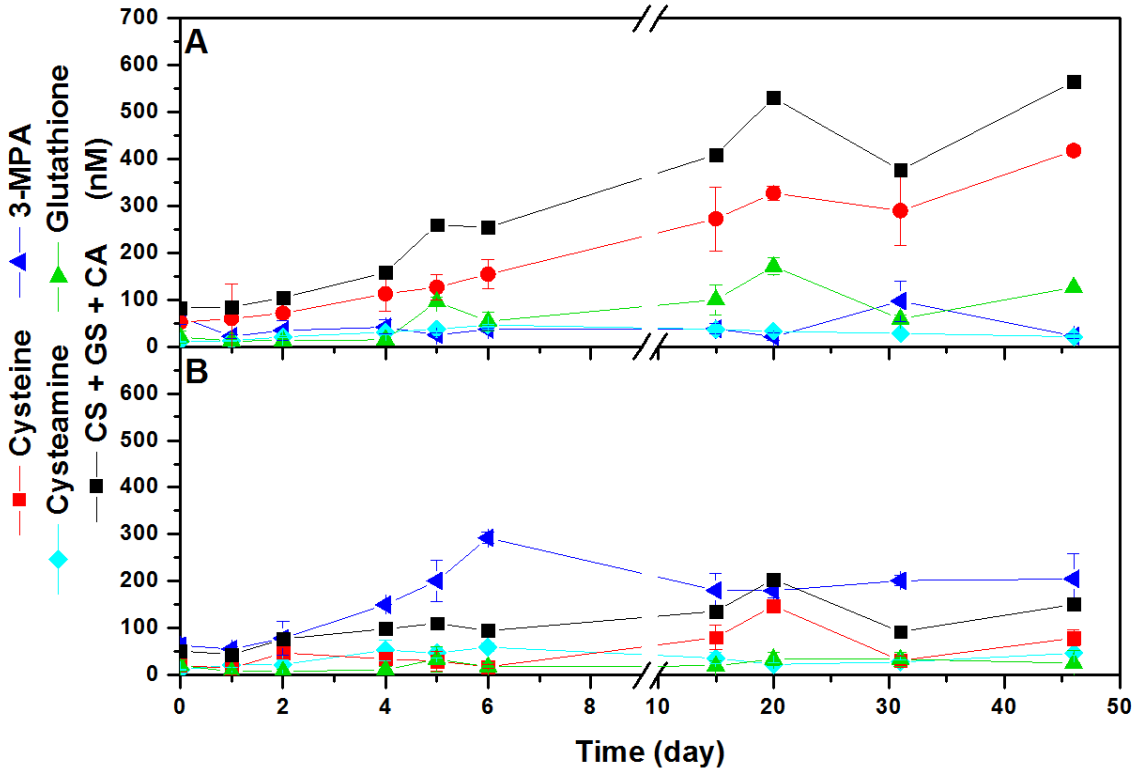

Figure 5-17 Temporal evolution of the thiols cysteine (CS), glutathione (GS), and cysteamine (CA) in: A) molybdate-amended; and B) molybdate-free sediment slurry incubations. The total concentration of thiols detected in the incubations is also provided for mass balance consideration.

5.5 Discussion

5.5.1 Thiols and Model Fe(III)-Reducing Bacteria

Incubations of *S. oneidensis* MR-1 with lactate as an electron donor and cystine as the electron acceptor (Figure 5-11) confirmed the reduction of disulfides by model Fe(III)-reducing bacteria and recycling of thiols during the process. Reduction of cystine was expected as previous experiments confirmed disulfide reduction by a number of Fe(III)-reducing bacteria (Doong and Schink, 2002; Kaden et al., 2002; Liu et al., 2014) and reduction of disulfides by *S. oneidensis* MR-1 has been studied in depth with different electron donors (Wee, 2013). However, this is the first time that disulfides and thiols were detected simultaneously in situ during incubations. Endogenous production of thiols in incubations of *S. oneidensis* MR-1 with lactate as electron donor and ferrihydrite as terminal electron acceptor (Figure 5-12, Figure 5-13) also confirmed previous incubations conducted under similar conditions (Cooper, 2015). The concentration of each thiol reported in the present incubations included both the thiol and disulfide species in solution (i.e, total thiols only), though both oxidized and reduced species were detected in similar incubations (Cooper, 2015). Thiol content was dominated by cysteine, which reached maximum concentrations in the first 72 hours. No other thiols displayed temporal correlations with either Fe^{2+} or org-Fe(III). Cysteamine concentrations were low throughout the incubation, and homocysteine appeared to be related to the other thiols as its concentration varied inversely proportionally to the cysteine and glutathione concentrations (Figure 5-12C). Glutathione concentrations were the second highest of all detected thiols, and generally increased over time. Visual inspection suggests that the increase in glutathione over time may be correlated to increase in Fe^{2+} (total and dissolved

measured by voltammetry and Ferrozine). Interestingly, neither cysteine, nor the calculated total thiol concentration correlated to Fe^{2+} concentrations over time. As relatively higher concentrations of cysteine were observed in the first 24 hr than later in the incubations (Figure 5-12C), the formation of cysteine appears to precede the formation of both the org-Fe(III) complexes determined voltammetrically (Figure 5-12A) and dissolved Fe(III) (Figure 5-12B). These findings suggest that thiol production may also be involved in signaling the cells for endogenous Fe(III)-binding ligand production.

Differences between dissolved Fe^{2+} detected by voltammetry (Figure 5-12A) and by Ferrozine (Figure 5-12B) have been previously observed during *Shewanella putrefaciens* incubations with ferrihydrite and attributed to the complexation of Fe^{2+} by the endogenous organic ligand which enhances the electron transfer at the voltammetric electrode (Taillefert et al., 2007a). As org-Fe(III) signals are based on the reactivity of the Fe(III) complexes at the electrode surface, which depends on both the size and type of ligand involved (Taillefert et al., 2000a), the discrepancy in temporal pattern between org-Fe(III) (Figure 5-12A) and dissolved Fe(III) determined by Ferrozine (Figure 5-12B) is not surprising. This difference may be due to production of different org-Fe(III) complexes over time, with initial org-Fe(III) having increased response at the electrode surface compared to the Fe(III) binding ligands produced as the incubation proceeds (Taillefert et al., 2007a). Flocculation of particles could also contribute to the decrease in org-Fe(III) signal over time (Taillefert et al., 2000a), though this effect may not be beneficial to the cells. Although thiols may complex other metals (Leal and Van den Berg, 1998; Walsh and Ahner, 2013) a thiol-Fe(III) species is not expected to contribute to the observed org-Fe(III) signal in these incubations as no org-Fe(III) signal was detected during the abiotic

reduction of ferrihydrite by thiols (Eitel and Taillefert, 2017). Surface complex formation greatly affects the rate of thiol oxidation by ferrihydrite (Eitel and Taillefert, 2017), and the rate of thiol oxidation decreases as a function of the Mn(III,IV) oxide crystallinity whereas the reduction of soluble Mn(III)-pyrophosphate by thiols is extremely rapid (Chapter 3). Therefore, it seems that the reduction of soluble org-Fe(III) complexes by thiols would be more rapid than reduction of solid Fe(III) unless the ligand stability was great enough to inhibit cysteine reaction. As organic-Fe(III) complexes produced as intermediates during DIR by *Shewanella* are proposed to destabilize Fe(III) oxides to accelerate the reduction process (Taillefert et al., 2007a), the results of these incubations suggest that thiol compounds are produced endogenously to reduce the organic-Fe(III) intermediates and facilitate recycling of the organic ligand.

5.5.2 Detection of Thiols in Natural Sediments

Cysteine, glutathione, cysteamine, and 3-MPA were detected in the sediments of all five locations studied. Although up to 20 thiols have been previously detected in marine sediments (Vairavamurthy and Mopper, 1987), glutathione, cysteine, and 3-MPA typically represent the main thiols reported in both water column and pore water samples. Thus, the present study is the first to report the occurrence of cysteamine in natural sediments. In the water column, glutathione (Table 5-1) and cysteine (Table 5-2) are generally associated with phytoplankton, and are detected in similar concentrations. In sediments, glutathione is reported in concentrations ranging between 40 nM and 8 µM (Table 5-1), whereas cysteine concentrations are slightly higher and range between 150 nM and 12.4 µM (Table 5-2). The source of glutathione and cysteine in sediments is poorly understood and often attributed to either microbial production for toxin complexation or sulfidization of organic

matter (OM). In contrast to cysteine and glutathione, 3-MPA is more commonly reported in sediment pore waters, and commonly attributed to the degradation of dimethylsulfoniopropionate (DMSP) (Table 5-3).

Table 5-1 Literature report of glutathione detection in water column and pore water samples.

Glutathione			
location	Source/notes	Maximum concentrations	Reference
Water column			
North East Atlantic	metal complexation	15 nM	(Le Gall and Van Den Berg, 1998)
Black Sea	sediment source	105 nM	(Luther et al., 1991)
Saanich Inlet, southern California	phytoplankton	600 pM	(Matrai and Vetter, 1988b)
Aulne Estuary, France	salinity	38 nM	(Marie et al., 2016)
Galveston Bay	phytoplankton	6 nM	(Tang et al., 2000)
Tamar Estuary, UK (metal contaminated)	phytoplankton	1800 pM	(Kawakami and Achterberg, 2012)
Mersey Estuary	salinity	320 nM	(Le Gall and van den Berg, 1993)
Chesapeake Bay	sediment source	25.3 nM	(Dryden et al., 2007)
Connecticut lake	phytoplankton	5 nM	(Hu et al., 2006)
Pore waters			
Freshwater and brackish wetlands, Canada	Microbial production and methylmercury complexation	40 nM	(Zhang et al., 2004b)
Contaminated lagoon, Italy	Sulfurization of OM and associated with Cu	6000 nM (glutathione equivalent)	(Chapman et al., 2009)
Biscayne Bay	Unknown	600 nM	(Kiene, 1991; Kiene and Taylor, 1988a)
Biscayne Bay	Unknown	Not reported	(Vairavamurthy and Mopper, 1987)
Chesapeake Bay	Unknown	8 µM	(Shea and Maccrehan, 1988)
Chesapeake Bay	Unknown	5.4 µM	(MacCrehan and Shea, 1995)

Table 5-2 Literature report of cysteine detection in water column and pore water samples.

Cysteine			
location	Source/notes	Maximum concentrations	Reference
Water column			
Black Sea	detection inhibited by Cl^-	350 nM	(Luther et al., 1991)
Chesapeake Bay	sediment source	35 nM	(Dryden et al., 2007)
Water column (Galveston Bay)	phytoplankton	56 uM/ g chl	(Tang et al., 2000)
Pore waters			
Freshwater and brackish wetlands, Canada	Microbial production and methylmercury complexation	150 nM	(Zhang et al., 2004b)
Chesapeake Bay	Unknown	nM (data not shown)	(Dryden et al., 2007)
Chesapeake Bay	Unknown	12 µM	(Shea and Maccrehan, 1988)
Chesapeake Bay	Unknown	12.4 µM	(MacCrehan and Shea, 1995)

Table 5-3 Literature report of 3-MPA detection in water column and pore water samples.

3-MPA			
location	Source/notes	Maximum concentrations	Reference
Water column			
Chesapeake Bay	sediment source	38.7 nM	(Dryden et al., 2007)
Connecticut lake	DMSP degradation, sulfidization of OM	340 nM	(Hu et al., 2006)
Pore waters			
Freshwater and brackish wetlands, Canada	Microbial production by DMSP degradation	250 nM	(Zhang et al., 2004)
Salt marsh	Particle bound sulfurization of DMSP	100 uM	(Vairavamurthy et al., 1997)
Biscayne Bay	Acrylate-sulfide pathway DMSP degradation	300 nM	(Kiene, 1991; Kiene and Taylor, 1988a)
Biscayne Bay	sulfidization of OM	µM (data not shown	(Vairavamurthy and Mopper, 1987)
Chesapeake Bay	Unknown	µM (data not shown	(Dryden et al., 2007)
Chesapeake Bay	Unknown	12 µM	(Shea and Maccrehan, 1988)
Chesapeake Bay	Unknown	11.8 µM	(MacCrehan and Shea, 1995)

Depth-integrated whole core concentrations showed that the highest average concentrations of Fe^{2+} in all sediment cores collected were observed at SERF sites, followed closely by CO, Rhône and LA which had similar averages, and then NC sites (Figure 5-18). Averages of all depth-integrated organic-Fe(III) signals at each site decreased from CO to SERF, were similar in the Rhône and NC sediments, and the lowest in LA sediments. Averages of depth-integrated cysteine concentrations in all sediments decreased following the order: CO > SERF > Rhône > LA > NC, and a similar pattern was observed with cysteamine although Rhône, LA, and NC were almost identical. Finally,

glutathione decreased from CO to SERF as well, but was higher in LA than the Rhône and NC sites. This behaviour is also apparent in representative depth profiles of Fe^{2+}, org-Fe(III), cysteine, and glutathione from each location (Figure 5-8).

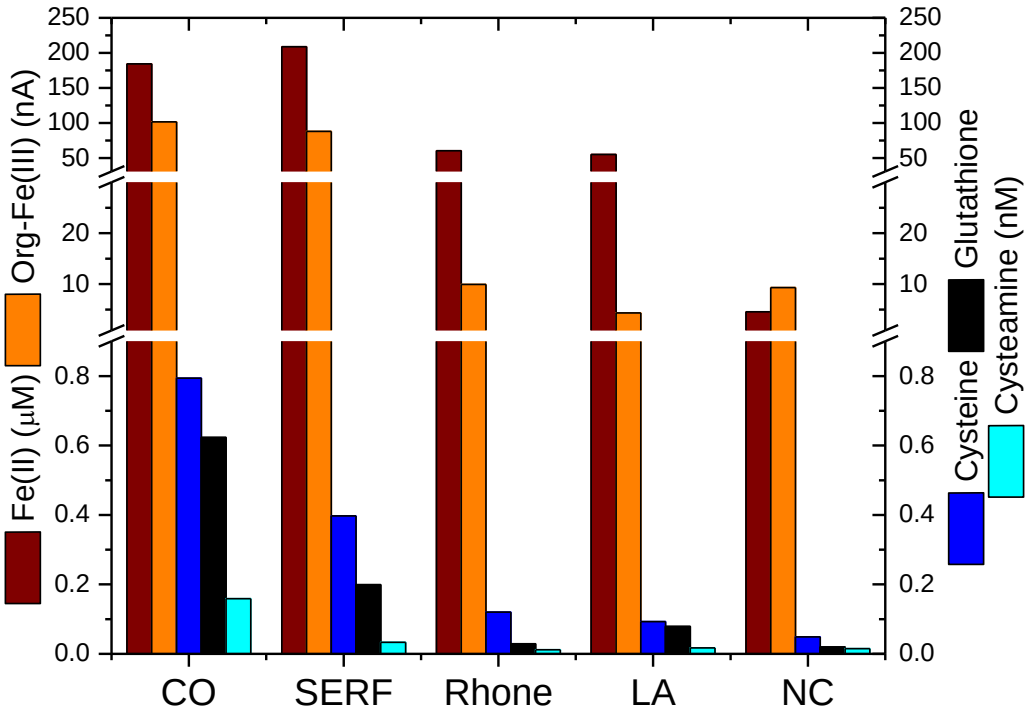

Figure 5-18 Average depth-integrated concentrations of Fe^{2+}, organic-Fe(III), cysteine, glutathione, and cysteamine from the Fraser Experimental Forest freshwater wetlands (CO), Salt Marsh Ecosystem Research Facility (SERF), Rhône River prodelta (Rhône), Louisiana continental margin (LA), and North Carolina continental margin (NC).

Simultaneously, the highest concentrations of both $\sum H_2S$ and FeS_{aq} were observed at SERF followed by LA (Figure 5-19), while the Rhône and NC sites displayed similar depth-integrated levels of $\sum H_2S$ and FeS_{aq}. Although $\sum H_2S$ and FeS_{aq} was not detected at CO, 3-MPA was detected but in lower concentrations than observed at SERF. In turn, relatively

lower 3-MPA concentrations were observed in continental margin sediments that progressively decreased in the order: Rhône > LA > NC sediments, following the decrease in intensity of sulfate reduction detected in these environments. Overall, the average depth-integrated concentrations of Fe^{2+}, org-Fe(III), $\sum H_2S$, and FeS_{aq} followed the general trends expected for each location. In the marine locations, terrigenous inputs likely decreased from the highly productive salt marsh wetland (i.e. SERF) which also stores significant amounts of organic carbon (Hedges et al., 1997; Mitsch and Gosselink, 1993; Peterson and Howarth, 1987; Pomeroy and Wiegert, 1981; Teal, 1962) to the Rhône River pro-delta which receives large inputs of organic matter and minerals (Cathalot et al., 2010; Cathalot et al., 2013; Lansard et al., 2008; Lansard et al., 2009; Pastor et al., 2011; Pozzato et al., 2017; Rassmann et al., 2016), the Mississippi River delta, which also receives large inputs of organic matter and minerals though spread over a larger surface area (Bianchi et al., 2010; Devereux et al., 2015; McKee et al., 2004), and the continental slope of Cape Lookout (NC), which is not exposed to major riverine inputs or upwelling (Blake et al., 1987; DeMaster et al., 1994; Schaff T., 1992) The resulting decrease in reactive Fe(III) oxides directly affected the intensity of DIR and the production of Fe^{2+} and org-Fe(III) (Figure 5-18), whereas the decrease in organic matter likely controlled the intensity of sulfate reduction and the production of $\sum H_2S$ and FeS_{aq} (Figure 5-19). As cores were collected from known locations of both sulfidic and iron rich sediment at the SERF site (Taillefert et al., 2007b), the large depth-integrated concentrations of species commonly indicative of both DIR (Fe^{2+} and org-Fe(III) in Figure 5-18) and MSR ($\sum H_2S$ and FeS_{aq} in Figure 5-19) was expected. Although intense sulfate consumption was observed at the Rhône site (Chapter 7), the precipitation of $FeS_{(s)}$ explains the generally low depth-

integrated concentrations of $\sum H_2S$ and FeS_{aq} (Figure 5-19). In turn, the low sulfate concentrations generally observed in freshwater explain the lack of $\sum H_2S$ and FeS_{aq} in the CO site.

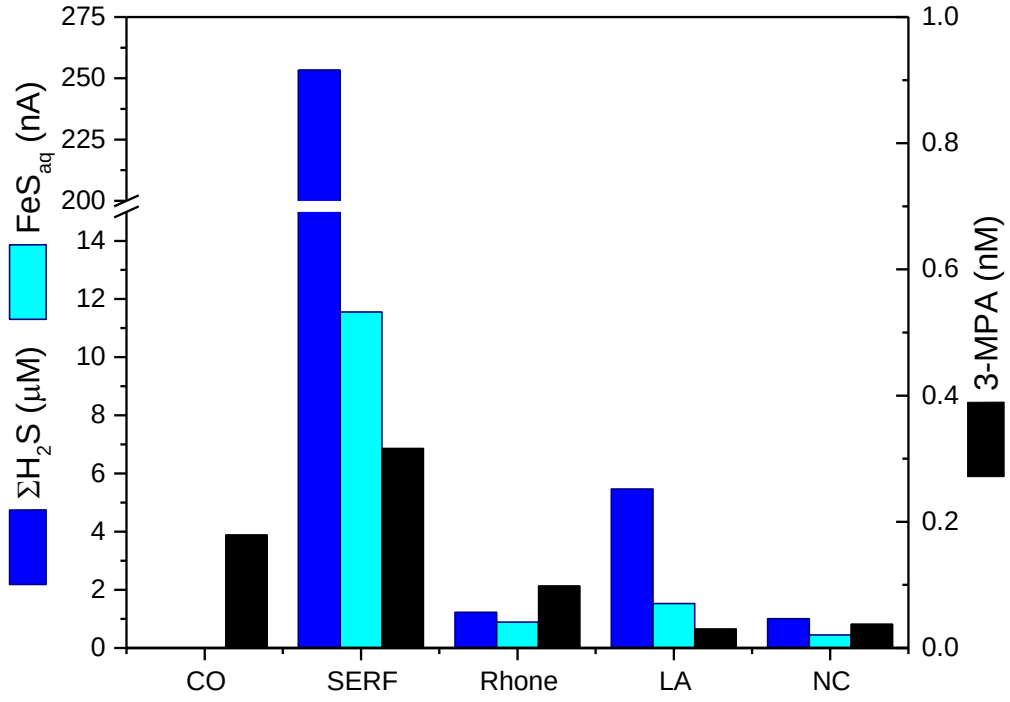

Figure 5-19 Average depth-integrated concentrations of $\sum H_2S$, FeS_{aq}, and 3-MPA from the Fraser Experimental Forest freshwater wetlands (CO), Salt Marsh Ecosystem Research Facility (SERF), Rhône River prodelta (Rhône), Louisiana continental margin (LA), and North Carolina continental margin (NC).

Although the relationship between Fe^{2+} and org-Fe(III) with cysteine and glutathione and between $\sum H_2S$ and FeS_{aq} with 3-MPA was visually evident from inspection of the depth profiles (e.g., Figure 5-8, Figure 5-9, Figure 5-10), demonstrating these relationships is difficult given the differences in spatial resolution between electrochemical measurements and thiol analysis and the number of processes that may affect the

concentrations of these compounds. For example, production of Fe^{2+} could be attributed to DIR or chemical reduction by $\sum H_2S$ produced during MSR which should decrease $\sum H_2S$, suppress org-Fe(III) signals, and either increase or decrease Fe^{2+} concentrations, depending on the intensity of MSR. In an attempt to account for the effect of sulfate reduction on iron reduction, depth-integrated concentrations and upward fluxes of dissolved species in non-sulfidic zones, as determined by absence of $\sum H_2S$ and FeS_{aq}, were examined only. In non-sulfidic sediment zones, depth-integrated concentrations of cysteine in both freshwater and all marine sediments correlated well with Fe^{2+} (Figure 5-20A) but not with org-Fe(III) (Figure 5-20B). Correlations between glutathione and Fe^{2+} (Figure 5-20C) were low in both freshwater and marine environments, as was the relationship between glutathione and org-Fe(III) (Figure 5-20D) in marine environments although correlations remained high in freshwater sediments. In turn, cysteamine correlated well with both Fe^{2+} (Figure 5-20E) and org-Fe(III) (Figure 5-20F) in freshwater sediments but not in marine sediments. Finally, neither freshwater or marine environments displayed significant correlations between 3-MPA and Fe^{2+} (Figure 5-20G) or org-Fe(III) (Figure 5-20H). Comparing diffusive fluxes of cysteine, glutathione, and cysteamine with diffusive fluxes of Fe^{2+} provided similar findings (Figure 5-21). The good correlations between depth-integrated concentrations of thiols and Fe^{2+} or org-Fe(III) in freshwater sediments were not affected by considering whole cores, including the sulfidic zone, as they lacked both $\sum H_2S$ and FeS_{aq}. In turn, these correlations decreased significantly in marine sediments (data not shown).

As 3-MPA in marine sediment is commonly attributed to sulfide degradation of DMSP (Table 5-3), 3-MPA was expected to correlate with $\sum H_2S$. However, the titration of

$\sum H_2S$ by Fe(III) in most marine sediments results in decreased sulfide concentrations and the formation of FeS or eventually pyrite. As FeS_{aq} is indicative of chemical sulfide oxidation by Fe(III), this species may provide a proxy for $\sum H_2S$ when rapid oxidation occurs. Indeed, comparison between whole core depth-integrated concentrations of thiols and $\sum H_2S$ or FeS_{aq} (Figure 5-22) demonstrated that only 3-MPA displayed good correlation with FeS_{aq} (Figure 5-22H) but, as expected, not $\sum H_2S$ (Figure 5-22G). The suspected relationship between cysteine, glutathione, and cysteamine with Fe^{2+} and 3-MPA with $\sum H_2S$ is further supported by the relatively high intra-thiol correlations of depth-integrated concentrations as cysteine, glutathione, and cysteine in all environments (Figure 5-23A,B,C) and the lack of correlation between 3-MPA with any of the other thiols (Figure 5-23D,E,F).

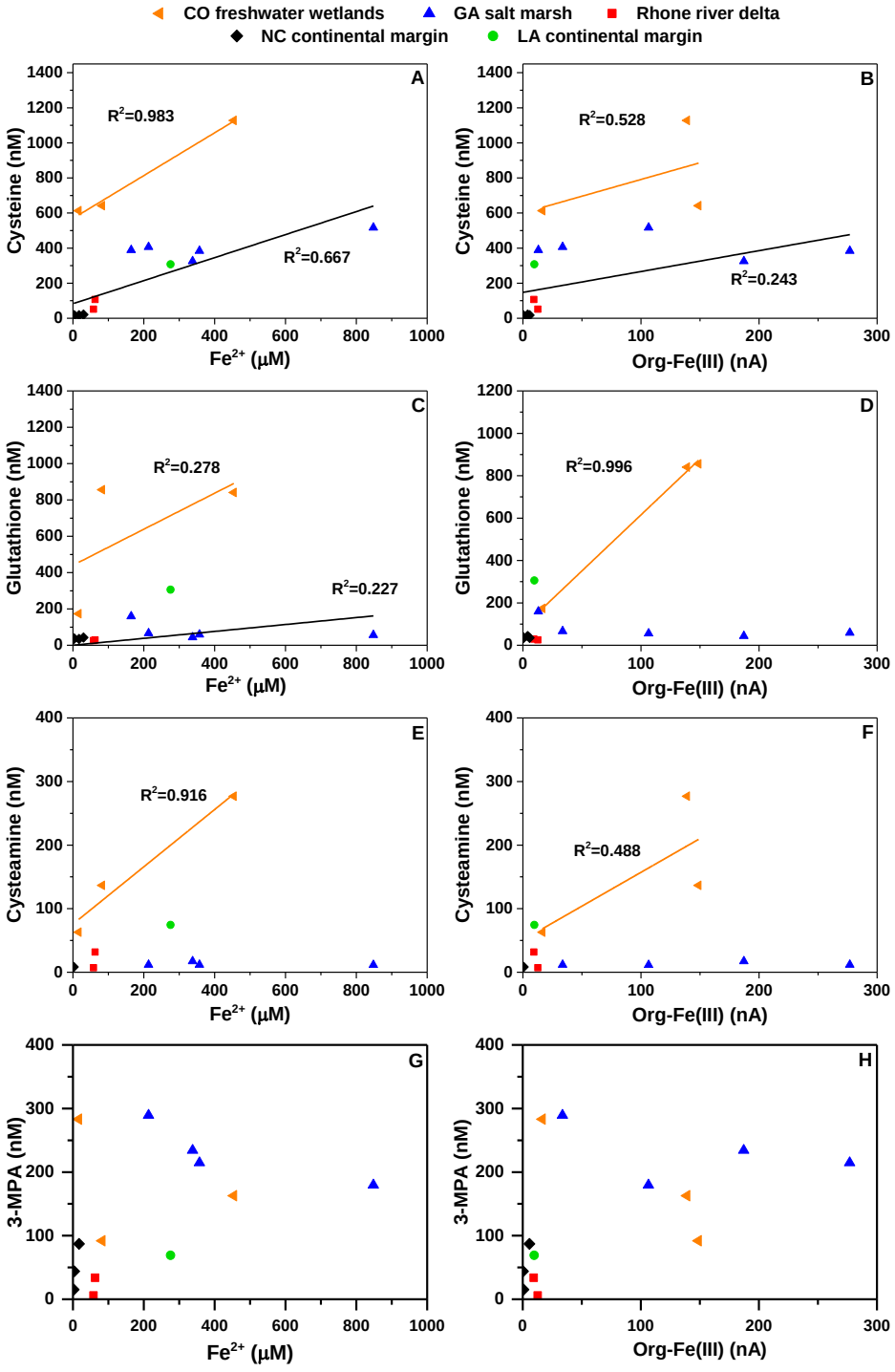

Figure 5-20 Comparison of depth-integrated concentrations of all four thiols with Fe^{2+} and org-Fe(III) in non-sulfidic sediment zones. Lines represent fresh (orange) and comined marine (black) correlations.

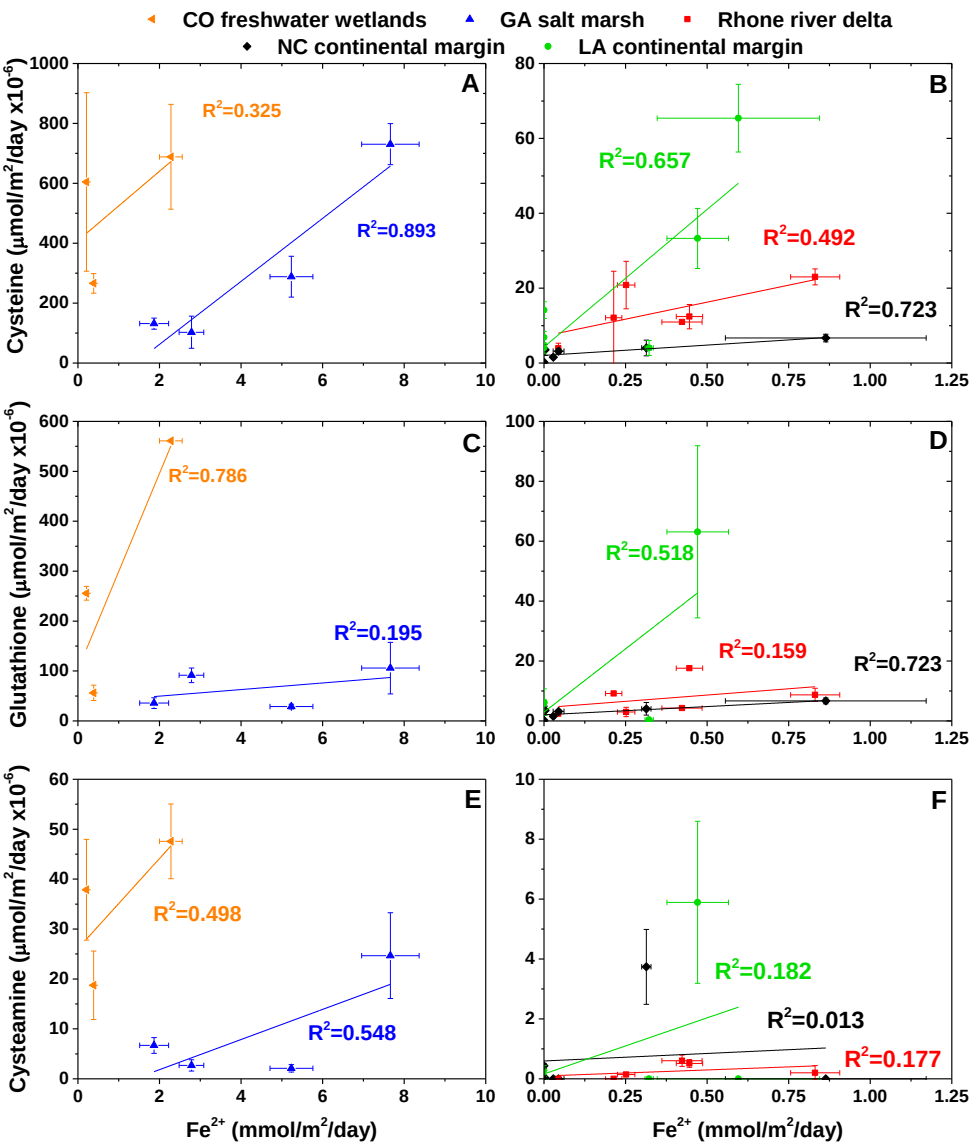

Figure 5-21 Comparison of diffusive fluxes of cysteine, glutathione, and cysteamine with Fe^{2+} in non-sulfidic sediment zones.

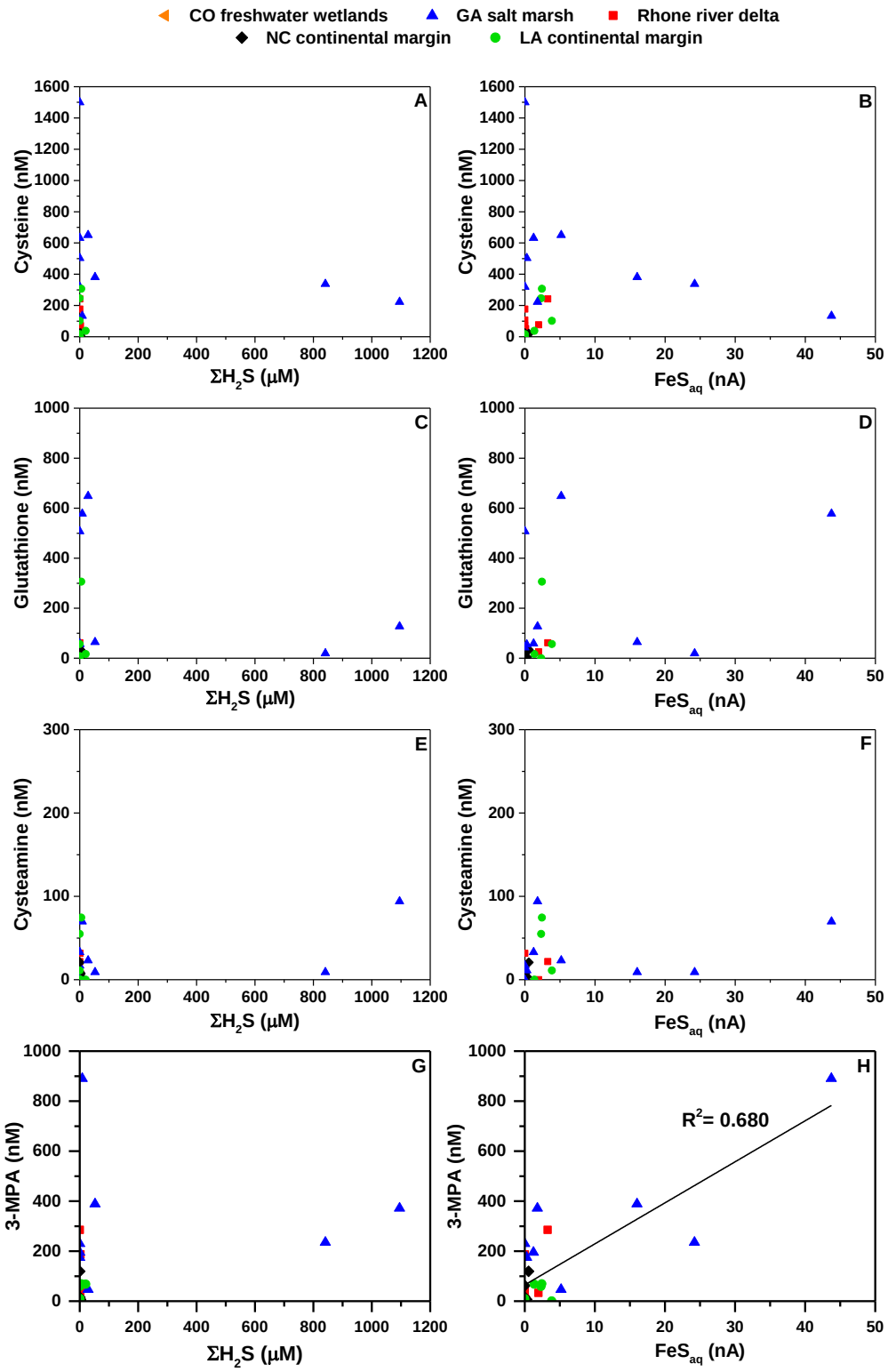

Figure 5-22 Comparison of depth-integrated concentrations of all four thiols with of ∑H_2S and FeS_{aq} in whole sediment cores.

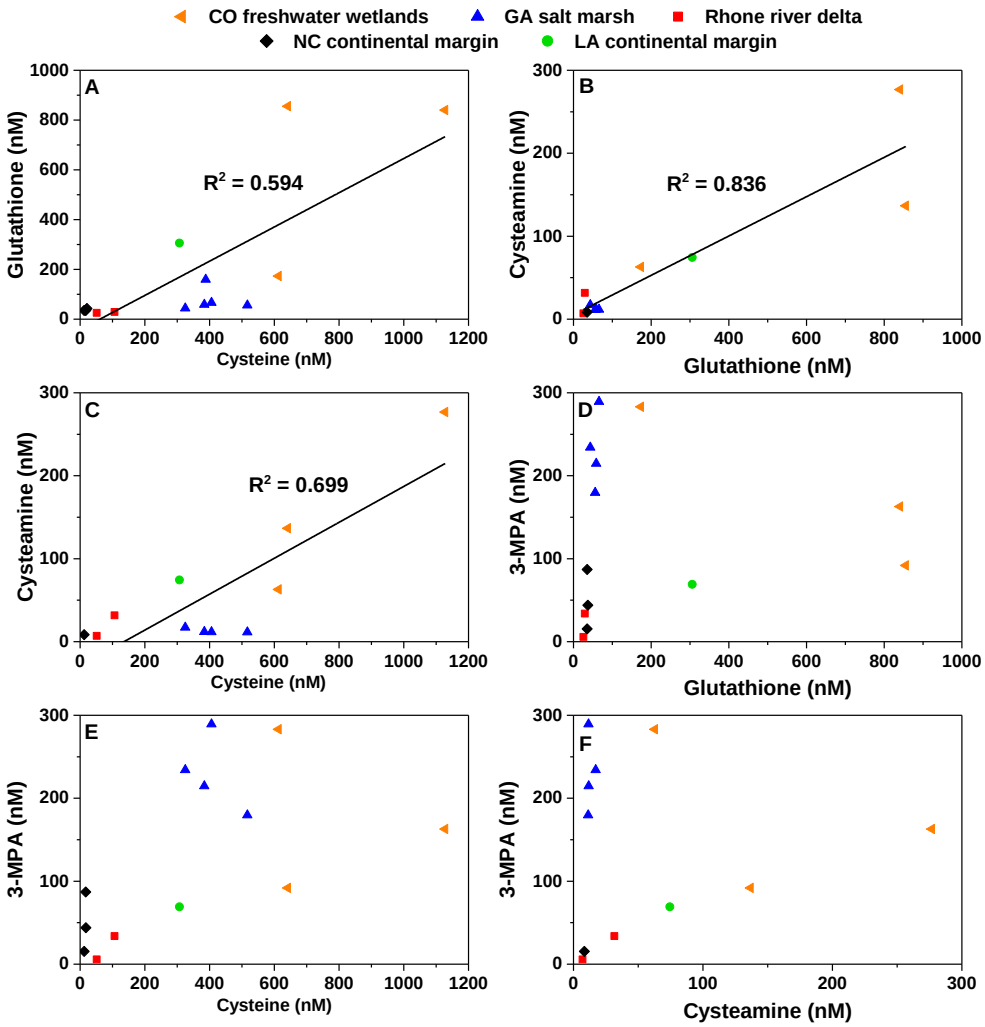

Figure 5-23 Comparison of depth-integrated concentrations of all four thiols with each other in non-sulfidic sediment zones.

5.5.3 Thiol Production in Sediment Slurries

To confirm that cysteine, glutathione, and, to a lesser extent, cysteamine production in sediments are linked to DIR and that endogenous production of thiols is not an artefact of pure culture incubations, sediments from SERF were incubated in a variety of conditions. Molybdate, a known inhibitor of MSR (Banat and Nedwell, 1984) confirmed in preliminary incubations (Figure 5-14) that $\sum H_2S$ produced during MSR would precipitate any produced Fe^{2+} as $FeS_{(s)}$ or pyrite (Carey and Taillefert, 2005; Koretsky et

al., 2003; Lowe et al., 2000) and rapidly reduce org-Fe(III) (Taillefert et al., 2000a). The preliminary incubations also demonstrated that addition of different thiols may influence natural populations differently as all cystine amendments increased both Fe^{2+} and org-Fe(III) after 41 days, whereas amendment of glutathione only increased org-Fe(III), and only amendments of cystamine greater than 100 µM resulted increased iron reduction relative to the unamended control (Figure 5-14). However, no major differences were observed between amendments of 100 µM cystine or glutathione in the sediment slurry incubations examined over time (Figure 5-15, Figure 5-16). Instead, major differences were primarily a result of molybdate amendments, which resulted in increased concentrations of Fe^{2+} (Figure 5-15A, A) and dissolved Fe(III) (Figure 5-16B), and to a lesser extent org-Fe(III) (Figure 5-15B). In samples without molydate, sulfate reduction clearly dominated as demonstrated by increased concentrations of both $\sum H_2S$ (Figure 5-15C) and FeS_{aq} (Figure 5-15D) and complete removal of org-Fe(III) after 30 days (Figure 5-15B) and dissolved Fe(III) after 20 days (Figure 5-16B). Interestingly, amendments of cystine and glutathione resulted in early production of FeS_{aq} (Figure 5-15D) in incubations lacking molybdate, which suggests that these disulfides either promote MSR or DIR to produce excess $\sum H_2S$ or Fe^{2+} in the pore waters that eventually exceed the solubility product of $FeS_{(s)}$. Addition of molydate to slurry incubations also had an important effect on endogenous thiol production (Figure 5-17). First, 3-MPA production increased significantly over time in the molybdate-free incubations (Figure 5-17B) compared to the incubations conducted in the presence of molybdate (Figure 5-17A). Similar results were previously observed in sediment incubations with molybdate (Kiene, 1991) and confirm the link between sulfate reduction and 3-MPA, possibly as a result of the sulfide

degradation of DMSP (Table 5-3). More importantly, cysteine, glutathione, and less significantly cystamine were progressively produced in the incubations amended with molybdate (Figure 5-17A) relative to the molybdate-free incubations which displayed no significant changes in these three thiols (Figure 5-17B). The increase production of these thiols occurred between 2 and 20 days, whereas the production of org-Fe(III) complexes was observed slightly later, between 6 and 15 days (Figure 5-15B), matching the sequential production of thiols and org-Fe(III) observed in the pure culture incubations (Figure 5-12A and C). These findings confirm the link of cysteine, glutathione, and eventually cysteamine to DIR and suggest that the change in concentrations of these thiols in marine sediments along with detection of org-Fe(III) complexes could be used to trace zones of DIR and therefore discriminate between microbial and abiotic production of Fe^{2+}. Overall, this study demonstrates endogenous production of cysteine and glutathione in natural sediments and to provides support for the involvement of thiols in DIR.

5.6 Conclusion

The distribution of small thiols in sediments of a variety of freshwater and marine sediments was determined and compared to the biogeochemical transformation of iron and sulfur in these environments. Detection of cysteine, glutathione, cysteamine, and 3-MPA in sediments from a wide variety of locations demonstrates that the distribution of these species is widespread. Significant correlations between cysteine, glutathione, and possibly cysteamine with Fe^{2+} and org-Fe(III) complexes in sediments not exposed to sulfate reduction suggest that these thiols may be involved in the dissimilatory reduction of Fe(III) oxides. Indeed, thiols are able to rapidly reduce Fe(III) oxides abiotically, and exogenous thiol and disulfide species increase both the rate and extent of Fe(II) production by metal-

reducing bacteria. In this study, the ability of the model metal-reducing bacteria *Shewanella* MR-1 to reduce cystine and produce endogenous thiols during the reduction of Fe(III) oxides was confirmed. More importantly, the endogenous production of cysteine, glutathione, and cysteamine during incubations of *Shewanella* MR-1 was evidenced and linked to the production of org-Fe(III) complexes, proposed to be generated as intermediate in dissimilatory iron reduction to destabilize Fe(III) from Fe(III) oxides and enhance the efficiency of the reduction process. These findings represent the first to demonstrate relationship between the electron shuttling and Fe(III)-solubilization bacterial mechanisms in *Shewanella* and suggest that bacterially-produced thiols may not only reduce org-Fe(III) complexes but also be involved in signaling the cells for endogenous production of the Fe(III)-binding ligands. Sediment slurry incubations provide additional evidence that glutathione and cysteine are microbially produced during DIR and may function as electron shuttles in natural environments. In addition to demonstrate that cysteine and glutathione could represent good proxies of dissimilatory iron reduction in sediments, these sediment incubations also highlight the good correlation between 3-MPA and $\sum H_2S$ or FeS_{aq} production and suggest that 3-MPA could be a good proxy of sulfate reduction in marine sediments.

5.7 Acknowledgments

I would like to thank Dr. Thomas DiChristina and the members of his lab group, Dr. Hyun-Dong Shin, Dr. Ramanan Sekar, and Dr. Rebecca Cooper for their microbial help. I would like to thank Dr. Frank Stewart and Dr. Christophe Rabouille for allowing me to participate in their research cruises, where I collected much of the data for this study. I would like to thank everyone who helped collect ancillary data on research cruises,

including Shannon Owings, Jens Rassmann, Ben Fields, Olivia Studebaker, and Joel Craig. I am grateful to Dr. Thomas Borch and Ellen Daugherty who collected and sent me sediment from Colorado. Finally, I would like to thank the captains and crews of the R/V Savannah, R/V Tethys II, and R/V Pelican.

CHAPTER 6. IRON FLUX AND SPECIATION IN CONTINENTAL MARGIN SEDIMENTS NOT DOMINATED BY MAJOR UPWELLING OR RIVERINE INPUTS

This is a manuscript, authored by Eryn M. Eitel[1], Shannon M. Owings[1], Keaton M. Belli[1], Jordon S. Beckler[1,2], Anna Williams[1], Benjamin P. Fields[1], Malory Brown[1], Joel Craig[1], Olivia Studebaker[1], Donald B. Nuzzio[3], Martial Taillefert[1] and entitled "Iron Flux and Speciation in Continental Margin Sediments Not Dominated by Major Upwelling or Riverine Inputs" that will be submitted to Marine Chemistry

[1]School of Earth and Atmospheric Sciences, Georgia Institute of Technology, Atlanta, GA 30332
[2]Present address: Harbor Branch Oceanographic Institute, Florida Atlantic University, Fort Pierce, FL 34946
[3]Analytical Instrument Systems, Inc., Ringoes, NJ 08551

6.1 Abstract

Despite the undeniable effect of iron on shaping patterns of ocean productivity, the sources of this limiting nutrient to the ocean are still under debate. Although global estimates indicate that sedimentary fluxes represent a significant input of iron to the oceans, these numbers are provided from a limited number of studies and mainly derived from continental margins exposed to either upwelling or large riverine inputs, environments that are not representative of the majority of the oceans. Additionally, the number of studies that determined iron benthic fluxes from continental slope sediments is limited, despite the fact that these regions between the shelf edge and the continental rise make up >5% of the sedimentary surface area of the global ocean. The sedimentary flux of iron has traditionally been considered negligible due to the poor solubility of Fe(III) formed by oxidation of Fe^{2+} diffusing out of the sediment into oxic waters. The recent realization that ferric iron may

be stabilized in solution by organic ligands during oxidation near the sediment-water interface suggests that organic-Fe(III) complexes may represent a significant portion of the sedimentary iron flux, potentially increasing transport and bioavailability in oxic waters. In this study, the diffusive flux and composition of iron were determined along a transect across the entire continental margin near Cape Lookout, North Carolina, a region not dominated by upwelling or riverine inputs that is representative of most passive continental margins. Rates of diffusive oxygen uptake (DOU) and the fluxes of both $Fe^{2+}$and organic-Fe(III) complexes decreased from the coastal zone to the continental shelf, remained low on the shelf and the upper continental slope, but rebounded to reach a maximum of up to 1.8 Fe^{2+} mmol m^{-2} day^{-1} in mid-slope sediments where concentrations of Fe(III) oxides were the highest along the transect. In turn, both DOU and iron fluxes decreased in lower-slope sediments, indicating that mid-slope sediments represent depocenters where Fe(III) oxides and organic matter may accumulate. The production of dissolved Fe(III) is likely regulated by a combination of aerobic oxidation in the presence of natural organic ligands near the sediment-water interface, dissimilatory iron reduction, or chemical oxidation of Fe(II) complexed to natural organic ligands. Pore water sulfate and sulfide concentrations as well as separate sediment incubations confirmed that sulfate reduction does not greatly influence the cycling of iron in these sediments. Extrapolation to the global ocean indicate that mid-slope depocenters from passive continental margins contribute considerably to the iron inventory of the ocean. Formation of organic-Fe(III) complexes in these sediments may stabilize dissolved iron and contribute to the transport of iron in oxygenated deep ocean waters.

6.2 Introduction

Iron exerts substantial control on ocean productivity and the export of organic matter to the deep ocean with potentially large-scale feedbacks within the global climate system (Falkowski et al., 1998; Jickells et al., 2005; Martin, 1990). Despite being the fourth most abundant metal in the Earth's crust, little dissolved iron is available in the oceans due to the rapid oxidation of Fe^{2+} in fully oxygenated waters (Millero et al., 1995) and low solubility of Fe(III) at circumneutral pH (Liu and Millero, 2002). As iron is an essential nutrient for phytoplankton, low concentrations may limit primary productivity in a large portion of the world's oceans including high-nutrient, low-chlorophyll (HNLC) regions (Coale et al., 1996; Kolber et al., 1994; Martin and Fitzwater, 1988), the low-nutrient South Pacific gyre (Behrenfeld and Kolber, 1999), the Southern Ocean (de Baar et al., 1990), and coastal upwelling regions were resuspension events may be unevenly distributed (Bruland et al., 2005; Hutchins and Bruland, 1998; Hutchins et al., 1998). Despite the considerable nutrient inputs from large rivers (Martin and Meybeck, 1979), iron-deficient conditions may also exist in coastal regions (Johnson et al., 1999), as the effective iron input to the oceans may be reduced up to 90% due to flocculation and precipitation during estuarine mixing (Boyle et al., 1977). The global flux of dissolved iron (< 0.45 μm) to the oceans from riverine sources has been estimated at 1.5-26 x 10^9 mol Fe yr^{-1} based on the average concentration of dissolved iron (40 nM Fe) in the major world rivers (Martin and Meybeck, 1979; Poulton and Raiswell, 2002). By providing a flux of 1-6 x 10^{11} mol Fe yr^{-1} (Fung et al., 2000; Jickells, 2001), wind driven, atmospheric inputs of land-derived particulate iron is also a major source of iron to the open ocean, despite its limited solubility in seawater (1-10%) (Jickells, 2001; Jickells et al., 2005; Johnson et al., 1997). However, large areas of the Antarctic and Southern Pacific Oceans receive low atmospheric iron inputs (Honjo

et al., 2000) such that alternative iron sources are required to account for the observed biological activity in these regions (Moore et al., 2002). Icebergs and glacial meltwater contribute comparable amounts of bioavailable iron, as aeolian dust in a limited number of polar regions (Bhatia et al., 2013; Raiswell et al., 2008). Hydrothermal vents may also sustain primary production even when atmospheric inputs are limited by generating an estimated dissolved iron flux of 0.9×10^9 mol Fe yr^{-1} (Tagliabue et al., 2010) which may constitute 10-20% of the dissolved iron pool in the deep ocean (Bennett et al., 2008). In addition, the mobilization and lateral advection of particulate iron from continental shelf sediments may provide a source of particulate iron to the ocean (Chase et al., 2005; Johnson et al., 1999) and HNLC zones (Lam and Bishop, 2008; Lam et al., 2006). Finally, dissolved iron diffusing out of margin sediments may be transported to surface waters in upwelling zones (Bruland et al., 2001; Coale et al., 1996; Elrod et al., 2004). Overall, benthic dissolved iron fluxes to the euphotic zone based on carbon oxidation rates and bottom water O_2 is predicted to be 72×10^9 mol Fe yr^{-1} from shelf sediments (<200 m) and 37×10^9 mol Fe yr^{-1} from slope sediments (200-2000 m) (Dale et al., 2015). However, such global estimates may currently be biased due to the number of studies investigating iron flux in zones of intense upwelling and the limited characterization of iron speciation in these studies.

Ferric iron is known to be stabilized in seawater by complexation with Fe(III)-binding ligands (Millero, 1998; Taillefert et al., 2000a; Wu et al., 2001). In fact, >90% dissolved Fe(III) in open ocean and coastal waters is complexed by strong organic Fe-binding ligands (Gledhill and Van Den Berg, 1994; Rue and Bruland, 1995; Rue and Bruland, 1997; van den Berg, 1995; Wu and Luther, 1994). Dissolved Fe is stabilized by dissolved organic

matter (DOM) from both riverine (Gerringa et al., 2007; Perdue et al., 1976) and sedimentary (Burdige et al., 1992a; Jones et al., 2011) origin, biologically-produced siderophores (Macrellis et al., 2001), and phytoplankton exudates (Chen et al., 2004), although strong L_1-type ligands not correlated with chlorophyll have been observed to dictate the concentration of dissolved Fe in river plume, estuary, and upwelled surface waters (Buck et al., 2007; Jones et al., 2011). Dissolved Fe(III) in similar concentrations as Fe^{2+} in the benthic boundary layer of continental margin sediments (Lohan and Bruland, 2008) and minimal oxidation of Fe^{2+} and removal as Fe(III) oxyhydroxide (Lohan and Bruland, 2008; Severmann et al., 2010) suggest iron may be stabilized in solution by complexation, potentially increasing bioavailability (Chase et al., 2005) and significantly impacting the offshore transport of dissolved iron of sedimentary origin (Buck et al., 2007; Chase et al., 2005; Jones et al., 2011).

Most benthic iron fluxes measured so far have been obtained from continental shelf sediments either associated with upwelling near HNLC regions (Berelson et al., 2003; Elrod et al., 2004; Esch et al., 2013; Lam and Bishop, 2008) or exposed to riverine inputs and seasonal hypoxia (Friedl et al., 1998; Friedrich et al., 2002; Lohan and Bruland, 2008; Noffke et al., 2012; Severmann et al., 2010). In upwelling regions, dissolved iron concentrations in the water column generally increase with continental shelf width (Bruland et al., 2001; Bruland et al., 2005; Chase et al., 2005) and decrease as upwelling persists (Fitzwater et al., 2003; Johnson et al., 2001). To our knowledge, however, iron reduction in continental margin sediments with limited upwelling or riverine input has never been measured. In addition, iron flux measurements from continental slope sediments are limited (Elrod et al., 2004; Noffke et al., 2012; Severmann et al., 2010)

despite the fact that these regions between the shelf edge and the continental rise make up >5% of the oceans sedimentary surface area compared to <9% for continental shelf sediments (Harris et al., 2014). In this study, the continental shelf and slope near Cape Lookout, North Carolina was investigated to evaluate the potential for passive continental margin sediments without large upwelling events or riverine input to act as an iron source to the ocean. As the speciation of dissolved iron may greatly affect its residence time, both dissolved Fe^{2+} and organic-Fe(III) complexes were measured, and the underlying biogeochemical processes affecting iron production and flux from these sediments were investigated.

6.3 Methods

6.3.1 Location Description

Sediment cores were obtained from the continental slope near Cape Lookout, North Carolina using either a single corer (Marinelli et al., 1998) or a MC-800 multicorer (Ocean Instruments, Inc.) during cruises conducted in June 2010, June 2011, June 2012, July 2015, and May 2016 on the R\V Savannah. Sediments were sampled in the coastal zone (0-20 m), across the shelf (20-50 m), over the upper-slope (50-500 m), the mid-slope (500-900 m), and the lower-slope (900-1500 m) (Figure 6-1, Table 6-1).

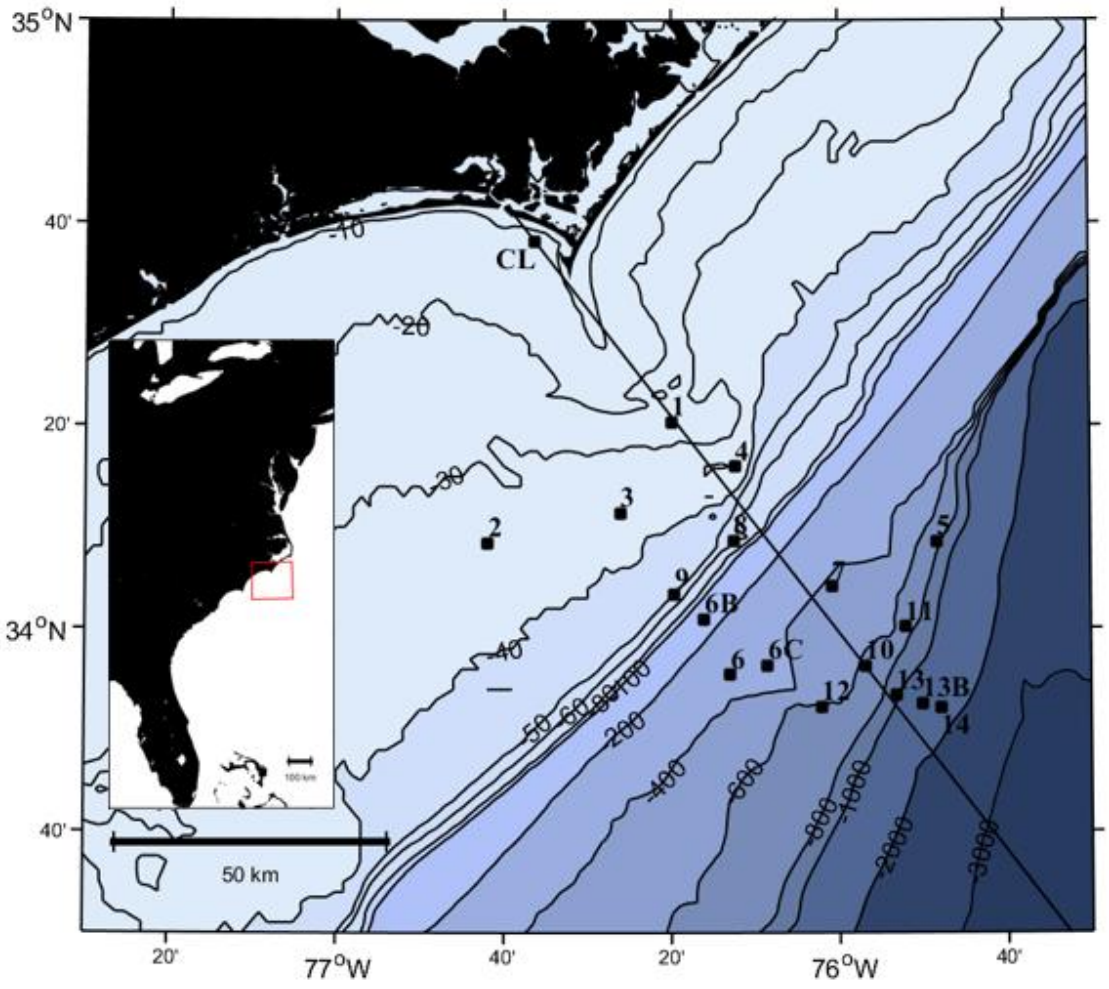

Figure 6-1 Bathymetric map of the North Carolina continental margin near Cape Lookout with locations of the stations where sediment cores were collected between 2010 and 2016. The black line transect was used to represent characteristic continental margin bathymetry.

Table 6-1 Sediment core collection date, location, water depth, and bottom water temperature and salinity.

Station	*Date*	*Lat. (°N)*	*Long. (°W)*	*Depth (m)*	*Temp (°C)*	*Salinity*	*O_2 (mM)*
1	5/30/2010	-76.3326	34.3391	28.6	21.7	34	0.226
2	5/31/2010	-76.6986	34.1411	36.7	23.8	34.7	0.225
3	6/1/2010	-76.4348	34.1903	33.8	24.7	36	0.236
2	6/3/2010	-76.6845	34.1465	37.2	24.8	33	0.224
1	6/4/2010	-76.3260	34.3392	27.7	22.9	31.2	0.224
3	6/5/2010	-76.4335	34.1905	33.9	26.4	32	0.231
3	6/4/2011	-76.4318	34.1924	33.4	24.8	35.5	0.223
1	6/9/2011	-76.3339	34.3386	28.3	21.1	35.75	0.223
3	6/10/2011	-76.4343	34.1913	31.4	23.3	38	0.213
4	6/13/2011	-76.6963	34.1408	28.2	23.4	35	0.213
4	6/11/2012	-76.6963	34.1408	65.2	23.7	37.5	0.220
1	6/13/2012	-76.3326	34.3391	22.3	24.5	36	0.209
CL	6/14/2012	-76.5952	34.6363	13.6	24.7	35.3	0.213
CL	6/16/2012	-76.6050	34.6350	14.7	25.2	35	0.197
3	6/18/2012	-76.4343	34.1913	33.4	24.7	35.8	0.146
2	6/20/2012	-76.6845	34.1465	37	27.1	35	0.203
4	7/8/2015	-76.2070	34.2660	40	25	36	0.210
3	7/9/2015	-76.4343	34.1913	30	26	37	0.205
6B	7/11/2015	-76.2690	34.0160	150	22.5	39	0.217
7	7/12/2015	-76.0150	34.0690	423	15	37	0.229
6	7/12/2015	-76.2170	33.9240	290	19	37	0.220
6C	7/13/2015	-76.1420	33.9400	335	17	38	0.240
5	7/19/2015	-75.8060	34.1430	589	17	36	0.225
11	7/19/2015	-75.8700	34.0030	665	19	38	0.223
12	7/20/2015	-76.0348	33.8715	580	18	36	0.239
10	7/20/2015	-75.9560	33.9360	596	17	38	0.229
8	5/17/2016	-76.2100	34.1440	57	23.9	39	0.211
CL	5/18/2016	-76.6050	34.6350	14.7	20.2	37	0.242
4	5/23/2016	-76.2070	34.2660	38	24.5	38	0.241
13	5/24/2016	-75.8870	33.8900	840	12.8	37	0.230
13B	5/24/2016	-75.8350	33.8770	1130	13.8	37	0.257
14	5/25/2016	-75.7990	33.8690	1450	12.4	37	0.254
9	5/26/2016	-76.3270	34.0570	63.7	25.2	40	-

To the south of Cape Lookout, the continental slope joins the Blake Ridge at about 32º30'N where the gradient of the slope averages 3.5º, whereas north of Cape Lookout near Cape Hatteras the slope gradient reaches a maximum of about 16º (Popenoe, 1980). The waters off the coast of North Carolina are primarily influenced by the Gulf Stream and the Western Boundary Undercurrent (WBUC). The WBUC flows southwest from the Labrador Sea and crosses below the Gulf Stream axis at depth of 2000 m near Cape Hatteras (Barrett, 1965; Richardson, 1977). To the south off Cape Lookout, an upper boundary of 1000 m is suggested for the WBUC (Rowe and Menzies, 1968). The Gulf Stream flows along the continental margin northeast from Florida over the Blake Plateau to Cape Hatteras where it turns easterly towards the North Atlantic. Near Cape Lookout, the lower boundary of the Gulf Stream may be as shallow as 600 m (Pratt, 1966), and not deeper than 1000 m on the Carolina margin, indicating that it does not mix with the WBUC (Johnson, 1989; Richardson, 1977; Rowe and Menzies, 1968). Therefore, the WBUC may influence the lower-slope and continental rise sediment, whereas the Gulf Stream tends to influence the bottom of the upper-slope, and the mid-slope receives the least direct influence from either of these currents (Blake et al., 1987). The Virginia Current, which flows south along the continental shelf in the Mid-Atlantic Bight converges with the Gulf Stream near Cape Hatteras and may contribute to limited local upwelling and intrusion events on the shelf or slope break, though these effects decrease to the south (Csanady and Hamilton, 1988; Janowitz and Pietrafesa, 1980; Pietrafesa et al., 1985).

Due to the divergence of the Gulf Stream, Cape Hatteras serves as an important oceanographic barrier separating the southern tropical waters from the northern temperate waters (Cerame-Vivas and Gray, 1966; Milliman et al., 1972; Stefánsson et al., 1971) and

is characterized by high deposition rates of organic matter and sediment particles despite no direct riverine inputs, high productivity, and completely oxygenated bottom waters (Blair et al., 1994; Blake et al., 1987; Blake et al., 1985; DeMaster et al., 1994; DeMaster et al., 2002; Diaz et al., 1994; Schaff T., 1992; Thomas et al., 2002). Historical data from the slope off Cape Hatteras, however, show this environment is atypical of the rest of the Atlantic slope (Rhoads and Hecker, 1994). In addition, the complex topography and numerous canyons, ridges, and gullies (McGregor, 1984; Mellor and Paull, 1994; Popenoe et al., 1982) make this sedimentary region difficult to study. As its sediment is more accessible and more representative of the Atlantic slope, the sampling location near Cape Lookout was chosen instead. The continental margin off Cape Lookout includes comparable total organic carbon in the upper 5 cm of slope sediment compared to locations north or south and is exposed to an intermediate sedimentation rate of 0.16 cm/yr (Blake et al., 1987; Schaff T., 1992). Finally, relatively little evidence of downslope sliding has been observed by either submersibles or high resolution seismic profiles (DeMaster et al., 1994), and limited sulfate reduction has been detected (DeMaster et al., 1994; Schaff T., 1992), indicating that dissimilatory iron reduction may represent a dominant anaerobic respiration process in these sediments.

6.3.2 Sediment sampling and analysis

Unless otherwise notes, all chemicals were of reagent grade or higher purity and obtained from Sigma-Aldrich. Depth profiles of dissolved O_2, Mn^{2+}, Fe^{2+}, total dissolved sulfide ($\sum H_2S = H_2S + HS^- + S(0) + S_x^{2-}$) as well as organic complexes of Fe(III) (org-Fe(III)) and iron sulfide clusters (FeS_{aq}) were obtained with mercury/gold amalgam (Hg/Au) voltammetric microelectrodes in intact sediment cores within 30 minutes after

collection. The Au solid state voltammetric microelectrodes were constructed from a 100 µm diameter Au wire immobilized in a Pyrex glass tube pulled to a tip of 0.4 mm diameter using marine epoxy and plated with mercury by electrodeposition of a $HgCl_2$ solution for 4 minutes at -0.1 V (Brendel and Luther, 1995). Voltammetric measurements were conducted in a three electrode configuration, including the Hg/Au voltammetric microelectrode, an Ag/AgCl reference electrode, and a Pt counter electrode using a computer-controlled DLK-70 potentiostat with DLK MAN-1 micromanipulator (Analytical Instrument Systems, Inc.). Dissolved O_2 was determined by linear sweep voltammetry (LSV) between -0.1 and -1.75 V at a scan rate of 200 mV/s with an initial conditioning step of 10 s at -0.1 V and calibrated *in situ* using temperature and salinity of the overlying water assuming oxygen was at saturation (Luther et al., 2008). All other species were determined by cathodic square-wave voltammetry (CSWV), between -0.1 and -1.75 V at a scan rate of 200 mV/s with a conditioning step of 10 s at -0.1 V (Brendel and Luther, 1995). When org-Fe(III) or $\sum H_2S$ were detected, an additional conditioning step of 10 s at -0.9 V was included prior the above procedure to clean the electrode (Taillefert et al., 2000b). Electrodes were calibrated for Mn^{2+} by CSWV with $MnCl_2$, and Mn^{2+} sensitivities were used to quantify Fe^{2+} and $\sum H_2S$ according to the pilot ion method (Luther et al., 2008). As org-Fe(III) and FeS_{aq} are not quantifiable, reported current intensities are normalized to average electrode sensitivity (Tercier-Waeber and Taillefert, 2008). All voltammetric data was integrated using VOLTINT, a semiautomated Matlab script with peak recognition software (Bristow and Taillefert, 2008). Depth profiles of pH were simultaneously obtained by deploying a 10 cm long MI-414B needle combination pH

minielectrode (Microelectrodes, Inc.) calibrated with TRIS buffer in synthetic seawater (Dickson, 1993) within 5 mm laterally from the Hg/Au voltammetric microelectrode.

After voltammetric profiling, pore waters were extracted from the same sediment cores in a glove bag (Sigma-Aldrich) extensively flushed with N_2 to avoid air contaminations. The overlying water was sampled and the sediment sectioned in 6-10 mm sections under N_2 atmosphere. The sediment sections were then centrifuged at 3000 rpm for 10 minutes and filtered using 0.2 µm Puradisc polyethersulfone (PES) syringe filters (Whatman) both under N_2 atmosphere. For sandy sediments, a screen insert was added to the centrifuge tubes to allow separation of pore waters from the above sediment during centrifugation. Filtered pore waters were then partitioned under N_2 atmosphere for onboard analyses of total dissolved orthophosphate ($\sum PO_4^{3-}$) and dissolved inorganic carbon (DIC). The remaining pore waters and solid sediments were frozen for analysis of inorganic anions (Cl^-, Br^-, NO_2^-, NO_3^-, SO_4^{2-}) in the dissolved phase and solid phase iron back at Georgia Tech. Total dissolved orthophosphate ($\sum PO_4^{3-}$) was quantified spectrophotometrically using the paramolybdate method (Murphy and Riley, 1962), whereas DIC was analyzed by flow injection analysis (Hall and Aller, 1992) with a conductivity meter (Fisher Scientifics, Inc.) and a computer-controlled LCC-100 Integrator (AIS, Inc.). Inorganic anions (Cl^-, Br^-, NO_2^-, NO_3^-, SO_4^{2-}) were determined in one step by high pressure liquid chromatography (HPLC) using a Metrohm Metrosep A supp 5 anion exchange column (150 mm x 4 mm) with a 3.2 mM Na_2CO_3 / 1.0 mM $NaHCO_3$ eluent, flow rate of 0.7 ml/min, and UV detection at 215 nm (Beckler et al., 2014). Finally, highly reactive and total Fe(III) (oxyhydr)oxides (hereafter referred to simply as Fe(III) oxides) were extracted using ascorbate and dithionite reagents, respectively (Kostka and Luther, 1994), and quantified

using the ferrozine method (Stookey, 1970). Crystalline Fe(III) oxides were quantified by difference between dithionite and ascorbate iron extractions, and both reactive and crystalline Fe(III) oxides were normalized to the mass of dry sediment, which was determined along with porosity in subsamples by weighing before and after drying at 40°C for several days.

6.3.3 Calculations

Diffusive oxygen uptake (DOU) fluxes of the sediment and maximum diffusive fluxes of Fe^{2+}, HPO_4^{2-} (as proxy for $\sum PO_4^{3-}$), and HS^- (as proxy for $\sum H_2S$) were determined from the steepest portion of pore water gradients in concentration of each species following a modification of Fick's first law to account for tortuosity (θ) (Boudreau, 1997):

$$F_x = -\varphi \frac{D_x^0}{\theta^2} \frac{dC_x}{dz} \tag{6-1}$$

where F_x is the diffusive flux of species x, φ is the sediment porosity, D_x^0 is the ionic or molecular diffusion coefficient of species x, C_x is the concentration of species x, and z is sediment depth. The tortuosity was estimated from Archie's law ($\theta^2 = \varphi^{(1-m)}$) with m = 2 for $\varphi \leq 0.7$ and m =2.5 for φ =0.7-0.9 (Ullman and Aller, 1982). The molecular diffusion coefficient for dissolved O_2, Fe^{2+}, HPO_4^{2-}, and HS^- were calculated based on temperature and the dynamic viscosity (μ) of seawater at the temperature, pressure, and salinity of the site:

$$D_{O_2}^0 = \left(m_0 + m_1 \frac{T}{\mu}\right) x10^{-5} \tag{6-2}$$

$$D^0_{(Fe^{2+},PO_4^{3-},HS^-)} = (m_0 + m_1 \cdot T)x10^{-6} \quad (6\text{-}3)$$

where m_0 and m_1 are constants determined for each species (Boudreau, 1997). Concentration of HS^- was determined from the measured $\sum H_2S$ concentration based on the pK_as for sulfide using the measured pH. The molecular diffusion coefficient constants for HS^- were used for the electrochemically measured ΣH_2S concentrations when pH values were not available (Appendix B.1). Molecular diffusion coefficient constants for HPO_4^{2-} were deemed sufficient for the pH range measured. As the composition of the org-Fe(III) complexes is unknown, the molecular diffusion coefficient was estimated from the Stokes-Einstein equation (Cornel et al., 1986), assuming spherical org-Fe^{3+} species (Eq. 6-4),

$$D^0_{Org-Fe(III)} = \frac{kT}{6\pi\mu\left(\frac{3}{4\pi}\frac{MW}{\rho N}\right)^{1/3}}\ cm^2s^{-1} \quad (6\text{-}4)$$

where *k* is the Boltzmann constant, *T* is temperature, μ is the dynamic viscosity, ρ is density, *N* is Avogadro's number, and *MW* is the molecular weight. A model molecular weight of 1 kDa was chosen along with a density of 1.13 g cm^{-3} based on humic-like substances (Jones et al., 2011). Diffusive fluxes into the oxic zone (as determined by the detection of dissolved O_2) were calculated for individual species when appropriate.

Whole core depth-integrated pore water concentrations (Z) of each species (x) were calculated at each station by integrating the concentration of each species over the thickness of each core section then dividing by the total core depth length:

$$Z_x = \frac{\varphi \int_0^{z_f} C_x dz}{z_f} \quad (6\text{-}5)$$

where φ is the sediment porosity, C_x is the concentration of species x (moles/l), z is the thickness of each core section (mm), and z_f is the total core length (mm).

6.3.4 Sediment Incubations

Sediment slurry incubations were carried out with sediments from four stations (6B, 6C, 7 and 11) collected in 2015. Bulk sections from within and outside organic-Fe(III) production zones at stations 6B (0-8; 8-16; 30-38 cm), 6C (0-5; 5-12; 12-24; 24-35 cm), 7 (0-4; 4-10; 10-18; 18-24; 24-30 cm), and 11 (0-5; 5-11; 11-22; 22-33 cm) were homogenized and incubated (Appendix B.2). Homogenized sediment (~ 20 % v/v) was mixed with the overlying water of each site in 28 mL hungate tubes (Chemglass), degassed for 10 minutes to remove the majority of dissolved oxygen, wrapped in tin foil, and placed on a rotary wheel. Samples were collected over time and filtered inside an anaerobic chamber (N_2 atmosphere) to prevent chemical oxidation of Fe^{2+}. Dissolved Fe^{2+} and total dissolved iron were measured spectrophotometrically by the Ferrozine method in each sample before and after addition of hydroxylamine, and dissolved Fe(III) was determine as the difference between total iron and Fe^{2+} (Stookey, 1970). Analysis of SO_4^{2-} was conducted by HPLC using the same procedures described above. Production rates of dissolved iron were calculated from the slope of the linear regression of concentration versus time at different depth intervals. For comparison to diffusive fluxes, depth-integrated rates (mmol cm^{-2} day^{-1}) were determined in the top incubation section at each station (Eq. 6-6):

$$Depth - integrated\ rate_x = \varphi \int_{z_i}^{z_f} R_x(z)dz \quad (6\text{-}6)$$

where φ is the sediment porosity, $R_x(z)$ is the depth distribution of the production of species x (mmol cm^{-3} day^{-1}), z_i is initial depth of the incubation zone (cm), and z_f is the final depth of the incubation zone (Canfield, 1989).

6.4 Results

6.4.1 Bottom Water Characteristics

Water depth was determined along the transect between 34.6802N 76.6469W and 33.4706N 75.5169W (Figure 6-1 black line) using 1-minute ETOPO1 bathymetry (Amante and Eakins, 2009) and represented against distance from shore (Figure 6-2). Past the coastal zone (0-20 m), the continental shelf (20-50 m) was dominated by sand and had an average gradient on the shelf of 0.03 ± 0.5º (Figure 6-2). The continental slope spans the outer margin of the continental shelf, beginning at the shelf break at ~60 m and extending to a depth of 2600 m. It can be divided into three subcategories: the upper-slope (50-500 m), mid-slope (500-900 m), and lower slope (900-2600 m) with average gradients of 0.73 ± 0.4º, 1.9 ±0.7º, and 5.6 ± 1.4º (Figure 6-2). Proportions of silt, clay, and mud increase from the upper to mid-shelf, then become dominated by clay in the lower-slope. Below 2600 m, the gradient decreases to 0.73 ± 0.6º (Figure 6-2), indicating the beginning of the continental rise. Bottom water temperatures decreased proportionally to water column depth (Table 6-1, Figure 6-2). At all stations bottom water salinities averaged 36 ± 2 (Table 6-1). The water column was fully oxygenated with bottom water concentrations averaging 0.223 ± 0.02 mM (Table 6-1).

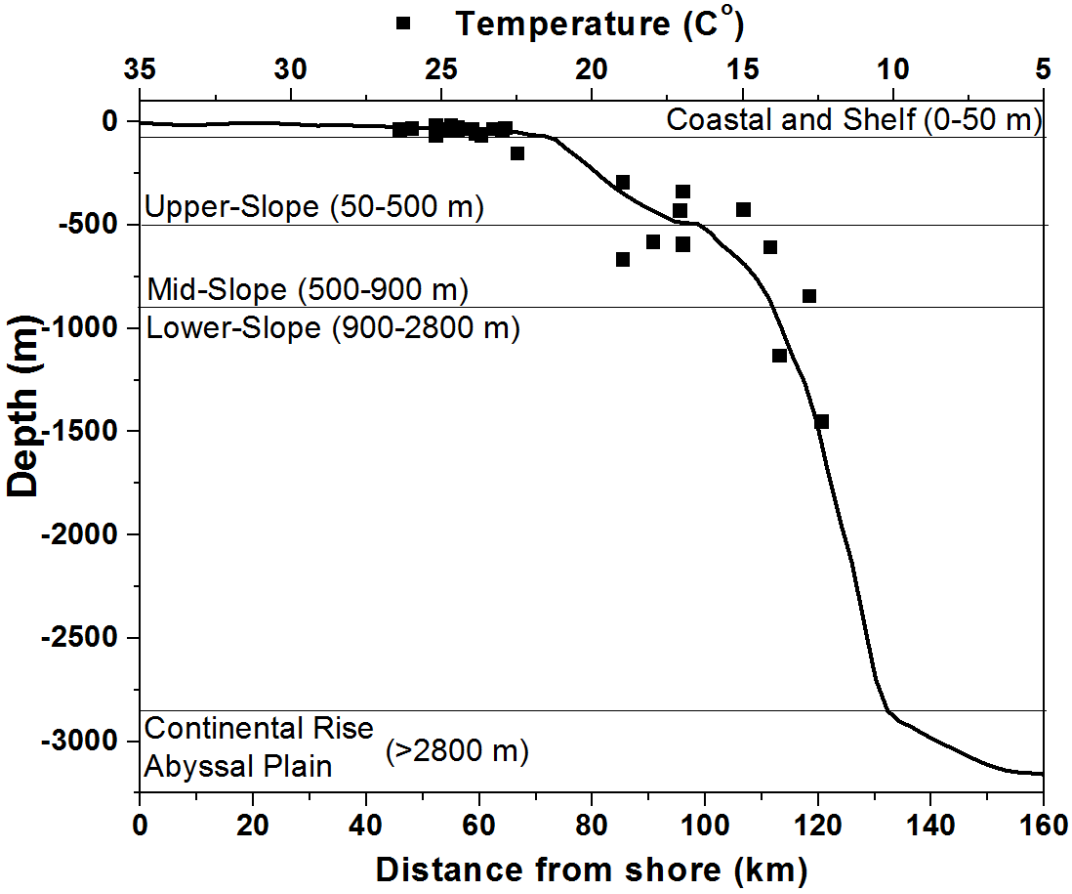

Figure 6-2 Bottom water temperature (°C) as a function of water depth (scatter points) and water depth as a function of distance from shore (black line) along the transect shown in Figure 6-1.

6.4.2 Pore Water Depth Profiles

Oxygen penetration depths (OPD) were small at coastline stations with an average of 2.5 ± 0.7 mm at all stations sampled nearshore (e.g., St. CL), increased from an average of 4.8 ± 6 to 14.5 ± 6 mm from the shelf to the upper-slope (e.g., St. 8, 6B, 7), then decreased to an average of 9.6 ± 2 mm on the mid-slope (e.g., St. 5, 11, 13). Finally, the OPD increased on the lower slope to an average of 20 ± 6 mm (e.g., St. 13B and 14) (Figure 6-3). Dissolved Fe^{2+} concentrations oscillated between below detection limit (< 20 µM)

and 170 µM over the first 80 mm in St. CL and were anti-correlated with current intensities of org-Fe(III) complexes (Figure 6-3). In turn, ΣH_2S and FeS_{aq} were below detection limit in the zone of iron reduction but increased with depth up to 230 µM and 20 nA, respectively, once Fe^{2+} and org-Fe(III) complexes were depleted. Additionally, St. CL was the only location were Mn^{2+} was observed with peaks up to 70 µM at 32 mm depth in 2015 (Figure 6-3) and similar concentrations and location in the depth profile measured in 2012 (data not shown). On the continental shelf (St. 1,2,3,4), Fe^{2+} and org-Fe(III) were not observed in the pore waters (e.g., St. 2 in Figure 6-3) except at stations 4 (not shown), where the onset of Fe^{2+} occurred at 46 ± 7 mm in average between 2015 and 2016 with maximum concentrations of 99 µM, while org-Fe(III) onset was slightly shallower at 38 ± 4 mm and had maximum signals of 8 nA. In turn, although $\sum H_2S$ was detected at every station on the shelf (e.g., St. 2 in Figure 6-3), a wide ΣH_2S onset depth of 77 ± 31 mm was observed between 2010 and 2016. Similar to St. 4, the onsets of Fe^{2+} and org-Fe(III) production were similar in the upper-slope (St. 6, 6B, 6C, 7, 7B, 8, and 9) at 52 ± 18 and 51 ± 11 mm in average between stations, and their concentrations and current intensities reached maximum concentrations of 110 µM and 6 nA at St. 6B. In turn, the onset of ΣH_2S descended to 108 ± 35 mm in average between 2015 and 2016 at these stations, when detected. On the mid-slope (St. 5, 10, 11, 12, and 13), the onset of dissolved Fe^{2+} and org-Fe(III) rose to 12 ± 5 and 22 ± 12 mm in average, close to the OPD, while ΣH_2S production also rose to 73 ± 32 mm with concentrations reaching maximums of 437 µM Fe^{2+} at St. 11 and 24 nA org-Fe(III) at St. 13. In turn, pore water Fe^{2+}, org-Fe(III), and ΣH_2S were not detected at any depth in the profiles on the lower slope (St. 13B and 14 in Figure 6-3).

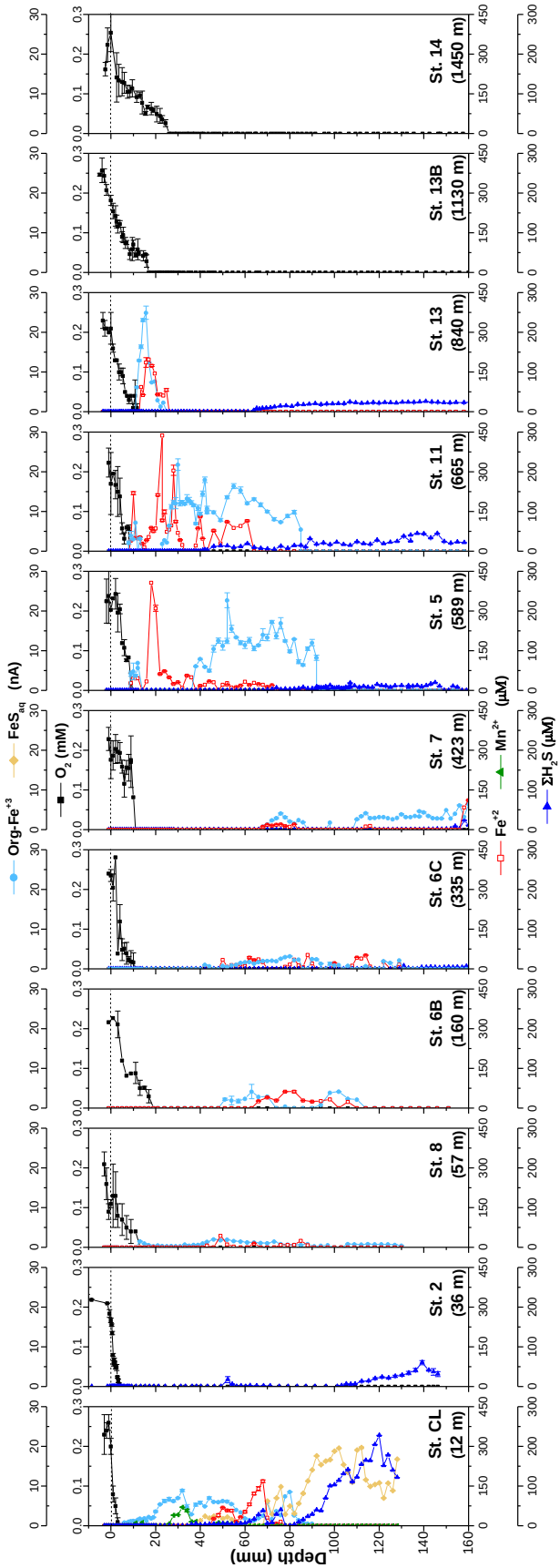

Figure 6-3 Depth profiles of dissolved O_2, Fe^{2+}, organic-Fe(III), FeS_{aq}, Mn^{2+}, and $\sum H_2S$ concentrations measured electrochemically in representative sediment cores as a function of water column depth between 2012 and 2016: coastal (St. CL), shelf (St. 2), upper-slope (St. 8, 6B, 7), mid-slope (St. 5, 11, 13), lower-slope (St. 13B, 14).

DIC concentrations increased slightly with depth at all location, although no major production (>5 mM) was detected (Figure 6-4). Not surprisingly, no significant changes in SO_4^{2-} were observed in any of the stations (Figure 6-4), except maybe a subsurface minimum in the first few centimeters at the deepest station (St. 14). In turn, ΣPO_4^{3-} produced subsurface maxima up to 15 µM at 30 mm in the coastal zone (St. CL), but did not reach concentrations above 5 µM on the shelf or the shallow upper-slope (St. 2, 8, 6B in Figure 6-4). Although ΣPO_4^{3-} concentrations maxima remained low at St. 7, with just 8 µM observed at 103 mm, ΣPO_4^{3-} concentrations generally increased as water depth increased. At St. 6C a maximum concentration of 22 µM was observed at 63 mm. On the mid-slope, ΣPO_4^{3-} increased to maximum concentrations of 16 ± 3 µM at 54 ± 5 mm in average between stations (St. 5 and 11). Deeper on the mid-slope (St. 13) and into the lower-slope (St. 13B), ΣPO_4^{3-} maxima reached shallower depths (44 ± 2 mm) but in lower concentrations (12 ± 3 µM) in average between these stations. Finally, ΣPO_4^{3-} gradually increased to 10 µM at 173 mm at the deepest location (St. 14).

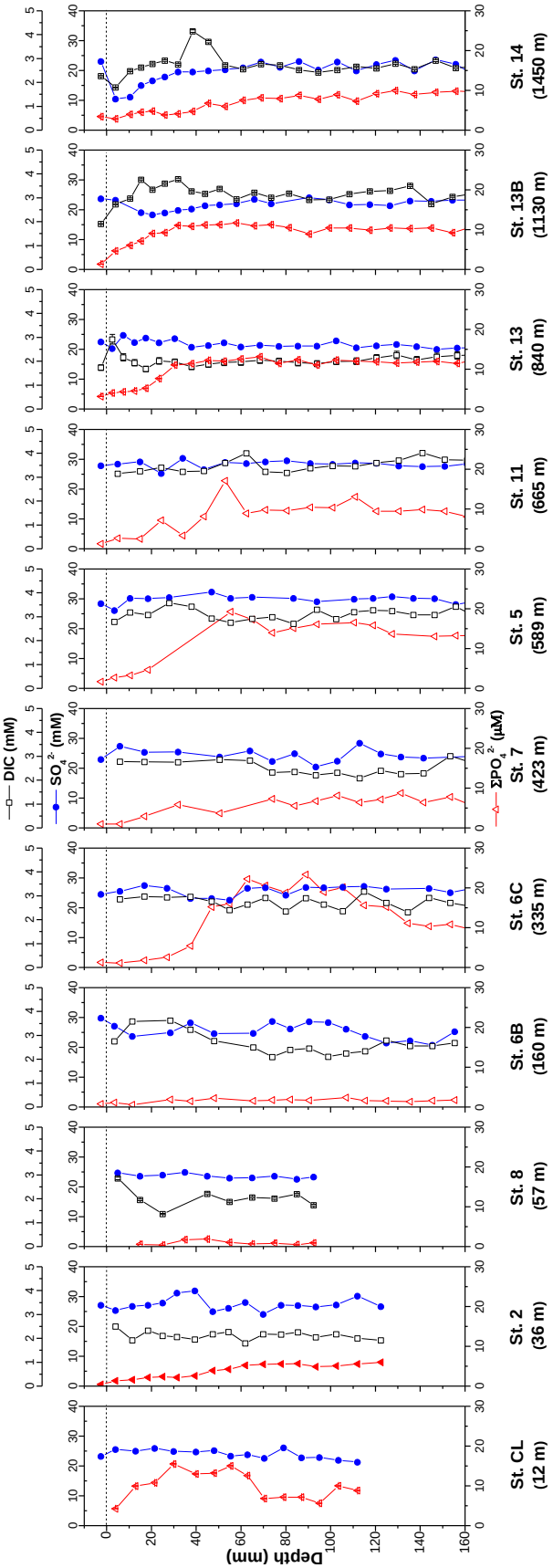

Figure 6-4 Depth profiles of dissolved DIC, SO_4^{2-} and $\sum PO_4^{3-}$ concentrations measured in pore waters of representative sediment cores as a function of water column depth between 2012 and 2016: coastal (St. CL), shelf (St. 2), upper slope (St. 8, 6B, 7), mid-slope (St. 5, 11, 13), lower-slope (St. 13B, 14).

6.4.3 Solid Phase Iron Depth Profiles

Almost no reactive Fe(III) oxides, as determined by ascorbate extraction, were detected in the shallow upper-slope sediments (St. 8 and 6B in Figure 6-5). Reactive Fe(III) oxide concentrations, however, generally formed subsurface maxima near the sediment-water interface that increased with water column depth to concentrations up to 6 and 5.8 µmol Fe/g dry weight (gdw) in the top 20 mm on the upper-slope (St. 6C and St. 7 in Figure 6-5) and up to 8.8 µmol Fe/gdw in the top 20 mm on the mid-slope (St. 5). Concentrations in the top 20 mm decreased with water depth from the mid to lower-slope (7.2 µmol Fe/gdw was observed at St. 11, 4.5 µmol Fe/gdw at St. 13, and 4.3 µmol Fe/gdw at St. 13B). Interestingly, at the deepest station (St. 14) concentrations of reactive Fe(III) oxides were as high as 7.2 µmol Fe/gdw in the top 30 mm. Except for the upper and mid-slopes (St. 6C, 7, 5, and 11), the concentration of reactive Fe(III) oxides was not significant deeper in the sediment cores.

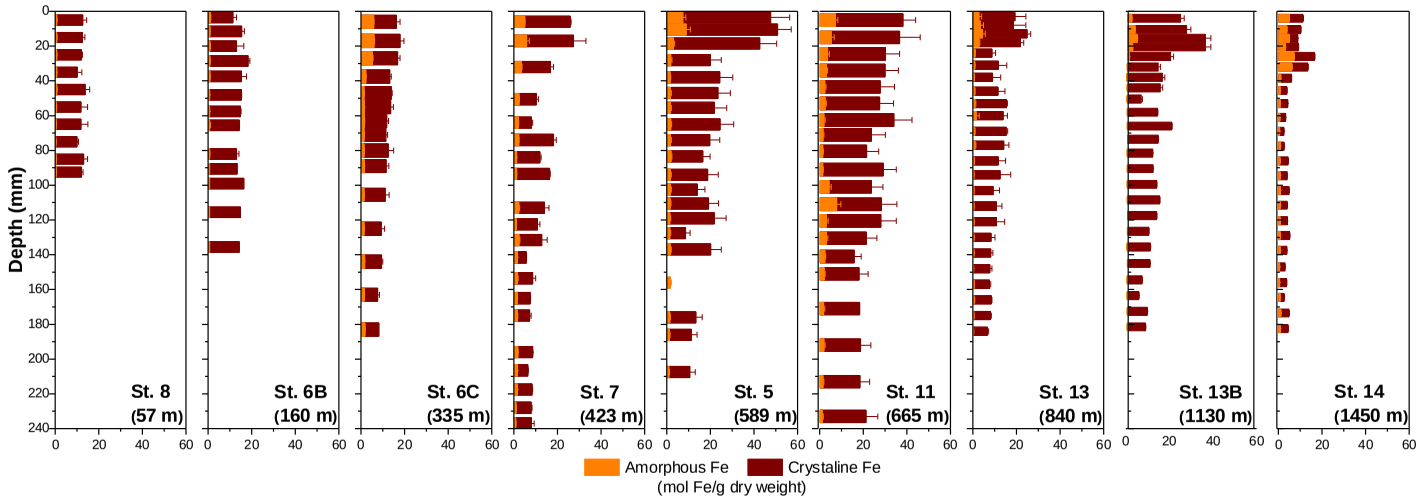

Figure 6-5 Depth profiles of amorphous Fe(III)-oxides determined by ascorbate extraction and total iron oxides (amorphous and crystalline Fe(III)-oxides, AVS) determined by dithionite extraction in representative sediments from the upper slope to the lower slope between 2015 and 2016.

Crystalline Fe(III) oxides, as determined by the difference between dithionite extractable and ascorbate extractable iron, only reached concentrations up to 13.7 and 15.4 µmol Fe/gdw on the shallow upper-slope (St. 8 and 6B) and remained constant with sediment depth (Figure 6-5). In turn, concentrations gradually decreased from 17.9 and 27.4 µmol Fe/gdw in the top 20 mm to 8.2 and 8.1 µmol Fe/gdw by 180 and 237 mm at St. 6C and St. 7, though a small rebound to 18.2 µmol Fe/gdw was observed at 74 mm in the St. 7 sediment core. Crystalline Fe(III) oxide concentrations were the highest on the mid-slope, with concentrations up to 50.9 and 38.2 µmol Fe/gdw in the top 20 mm of St. 5 and St. 11 (Figure 6-5). However, concentrations decreased sharply to 20 µmol Fe/gdw at 28 mm, then gradually decreased to 10.1 µmol Fe/gdw at 207 mm at St. 5, whereas the concentrations gradually decreased to 18.47 µmol Fe/gdw at 213 mm at St. 11. Crystalline Fe(III) oxide concentrations decreased with increased water depth on the mid-slope (Figure 6-5). At St. 13 crystalline Fe(III) oxides reached concentrations of 20.4 µmol Fe/g dry weight in the top 20 cm, decreased to 7.8 µmol Fe/g dry weight between 20 and 53 mm, rebounded to 14.5 µmol Fe/g dry weight, and were followed by a gradual decrease with depth below 70 mm. Similar patterns were observed at St. 13B, albeit at concentrations peaking at 33.3 µmol Fe/g dry weight around 20 mm, decreasing to 6.6 µmol Fe/g dry weight at 50 mm, rebounding to 20.4 µmol Fe/g dry weight at 66 mm, and then decreasing with depth below 110 mm. Although concentrations as high as 3.9 µmol Fe/g dry weight were determined in the top 35 mm at St.14, crystalline Fe(III) oxide concentrations were generally low and decreased with depth to 1.1 µmol Fe/g dry weight.

6.4.4 Sediment Incubations

Concentrations of both dissolved Fe^{2+} and dissolved Fe(III) generally increased over the 52-day incubation period whereas no change in SO_4^{2-} concentrations was observed in any of the incubations (not shown). Minimal dissolved $Fe^{2+}$and Fe(III) were produced during incubations of any sediment sections from the shallow (St. 6B; 150 m water depth) and middle (St. 6C; 335 m water depth) upper-slope sediments (not shown), and similar Fe^{2+} production rates were observed at both stations (Figure 6-6A), reflecting the generally low Fe^{2+} concentrations and org-Fe(III) current intensities measured in the depth profiles (Figure 6-3). Simultaneously, higher concentrations (not shown) and higher production rates (Figure 6-6B) of dissolved Fe(III) were observed at St. 6C than St. 6B, and rates tended to decrease with depth below the SWI at St. 6C while they remained constant with depth at St. 6B. Deeper on the upper-slope (St.7; 423 m water depth), Fe^{2+} production rates were generally higher and increased slightly with sediment depth below 7 cm (Figure 6-6A), while dissolved Fe(III) production rates were maximum at 7 cm and generally decreased deeper in the sediment (Figure 6-6B). Both Fe^{2+} and org-Fe(III) complexes formed small peaks between 4-10 cm with depth in the pore waters (Figure 6-3), whereas small concentrations of Fe^{2+} and $\sum H_2S$ and a broad but small org-Fe(III) signal was detected between 10-24 cm in St. 7 sediments. The highest rates of both Fe^{2+} and Fe(III) production were observed on the mid-shelf (St. 11; 665 m water depth), where rates of 4.6 ± 0.4 µM Fe^{2+} day^{-1} (Figure 6-6A) and 7.7 ± 0.3 µM Fe(III) day^{-1} (Figure 6-6B) were measured in the 5 cm of the sediment, but decreased to stabilize around 1.8 ± 0.1 µM Fe^{2+} day^{-1} and 2.2 ± 0.3 µM Fe(III) day^{-1} below 16 cm. The high rates in Fe^{2+} and dissolved Fe(III) production coincide with the high Fe^{2+} concentrations and org-Fe(III) current

intensities detected in the top 5 cm of the sediment and their disappearance below the onset depth of dissolved sulfide production at 4.5 cm (Figure 6-3).

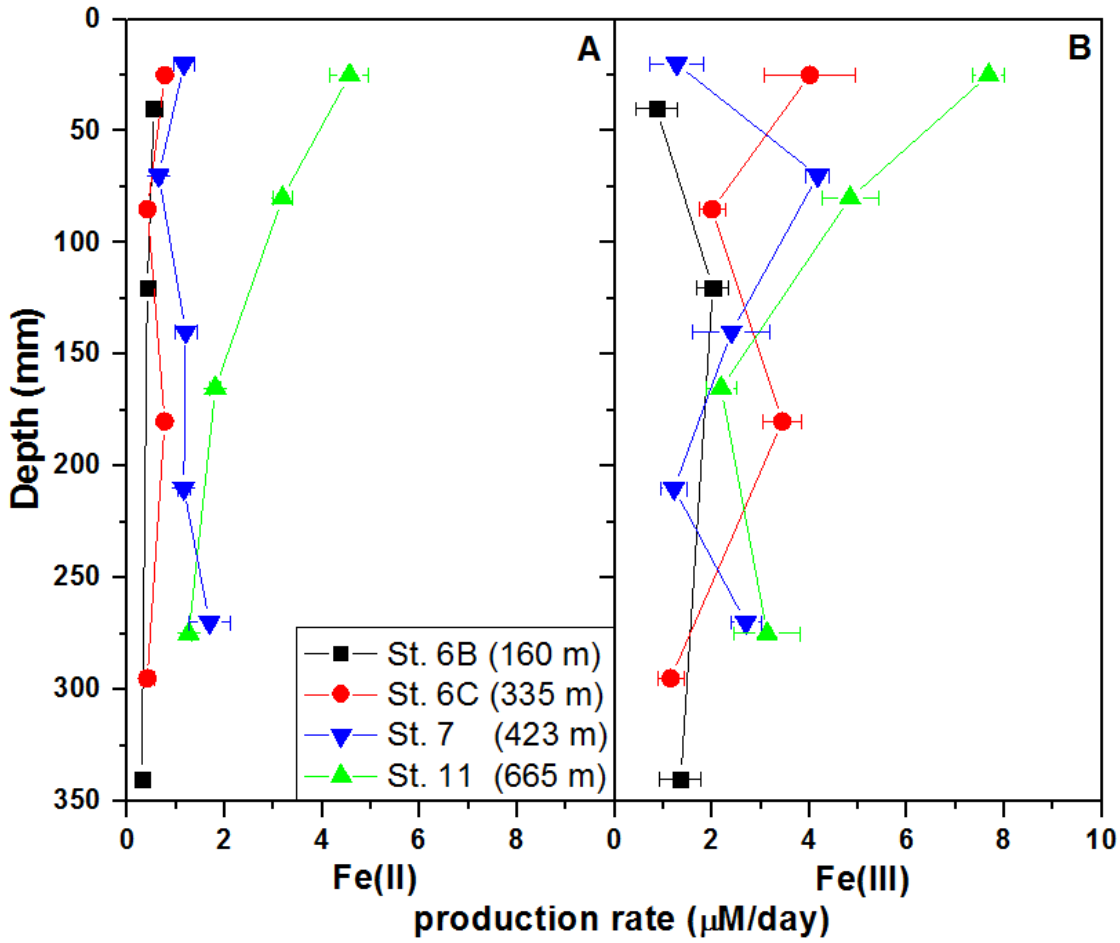

Figure 6-6 Depth distributions of (A) dissolved Fe^{2+} and (B) Fe(III) production rates determined from sediment slurry incubations. Error bars represent the standard deviation of the slope of regression lines of concentration vs. time for duplicate incubations.

6.5 Discussion

6.5.1 Continental Slopes as Zones of Intense Carbon Remineralization

The variations in diffusive fluxes (Figure 6-7) and depth-integrated concentrations (Figure 6-8) of all pore water species as a function of water column depth across Cape

Lookout's continental margin reflect the changes in carbon remineralization processes expected to occur in passive continental margins not exposed to significant riverine inputs or upwelling. DOU fluxes (Figure 6-7A), maximum diffusive fluxes (Figure 6-7B and C), and depth-integrated concentrations (Figure 6-8) of Fe^{2+}, org-Fe(III) complexes, $\sum H_2S$, and $\sum PO_4^{3-}$ all decreased from the coast to the shelf and upper-slope, then rebounded on the mid-slope and decreased again on the lower-slope. Simultaneously, reactive and crystalline Fe(III) oxide concentrations also increased in the top 20 cm of mid-slope sediments relative to continental shelf and lower-slope sediments (Figure 6-5). Finally, sediment slurry incubations demonstrated similar changes with water depth (Figure 6-6), as rates of both Fe^{2+} and Fe(III) production gradually increased from the shallow upper slope (St. 6B, 6C, and 7) to the mid-slope (St. 11). Based on these results and despite the fact that total organic carbon or sedimentation rates were not confirmed in this study, the mid-slope off Cape Lookout can be considered a depocenter where the influx of organic matter and terrigenous material increases aerobic and anaerobic respiration processes in these sediments compared to the continental shelf. Continental slopes as depocenters is not a novel observation. High concentrations of organic carbon have been observed in a number of continental slope sediments, including Cape Hatteras as well as to the north and south on the Carolina coast (Alperin et al., 2002; Blake et al., 1987; DeMaster et al., 1994; Milliman, 1994; Schaff T., 1992), across the mid-Atlantic Bight (Anderson et al., 1994; Walsh et al., 1988; Walsh et al., 1985), Bering Sea (Walsh et al., 1985), and Peru coast (Noffke et al., 2012; Walsh et al., 1985), the Oman margin of the Arabian Sea (Pedersen et al., 1992), the Washington coast (Carpenter, 1987), the Santa Catalina Basin (Smith et al., 1987), and near Monterey Bay (Murray and Kuivila, 1990), suggesting that all slopes

may represent organic carbon depocenters (Premuzic et al., 1982; Walsh et al., 1985). Indeed, low physical turbulence is typically observed in upper slope sediments (Csanady, 1990), and the high flux and accumulation of sediment on the mid-slope on the Mid-Atlantic Bight (Biscaye et al., 1988) and Carolina coast (DeMaster et al., 1994; Diaz et al., 1994) support the formation of these depocenters. Furthermore, incubations have demonstrated that microbial populations are growing at or near their maximum rates in mid-slope relative to continental shelf sediments, suggesting that these sediments are not nutrient limited (Kemp, 1994).

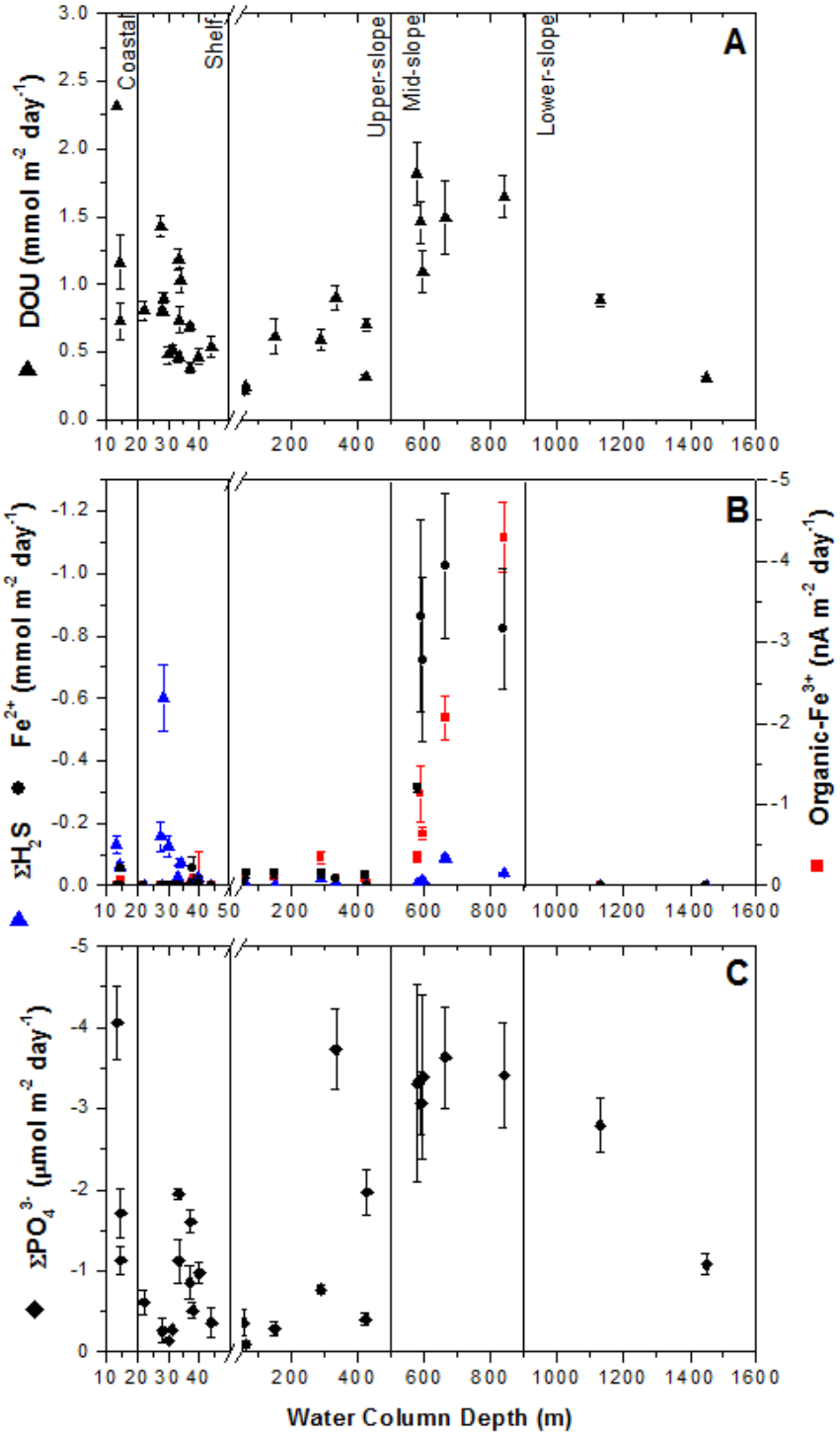

Figure 6-7 (A) Diffusive oxygen uptake (DOU), (B) Maximum diffusive fluxes of dissolved Fe^{2+}, org-Fe(III) complexes, and $\sum H_2S$, and (C) Maximum diffusive flux of

$\sum PO_4^{3-}$ with water column depth across the continental margin sediments of Cape Lookout (NC).

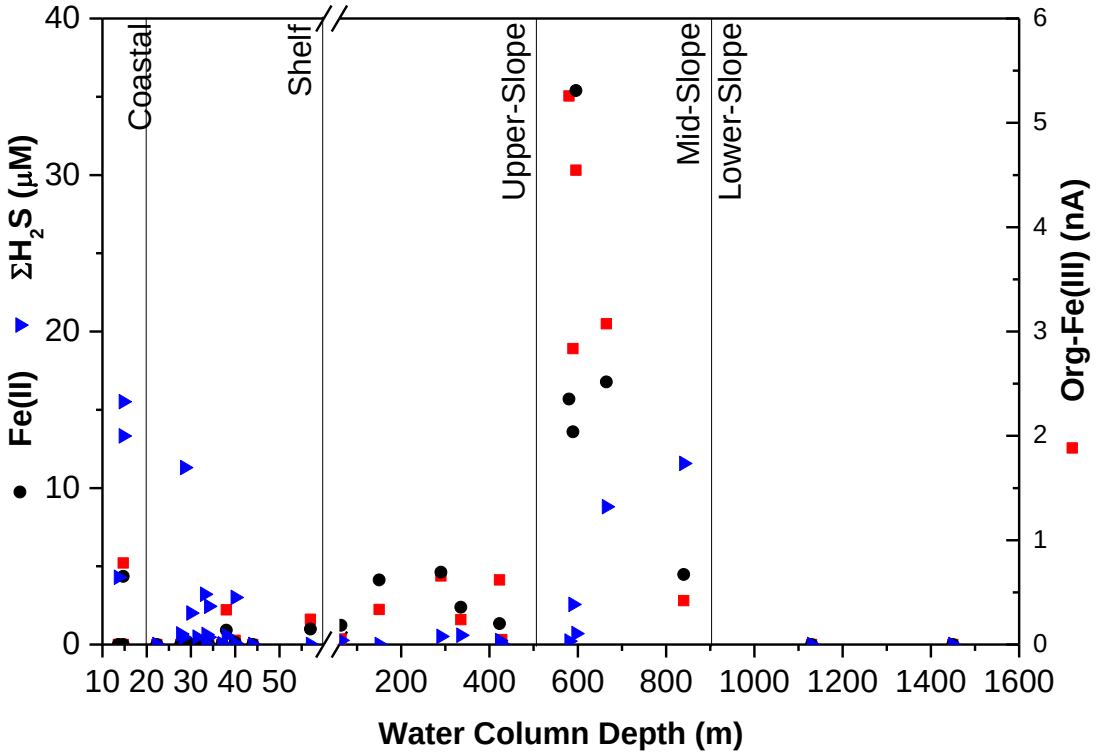

Figure 6-8 Whole core concentrations of dissolved Fe^{2+}, organic-Fe^{3+}, and $\sum H_2S$ with water column depth across the continental margin of Cape Lookout between 2010 and 2016. Whole core concentrations were obtained by integrating the mole content of each species as a function of depth and normalizing to the total volume of each sediment core.

6.5.2 Benthic Oxygen Consumption

Dissolved oxygen consumption in marine sediments may result from either aerobic respiration or re-oxidation of the reduced inorganic products of anaerobic respiration. Although the relative importance of these two processes towards DOU fluxes cannot be directly quantified, knowledge of the environment and the biogeochemical processes

occurring deeper in the sediment may provide insight into the main mechanism of oxygen consumption. The high DOU flux in the coastal zone and nearshore continental shelf (Figure 6-7A) was likely due to the relatively high input of natural organic matter and terrigenous material. In these sediments, dissolved O_2 is likely consumed via both aerobic respiration and re-oxidation of the reduced compounds produced by anaerobic respiration at depth. Indeed, at St. CL, realatively large concentrations of anaerobic respiration products were observed (Figure 6-3), including $FeS_{(aq)}$ species and $\sum H_2S$, indicating these sediments were dominated by microbial sulfate reduction (MSR) despite no significant changes in SO_4^{2-} profiles (Figure 6-4). Over the shelf, DOU generally decreased with water column depth as continental inputs dissipated, following previous observations of the decrease in sediment oxygen demand with water depth (Heip et al., 1995; Kemp et al., 1992). As shelf sediment became dominated by sand, decreased concentrations of dissolved anaerobic respiration products were detected (Figure 6-3) and a majority of O_2 consumption was likely due to aerobic respiration. Comparable concentrations of crystalline iron and low reactive Fe(III) oxides (Figure 6-5) likely contributed to the similar and relatively stable DOU over the upper-slope (Figure 6-7A), and increased onset depths of dissolved Fe^{2+} with distance from shore (Figure 6-3) indicate that O_2 consumption was entirely controlled by aerobic respiration. As the sediment shifted from sand to silt and clay on the mid-slope and both reactive and crystalline Fe(III) oxide concentrations increased (Figure 6-5), DOU increased simultaneously (Figure 6-7A). Detection of Fe^{2+} (Figure 6-3) directly below the OPD, points towards O_2 consumption linked to the reoxidation of reduced metabolites. Similar increases in oxygen demand have been observed in mid-slope sediments along the Mid-Atlantic Bight and attributed to lateral inputs of organic matter

from the much larger continental shelf to slope sediments (Anderson et al., 1994; Rowe et al., 1994), and discrepancies between O_2 consumption maxima and patterns of aerobic bacterial production were attributed to subsequent reoxidation of reduced metabolites produced by anaerobic processes deeper in the sediment (Kemp, 1994). Finally, the DOU flux decreased (Figure 6-7A) concomitantly with the reactive and crystalline Fe(III) oxide concentrations (Figure 6-5) on the lower-slope as expected based on numerous observations of decreased sediment oxygen demand on the continental rise and abyssal plain (Glud, 2008).

6.5.3 Benthic Iron Production

The benthic production of iron from continental shelves (Elrod et al., 2004; Noffke et al., 2012; Severmann et al., 2010) and its effect on the supply of iron to the water column (Bruland et al., 2001; Fitzwater et al., 2003; Johnson et al., 1999; Lohan and Bruland, 2008) have been mainly determined in upwelling zones and attributed either to a direct flux of Fe^{2+} in oxygen minimum zones, reoxidation and stabilization of iron under the form of dissolved Fe(III) complexes (Elrod et al., 2004; Lohan and Bruland, 2008; Noffke et al., 2012; Severmann et al., 2010), or the resuspension of particles (Bruland et al., 2001; Chase et al., 2005; Fitzwater et al., 2003; Johnson et al., 1999). Upwelling zone, however, are not representative of the majority of the oceans. In this study, the benthic production of dissolved iron and the biogeochemical processes responsible for this flux were examined in continental margin sediments with limited upwelling and sediment resuspension (Csanady and Hamilton, 1988; Janowitz and Pietrafesa, 1980; Pietrafesa et al., 1985). Although dissolved Fe^{2+} has been detected in sediment pore waters at water depths between 60 and 2000 m in zones of the Mid-Atlantic Bight, where sulfate reduction did not

contribute significantly to organic carbon remineralization, Fe^{2+} concentrations were not reported (Anderson et al., 1994). Similarly, production of dissolved iron has not been investigated on the Carolina coast (Alperin et al., 1999; Jahnke and Jahnke, 2000; Thomas et al., 2002). The millimeter resolution of pore water profiles collected in Cape Lookout continental margin sediments, backed up by diffusive flux calculations and whole core depth-integrated concentrations of pore water constituents demonstrate that dissolved iron is produced in these sediments and provides insight into the biogeochemical processes that regulate iron reduction and the potential release of iron across the SWI.

In the coastal zone, the diffusive ΣH_2S flux was greater than the Fe^{2+} flux (Figure 6-7B), though pore water profiles (Figure 6-3) and depth-integrated concentrations (Figure 6-8) demonstrate that both Fe^{2+} and org-Fe(III) complexes were produced in these sediments. Org-Fe(III) complexes are rapidly reduced by dissolved sulfide(Taillefert et al., 2000a), and may be formed either by abiotic oxidation of Fe^{2+} by dissolved O_2 (Taillefert et al., 2000a), aerobic Fe-oxidizing bacteria in the presence of organic ligands (Roden et al., 2004; Sobolev and Roden, 2001), abiotic oxidation of complexed Fe(II) by Fe(III) (Beckler et al., 2015; Luther et al., 1992), or production during dissimilatory iron reduction (DIR) (Beckler et al., 2015; Fennessey et al., 2010; Jones et al., 2010; Nevin and Lovley, 2002; Taillefert et al., 2007a). Production of soluble org-Fe(III) complexes at much deeper depths than the OPD indicates that these species likely did not form via aerobic processes. However, it is difficult to determine if they were produced microbially or via chemical oxidation of complexed Fe(II). Detection of FeS_{aq} and $\sum H_2S$ below Fe^{2+} in coastal zone sediments (St. CL, Figure 6-3) points towards abiotic reduction of Fe(III) oxides by $\sum H_2S$. Simultaneouly, the production of soluble org-Fe(III) complexes above Fe^{2+} (St. CL, Figure

6-3) suggests formation of soluble org-Fe(III) as complexed Fe(II) diffused upwards and was oxidized.

Although similar ΣH_2S fluxes (Figure 6-7B) and depth-integrated concentrations (Figure 6-8) were observed on the shallow shelf and in the coastal zone, ΣH_2S fluxes and depth-integrated ΣH_2S concentrations decreased toward the upper-slope where only small concentrations of ΣH_2S were detected. As Fe^{2+} or org-Fe(III) complexes were not detected in the shallow shelf pore waters besides St. 4 (Figure 6-3), MSR appears to be the main anaerobic respiration process on the continental shelf. Based on DOU fluxes (Figure 6-7A), anaerobic respiration was expected to be lower in upper-slope compared to shelf sediments. Indeed, the generally low production rates of dissolved Fe^{2+} and Fe(III) in the slurry incubations with sediments from St. 6B, 6C, and 7 (Figure 6-6) indicate reduced microbial activity in these sandy sediments. Although Fe^{2+} and org-Fe(III) fluxes (Figure 6-7B) and depth-integrated concentrations (Figure 6-8) were higher in upper-slope than shelf sediments, their values remained relatively low. Despite their low concentrations, both Fe^{2+} and org-Fe(III) complexes were detected at similar depths in the sediment of these three stations (Figure 6-3), suggesting that org-Fe(III) complexes were formed during DIR rather than as a result of Fe^{2+} oxidation. Increased concentrations (Figure 6-4) and diffusive flux (Figure 6-7C) of ΣPO_4^{3-} with water depth over the upper-slope point towards increased reduction of iron oxides (Anschutz et al., 1998; Rozan et al., 2002). In addition, no significant changes in SO_4^{2-} or DIC concentrations with depth (Figure 6-4) and low or lack of ΣH_2S and FeS_{aq} (Figure 6-3) suggest that MSR was limited in these sediments. To compare with diffusive fluxes at the same station, depth-integrated rates of Fe^{2+} and Fe(III) production were calculated in sediment incubations closest to the SWI (Table 6-2). Depth-

integrated rates cannot be directly compared to diffusive org-Fe(III) fluxes as org-Fe(III) cannot be quantified. However, both the depth-integrated rates of Fe^{2+} and Fe(III) and diffusive fluxes of Fe^{2+} and org-Fe(III) generally increased with water column depth and similar values were found between Fe^{2+} depth-integrated rates and diffusive fluxes at upper-slope stations (St. 6B, 6C, 7). Additionally, the depth-integrated rates of Fe(III) suggest that complexation by organic ligands may stabilize iron in these sediments.

Table 6-2 Maximum diffusive fluxes and depth-integrated rates in the top section of sediment incubated from stations on the upper and mid-slope.

		Fe^{2+}		*Fe(III)*	
Station	*Depth (m)*	*Maximum diffusive flux (mmol m^{-2} day^{-1})*	*Depth-integrated rate (mmol m^{-2} day^{-1})*	*Maximum diffusive flux (nA m^{-2} day^{-1})*	*Depth-integrated rate (mmol m^{-2} day^{-1})*
6B	150	-0.030 ± 0.01	0.017 ± 0.0003	-0.083 ± 0.03	0.028 ± 0.0009
6C	335	-0.028 ± 0.01	0.017± 0.0002	-0.095 ± 0.02	0.090 ± 0.004
7	423	-0.045 ± 0.02	0.021± 0.0002	-0.140 ± 0.06	0.023 ± 0.0005
11	665	-1.02 ± 0.2	0.160± 0.005	-2.07 ± 0.3	0.269 ± 0.004

Diffusive fluxes (Figure 6-7B) and depth-integrated concentrations (Figure 6-8) of Fe^{2+} and org-Fe(III) in mid-slope sediments were the highest on the continental margin. Although diffusive fluxes of $\sum H_2S$ were lower than Fe^{2+} fluxes on the mid-slope and $\sum H_2S$ fluxes in the coastal zone or inner-shelf (Figure 6-7B), depth-integrated $\sum H_2S$ concentrations at depths greater than 650 m were similar to the coastal zone and inner shelf (Figure 6-8). Both Fe^{2+} and $\sum H_2S$ diffusive fluxes peaked at St. 11 (665 m), whereas org-Fe(III) fluxes continued to increase with water depth over the mid-slope (Figure 6-7B). These measurements differed slightly from the depth-integrated concentrations, which showed peaks in Fe^{2+} and org-Fe(III) concentrations around 600 m and an increase in $\sum H_2S$

concentrations with depth (Figure 6-8). Again, the lack of $FeS_{(aq)}$, the relatively low $\sum H_2S$ concentrations (<25 µM) in the depth profiles (Figure 6-3), and the small changes in SO_4^{2-} and DIC concentrations with depth (Figure 6-4) indicate that MSR was not dominant in these mid-slope sediments. In turn, ΣPO_4^{3-} increased with sediment depth at both St. 5 and 11 (Figure 6-4), and the highest diffusive ΣPO_4^{3-} fluxes were detected on the mid-slope (Figure 6-7C), confirming increased rates of anaerobic respiration. The simultaneous production of both Fe^{2+} and org-Fe(III) directly below the OPD (9-12 mm) suggests active DIR in the first 15 to 60 mm of the mid-slope sediments (Figure 6-3), but the sharp decrease in Fe^{2+} and org-Fe(III) below 60 mm at St. 5, 40 mm at St. 11, and 15 mm at St. 13 indicate that MSR migrated upward in the sediment column and progressively compressed the DIR zone below the sediment-water interface as water column depth increased. This compression of the DIR zone may have increased the upward organic-Fe(III) flux as a function of water depth on the mid-slope (Figure 6-7B). These processes were likely more evident than in the upper-slope due to the increased accumulation of both organic carbon and iron oxides (Figure 6-5) on the mid-slope. Incubations of St. 11 sediments confirm increased production of both dissolved Fe^{2+} and Fe(III) in the upper sediment of the mid-slope (Figure 6-6). Unlike the upper-slope, however, Fe^{2+} depth-integrated rates were an order of magnitude lower than the diffusive fluxes (Table 6-2). Although no changes in sulfate were observed in the incubations, the differences between depth-integrated rates and diffusive fluxes could be due to precipitation of Fe^{2+} with sulfide and may be promoted on the mid-slope depocenter due to the increased organic matter available for anaerobic respiration. However, depth-integrated rates of Fe(III) production larger than Fe^{2+} suggest that even with increased removal of Fe^{2+} by sulfide, significant amounts of Fe(III) may be

stabilized by organic complexation. Thus, depth-integrated rates determined from incubations may represent lower limits of mid-slope iron production. Although previous studies observed a significant decrease in SO_4^{2-} concentrations with sediment depth along the mid-slope of Cape Hatteras, MSR was not significant in the top 50 cm of sediment in continental shelf, upper slope, and deeper water depths (Alperin et al., 1999; Jahnke and Jahnke, 2000; Thomas et al., 2002). Similarly, MSR was not significant in the top 30 cm of sediment at mid-slope stations of Cape Lookout and Cape Fear (DeMaster et al., 1994; Schaff T., 1992), supporting the results of this study.

6.5.4 Global Significance of Iron Production from Continental Margin Sediments

Although maximum diffusive fluxes were calculated for all stations where dissolved species were detected regardless of the onset depth in the sediment, diffusive fluxes of Fe^{2+} and org-Fe(III) into the oxic zone (as determined by the OPD) could only be quantified on the mid-slope (Table 6-3). Diffusive fluxes into the oxic zone of -0.82 ± 0.2 to -0.89 ± 0.2 mmol Fe^{2+} m^{-2} day^{-1} and -4.29 ± 0.4 to -1.38 ± 0.6 nA org-Fe(III) m^{-2} day^{-1} were observed at St. 11 (665 m) and St. 13 (840 m). Benthic Fe^{2+} fluxes of the same order of magnitude have previously been observed between 638-905 m up to -0.289 mmol Fe^{2+} m^{-2} day^{-1} (Elrod et al., 2004) and as high as -0.568 mmol Fe^{2+} m^{-2} day^{-1} at 900 m water depth (Severmann et al., 2010) in oxygen minimum zones along the California coast. Increased benthic Fe^{2+} production was not observed on the Peruvian coast at similar water column depths even though the reactive iron content was significant, indicating that bottom water O_2 concentrations control benthic Fe^{2+} fluxes (Noffke et al., 2012). The negative correlation between bottom O_2 concentrations and benthic dissolved Fe fluxes in upwelling zones is well known (Dale et al., 2015) and suggests that the Fe^{2+} diffusive flux should be maximum

at low DOU fluxes. In contrast, DOU fluxes in the present study varied concomitantly with maximum diffusive fluxes of Fe^{2+} across the continental margin (Figure 6-7A,B), suggesting that this negative relationship does not necessarily apply to fully oxygenated bottom waters not exposed to upwelling. In these conditions, diffusive Fe^{2+} fluxes provide insight into the mechanism of O_2 consumption in the sediment rather than indicating dependence on bottom water O_2 concentrations. More importantly, the detection of an org-Fe(III) diffusive flux into the oxic zone on the mid-slope indicates that slope sediments may contribute substantial amounts of bioavailable iron to the ocean even in completely oxic bottom waters.

Table 6-3 Comparison of maximum diffusive fluxes and fluxes into the oxic zone of Fe^{2+} and organic-Fe(III) complexes at all mid-slope stations. For comparison, maximum dissolved sulfide fluxes are also provided. Fluxes of Fe^{2+} and $\sum H_2S$ are in mmol m^{-2} day^{-1}, whereas org-Fe(III) flux is in nA m^{-2} day^{-1}.

	Depth	*Maximum diffusive flux*			*Flux into oxic zone*	
Station	*(m)*	*Fe^{2+}*	*Org-Fe(III)*	*ΣH_2S*	*Fe^{2+}*	*Org-Fe(III)*
12	580	-0.31 ± 0.01	-0.35 ± 0.07	-0.0025 ± 0.0004	0	0
5	589	-0.86 ± 0.3	-1.13 ± 0.4	-0.0098 ± 0.002	-0.49 ± 0.05	-1.13 ± 0.4
10	596	-0.72 ± 0.3	-0.63 ± 0.08	-0.017± 0.003	-0.72 ± 0.3	0
11	665	-1.02 ± 0.2	-2.07 ± 0.3	-0.087 ± 0.01	-0.89 ± 0.2	-1.38 ± 0.6
13	840	-0.82 ± 0.2	-4.29 ± 0.4	-0.039 ± 0.004	-0.82 ± 0.2	-4.29 ± 0.4

Dissolved iron input of 8.9 x 10^{10} mol yr^{-1} based on a mean shelf flux of 4.3 µmol Fe^{2+} m^{-2} day^{-1} extrapolated over the global shelf area (Elrod et al., 2004) has been widely used in biogeochemical models (Moore et al., 2004; Muglia et al., 2017; Raiswell et al., 2006), however iron input from continental slopes has been mostly overlooked. Based on the Cape Lookout slope transect (Figure 6-1), mid-slope depocenters compose approximately 12% (3.9 x 10^{12} m^2) of continental slope area (3.25 x 10^{13} m^2 (Walsh,

1989)). Extrapolation of benthic Fe^{2+} fluxes determined on the California slope (-0.289 mmol m^{-2} day^{-1} (Elrod et al., 2004), -0.568 mmol m^{-2} day^{-1} (Severmann et al., 2010) over the area of slope depocenters results in a global Fe^{2+} input of 4.1 – 8.1 x 10^{11} mol yr^{-1}. Extrapolation of the average diffusive flux of Fe^{2+} into the oxic zone determined on the mid-slope of the Cape Lookout depocenter (-0.731 ± 0.2 mmol Fe^{2+} m^{-2} day^{-1}) and the depth-integrated rate determined from the mid-slope sediment incubations (0.16 mmol Fe^{2+} m^{-2} day^{-1}) over the total surface area of slope depocenters around the globe, translates into a dissolved Fe^{2+} input to the overlying waters ranging between 2.3 – 10.4 x 10^{11} mol yr^{-1}. These integrated rates fall near the range of estimates calculated from the California and Oregon slope (Elrod et al., 2004; Severmann et al., 2010). Recent global estimates, which are unable to capture the extreme fluxes observed in mid-shelf sediments, report input from total slope sediments of just 0.37 x 10^{11} mol yr^{-1} (Dale et al., 2015). Although much of the Fe^{2+} may be rapidly oxidized at the SWI, extrapolation of depth-integrated rates of dissolved Fe(III) determined in the incubations provide insight into the amount of bioavailable Fe(III) produced in these sediments. A depth-integrated rate of 0.27 mmol Fe(III) m^{-2} day^{-1} was determined from the Cape Lookout mid-slope sediments (St. 11), resulting in an overall input of 3.8 x 10^{11} mol yr^{-1} to the global ocean. These global inputs of Fe^{2+} and dissolved Fe(III) from slope sediments rival global estimates of iron inputs derived from aerosols (1-6 x 10^{11} mol Fe yr^{-1} (Fung et al., 2000; Jickells, 2001)), rivers (1.5-26 x 10^{9} mol Fe yr^{-1} (Martin and Meybeck, 1979; Poulton and Raiswell, 2002)), and hydrothermal vents (0.9 x 10^{9} mol Fe yr^{-1} (Tagliabue et al., 2010)). Clearly slope depocenters from passive continental margins clearly contribute considerably to the iron

inventory of the ocean, and benthic flux of dissolved Fe should be determined in these environments.

6.6 Conclusion

In this study, the diffusive flux of iron and its speciation in the sediment was determined along a transect across the continental shelf and slope near Cape Lookout, North Carolina to investigate the potential for passive continental margin sediments without large upwelling events or riverine input to provide dissolved iron to the ocean. High diffusive fluxes of both dissolved Fe^{2+} and org-Fe(III) complexes over the mid-slope, backed up by increased depth-integrated rates of dissolved Fe^{2+} and Fe(III) determined from sediment incubations, demonstrate that mid-slope depocenters may just represent as important sources of iron to the oceans as shelf sediments, aerosols, rivers, or hydrothermal vents. The production of dissolved Fe(III) is likely regulated by a combination of aerobic oxidation in the presence of natural organic ligands near the sediment-water interface, DIR deep in the sediments, or chemical oxidation of Fe(II) complexed to natural organic ligands across the sediment column. Although the diffusive flux of iron may be controlled by MSR, which reduces and immobilize iron rapidly, MSR in mid-slope depocenters does not appear to affect the iron flux significantly. Extrapolation of the sedimentary flux from the Cape Lookout mid-slope depocenter to the global ocean indicates that this iron flux rival global estimates of iron inputs derived from aerosols, rivers, and hydrothermal vents. These findings demonstrate that passive margins that are generally overlooked in global estimates generate a significant flux of iron to the overlying waters.

CHAPTER 7. BENTHIC ALKALINITY FLUXES IN THE RHONE RIVER PRODELTA GENERATED BY DECOUPLED AEROBIC AND ANAEROBIC PROCESSES

This manuscript, authored by Jens Rassmann[1,2]*, Eryn Eitel[3]*, Cecile Cathalot[4], Christophe Brandily[4], Martial Taillefert[3], and Christophe Rabouille[1] entitled "Benthic Alkalinity Fluxes in the Rhone River Prodelta Generated by Decoupled Aerobic and Anaerobic Processes" is currently under revisions in *Marine Chemistry*. *co-first author contributions.

[1] Laboratoire des Sciences du Climat et de l'Environnement, LSCE/IPSL, CEA-CNRS-UVSQ-Université Paris Saclay, Gif-sur-Yvette, 91198, France
[2] Université de Liège, ULG, 4000 Liège, Belgium
[3] School of Earth and Atmospheric Sciences; Georgia Institute of Technology, GA 30332 Atlanta, USA
[4] IFREMER, Laboratoire Environnement Profond, 29280 Plouzané, France

7.1 Abstract

Estuarine regions are generally considered a net source of atmospheric CO_2 due to the high rates organic carbon mineralization in sediments. Although both aerobic and anaerobic benthic mineralization pathways produce dissolved inorganic carbon (DIC), only anaerobic processes lead to significant alkalinity production in sediments. This alkalinity may buffer the acidity generated by respiration processes in the sediments and oceanic CO_2 uptake on long time scales. In contrast to DIC, however, alkalinity may be consumed within the sediments by a variety of oxidation reactions. In this study, a benthic chamber was

deployed in the Rhône River prodelta (NW Mediterranean) to assess the fluxes of DIC and alkalinity from the sediment. At the same stations, *in situ* microprofiles of O_2 were recorded to quantify dissolved oxygen uptake (DOU) and sediment cores were taken to identify the main biogeochemical processes controlling the net production of alkalinity in these sediments. DIC and alkalinity fluxes were up to 8 times higher than DOU close to the river mouth but decreased in intensity offshore. Sediment pore water profiles indicated that the majority of the total alkalinity and DIC was produced by sulfate and iron reduction. Despite the complete removal of sulfate from the pore waters, dissolved sulfide concentrations were rather low due to the precipitation and burial of iron sulfide minerals while soluble organic-Fe(III) complexes were simultaneously found throughout the sediment column. The presence of organic-Fe(III) complexes together with low sulfide concentrations and high sulfate consumption suggests a highly dynamic system driven by the input of organic and inorganic riverine particles. By preventing reduced substances from being reoxidized, the precipitation and burial of iron sulfide decouples the iron and sulfur cycles from oxygen, therefore allowing a flux of alkalinity out of the sediments. In these conditions, sediments provide a source of alkalinity to the bottom waters which, may enhance the buffering capacity of coastal waters.

7.2 Introduction

As a link between continental and marine environments, continental shelf regions play a key role in the global carbon cycle (Bauer et al., 2013). Particularly large fluxes of dissolved and particulate organic carbon are delivered by rivers to their neighboring continental shelves (Bianchi et al., 2009). In fact, even though the surface area of shelf regions occupies around 7 % of the global ocean (Jahnke in Liu et al., 2010), more than

40 % of organic carbon burial in the oceans occurs in shelf regions, of which about half is buried in river deltas and estuarine regions (Hedges and Keil, 1995; McKee et al., 2004; Müller-Krager et al., 2005; Chen and Borges, 2009). These environments are typically shallow, such that the amount of natural organic carbon that settles to the sea floor leads to high organic carbon content in the sediments and thus enhanced mineralization rates (Andersson et al., 2012). The chemical fluxes across the sediment-water interface (SWI) related to this enhanced mineralization allow estuarine regions to constitute a net source of CO_2 to the atmosphere, whereas shelf regions typically represent a sink (Chen and Borges, 2009; Cai, 2011; Bauer et al., 2013)

High sedimentation rates of material containing large concentrations of organic carbon increase the relative contribution of the anaerobic degradation of organic carbon compared to its aerobic degradation (Canfield et al., 1993) as the residence time of organic carbon in the oxic sediment layer decreases (Hartnett et al., 1998). Anaerobic respiration processes, including denitrification, iron reduction, manganese reduction, and sulfate reduction, create total alkalinity (Berner, 1970; Dickson, 1981; Wolf-Gladrow et al., 2007) which increases the buffer capacity of pore waters (Ben Yaakov, 1973; Soetaert et al., 2007) and may potentially be transferred across the SWI to bottom waters (Krumins et al., 2013; Brenner et al., 2016). The alkalinity release from the sediments could influence the coastal carbon cycle by increasing the CO_2 uptake capacity of seawater over long time scales (Thomas et al., 2009; Andersson et al., 2012; Brenner et al., 2016).

Sulfate reduction typically represents a major pathway of organic carbon mineralization in organic rich sediments as two moles of carbon are oxidized by one mole of sulfate by this process (Canfield et al., 1993; Burdige et al., 2011).

$$2CH_2O + SO_4^{2-} \rightarrow 2HCO_3^- + H_2S \quad (7\text{-}1)$$

Sulfate reduction creates 2 moles of dissolved inorganic carbon (DIC) and total alkalinity (TA) per mole of sulfate reduced, or alkalinity to dissolved inorganic carbon stoichiometric ratio (r_{AD}) of 1. If sulfate is used for the anaerobic oxidation of methane (AOM):

$$CH_4 + SO_4^{2-} + H^+ \rightarrow HCO_3^- + H_2S + H_2O \quad (7\text{-}2)$$

the r_{AD} ratio increases to 2:1 (Soetaert et al., 2007). Dissimilatory iron reduction (Eq. 7-3):

$$\frac{1}{4}CH_2O + Fe(OH)_3 + \frac{7}{4}H^+ \rightarrow \frac{1}{4}HCO_3^- + Fe^{2+} + \frac{5}{2}H_2O \quad (7\text{-}3)$$

produces ¼ moles of HCO_3^- and consumes 7/4 moles of H^+ per mole of Fe, leading to a r_{AD} ratio of 8 (+8/4 moles TA and +1/4 moles DIC), whereas manganese reduction (Eq. 7-4):

$$\frac{1}{2}CH_2O + MnO_2 + \frac{3}{2}H^+ \rightarrow \frac{1}{2}HCO_3^- + Mn^{2+} + H_2O \quad (7\text{-}4)$$

produces 1/2 moles of HCO_3^- per mole of Mn with a consumption of 3/2 moles of H^+, leading to a r_{AD} ratio of 4 (+4/2 moles TA and +1/2 moles DIC). These three processes also produce 2 TA per mole of terminal electron acceptor (SO_4^{2-}, $Fe(OH)_3$, MnO_2).

These reactions contribute to the alkalinity increase in sediment pore waters, drive the carbonate saturation state of the pore waters towards oversaturation, and potentially trigger carbonate precipitation (Gaillard et al., 1989; Mucci et al., 2000; Jørgensen and Kasten, 2006; Soetaert et al., 2007; Burdige et al., 2011). The precipitation of carbonate species, such as calcite and aragonite, and reduced iron and sulfur metabolites consume alkalinity within the sediments (Berner, 1970; Soetaert et al., 2007; Krumins et al., 2013;

Brenner et al., 2016). In addition, the aerobic reoxidation of reduced species such as NH_4^+, Fe^{2+}, Mn^{2+} and HS^-, close to the SWI consumes the alkalinity produced anaerobically (Jourabchi et al., 2005; Krumins et al., 2013; Brenner et al., 2016). Thus, the net alkalinity transferred across the SWI depends on the type and intensity of respiration rates and whether reduced species are reoxidized by dissolved oxygen after diffusion upwards or trapped in anaerobic sediment layers by precipitation (Krumins et al., 2013).

To characterize the biogeochemical conditions in which sediments provide an alkalinity source to coastal waters, it is crucial to relate this reaction network to net benthic fluxes of alkalinity and DIC measured *in situ*. The objective of this study was to investigate if sediments from deltaic regions exposed to large riverine inputs of carbon and minerals represent an alkalinity source to the bottom waters and to investigate the processes underlying these sources of alkalinity.

7.3 Study Site and Methods

7.3.1 The Rhone River Prodelta

With a mean water discharge of 1700 $m^3\ s^{-1}$, the Rhône River is the main source of freshwater and land-derived particles for the Mediterranean Sea (Sempere et al., ,2000). The Rhône River prodelta is a wave-dominated microtidal environment, located in the Gulf of Lions. The river plume is generally oriented southwestward due to the combined effects of wind forcing and the Coriolis force Estournel et al., 1997). Based on bathymetry and sedimentation rates, the Rhône River prodelta can be divided into three main areas (Got et al., 1990): the proximal domain within a 2 km radius of the river outlet and with water depths between 10 and 20 m; the prodelta domain between 2 and 5 km with water depths

ranging from 30 to 70 m; and the distal domain further offshore with water depths greater than 70 m. The sediments of the three domains are characterized by a strong biogeochemical gradient from the Rhône River mouth to the Gulf of Lions continental slope (Lansard et al., 2009).

Most of the riverine particles settle in the vicinity of the river mouth leading to sedimentation rates up to 30-48 cm yr^{-1} (Charmasson et al., 1988), including about 80 % of the particles deposited during flood events (Cathalot et al., 2010). Thus, sediments from the proximal domain are dominated by the periodic accumulation of terrestrial organic-rich particles (Radakovich and Heussner, 1999; Roussiez et al., 2005). Offshore, sedimentation rates decrease and reach typical values for shelf regions (distal domain) below 0.1 cm yr^{-1} (Miralles et al., 2005). The total organic carbon content of the sediment is higher than 2 % close to the river mouth and decreases offshore (Lansard et al., 2008). The sedimentary inorganic carbon content is about 28 to 38 % (Roussiez et al., 2005) and is mostly composed of calcite and magnesium calcite Rassmann et al., 2016). Sediment respiration rates are high in the proximal domain and decrease offshore (Lansard et al., 2009; Pastor et al., 2011; Cathalot et al., 2013; Rassmann et al., 2016). Sediments of the Rhône River delta are characterized by strong anaerobic buildup of DIC and alkalinity (Rassmann et al., 2016), but whether this alkalinity is consumed in the oxic sediment layer or released to the bottom waters has yet to be determined. The AMOR-B-Flux cruise took place onboard the RV Tethys II in September 2015, a windy period with potentially high mixing and surface sediment resuspension events. Stations were located in the river plume along a nearshore - offshore gradient (Figure 7-1, Table 7-1).

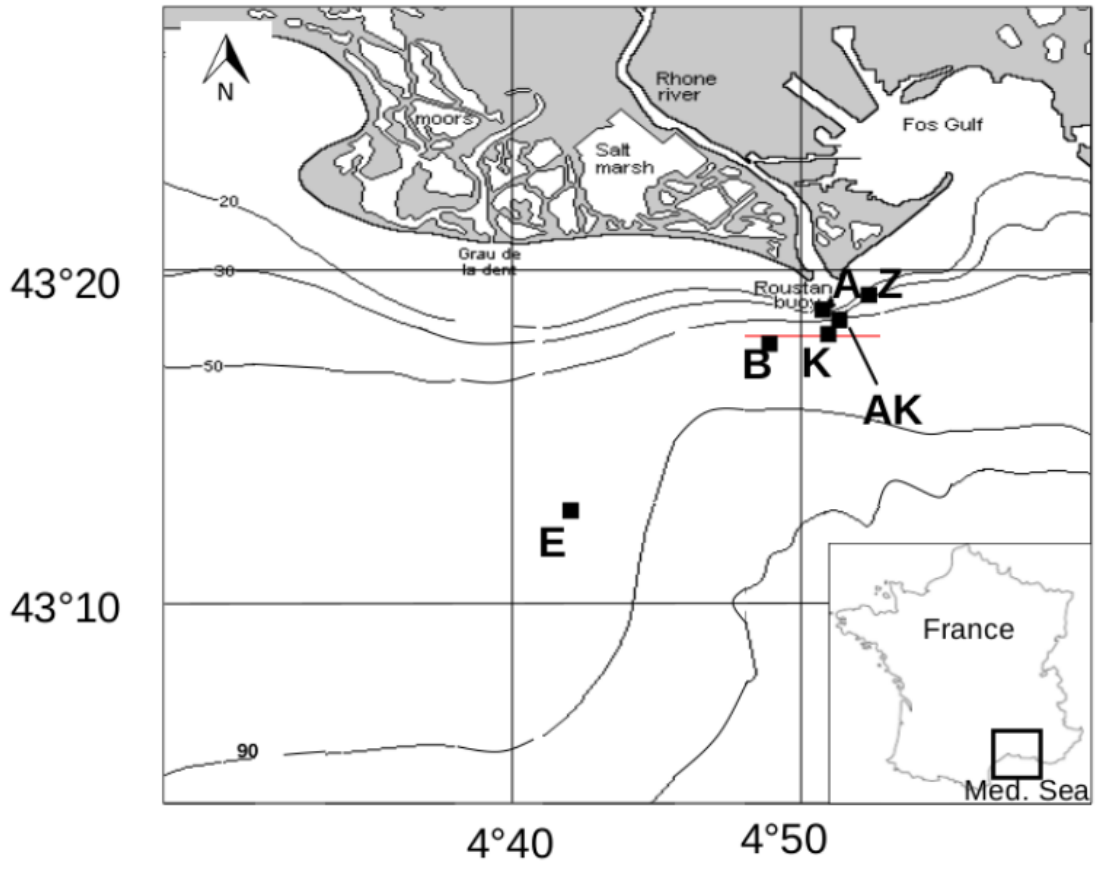

Figure 7-1 Map of the Rhône River prodelta with the stations investigated during the AMOR-B-Flux cruise in September 2015

Table 7-1 Sampling sites during the AMOR-B-Flux cruise in September 2015 and main characteristics of bottom waters, dist. = distance to the Rhône River mouth.; ω = sedimentation rate. Station Z was sampled twice in order to investigate temporal variability.

Domain	Proximal			Prodelta			Distal
Stations	A	Z(08.09.15)	Z'(14.09.15)	AK	B	K	E
Long. °E	4.850	4.868	4.868	4.853	4.833	4.858	4.684
Lat. °N	43.311	43.318	43.318	43.307	43.305	43.301	43.220
dist. [km]	2.1	2.2	2.2	2.8	3.0	3.3	14.3
Depth [m]	20.0	20.0	20.0	42.0	50.0	58.0	72.5
T [°C]	16.3	19.6	14.7	16.2	20.6	14.7	14.3
Salinity	37.5	37.6	37.7	37.7	38.0	37.7	37.8
O_2 [μM]	253.1 ± 0.3	249.5 ± 0.3	242.6±0.2	250.2 ± 0.1	n.d.	241.8 ± 0.2	221.5 ± 0.3
DIC [mM]	2.292 ± 0.002	2.308 ± 0.004	n.d.	2.281 ± 0.003	2.267 ± 0.002	2.307 ± 0.001	2.328 ± 0.003
TA [mM]	2.606 ± 0.022	2.599 ± 0.002	n.d.	2.598 ± 0.015	2.598 ± 0.003	2.596 ± 0.015	2.607 ± 0.007
pH_T	8.079 ± 0.007	8.057 ± 0.004	8.085 ± 0.003	8.089 ± 0.007	8.066 ± 0.005	8.075 ± 0.005	8.048 ± 0.006
mean porosity	0.69 ± 0.04	0.65 ± 0.04	0.65 ± 0.04	0.68 ± 0.02	0.66 ± 0.03	0.65 ± 0.05	0.64 ± 0.04
ω [cm yr^{-1}]	30 to 40 (Charmasson et al., 1998)			1 to 4(Lansard et al., 2009)			0.1 to 1 (Miralles et al., 2005)

7.3.2 In Situ Benthic Chamber Deployments

Benthic fluxes and sediment depth profiles of the main redox species involved in the remineralization of organic carbon were determined with an autonomous benthic lander (Jahnke et al., 1989). The lander was equipped with a benthic chamber, water syringe sampling system, and retrofitted with a programmable, battery-powered *in situ* electrochemical analyzer from Analytical Instrument Systems, Inc. (AIS, Inc.) and a SUBMAN-1 *in situ* micromanipulator (AIS, Inc.) to simultaneously obtain depth profiles of redox chemical species with mercury/gold (Hg/Au) amalgam voltammetric microelectrodes (Brendel et al., 1995; Tercier-Waeber and Taillefert, 2008). The chamber encloses 30 x 30 cm of sediment surface with a certain volume of overlying water determined by measuring the concentration of two injected tracers (iodide and bromide) after each deployment. Homogenization of the overlying water was assured with a stirrer integrated in the chamber lid. The collected water samples were analyzed for alkalinity and DIC concentrations. The concentrations changed linearly with time and benthic fluxes across the SWI were calculated from the slopes of these concentration-time-plots and the chamber volume.

7.3.3 In Situ Microprofiling of Dissolved Oxygen

A separate benthic lander, carrying a benthic microprofiler (Unisense), was deployed to measure *in situ* microprofiles of dissolved oxygen (Cai and Reimers, 1993; Rabouille et al., 2003) using Clark type gold electrodes with integrated Ag/AgCl reference. Up to five oxygen microelectrodes were simultaneously deployed, and vertical depth profiles were measured with a 200 μm resolution. As their response to variations in oxygen

concentrations is linear, the microelectrodes were calibrated with a two-point calibration technique using the bottom water O_2 concentration determined by Winkler titration and the anoxic pore waters. Signal drift during profiling was checked to be less than 5 %.

7.3.4 Sediment Sampling and Ex Situ Analysis

At each sampling station, sediment cores were collected using an UWITEC® single corer (length 60 cm, inner diameter 9 cm) within 30 m from the site where the landers were deployed and processed within 30 minutes after collection. Sub cores were collected at station A, Z and AK and stored in a saturated $HgCl_2$ solution for methane analysis.

Ex situ voltammetric profiles were obtained with a a DLK-70 potentiostat (AIS, Inc.) in a three electrode configuration, including Hg/Au amalgam working microelectrode constructed from Pyrex glass pulled to a tip of 0.4 mm diameter to minimize particle entrainment during the profiles, a Ag/AgCl reference electrode, and a platinum counter electrode. The Hg/Au voltammetric electrode was deployed in the sediment using a DLK MAN-1 micromanipulator (AIS, Inc). Using a combination of linear sweep and anodic and cathodic square wave voltammetry, Hg/Au voltammetric microelectrodes are able to simultaneous quantify dissolved O2, Mn^{2+}, Fe^{2+}, total dissolved sulfide ($\Sigma H_2S = H_2S + HS^- + S^0 + S_x^{2-}$), as well as organic complexes of Fe(III) (org-Fe(III)) and iron sulfide clusters (FeS_{aq}), which are not quantifiable but reported in normalized current intensities (Tercier-Waeber and Taillefert, 2008). Hg/Au microelectrodes were calibrated for dissolved O_2 *in situ* using temperature and salinity of the overlying water to determine the O_2 concentrations at saturation (Luther et al., 2008). Hg/Au microelectrodes were also calibrated externally with $MnCl_2$ to quantify all other species according to the pilot ion method (Brendel et al., 1995). All voltammetric data was integrated using VOLTINT, a

semiautomated Matlab® script with peak recognition software (Bristow and Taillefert, 2008).

Sediment porosity profiles were determined by slicing one of the cores with a 2 mm resolution until 10 mm depth, a 5 mm resolution until 60 mm and a 10 mm resolution down to the bottom of the cores. Porosity was calculated from the bottom water salinity, an average sediment density of 2.65 g cm^{-3} and the weight difference between the wet and dried sediment after one week at 60 °C.

7.3.5 Water Sampling, Pore Water Extractions, and Analysis

Seawater samples were collected with 12-L Niskin® bottles as close as possible to the seafloor. The seawater temperature was measured using a thermometer with a precision of 0.1 °C and the salinity with a conductivity based thermosalinometer with a precision of 0.1.

Triplicate pH measurements were carried out within 1 hour after sampling by spectrophotometry (Clayton and Byrne, ,1993), using m-cresol purple as indicator dye with a precision of +/- 0.005 pH units. pH is reported on the total proton scale. Oxygen concentrations were analyzed by Winkler titration within twelve hours after sampling with a precision of +/- 0.1 μM.

Pore waters were extracted using rhizon filters with a mean pore size of 0.1 μm (Seeberg-Elverfeldt et al., 2005) in a glove bag that was extensively flushed with N_2 to create an anaerobic atmosphere. Pore waters were analyzed immediately onboard for dissolved phosphate concentrations using the paramolybdate method (Murphy and Riley, 1962) as well as for dissolved Fe^{2+} and total dissolved iron concentrations using the ferrozine method (Stookey, 1970). Pore water and bottom water fractions were poisoned

with $HgCl_2$ and stored at 4 °C for alkalinity, DIC, and sulfate analysis in the laboratory. Total alkalinity was measured by open cell titration with 0.01 M HCl (Dickson et al., 2007). DIC concentrations were analyzed with a DIC analyzer (Apollo/SciTech®) on 1 ml samples (see Rassmann et al. (2016) for details). The method was calibrated using certified reference materials for oceanic CO_2 measurements provided by the Scripps Institution of Oceanography (A. Dickson, Batch n° 136). The relative uncertainty for both DIC and alkalinity was +/- 0.5 % of the final value. Sulfate concentrations were quantified after dilution by ion chromatography on an ICS 1000 chromatograph (Dionex) with an IonPac AS 9 HC column and AG 9 HC guard by conductivity suppresion with a AERS 500 suppressor (ThermoFisher Scientific). A 9 mM solution of Na_2CO_3, at a flow rate 1 ml min^{-1} was used as the eluent. The relative uncertainty of this method was +/- 1.6 %. Separate pore water fractions were frozen at -18 °C for sulfate analysis by HPLC (Beckler et al., 2014). Pore water fractions were also acidified with HCl to 2 % for Ca^{2+} analysis by inductively-coupled plasma atomic emission spectroscopy with a Ultima 2 (Horiba Scientific). The method was validated with mono-elemental standards and standard solutions (IAPSO, CASS-4 and NASS-6 seawater reference materials) and displayed a relative uncertainty of +/- 0.75 %.

Acid volatile sulfur (AVS) for the determination of FeS_s was extracted from the same sediment used for the pore water extractions and conducted in triplicate by cold acid distillation of H_2S (g) under anoxic conditions that was trapped by NaOH (Heneke et al., 1991).

Methane samples were degassed and methane was quantified by gas chromatography with a relative uncertainty of +/- 5 % (Sarradin and Caprais, 1996). The

position of the sulfate-methane transition zone (SMTZ) was determined as the zone around the depth where $[SO_4^{2-}]=[CH_4]$ (Komada et al., 2016).

7.3.6 Calculations of Oxygen Uptake and AVS Burial Rates

Diffusive fluxes of O_2 were calculated using Fick's first law (Berner, 1980):

$$DOU = -\varphi D_s \frac{dO_2}{dz}_{z=0} \quad (7\text{-}5)$$

where DOU is the diffusive oxygen uptake rate, φ is the sediment porosity, D_s is the diffusion coefficient in the sediments, $\frac{dO_2}{dz}_{z=0}$ is the oxygen gradient below the sediment-water interface. The apparent diffusion coefficients (D_s) were adjusted for diffusion in a porous environment according to $D_s = D_0/(1+3\cdot(1-\varphi))$ with the diffusion coefficient in free water (D_0) chosen according to Broecker and Peng, (1974) and recalculated to *in situ* temperature by the Stokes-Einstein relation (Li and Gregory, 1974). DOU rates were calculated from linear approximation of the *in situ* oxygen gradient at the SWI.

Burial AVS rates were calculated using available data about sedimentation rates and averaged porosity values:

$$Burial\ AVS = (1-\varphi)\cdot\omega\cdot AVS\cdot\rho \quad (7\text{-}6)$$

where φ is porosity, ω is sedimentation rate and ρ is sediment dry bulk density (used values are given in Table 7-4).

7.3.7 Molar Ratios

To understand how much DIC, TA, and sulfate were produced or consumed relative to each other, the changes in DIC (ΔDIC), TA (ΔTA), and sulfate (ΔSO_4^{2-}) were represented

by property-property relationships to derive the stoichiometric ratios of production/consumption of TA relative to DIC (r_{AD}) as well as TA (r_{AS}) and DIC (r_{DS}) relative to sulfate consumption. For each couple, the pore water concentrations relative to the bottom water concentrations (ΔDIC, ΔTA, ΔSO_4^{2-}) were represented against each other and the linear regression of each relationship calculated. The corresponding stoichiometric ratio (r_i) was derived from the slope and standard deviation of this linear function after correcting for the transport of DIC, TA, and SO_4^{2-} in the sediments. As the sediments of the study area are cohesive, diffusive transport dominates the transport of solutes in pore waters and the equation that gives r_i becomes (Berner, 1980):

$$r_i = \frac{D_a \cdot \Delta a}{D_a \cdot \Delta a} \tag{7-7}$$

where a is the concentration of either DIC or TA, b the concentration of SO_4^{2-} or DIC and D_a and D_b are the corresponding diffusion coefficients. At the given pH of the pore waters, more than 90 % of DIC and carbonate alkalinity are under the form of HCO_3^-. Given the relatively small difference in the diffusion coefficients of HCO_3^- and CO_3^{2-} (10.8 and 9.55 $\cdot 10^{-6}$ cm^2 s^{-1}) and the high proportion of HCO_3^- relative to CO_3^{2-} at the pH of these sediments, the diffusion coefficient of HCO_3^- was assumed to be representative of both DIC and TA.

Total alkalinity and DIC in these sediments are mainly produced during the mineralization of organic matter and partially consumed during calcium carbonate precipitation (Rassmann et al., 2016).

$$Ca^{2+}CO_3^{2-} \leftrightarrow CaCO_3 \tag{7-8}$$

As the precipitation of calcium carbonate consumed twice as much TA as DIC, its effect on DIC and TA variations was accounted for by recalculating the stoichiometric rations in another series of property-property relations which considered the Ca^{2+} gradients in the pore waters. For these calculations, the absolute value of the Ca^{2+} concentration relative to its bottom water concentration (ΔCa^{2+}) was added to the ΔDIC or ΔTA after taking the corresponding diffusion coefficients into account ($D_{DIC}\Delta$ DIC + $D_{Ca}|\Delta\ Ca^{2+}|$ for DIC and $D_{TA}\Delta$ TA + $2D_{Ca}|\Delta\ Ca^{2+}|$ for alkalinity) and represented against $D_{SO42-}\Delta\ SO_4^{2-}$. The calculated slope provides a stoichiometric ratio corrected for the precipitation of calcium carbonate (r_{ic}).

7.4 Results

7.4.1 Bottom Water and Surface Sediment Characteristics

At all stations, bottom water salinities ranged from 37.5 to 38.0 and temperatures varied from 14.7 to 20.6 °C (Table 7-1). Alkalinity was relatively high compared to the Mediterranean average (Table 7-1), but common for the Gulf of Lions (Cossarini et al., 2015). DIC concentrations were relatively high as well. The pH of the bottom waters varied from 8.05 to 8.09 with the highest value observed at station AK and the lowest at station E (Table 7-1). Although the oxygen concentration decreased with water depth, bottom waters were always well ventilated, with O_2 concentrations higher than 240 µmol L^{-1}. Porosities at the SWI ranged between 0.7 and 0.8. Despite known large (Charmasson et al., 1988; Radakovich and Heussner, 1999) and episodic (Cathalot et al., 2010) sedimentation, average porosities at depth between 20 and 400 mm were similar for all stations (Table 7-1).

7.4.2 Benthic and Total Diffusive Fluxes

The O_2 distribution below the SWI reflects the differences between the three study domains under the influence of the Rhône River plume (Figure 7-2). In the proximal zone (Stations A and Z), oxygen penetrated only 1 to 3 mm into the sediment and was confirmed by separate voltammetric measurements (Figure 7-5). The oxygen penetration depth increased from 2 to 6 mm at station K and reached 8 to 11 mm at the most offshore station E. Unfortunately, as a result of bad weather conditions, no exploitable microprofile was recorded at stations AK and B, although voltammetric profiles determined oxygen penetration depths of 4 and 2 mm respectively (Figure 7-5). At stations A and Z, DOU rates reached 10.2 and 10.4 mmol m^{-2} d^{-1} and decreased in offshore direction to 5.9 mmol m^{-2} d^{-1} at station K and 3.6 mmol m^{-2} d^{-1} at station E.

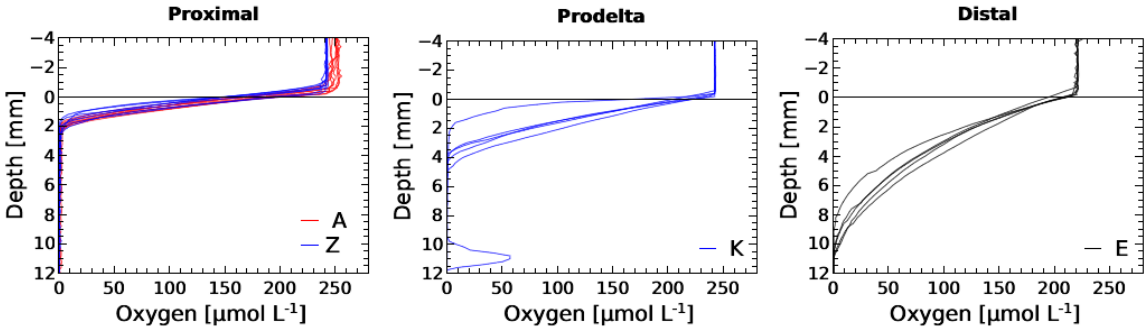

Figure 7-2 Oxygen pore water profiles recorded *in situ* during the AMOR-B-Flux cruise

The benthic chamber was deployed once at stations A and E and twice at station Z. During all incubations, alkalinity and DIC concentrations in the chamber increased linearly with time at a rate that diminished in intensity when moving offshore (Figure 7-3).

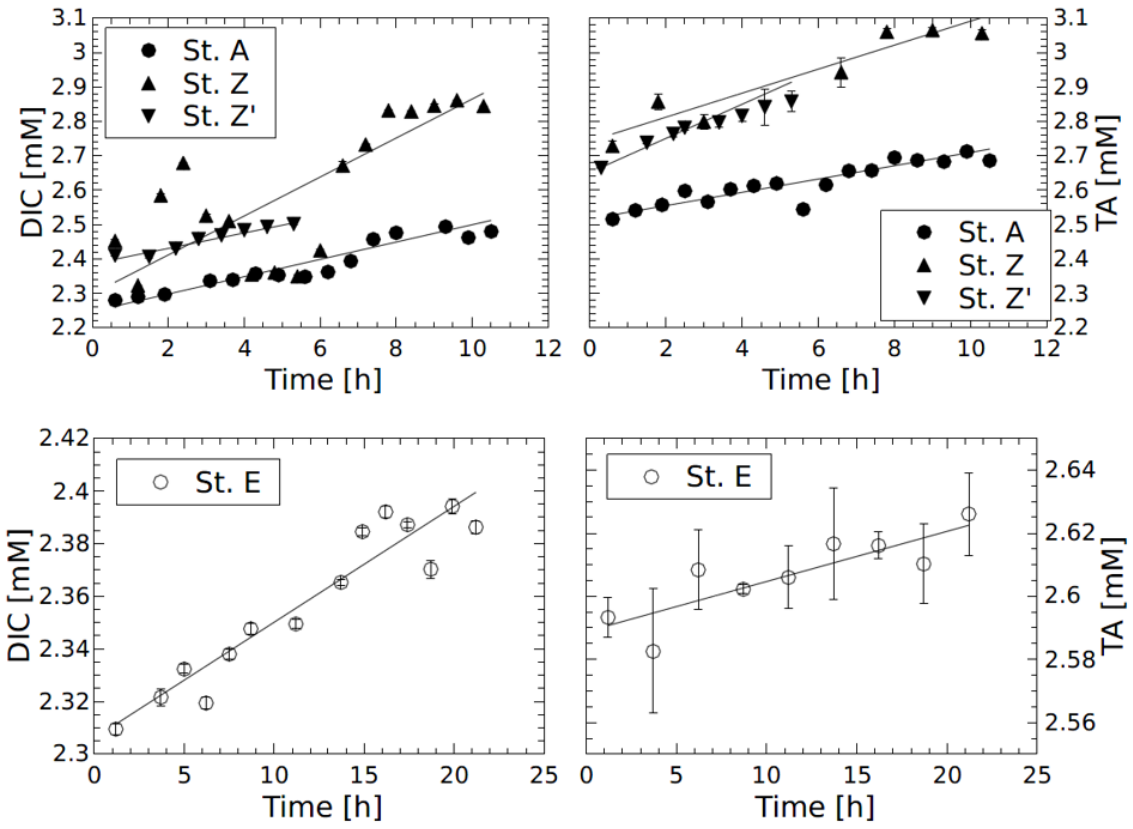

Figure 7-3 Temporal evolution of DIC and alkalinity concentrations in the benthic chamber. Error bars are analytical uncertainties. The slopes and determination coefficients are given in Table 7-2. The total fluxes and their standard deviations are provided in the text and in Figure 7-4.

Table 7-2 Parameters of the linear approximations of the temporal evolution of TA and DIC concentrations during the benthic chamber deployments (Figure 7-3)

Station	TA slope [mM h^{-1}]	r^2	DIC slope [mM h^{-1}]	r^2
A	0.018 ± 0.002	0.8342	0.022 ± 0.002	0.9103
Z	0.038 ± 0.012	0.5967	0.048 ± 0.012	0.5281
Z'	0.029 ± 0.009	0.5770	0.028 ± 0.006	0.7086
E	0.002 ± 0.001	0.7290	0.004 ± 0.001	0.9001

Benthic fluxes were highest for the two deployments at station Z, with alkalinity fluxes of 73.7 and 55.6 mmol m^{-2} d^{-1} and DIC fluxes of 93.1 and 53.7 mmol m^{-2} d^{-1} (Figure 7-4). At station A, the benthic alkalinity and DIC fluxes reached the much lower values of 14.2 and 17.8 mmol m^{-2} d^{-1} respectively. Benthic fluxes were lowest at Station E, with an alkalinity flux of of 3.8 mmol m^{-2} d^{-1} and a DIC flux of 10 mmol m^{-2} d^{-1}. At the proximal stations (stations A and Z), the alkalinity and DIC fluxes were 2.5 to 8 times larger than the DOU rate (Figure 7-4). The relative importance of DOU compared to the alkalinity and DIC fluxes increased when moving offshore. At station E, both the alkalinity and DIC fluxes were twice as large as the DOU flux (Figure 7-4).

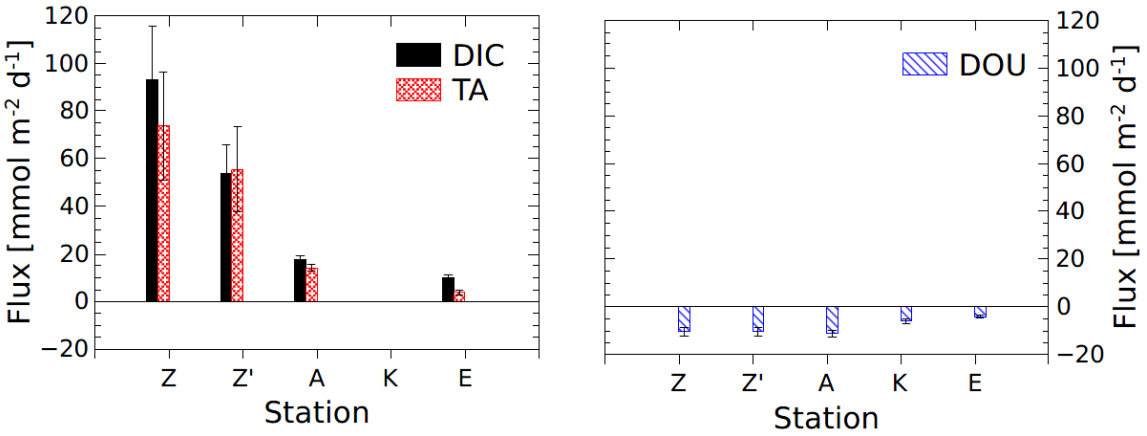

Figure 7-4 DIC and total alkalinity (TA) fluxes measured with the benthic chamber and diffusive oxygen uptake (DOU) rates calculated from *in situ* microelectrode measurements. Error bars represent either uncertainties about the linear regression in the benthic DIC and TA fluxes or error propagation and standard deviations between multiple DOU measurements. Fluxes out of the sediment are positive and fluxes into the sediment are negative. Stations A and Z are located in the proximal zone, K in the prodelta and E in the distal zone (i.e. continental shelf).

7.4.3 Electrochemically Measured Species

Dissolved Fe^{2+} concentrations as a function of depth in the sediment mirrored the voltammetric signals of soluble organic-Fe(III)-complexes at stations A, Z, AK, B, and K

(Figure 7-5). High concentrations of dissolved Fe2+ were observed in the proximal domain at stations A (341 +/- 22 μM) and Z (234 +/- 25 μM), where dissolved ΣH_2S was not detected (Figure 7-5). At station AK, the shallowest station in the prodelta domain, dissolved Fe^{2+} increased to a maximum concentration of 255 μM around 2 cm depth and then decreased with sediment depth, as FeS_{aq} was detected below 6.5 cm followed by small concentrations of dissolved ΣH_2S around 17 cm (Figure 7-5). The two deeper prodelta stations, B and K, displayed low concentrations of Fe^{2+}, including one peak not exceeding 81 μM (station B) or 73 μM (station K) in the top 2 cm of the sediment and a second peak not exceeding 50 μM between 12-14 cm (station B) and 86 μM between 5-7.5 cm (Station K) in the sediment. Soluble organic-Fe(III) signals mirrored the Fe^{2+} profiles at stations B and K, though in much higher current intensities at station B. Although FeS_{aq} was only detected below 15 cm at station B, ΣH_2S was produced in low concentrations (< 5 μM) around 6.5 cm at both stations (Figure 7-5). Both stations also displayed small concentrations of Mn^{2+}. A peak of Fe^{2+} was initially formed in the top 5 cm of the distal domain (Station E) but decreased to a minimum value with depth and did not correlate with the organic-Fe(III) signal, which also remained low throughout the profile (Figure 7-5). Station E revealed generally low concentrations of ΣH_2S in the pore waters (<6 μM), although the onset of ΣH_2S production was much shallower (2.5 cm) and ΣH_2S concentrations were consistent.

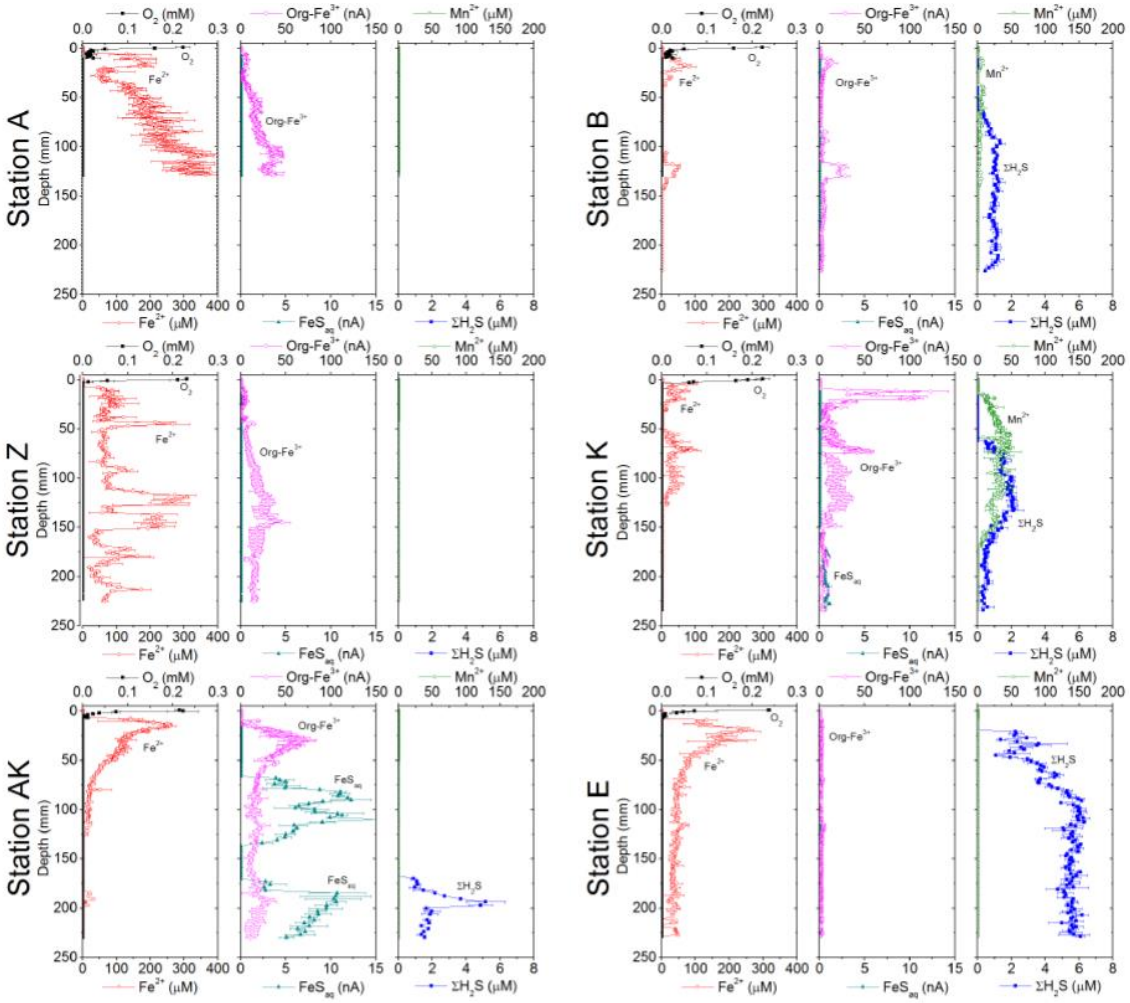

Figure 7-5 Depth profiles show concentrations of dissolved O_2, Fe^{2+}, organic-Fe^{3+}, FeS_{aq}, Mn^{2+} and ΣH_2S measured electrochemically. Organic-Fe(III) and FeS_{aq} are reported in normalized current intensities (nA).

7.4.4 Additional Pore Water Measurements

Both alkalinity and DIC concentrations increased rapidly within the sediment to uncommonly high values for marine sediments (Figure 7-6), likely reflecting high organic carbon mineralization rates in these sediments. At all stations, DIC pore water concentrations correlated well with alkalinity (overall slope: 1.01 +/- 0.006, r^2=0.9953, n=134) though lower slopes and higher uncertainties were evident at station A and K. The

alkalinity and DIC gradients were highest at stations A and Z, where maximum concentrations of both species reached around 55 mM (Figure 7-6). At station AK, alkalinity and DIC concentrations reached a maximum of 15 mM at 25 cm depth, but the alkalinity decreased to 6 mM at the bottom of the core. The maximum concentrations of DIC and alkalinity of 35 mM observed at station B, were more comparable to the stations in the vicinity of the river mouth (Stations A and Z) than other stations located in the prodelta domain (Stations AK and K). At station K, alkalinity and DIC concentrations reached 10 mM, whereas the lowest alkalinity and DIC gradients were measured at station E, with concentrations reaching only 4.6 mM at the bottom of the cores (30 cm). These pore water concentrations, however, are still relatively high for coastal sediments. Sulfate was completely removed from the pore waters at station A, Z, and B at depths of 35, 24, and 45 cm, respectively. In turn, sulfate concentrations at stations AK and K decreased to a minimum concentration of 20 mM at 29 cm and 24 cm depth, respectively. Sulfate consumption was much smaller at station E with a minimum concentration of 28 mM. Alkalinity, DIC and sulfate concentrations at a given depth were anticorrelated with high r^2 values at stations A, Z, AK, and B (Table 7-3). Although DIC and sulfate anti-correlated strongly at station K, the decrease in alkalinity with depth (Figure 7-6) prevented good anti-correlation with sulfate. Similarly, alkalinity and DIC demonstrated a strong correlation at stations Z, AK, B, and E, but a lesser correlation at station A and no correlation at station K (Table 7-3). At station E, the consumption of sulfate was too low to correlate with the production of DIC.

Table 7-3 Diffusion corrected ratios and parameters of the linear r_{AD} , r_{DS} and r_{AS} correlations and the corresponding ratios corrected for carbonate precipitation.

Parameter	A	Z	AK	B	K	E
r_{AD}	0.99 ± 0.01	1.08 ± 0.03	1.02 ± 0.02	1.02 ± 0.01	0.98 ± 0.05	0.90 ± 0.04
r_{ADc}	1.10 ± 0.01	1.16 ± 0.03	1.07 ± 0.02	1.15 ± 0.02	1.06 ± 0.07	1.15 ± 0.11
r_{DS}	-1.67 ± 0.06	-1.87 ± 0.17	-1.85 ± 0.05	-1.18 ± 0.05	-1.72 ± 0.03	-
r_{DSc}	-1.88 ± 0.05	-2.05 ± 0.18	-1.95 ± 0.05	-1.37 ± 0.05	-1.86 ± 0.07	-
r_{AS}	-1.66 ± 0.07	-2.03 ± 0.17	-1.89 ± 0.06	-1.21 ± 0.04	-1.69 ± 0.07	-
r_{ASc}	-2.07 ± 0.05	-2.39 ± 0.18	-2.08 ± 0.07	-1.57 ± 0.05	-1.95 ± 0.18	-

Significant methane concentrations (> 50 µM) were detected at the bottom of station A, Z, and AK, whereas methane was below 50 µM throughout the core at station K (Figure 7-6). The SMTZ was located between 28 and 39 cm at station A and between 19 and 39 cm at station Z. The SMTZ was not determined at stations AK and K, as sulfate was not completely consumed inside the sediment core. Methane analysis were not carried out for the other stations.

All stations displayed overall oversaturation with respect to calcite (Ω_{Ca}>1). At stations A, Z, and B, decreasing Ca^{2+} concentrations in the pore waters indicated precipitation of $CaCO_3$, whereas Ca^{2+} concentrations remained relatively high throughout the sediment at the other stations (Figure 7-6). Dissolved phosphate concentrations (ΣPO_4^{3-}) were high for the majority of the profile (<50 µM) at both stations A and Z, though at station Z a large increase in concentration (up to 160 µM) was observed below 22.5 cm. At station AK, ΣPO_4^{-3} concentrations increased to around 75 µM around 10 cm and then remained relatively constant with depth. Concentrations of ΣPO_4^{-3} increased to around 50 µM at 15 cm at station K, whereas ΣPO_4^{-3} production was minimal throughout station E (<10 µM). Phosphate was not measured at station B. Sediment samples were analyzed for

AVS as a function of depth at stations A, AK, and E to assess one station in each domain (Figure 7-6). At station A, a peak in AVS (65 μmol g^{-1}) was measured around 8.0 cm followed by a second, smaller peak (22 μmol g^{-1}) at 14 cm, after which AVS decreased with depth. The AVS values at station AK were low in the top portion of the sediment, but increased to 100 μmol g^{-1} around 15 cm and increased with depth. At station E, only a small AVS peak of 20 μmol g^{-1} was observed at 14 cm.

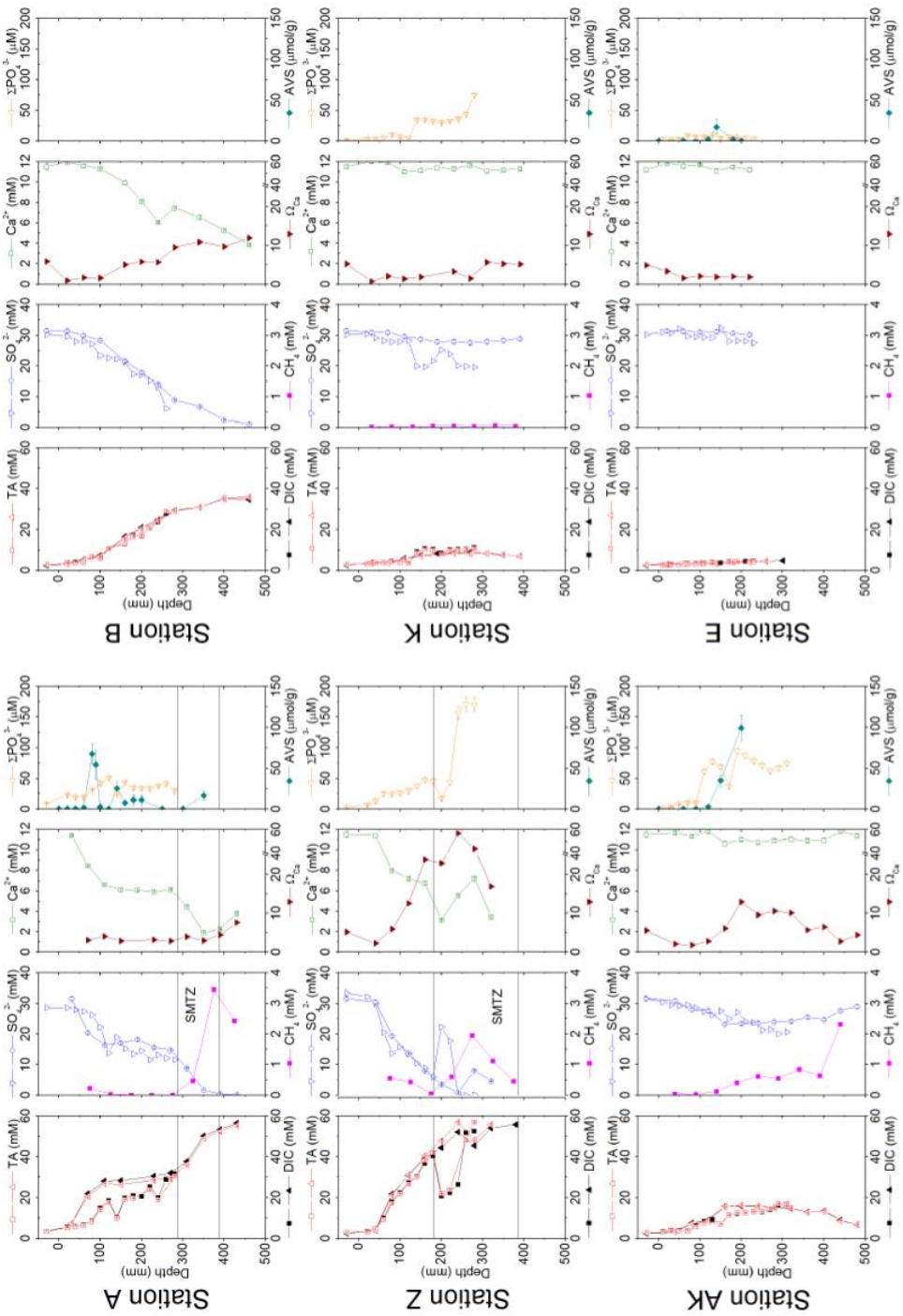

Figure 7-6 Depth profiles show pore water alkalinity and concentrations of DIC, CH_4, PO_4^{3-}, SO_4^{2-}, Ca^{2+} with alternating symbol shapes indicating data collected from duplicate long and short cores. The calcium carbonate (calcite) saturation state(Ω) is calculated and AVS (μmol g^{-1}) is determined from the solid phase. Two horizontal lines identify the sulfate-methane transition zone (SMTZ) found at stations A and Z. Error bars represent standard deviations between multiple measurements for the concentrations and error propagation for Ω. For stations B, K and E, CH_4 concentrations were not measured.

7.5 Discussion

7.5.1 DIC and Alkalinity Fluxes from the Sediment

The sediments of the Rhône proximal and prodelta zones represent important sources of both DIC and alkalinity to the bottom waters (Figure 7-4). The observed fluxes are in the range of previously measured fluxes in other deltas where anaerobic mineralization processes are dominant. DIC fluxes ranging between 15-20 and 36-53 mmol m^{-2} d^{-1} were measured by core incubations or with benthic chambers in Mississippi delta sediments (Lehrter et al., 2012; Rowe et al., 2002), which is in the lower-middle range of the fluxes observed in this study (18-93 mmol m^{-2} d^{-1}). In the Danube delta nearshore sediments (NW Black Sea), benthic carbon mineralization rates averaging 25 mmol C m^{-2} d^{-1}, with rates expected to be as high as 40 mmol C m^{-2} d^{-1} in the summer, have been determined (Capet et al., 2016). These rates fall in the middle of the range of values reported in the present study for the summer. Interestingly, similar high CO_2 production fluxes (35-42 mmol m^{-2} d^{-1}) were measured in the mangrove channel and sediments of the topset sites of the Fly River delta in the most active season (Aller et al., 2008). In contrast, relatively few alkalinity fluxes have been measured in river deltas, though those obtained from benthic chambers in the Danube and Dniester deltas in the Northwest Black Sea , varied between 21 and 67 mmol m^{-2} d^{-1} (Friedl et al., 1998), in the range of values reported in this study (14-74 mmol m^{-2} d^{-1}). The biogeochemical origin of these high benthic fluxes will be discussed in the next sections.

7.5.2 Sulfate Reduction and Anaerobic Oxidation of Methane

The intense sulfate consumption at depth (Figure 7-6) confirms that sulfate reduction is one of the dominant mineralization pathways in the Rhône prodelta sediments (Pastor et al., 2011; Rassmann et al., 2016). Considering carbonate precipitation using the pore water Ca^{2+} data, the r_{DSc}) were determined to be between -2.04 and -1.4 with the lowest ratio at station B (Table 7-3) and the r_{ASc} ratios between -1.6 and -2.4 (Table 7-3). According to Eq. 7-1, the r_{DSc} and r_{ASc} should equal -2, suggesting that other processes influence r_{ASc} and r_{DSc}. In addition to bacterial sulfate reduction, anaerobic oxidation of methane (Eq. 7-2) at the bottom of the sulfate reduction zone may also account for some of the sulfate consumption (Borowsi et al., 1996; Niewöhner et al., 1998, Jørgensen and Kasten, 2006; Komada et al., 2016). This reaction increases the carbonate saturation state by producing more alkalinity than DIC (2 mole of alkalinty for 1 mole of DIC) and leads to the precipitation of calcium carbonates (Komada et al., 2016). In the sediments of the Rhône prodelta, a clear sulfate-methane transition zone was observed at station A and Z, (Figure 7-6), suggesting that AOM coupled to sulfate reduction occurs in these sediments. AOM should lead to $r_{AD} = 2$, but the precipitation of calcium carbonate minerals (Eq. 7-8) brings the ratio back to $r_{AD} = 1$. Indeed, alkalinity and DIC displayed good correlations and r_{ADc} ratios were close to 1 (Table 7-3). A comparison of the sulfate and methane gradient at the top of the SMTZ of the Rhône prodelta sediments indicate that up to 30 % of the sulfate is consumed by AOM. However, the limited number of data points deeper in the sediment makes quantifying the effect of AOM on the alkalinity and DIC fluxes difficult.

7.5.3 Influence of Other Anaerobic Processes on Alkalinity and DIC

The complete depletion of sulfate by sulfate reduction in the first 30 cm of the sediment at stations A, Z, and B implies an equivalent production of dissolved sulfide (ΣH_2S). If all of the produced ΣH_2S diffused upward and reacted in the oxic sediment layer, the alkalinity produced by sulfate reduction would be consumed by the oxidation of ΣH_2S by O_2 (Eq. 7-9).

$$H_2S + 2O_2 \rightarrow SO_4^{2-} + 2H^+ \quad (7\text{-}9)$$

Although ΣH2S was nearly absent of the pore waters (Figure 7-5), the observed alkalinity and DIC fluxes across the SWI were in the same order of magnitude (Figure 7-4). These findings suggest that ΣH_2S was removed from the pore waters below the oxic layer, likely by oxidation by Fe(III) oxides (Eq. 7-10), precipitation of FeS in the anoxic zone (Eq. 7-11; Berner, 1970; Pyzik and Sommer, 1981; Carman and Rahm, 1997, Soetaert et al., 2007), and eventually formation of pyrite (Eq. 7-12; Rickard and Luther (1997)):

$$2Fe(OH)_3 + H_2S + 4H^+ \rightarrow 2Fe^{2+} + S(0) + 6H_2O \quad (7\text{-}10)$$

$$Fe^{2+} + H_2S \rightarrow FeS + 2H^+ \quad (7\text{-}11)$$

$$FeS + H_2S \rightarrow FeS_2 + H_2 \quad (7\text{-}12)$$

As the abiotic reduction of Fe(III) oxides by ΣH_2S (Eq. 7-10, Δ TA = +2 per mole of $Fe(OH)_3$) coupled with either FeS (Eq. 7-11), Δ TA = -2 per mole of Fe^{2+}) or FeS and pyrite precipitation (Eq. 7-12, Δ TA = 0) does not alter alkalinity overall, bacterial sulfate

reduction followed by abiotic precipitation of iron and sulfide from the pore waters to either FeS (Eq. 7-13) or pyrite (Eq. 7-14) should result in r_{AD} = 1 and r_{DS} = -2.

$$6CH_2O + 3SO_4^{2-} + 2Fe(OH)_3 \rightarrow 6HCO_3^- + S(0) + 2FeS + 6H_2O \quad (7\text{-}13)$$

$$10CH_2O + 5SO_4^{2-} + 2Fe(OH)_3 \rightarrow 10HCO_3^- + S(0) + 2FeS_2 + 6H_2O + 2H_2 \quad (7\text{-}14)$$

If Fe^{2+} is formed by dissimilatory iron reduction (Eq. 7-3), which produces ΔTA = +2 and ΔDIC = +1/4 per mole iron, while ΣH_2S is concomitantly produced from bacterial sulfate reduction (Eq. 7-1; ΔTA = +2 and ΔDIC = +2 per mole of SO_4^{2-}) followed by precipitation of FeS (Eq. 7-11), the net r_{AD} and r_{DS} ratios should decrease to 0.89 and -2.25 (Eq. 7-15).

$$\frac{9}{4}CH_2O + SO_4^{2-} + Fe(OH)_3 \rightarrow \frac{9}{4}HCO_3^- + \frac{1}{4}H^+ + FeS + \frac{5}{2}H_2O \quad (7\text{-}15)$$

With formation of pyrite, theoretical mole ratios may change slightly to r_{AD} = 0.94 and r_{DS} = -2.125 (Eq. 7-16).

$$\frac{17}{4}CH_2O + 2SO_4^{2-} + Fe(OH)_3 \rightarrow \frac{17}{4}HCO_3^- + \frac{1}{4}H^+ + FeS_2 + \frac{5}{2}H_2O + H_2 \quad (7\text{-}16)$$

The r_{DS}, r_{AD}, and r_{AS} ratios provide a qualitative overview of the main biogeochemical processes taking place at each station. In general, the r_{DS} values were higher than the theoretical value of -2 (Eq. 7-1) and can be explained by carbonate precipitation (Table

7-3; Rassmann et al. (2016)) and presumably by the oxidation state of the organic matter undergoing mineralization (Cathalot et al., 2013).

The r_{DSc} ratios close to -2 at stations A, Z, and AK (-1.88, -2.05, -1.95, Table 7-3) seem to indicate that sulfate reduction was the dominant ongoing mineralization process. In contrast, the r_{DSc} ratios (-1.37 and -1.86, Table 7-3) in the prodelta (stations B and K) either indicate a sink of DIC that is not related to calcium carbonate precipitation or suggest either ongoing AOM or that the organic matter undergoing mineralization was already partly oxidized (Burdige et al., 2011). Simultaneously, the r_{AS} ratios were either around or below the theoretical values of -2 at the closest stations to the river mouth (stations A, Z, and AK), when factoring carbonate precipitation using the Ca^{2+} data (r_{ASc} = -2.07, -2.39, -2.08; Table 7-3), but tended to be slightly higher offshore (station B and K), supporting the hypothesis of another carbonate sink in the prodelta (r_{ASc} = -1.57, -1.95; Table 7-3). Similarly when considering carbonate precipitation, the r_{ADc} ratios were slightly above their theoretical values of 1 at all stations suggesting that other respiration processes, such as microbial iron reduction, may have contributed to the excess alkalinity in these sediments.

These findings indicate the coexistence of sulfate reduction, iron reduction, and the precipitation of sulfide minerals in the proximal domain but also indicate that the total alkalinity was consumed in the sediment of the prodelta domain, likely by precipitation or reoxidation of the reduced iron and sulfide metabolites. The occurrence of dissimilatory iron reduction in the proximal and prodelta domains is substantiated by several pieces of evidence. First, the production of soluble organic-Fe(III) complexes deeper than the oxygen penetration depths indicates that these species did not result from the oxidation of

Fe^{2+} by dissolved oxygen in the presence organic ligands (Taillefert et al., 2000). Second, soluble organic-Fe(III) complexes are produced as intermediates in the reduction of Fe(III) oxides by iron reducing bacteria (Taillefert et al., 2007; Jones et al., 2010). Their concomitant detection with Fe^{2+} at all the stations in the proximal and prodelta domains (Figure 7-5) therefore suggests they were produced during dissimilatory iron reduction. Third, the positive correlation between the current intensities of organic-Fe(III) complexes and Fe^{2+} concentrations is in line with the same correlation obtained in an iron-rich estuarine sediment (Figure 7-7) where sulfate reduction was not significant (Beckler et al., 2016). Finally, as these organic-Fe(III) complexes are readily reduced by dissolved sulfides (Taillefert et al., 2000), their presence in zones of sulfate reduction suggest that these sediments are highly dynamic with periods of intense sulfate reduction alternating with periods during which sulfate reduction is repressed and replaced by microbial iron reduction. These dynamics may be controlled by the input of organic and inorganic material from the Rhône River, especially during floods, as previously demonstrated in the vicinity of the river mouth (Cathalot et al., 2010; Cathalot et al., 2013; Pozzato et al., 2017) and underlines the concept of estuarine regions as a dynamic benthic reactor system (Aller et al., 1998).

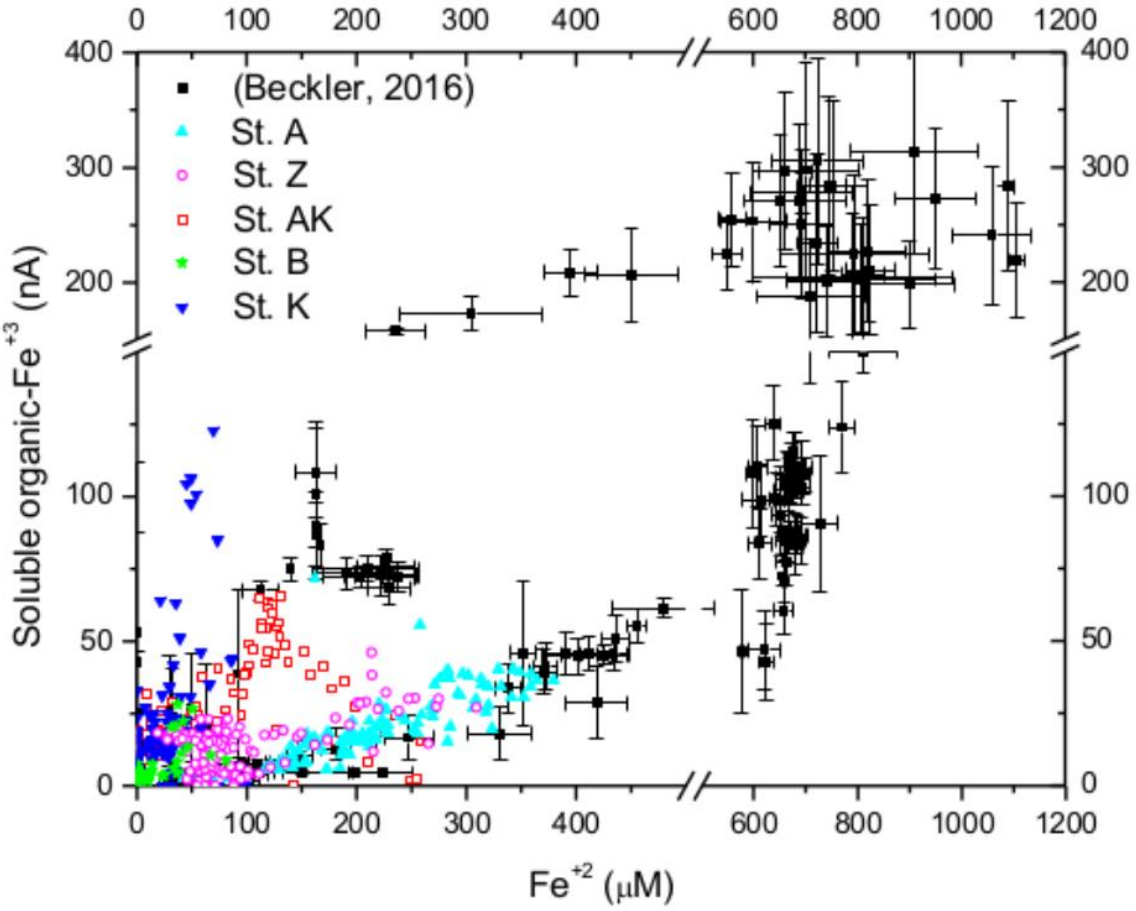

Figure 7-7 Current intensities of organic-Fe^{+3} complexes as a function of Fe^{+2} concentrations measured at each depth for stations A, Z, AK, B, and K compared to the same data obtained from iron-rich estuarine sediments (Beckler et al., 2016).

7.5.4 Formation of Iron Sulfide

The discrepancy between sulfate consumption and the low concentration of dissolved sulfide clearly demonstrates that much of the sulfur was buried in the solid phase. Indeed, the large phosphate concentrations observed at depth in the proximal and prodelta domains suggest that ΣPO_4^{3-} adsorbed to Fe(III) oxides is released in the pore waters during secondary conversion of Fe(III) oxides to FeS (Anschutz et al., 1998; Rozan et al., 2002).

At millimolar concentrations of Fe^{2+} and ΣH_2S, non-crystalline amorphous FeS is the first iron-sulfide mineral to precipitate (Berner, 1970; Rickard, 1989; Davison, 1991; Schoonen and Barnes, 1991; Rickard, 1995) whereas soluble FeS complexes can form without precipitation of FeS mineral at lower concentrations of Fe^{2+} and ΣH_2S (Luther et al., 1996). Considering the intensity of sulfate reduction in most of the sediments, it is likely that most Fe^{2+} in the pore water may be mainly in the form of aqueous FeS nanoparticles (FeS_0). As a significant fraction of FeS nanoparticles may pass through the rhizon filters (0.12 to 0.18 μm) (Nakayama et al., 2016) and the ferrozine method is well known to dissolve FeS complexes (Davison et al., 1998), the concentration of Fe^{2+} determined in the pore waters spectrophotometrically, may have been dominated by FeS_0. Indeed, previous discrepancies between sulfide concentrations determined electrochemically and spectrophotometrically in filtered samples have been attributed to FeS nanoparticles (Bura-Nakic et al., 2009). As a significant fraction of FeS nanoparticles may pass through the rhizon filters (0.12 to 0.18 μm) (Nakayama et al., 2016), the concentration of Fe^{2+} determined in the pore waters spectrophotometrically, may have been dominated by FeS_0. Thus, the total value of soluble FeS_0 could be estimated by subtracting the concentration iron determined electrochemically (Fe^{2+}_{echem}) from iron determined by the ferrozine analysis (ΣFe^{2+}_{FR}; Eq. 7-17).

$$[\sum Fe^{2+}]_{FR} - [Fe^{2+}{}_{echem}] = [FeS_0] \quad (7\text{-}17)$$

These calculations indicate that the concentration of FeS_0 was similar at stations A and Z with two broad peaks in each core and maximum concentrations around 1 mM (Figure 7-8). Station AK displayed the most FeS_0, with concentrations up to 6 mM, though FeS_0 concentrations decreased below 150 mm. Finally, FeS_0 concentrations also decreased with

distance from shore. The existence of FeS_0 suggests that large fractions of Fe^{2+} and ΣH_2S were removed from the pore waters and eventually may be immobilized under the form of FeS minerals and eventually pyrite. However, electrochemical detection of soluble FeS_{aq} clusters, which are considered a good indicator of the active precipitation of iron sulfide minerals (Luther and Ferdelman, 1993; Davison et al., 1998; Taillefert et al., 2000), were rarely observed in this study (Figure 7-7). Indeed, these clusters must be smaller than 5 nm in diameter to be detected electrochemically (Buffle, 1988), and the voltammetric peak for FeS_{aq} is typically only observed when the ion activity product (pIAP) is above the K_{sp} (Theberge and Luther, 1997; Buffle, 1988). Given the pIAPs calculated at most stations were close to the solubility of amorphous FeS or mackinewite (Figure 7-9), the generally small FeS_{aq} signals detected are not too surprising. Overall, calculated undersaturations resulted from either the low concentrations (stations AK, B, and K) or complete absence (stations A and Z) of dissolved sulfide. However, it is important to note that these calculations assume equilibrium conditions, which are likely difficult to meet in such a dynamic system. Indeed, the large concentrations of dissolved FeS_0 compared to the small electrochemically active FeS_{aq} complexes indicate that the precipitation of FeS minerals was much more advanced in its coagulation process during this time period, thus corroborating that the system is dynamic and not adequately described by thermodynamic equilibrium. Overall, the presence of soluble organic-Fe(III) complexes along with dissolved Fe^{2+} throughout the profiles, the absence of dissolved sulfide and FeS_{aq}, and the large concentrations of dissolved FeS_0 found in the pore waters despite complete removal of sulfate in the proximal and some of the prodelta stations provide strong evidence that

sulfate-reducing conditions may alternate with iron-reducing conditions as already observed seasonally in estuarine sediments (Taillefert et al., 2002).

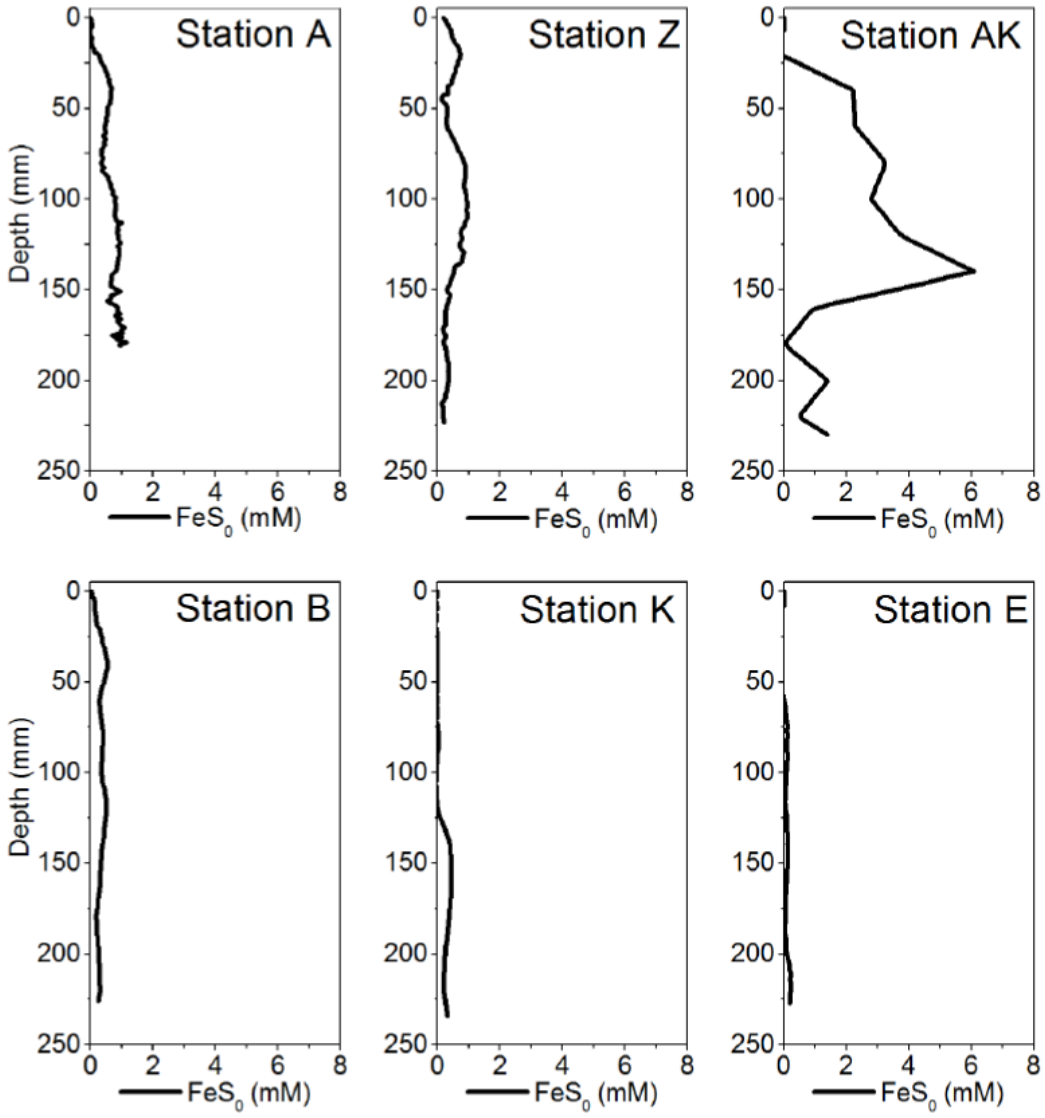

Figure 7-8 Depth profiles for calculated values of FeS_0 (mM).

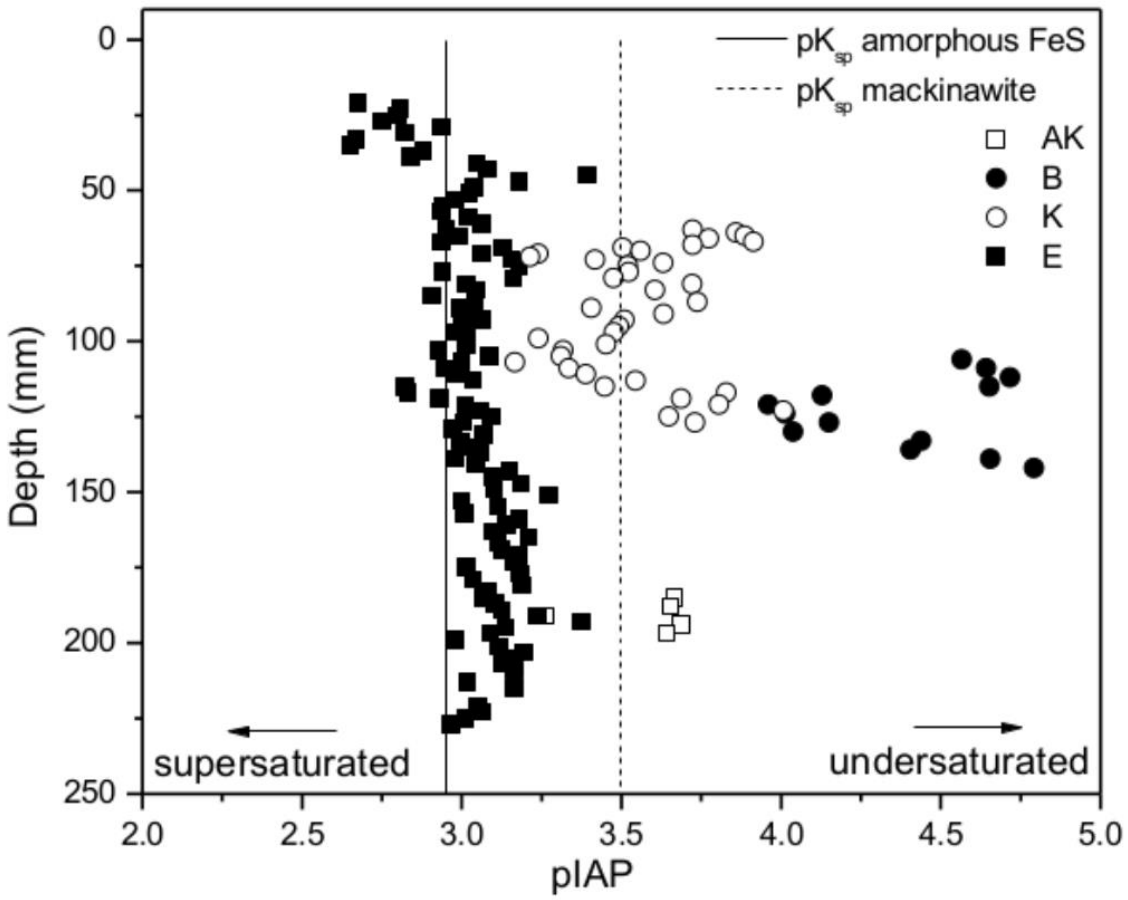

Figure 7-9 Calculated pIAP values with depth compared to the pK_{sp} of amorphous FeS and mackinawite. Due to the lack of dissolved HS^- the pIAP values in the pore waters of station A and Z are so elevated that they cannot be represented on this figure.

7.5.5 Alkalinity Release Due to the Burial of Iron Sulfide

The pore water concentration of FeS_0 was high in the proximal domain and decreased with distance from shore (Figure 7-8). Simultaneously, accumulation of AVS are observed in the proximal and prodelta domain (station A and AK) (Figure 7-6). With precipitation FeS about 2 to 2.3 moles of alkalinity equivalent should be produced for each mole of sulfur precipitated (Eq. 7-13 to 7-16). The burial of FeS thus represents a net source of alkalinity as the extreme sedimentation rates in the proximal domain prevent the short-

term re-oxidation of sulfide to occur (Berner, 1982; Hu and Cai, 2011; Brenner et al., 2016). The alkalinity production flux estimated from the AVS burial fluxes (Table 7-4) is thus approximately 25 +/- 8 mmol m^{-2} day^{-1} in the proximal domain, which is slightly smaller than the average alkalinity flux measured by benthic chamber (48 +/- 30 mmol m^{-2} day^{-1}). In the prodelta, the equivalent alkalinity flux is 10 +/- 3 mmol m^{-2} day^{-1}, which unfortunately cannot be compared to benthic alkalinity fluxes as they were not measured. In the distal domain, a low alkalinity flux of 0.04 +/- 0.1 mmol m^{-2} day^{-1} is estimated from the AVS burial flux. This flux is much less than the 4 +/- 9 mmol m^{-2} day^{-1} flux measured by benthic chamber. These findings corroborate the r_{AD} ratios that suggest that sulfide and iron oxidation also control the alkalinity flux offshore (Aller et al., 1986). Overall, the present findings indicate that FeS burial modifies the alkalinity budget and thus the carbon cycle (Brenner et al., 2016). As the order of magnitude of the measured benthic alkalinity fluxes is compatible with the alkalinity generated during the reduction of iron oxides, sulfate, and subsequent FeS burial, these processes are likely responsible for the large alkalinity fluxes reported in this high-sedimentation delta, and potentially in similar systems (Hu and Cai, 2011).

Table 7-4 Calculations of FeS burial for station A and Z in the proximal zone and comparison to alkaliniy fluxes

	A and Z	AK	E
ω[cm yr^{-1}]	30	3	0.1
ϕ	0.67	0.68	0.64
Mean [AVS][μmol g^{-1}]	19.5 ± 4.9	45.0 ± 11.3	9.0 ± 2.3
sediment density ρ_{solid}		2.5 g cm^{-3}	
Burial FeS [mmol S m^{-2} d^{-1}]	12.5 ± 3.8	4.9 ± 1.4	0.02 ± 0.01
Equivalent TA prod (= 2· FeS) [mM TA m^{-2} d^{-1}]	**25.0 ± 7.7**	**9.9 ± 2.8**	**0.04 ± 0.1**
Mean TA flux at SWI [mM TA m^{-2} d^{-1}]	**47.8 ± 30.4**		**3.9 ± 9.0**

7.5.6 Linking Alkalinity and DIC Fluxes withMineralization Processes

The DIC resulting from organic carbon mineralization leads to benthic DIC fluxes that are only modulated by the precipitation of calcium-carbonates. The situation is more complex with total alkalinity as alkalinity can be consumed by a variety of diagenetic processes, including reoxidation of reduced species (i.e., Fe^{2+}, Mn^{2+}, HS^-, NH_4^+) that are transported back to the oxic sediment layers by bioirrigation or diffusion (Soetaert et al., 2007; Krumins et al., 2013; van Velde and Meysman, 2016). If these reduced species are buried, however, significant amounts of the anaerobically produced alkalinity may be transferred into the water column (Figure 7-10). The findings of the present study demonstrate that if the supply of organic matter and Fe(III) oxides to the sediment are high, as at station A and Z, the intensity of iron and sulfate reduction is enhanced (Figure 7-5, Figure 7-6). Simultaneously, the high sedimentation rates at these stations keep the

majority of reduced iron and dissolved sulfide buried under the form of FeS and potentially pyrite within the anaerobic sediments (Aller et al., 1986). Consequently, less alkalinity-consuming reactions occur in the oxic sediment layers and a significant fraction of the anaerobically-produced alkalinity is transferred across the SWI (Figure 7-10, red dashed line). In these conditions, anaerobic and aerobic processes are decoupled, and the consumption of oxygen no longer reflects overall respiration rates within these sediments (Pastor et al., 2011), as observed by the much lower oxygen fluxes compared to alkalinity and DIC fluxes in the proximal domain (Figure 7-4).

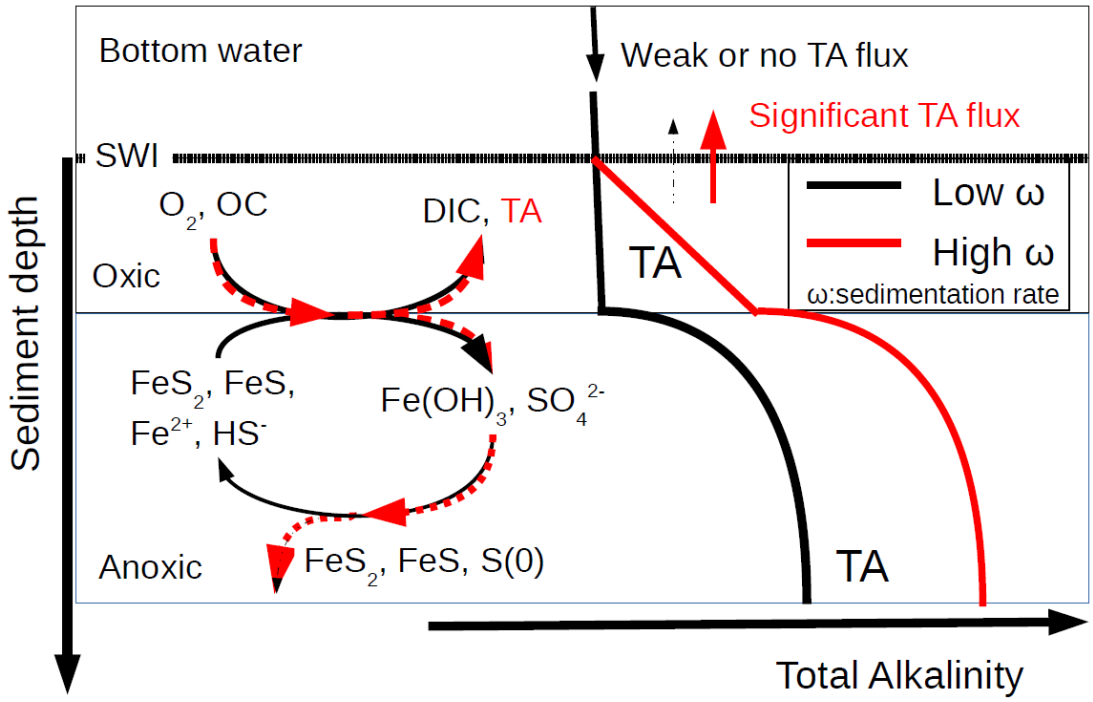

Figure 7-10 Conceptual model to visualize the link between the burial of iron sulfide species and benthic alkalinity fluxes. Alkalinity produced under anaerobic conditions at depth diffuses upwards towards the aerobic sediment layer where it can be consumed by high reoxidation of Fe^{2+} and H_2S by dissolved oxygen (black). If the precipitation of sulfide minerals is significant, the reduced iron and sulfide metabolites produced during anaerobic respiration are not reoxidized by dissolved oxygen, and the alkalinity produced is able to reach the bottom waters (red). The

intensity of the alkalinity flux into the bottom waters is indicated by the thickness of the arrow at the SWI.

Moving offshore, the sedimentation rates (Table 7-1), overall respiration rates (Figure 7-4), and the intensity of the corresponding pore water gradients (Figure 7-6) decrease, and the proportion of aerobic processes increases (Pastor et al., 2011). Despite the relatively small decrease in pore water sulfate concentrations with depth at the most offshore station E, the dissolved sulfide concentrations, though below 10 μmol L^{-1}, were the highest of all the stations. These findings likely reflect the fact that less riverine Fe(III) oxides were available for FeS precipitation. With low sedimentation rates and thus low input of organic matter and Fe(III) oxides, the overall carbon turnover is decreased and the reduced byproducts of sulfate and/or iron reduction may be transported back to the oxic sediment layers to be reoxidized by dissolved oxygen. In this case, the alkalinity generated by the anaerobic processes is consumed by reoxidation of the reduced metabolites, and the flux of alkalinity near the sediment-water interface decreases offshore (Hu and Cai, 2011; Brenner et al., 2016) to weak or negligible values at station E (Figure 7-4 and Figure 7-10, black line). In general, the strong alkalinity flux to the overlying waters measured in the Rhône River delta, may contribute, along with riverine input, to the overall high alkalinity of the Gulf of Lions waters compared to the Mediterranean average (Cossarini et al., 2015) and suggests that such benthic pelagic coupling may contribute to the buffering capacity of seawater in coastal environments.

7.6 Conclusion

In this study, benthic respiration, alkalinity and DIC fluxes were quantified in the Rhône River prodelta using benthic landers and pore water profiles. These sediments were

demonstrated to represent an alkalinity source to the water column. The strongest alkalinity and DIC fluxes were detected in the vicinity of the river mouth and were much stronger than fluxes of dissolved oxygen, indicating the decoupling of oxic and anoxic biogeochemical processes. The high benthic alkalinity fluxes resulted from the high intensity of anaerobic respiration processes, via sulfate reduction mainly, but also with contributions from iron reduction and AOM. The intensity of sulfate reduction in the proximal domain resulted in precipitation of iron sulfide minerals while a significant fraction of the DIC produced was consumed by precipitation of authigenic carbonates. As the reduced metabolites of organic matter mineralization were buried in the solid phase, less alkalinity was consumed by the reoxidation of HS^- and Fe^{2+} in the oxic layers of these sediments with an average of 47.8 mmol m^{-2} d^{-1} of alkalinity transferred to the bottom waters. Although sulfate reduction dominated the proximal and prodelta domains, evidence for dissimilatory reduction of Fe(III) oxides is observed in the depth profiles, suggesting that anaerobic processes in the Rhône River prodelta are dynamic and potentially controlled by pulsed sediment accumulations. The intensity of the alkalinity and DIC fluxes decreased offshore as the sedimentation rate and the relative importance of anaerobic mineralization pathways compared to aerobic processes decreased. In these conditions the more classical coupling between aerobic and anaerobic process occurs, lowering the benthic alkalinity fluxes. Overall, these findings suggest that deltaic sediments exposed to large riverine inputs of inorganic and organic material may provide a source of alkalinity to the overlying waters and may help buffer the acidification of coastal waters.

7.7 Acknowledgments

We are thankful to Professor Bianchi, Dr. Alexandra Rao and four anonymous reviewers who helped significantly to improve the quality of our manuscript. The authors thank the captain and crews of the RV Tethys II for their support at sea and Bruno Bombled for technical help onboard and in the lab. We thank Gael Monvoisin for the analysis of sulfate samples at GEOPS (Paris-Sud University), Joel Craig and Olivia Studebaker for the analysis of nutrients and AVS at Georgia Tech, and Celine Liorzou for the ICP-AES measurements at Pôle Spéctrométrie Océan in Brest. We are grateful to Sabine Kasten, Sandra Arndt and Andrew Dale for interesting discussions about the interactions of AOM with carbonates and iron minerals and non steady state dynamics. This research was financed by the project Mistrals/MERMEX-Rivers and AMORAD (ANR-11-RSNR-0002) and by the National Science Foundation (OCE-1438648).

CHAPTER 8. DEVELOPMENT OF AN IMMOBILIZED METAL AFFINITY CHROMATOGRAPHY (IMAC) METHOD FOR THE ISOLATION OF NATURAL ORGANIC FE-BINDING LIGANDS FROM MARINE PORE WATERS

8.1 Abstract

The composition of organic-Fe(III) detected in both natural sediments and pure culture incubations throughout this thesis are unknown. Thus, an immobilized metal affinity chromatography (IMAC) procedure was developed to isolate and identify the natural ligands involved in the solubilization of Fe(III) oxides. The method was optimized with model hydrophobic iron binding ligands riboflavin and desferroxamine-B through IMAC coupled with solid phase extraction (SPE), reverse phase liquid chromatography (LC), and electrospray ionization mass spectrometry (ESI-MS). More polar iron binding ligands such as citrate and EDTA required normal phase LC with a hydrophilic interaction (HILIC) column and were generally more difficult to observe by ESI-MS, although all complexes were confirmed in both positive and negative mode. Isolation of these model iron binding ligands by this procedure demonstrates its potential for the extraction of natural iron-binding ligands from marine pore waters.

8.2 Introduction

Immobilized metal affinity chromatography (IMAC) is a useful technique to separate biomolecules and other organic ligands. In IMAC, a metal is immobilized on to a solid phase support and metal specific ligands will be retained by the bound metal. The

metal specific ligands can then be eluted and may be further concentrated by solid phase extraction (SPE) or directly analyzed. Surprisingly, application of IMAC to natural settings has been limited. Naturally occurring Cu-complexing ligands have been isolated from seawater using Cu-IMAC (Ross et al., 2003) and the fractionation of soluble humic substances and characterization of their heavy metal complexes has been investigated using Fe(III)-IMAC (Burba et al., 2000). In iron-deprived bacterial cultures, Ni(II)-IMAC was chosen to investigate the production of siderophores and other Fe(III)-responsive species due to the affinity between Ni(II) and hydroxamic acids (Braich and Codd, 2008). However, Fe(III)-IMAC has traditionally been employed for the purification of phosphopeptides and phosphoproteins due to the strong interactions between chelated Fe(III) ions on the IMAC column and phosphate groups (Cao and Stults, 1999; Dobrowolska et al., 1991; Holmes and Schiller, 1997; Muszynska et al., 1992). Interestingly, Fe(III)-IMAC has yet to be employed to separate and identify Fe(III)-binding ligands in natural environments.

Complexation by organic ligands may allow Fe(III) to remain in solution (Hunter and W. BoydA, 2007), thus increasing transport and bioavailability of iron in the oceans (Buck et al., 2007; Gledhill and Buck, 2012; Rue and Bruland, 1995; van den Berg, 1995). Dissolved organic-Fe(III) complexes have been detected in various aquatic environments, including freshwater bogs, salt marshes, river deltas, and continental marine sediments as demonstrated in Chapters 5, 6, and 7 of this thesis. Additionally, dissolved organic-Fe(III) complexes have previously been detected in salt marsh (Bull and Taillefert, 2001; Luther et al., 1996; Taillefert et al., 2007b; Taillefert et al., 2002b), estuarine (Brendel and Luther, 1995; Meiggs and Taillefert, 2011; Taillefert et al., 2002a), and continental shelf (Taillefert

et al., 2000b) sediments. Soluble organic-Fe(III) complexes have also been detected in incubations of several model Fe(III)-reducing bacteria (Jones et al., 2010; Nevin and Lovley, 2002; Taillefert et al., 2007a; Chapter 5 of this dissertation) and of marine sediment (Carey and Taillefert, 2005; Chapters 5 of this dissertation). Although the composition of Fe(III)-ligands is likely different in marine sediments and pure culture incubations, these species have yet to be isolated and characterized.

Isolation of naturally occurring Fe(III)-binding ligands is not a trivial task. Although Fe(III)-IMAC represents a promising technique for isolation and concentration of organic ligands for secondary analysis, several key steps in the experimental design may irreversibly affect the separation of the species of interest. This work evaluated individual steps of a multi-step experimental procedure to improve a previously proposed method (Beckler, 2014) based on an in-depth analysis of the literature. The new method improved the generation of the Fe(III)-Chelex chromatographic column used for the IMAC separation and the natural ligands elution sequence. During early IMAC evaluation, liquid chromatography (LC) was used to separate compounds prior to electrospray ionization (ESI) for mass spectrometry (MS) analysis. After investigation of LC specifics, however, the focus shifted to other steps of the overall method, such as ionization of model Fe(III)-ligands, solid phase extraction (SPE) methods, and methods besides MS to analyze the composition of the IMAC eluate. This work provides a solid foundation for the isolation of natural Fe(III)-binding ligands from marine sediments and pure cultures of Fe(III)-respiring bacteria using Fe(III)-IMAC.

8.3 Experimental Design, Methods, and Chemical Analyses

8.3.1 Microbial Incubations

All chemicals used in this study were of ACS reagent grade and from Sigma-Aldrich unless otherwise noted. The model Fe(III)-reducing bacterium *S. oneidensis* MR-1 was grown anaerobically in a defined minimal salt medium (M1) (Myers and Nealson, 1988) with 15 mM lactate, 60 mM fumarate, and buffered with 9 mM phosphate at pH 7. Cells were harvested in late lag phase and washed for batch incubations. Large scale batch incubations (500mL) were performed with initial cell concentration of approximately $1x10^7$ cell/mL (OD_{600}) in M1 medium with 15 mM lactate, decreased phosphate concentrations (100 µM), 40 mM ferrihydrite, and buffered with 9 mM PIPES at pH 7 by Dr. Hyun-Dong Shin. Small aliquots were taken and analyzed for dissolved Fe^{2+} and organic-Fe(III) compounds using Au/Hg microelectrodes that were prepared, calibrated, and employed as described in previous chapters. At chosen time points, 90 mL of medium was also taken from the incubation and filtered. Samples were frozen until IMAC analysis. For comparison of dissolved Fe^{2+} and organic-Fe(III) compounds only, separate incubations were conducted in specially designed polyetheretherketone (PEEK^{TM}) reactors that include inlet and outlet ports to inject reactants, collect samples, add UHP-N_2 gas lines, and receive an Au/Hg voltammetric microelectrode along with its Ag/AgCl reference and Pt counter electrodes to monitor for iron reduction and the production of organic-Fe(III) complexes in real time in situ (This thesis, Chapter 5).

8.3.2 Natural Samples

Sediments were collected off Cape Lookout, NC, according to the procedure detailed in Chapter 6. Briefly, sediment cores were sectioned in bulk and pore waters collected by centrifuging sections of sediment at 3000 rpm for 5-10 minutes. The unfiltered pore waters were frozen at 4ºC until analysis. Sediments were profiled with Au/Hg microelectrodes as previously described in Chapter 6.

8.3.3 On Column Formation of the Fe(III)-Chelex for IMAC Separation

To correctly complex Fe(III) without precipitation, the pH of the chelex must first be adjusted and a form of Fe(III) which does not complex in solution must be used. Although an iron form of Chelex®-100 is commercially available (Bio-Rad Cat#1422825), the manufacturing process is classified and remains unavailable. Based on personal communications with the manufacturer, a method for sorption of Fe(III) to the Chelex beads was chosen. Initially 1-1.5 g of Chelex®-100 resin was packed into a low-pressure column (Kontes, Flex-column). It is important to note that the size of the Chelex beads dramatically changes based on its form and pH. For example, the resin volume in water in its Na-form is 1.00 while the volume of the H-form is 0.45. These effects must be accounted for when packing the column, and the column size may need to be adjusted to account for bead expansion or shrinking. After the Chelex beads are in the column, the beads must be converted to the Na-form if they are in any other form. This can be accomplished by washing the beads with ~15 mL of 1 M NaOH injected into the bottom of the column using a low speed peristaltic pump (Ismatec®). The pH may then be lowered with ~15 mL of a 0.5 M sodium acetate solution at pH 5.7. A 5 mL solution of 100 mM $Fe(NO_3)_3$ in 0.5 M

sodium acetate (pH 5.7) may then be slowly eluted through the column, followed by a sodium acetate solution at pH 5.7 to rinse the beads of the excess Fe(III) until the effluent is colorless (~10 mL). Using this procedure, the beads should be completely complexed by Fe(III), and any pH changes should not precipitate Fe(III) oxides in the column.

8.3.4 IMAC Sample Loading and Elution of the Retained Fe(III)-Binding Ligands

Samples were loaded onto the Fe(III)-Chelex-packed low-pressure column at a flow rate of 0.05 mL/min. The column was then rinsed with three column volumes of deionized water, or the preferred rinse solution depending on the type of sample extracted. After the rinsing step, the Fe(III)-binding organic ligands were eluted with ~10 mL of 1 M NaOH.

8.3.5 Validation of the IMAC Separation Procedure

On three separate IMAC columns, 90 mL samples of 0.1 mM DFOB, filtrate of *S. oneidensis* MR-1 incubations after 27 hours, and M1 medium, as a blank, were loaded. The columns were eluted with 20 mL of 0.5 M NaOH and fractions were collected. The fractions were analyzed for pH (sym**pH**ony), and absorbance (Beckman-Coulter DU720) at 254 and 450 nm before and after an Fe(III) addition assay with 3.3 mM $Fe(ClO_4)_3$ in 0.073 M $HClO_4$ (Carson et al., 1992).

8.3.6 Solid Phase Extraction (SPE) Procedure to Concentrate Fe(III)-Binding Ligands

Solid phase extraction (SPE) was performed in two subsequent steps to concentrate both basic and acidic Fe(III)-binding organic ligands and simultaneously remove salts from marine samples to facilitate MS analyses (Figure 8-1).

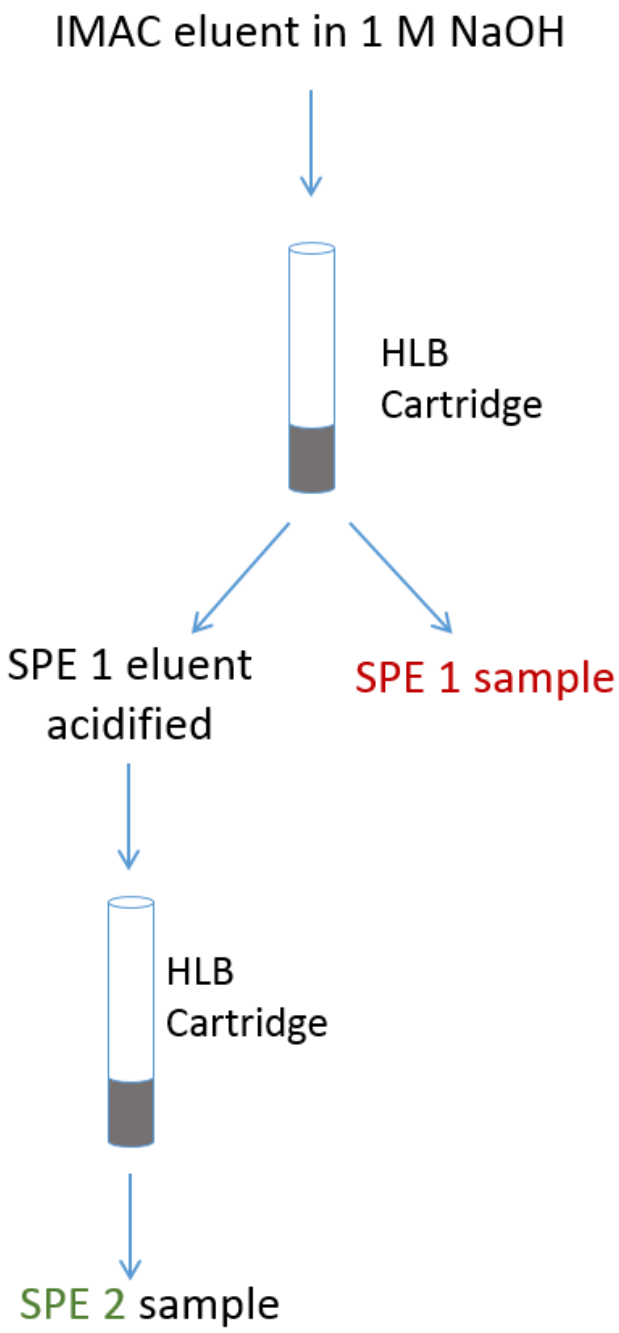

Figure 8-1. Solid phase extraction scheme used to preconcentrate the separated Fe(III)-binding ligands. The IMAC eluate is first passed through the HLB cartridge and collected for a second extraction. The ligands of interest retained on the HLB cartridge are then eluted with the appropriate solvent and collected as the SPE1 fraction. The eluate initially collected from the HLB cartridge is then acidifed and passed through a second HLB cartridge. The ligands concentrated on the second HLB

cartridge are then eluted with the appropriate solvent and collected as the SPE2 fraction.

For the first extraction (SPE1), solid-phase extraction cartridges (Supelco, Select HLB SPE tube 60 mg) were initially conditioned and rinsed by gravity elution with 3 mL of 50/50 (v/v) methanol/acetonitrile (MeOH/ACN) and 3 mL of deionized water. The IMAC eluate (a 1 M NaOH matrix) was then added to the HLB cartridge to concentrate basic organic ligands, and the SPE1 eluate was collected for the second extraction in acidic conditions (see below). The retained compounds were subsequently eluted with 1 mL 50/50 (v/v) MeOH/ACN in 2% acetic acid. The samples may be evaporated by blowing UHP N_2 gas over them, then reconstituted in 200 µL of 50/50 (v/v) MeOH/ACN with 2% acetic acid to form the final SPE1 sample. The SPE1 eluate was then acidified with concentrated HCl (~0.4 mL conc. HCl for 10 mL sample) for the second extraction of acidic compounds (SPE2). The same HLB cartridge was conditioned again with 3 mL of 50/50 (v/v) methanol/acetonitrile (MeOH/ACN) and rinsed with 3 mL of deionized water. The acidified sample was eluted through the column, then the retained ligands subsequently eluted with 50/50 (v/v) MeOH/ACN in 2% ammonium hydroxide, evaporated, and reconstituted to form the final SPE2 sample.

8.3.7 Liquid Chromatography (LC) Separations

Liquid Chromatography may separate ligands directed before ESI-MS detection, and could increase sensitivity of compounds which do not easily ionize. Reverse phase (RP)-LC separates hydrophobic compounds and was conducted on a Phenomenex Gemini C18 column (2x150 mm). Gradient elution was run with two solutions: A) 95:5% water:ACN ratio and B) 5:95% water:ACN ratio. The run was isocratic with 100% A for

the first 7 minutes, then a linear gradient from 100% A to 100% B from 7 to 44 minutes was implemented, followed by isocratic separation with 100% B from 44 to 52 minutes, linear gradient from 100% B to 100% A from 52 to 53 minutes, and finally isocratic with 100% A from 53 to 60 minutes. The flow rate was 200 µL/min with a pressure of 400 psi and a sample loop of 20 µL.

Hydrophilic interaction liquid interface chromatography (HILIC) is a type of normal phase LC used to separate hydrophilic compounds and was run on a SeQuest ZIC-HILIC column (2x100 mm) using another gradient elution method with eluent: A) 5:95% water:ACN ratio; and B) 95:5% water:ACN ratio. The separation was isocratic with 100% A for the first 5 minutes, then a linear gradient from 100% A to 40% B 60% A betweeen 5 to 45 minutes was implemented, followed by isocratic separation with 40% B and 60% A from 45 to 50 minutes, a linear gradient from 40% B 60% A to 100% A from 50 to 51 minutes, then isocratic with 100% A from 51 to 60 minutes. The flow rate was 100 µL/min with a pressure of 400 psi and 10 µL of sample injected.

8.3.8 Analyses by Electrospray Ionization-Mass Spectrometry (ESI-MS)

Samples were analyzed by ESI-MS in both the positive and negative modes and data was collected for the mass range 150-1000 m/z using a triple quadrupole mass spectrometer (Micromass Quattro LC). When LC was not interfaced to ESI-MS, samples were either run directly by infusion or after a 1:1 dilution with 4% acetic acid in MeOH. When LC was interfaced to the MS, the analysis of the resulting total ion chromatograms (TIC) was performed manually and extracted ion chromatograms (EIC) of the expected ions were generated when necessary. Sample adducts were determined using a premade

template (http://fiehnlab.ucdavis.edu/staff/kind/metabolomics/ms-adduct-calculator) (Huang et al., 1999).

8.4 Results and Discussion

8.4.1 Formation of Fe(III)-Chelex for IMAC separation

Before Fe(III)-IMAC separation can be utilized to separate Fe(III)-binding ligands, the Fe(III)-IMAC column must be prepared. In this work the chelating cation-exchange resin Chelex®-100 was chosen as the stationary phase. Chelex consists of a cross-linked polystyrene matrix with iminodiacetic acid (IDA) as the functional group. IDA is a "tridentate" chelator which binds metal ions through two carboxylate oxygens and a nitrogen atom. When bound to IDA, metals retain 1-3 coordination sites which can bind other ligands. The formation of this ternary complex between the chelate (IDA), bound metal, and additional metal binding ligands leads to retention in IMAC. The chosen method was determined based on understanding of the reactions between IDA and Fe(III) and did not result in any observable iron precipitate. While much is known about the sorption of divalent cations to chelex, little is known about the sorption of trivalent metals. The sorption of Fe(III) to IDA has a net positive charge versus the net neutral charge obtained with Fe(II), and results in a much more efficient cation exchange resin (Holmes and Schiller, 1997). Unfortunately, sorption of Fe(III) to Chelex is challenging due to the precipitation of Fe(III) at circumneutral pH.

Chelex®-100 is usually sold in the Na-form, and has a pH around 11. At this high pH, IDA is negatively charged and its structure is open, allowing cations to easily bind (Figure 8-2). However due to the high pH, addition of $FeCl_3$ will result in immediate

precipitation. Chelex-100 has a high affinity for H^+, and washing with 1 M HCl immediately converts the Na-form to the H-form. In the H-form the IDA structure is flat and functions as a weak anion exchange resin instead of its usual cation exchange form (Figure 8-2). In the anion exchange form, the ammonium groups of the IDA are able to sorb negatively charged metal complexes with different efficiency depending on the stability of the metal with the ligand (Heitnerwirguin and Markovits, 1963; Samczynski, 2006). Unfortunately, the strength of the chloro complexes of Fe(III) is so high that addition of $FeCl_3$ to Chelex®-100 in the H-form does not truly complex Fe(III) to the resin and instead results in the precipitation of Fe(III) oxides when the pH is raised to circumneutral values (Matsuura et al., 2008).

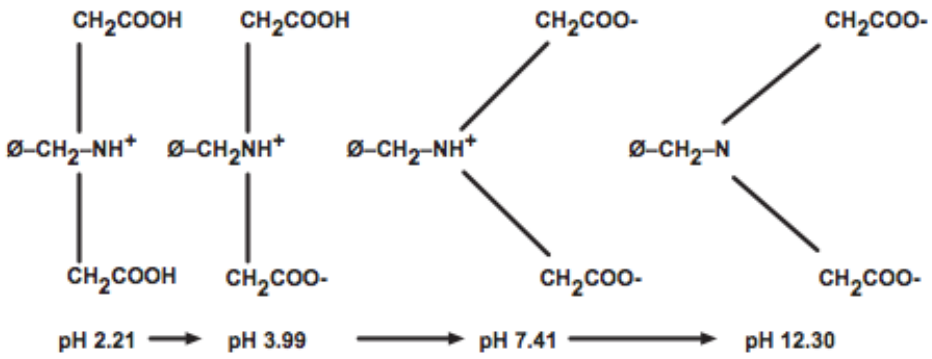

Figure 8-2. Zwitterionic forms of IDA in Chelex®-100 as a function of pH.

Previous reports have been unclear about the exact Fe(III)-loading procedure on the Chelex®-100 resin. Some reports only indicated that "Chelex 100 was loaded at pH values of 5-6 to 90% of its capacity with Fe(III)" (Burba et al., 2000). Others have mentioned the use the H-form without indicating how Fe(III) was loaded (Atzei et al., 2001) or provided the type of Fe(III) complexes used (i.e., $Fe(NO_3)_3$) but not the Chelex form (Sanchiz et al.,

1999). A few studies have described addition of $FeCl_3$ to an undescribed from of Chelex with at least 2 hours of continuous mixing followed by washing with excess water (Cao and Stults, 1999; Muszynska et al., 1992; Uygun et al., 2015). This method with additional mixing time may be acceptable for sorption of Fe(III) to the Chelex but requires to load the column after Fe(III)-binding. In addition, the rapid succession of washing steps may not provide sufficient time for Fe(III) to complex with the Chelex beads. Finally, insufficient rising of the Fe(III) loading solution before subsequent elution steps results in unbound Fe(III) that may precipitate at circumneutral pH. Although Fe(III) precipitates may be able to isolate Fe(III)-binding ligands, their efficiency is likely not as good as a Fe(III) ion and by definition is not *immobilized* metal affinity chromatography. The method used in the present study did not result in any observable iron precipitate. It required to reduce the pH of the Na-form of the Chelex®-100 once it was loaded on the column with a 0.5 M sodium acetate solution at pH 5.7, then slowly eluting 5 mL of a 100 mM $Fe(NO_3)_3$ solution in 0.5 M sodium acetate (pH 5.7), and washing the excess Fe(III) using a sodium acetate solution at pH 5.7.

8.4.2 Determination of Ligand Elution Method

Three methods are typically used for elution of ligands from IMAC columns: ionic strength gradient, competitive elution, and pH gradient. Often multiple influences on the stationary phase-ligand relationship must be considered. For example, an increase in ionic strength with 3 M NaCl eluent resulted in desorption of peptides from Fe(III)-IMAC at a pH 0.5 units lower than with 1 M NaCl (Muszynska et al., 1992).

Decreasing the ionic strength may cause elution as some compounds may bind to the stationary phase via hydrophobic interactions (Li et al., 2001). In the present study, the ionic strength gradient method was not investigated further given the range of ionic strength encountered in natural samples where dissimilatory Fe(III) reduction is known to exist.

Competitive elution may occur with Fe(III)-binding ligands such as orthophosphates, which outcompete phosphopeptides on the Chelex-Fe(III), or with a ligand binding cation such as Mg(II), which binds to the phosphate groups of phosphopeptides and desorbs them from the Chelex-Fe(III) resin (Holmes and Schiller, 1997). Strong Fe(III) ligands such as EDTA may even strip the Fe(III) from the stationary phase (Beckler, 2014). When coupling IMAC to LC-ESI-MS analysis, however, excess Fe(III) in the samples may reduce LC sensitivity by converting a C18 column (RP) to an unwanted version of IMAC (Seidler et al., 2011; Winter et al., 2009). The use of excess Mg(II) may result in the same issues. In addition, Mg(II) is not known to compete with ligands lacking phosphate groups (Holmes and Schiller, 1997), therefore limiting its use for environmental samples. Finally, large concentrations of competitive ligands may negatively affect the LC-ESI-MS by co-elution and decrease in ionization of desired compounds (Peri-Okonny, 2001). In this regard, competitive ligands such as orthophosphates may not be suitable for ESI-MS.

In the pH gradient method, a decrease in pH may completely strip the Fe(III)-ligands from the solid phase but also introduce excess Fe(III) to any LC system coupled to ESI-MS. In turn, raising the pH to alkaline values allows hydroxyl ions to outcompete ligands on the Fe(III)-Chelex without addition of any species to solution that could

complicate LC-ESI-MS or direct ESI-MS analyses. Adsorption of phosphoamino acids, phosphopeptides, phosphoproteins, and their non-phosphorylated counterparts demonstrates specific elution patterns with increased pH, demonstrating that adjacent carboxylic and phenolic groups may cooperatively increase binding to the immobilized Fe(III) at circumneutral pH (Muszynska et al., 1992). Multiple studies using IMAC to isolate compounds of interest have preferred increased in pH as elution method (Burba et al., 2000; Cao and Stults, 1999; Kavaklı et al., 2014; Muszynska et al., 1986; Muszynska et al., 1992; Uygun et al., 2015). Therefore, increase in pH appears to be the best method for elution of all ligands without addition of another compound which may negatively affect subsequent steps in the analysis of the Fe(III)-binding ligands.

8.4.3 Identification of Model Fe(III)-Binding Organic Ligands by LC-ESI-MS

Following preliminary results (Beckler, 2014), it was determined that the LC-ESI-MS method could be optimized for better detection of model Fe(III)-binding organic ligands and ultimately natural Fe(III) complexes from marine pore waters. Indeed, metal-ligand complexes have previously been identified by LC-ESI-MS (Ross et al., 2000). Four well known Fe(III)-binding ligands: riboflavin, deferoxamine-B (DFOB), citrate, and ethylenediaminetetracetic acid (EDTA), were chosen to represent both polar and nonpolar compounds with a range of acidities to investigate LC-ESI-MS parameters. Riboflavin (376.37g/mol) is a hydrophobic bidentate ligand with pK_as at 4.0 and 10.2. Endogenous production of riboflavin has been observed during dissimilatory iron reduction by *Shewanella* sp. (Marsili et al., 2008). DFOB (560.69 g/mol) is a hydrophobic ligand with high specificity for Fe(III) and pK_as of 7.9 and 10.2 that is often used as a model siderophore (Kalinowski et al., 2000; McCormack et al., 2003). Citrate (192.12g/mol) and

EDTA (292.24 g/mol) are both small, hydrophilic multidentate ligands known to bind Fe(III). The pK_as for citrate are 3.1, 4.7, and 6.4, whereas the pK_as of EDTA are 2.0, 2.7, 6.2, and 10.3.

Understanding general LC and MS characteristics allows insight into which method results in the best detection of each standard (Kiontke et al., 2016; Peri-Okonny, 2001). According to MS theory, basic compounds should ionize better at pH values below their pK_as, and therefore better detection of compounds containing amines, amides, and carbonyls would be expected in positive ion mode (Peri-Okonny, 2001) A mobile phase 1-2 pH units below the pK_a of the sample is suggested, and adding an acidic reagent may also increase the sensitivity in positive ion mode (Peri-Okonny, 2001). On the other hand, acidic compounds ionize better at pH values above there pK_as, therefore increased detection of compounds containing carboxyl and phenolic hydroxyls is expected in negative ion mode (Peri-Okonny, 2001). Mobile phases at higher pH and addition of a base may increase the sensitivity in negative ion mode (Peri-Okonny, 2001). To ionize neutral compounds, it is often suggested to add a volatile salt such as ammonium acetate to increase ionization (Peri-Okonny, 2001). In RP-LC, hydrophilic compounds elute immediately due to their solubility in water, while hydrophobic compounds are typically retained in aqueous solutions and elute with increasing percentage of organics in the eluent. The opposite is true with HILIC columns which prefer a gradient from high to low organic content in their eluent. In recent years, HILIC has becoming increasingly popular and has been used to analyze a variety of compounds not well detected by RP (Periat et al., 2015). Overall, it is expected that the detection of riboflavin and DFOB would be best achieved with RP-LC and ionization at a lower pH with analysis in the positive ion mode. In turn, citrate and

EDTA, or similar polar compounds, would immediately elute and not be detected by RP-LC-ESI-MS. Instead, citrate and EDTA would be easily detected with HILIC and ionization at an increased pH in the negative ion mode.

To investigate the efficiency of LC-ESI-MS separation, a mixed standard made of 40 µM riboflavin, 600 µM citrate, 600 µM EDTA, and 600 µM DFOB was prepared to reflect concentrations found in sediments. A mixed sample was assumed to be the best method to minimize the number of MS runs as compounds should be separated by LC prior to ionization. After RP-LC, adducts of riboflavin and DFOB were observed in positive ion mode (Figure 8-3A) and to a lesser extent negative ion mode (Figure 8-3B), however

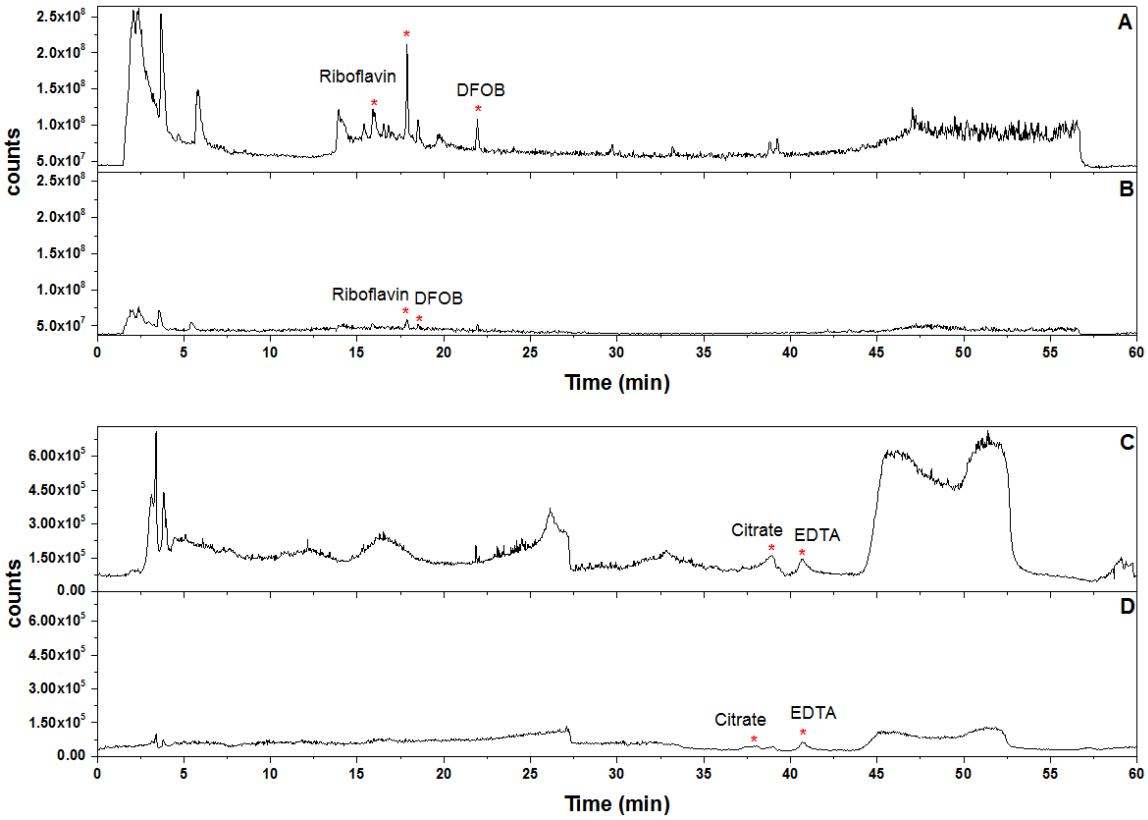

adducts of EDTA or Citrate were not detected. In turn, after HILIC-LC, Citrate and EDTA adducts were detected in both positive (Figure 8-3C) and negative (Figure 8-3D) ion modes, however riboflavin and DFOB were not detected.

Figure 8-3 Total ion chromatogram (TIC) of standard mixtures after either RP-LC in A) positive and B) negative ion mode, or with HILIC-LC in C) positive and D) negative ion mode. Peaks corresponding to standard compounds are denoted with red stars.

Although some peaks were observed after searching for adduct masses, signals were relatively low, suggesting that identification of peaks in TICs without knowledge of the mass of the species of interest would be difficult. Therefore, to investigate the other steps in the separation procedure (i.e., IMAC separation, SPE concentration, and direct ionization) and the effect of additives to increase MS ionization efficiency, LC was put aside. Eventually, LC could be reintroduced, and would result in better detection of compounds if the correct mobile and stationary phases are used.

8.4.4 Identification of Model Fe(III)-Binding Organic Ligands by ESI-MS

Samples were injected directly into ESI-MS to investigate fractionation and formation of adducts during ionization. EDTA was chosen to represent small, polar ligands and DFOB represented larger, nonpolar ligands. In negative ion mode, all samples displayed peaks at 205 m/z (Figure 8-4). Both the blank and EDTA showed peaks at 295 m/z. Beginning at 311 m/z, the blank had three successive and decreasing peaks 14 units apart. Similar peaks were observed in the EDTA samples as well, although they began at 313 m/z and the subsequent peaks were 20 units apart. The peak at 313 m/z may represent $[M+Na-2H]^-$. In DFOB, peaks were observed at 240, 400, 441, and 600.5 m/z. Although the peak at 600.5 m/z was quite intense, it did not represent the m/z of any known adduct.

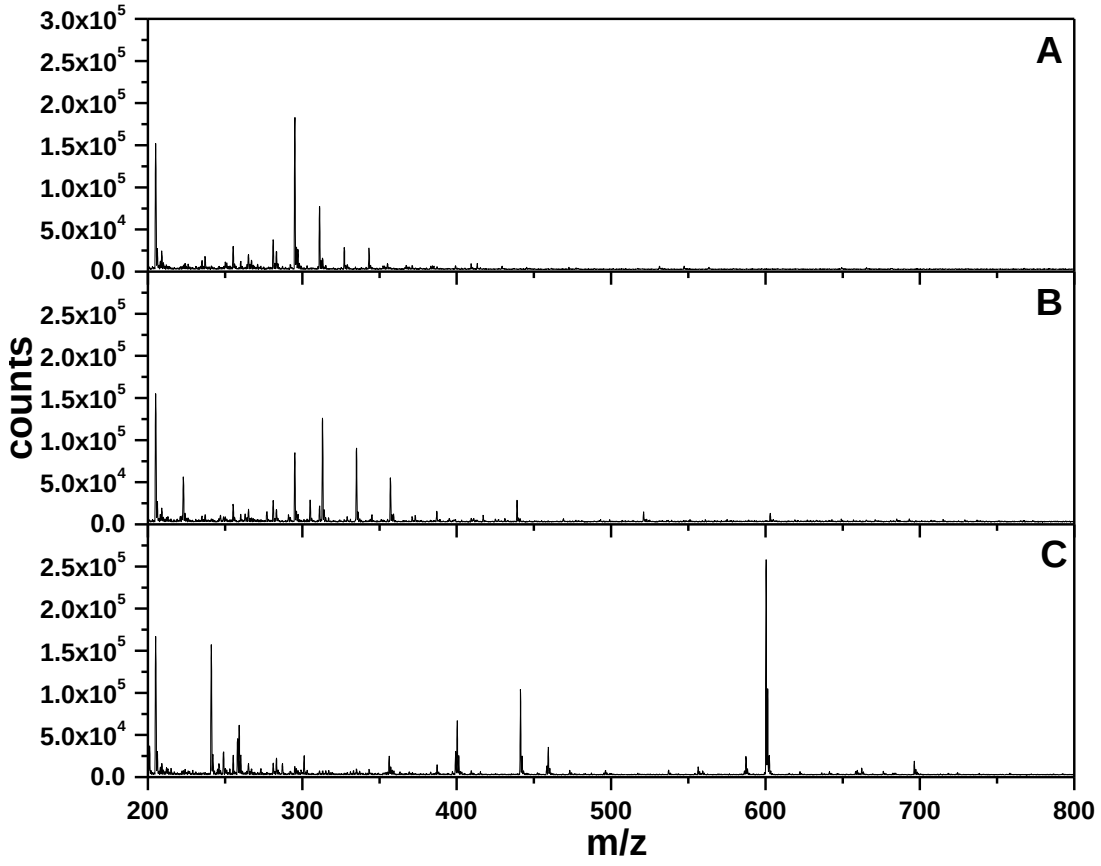

Figure 8-4. Mass spectra of: A) deionized water; B) 1 mM EDTA; and C) 1 mM DFOB in negative ion mode with 2 % ammonium hydroxide.

In positive ion mode, peaks were observed in both the blank and EDTA sample at 643 m/z (Figure 8-5). A relatively large peak was observed at 227 m/z for EDTA, but did not relate to any known adducts. For DFOB, major peaks were observed at 362 m/z, which did not correlate to any known adducts, and 562 m/z, which corresponded to $[M+H]^+$.

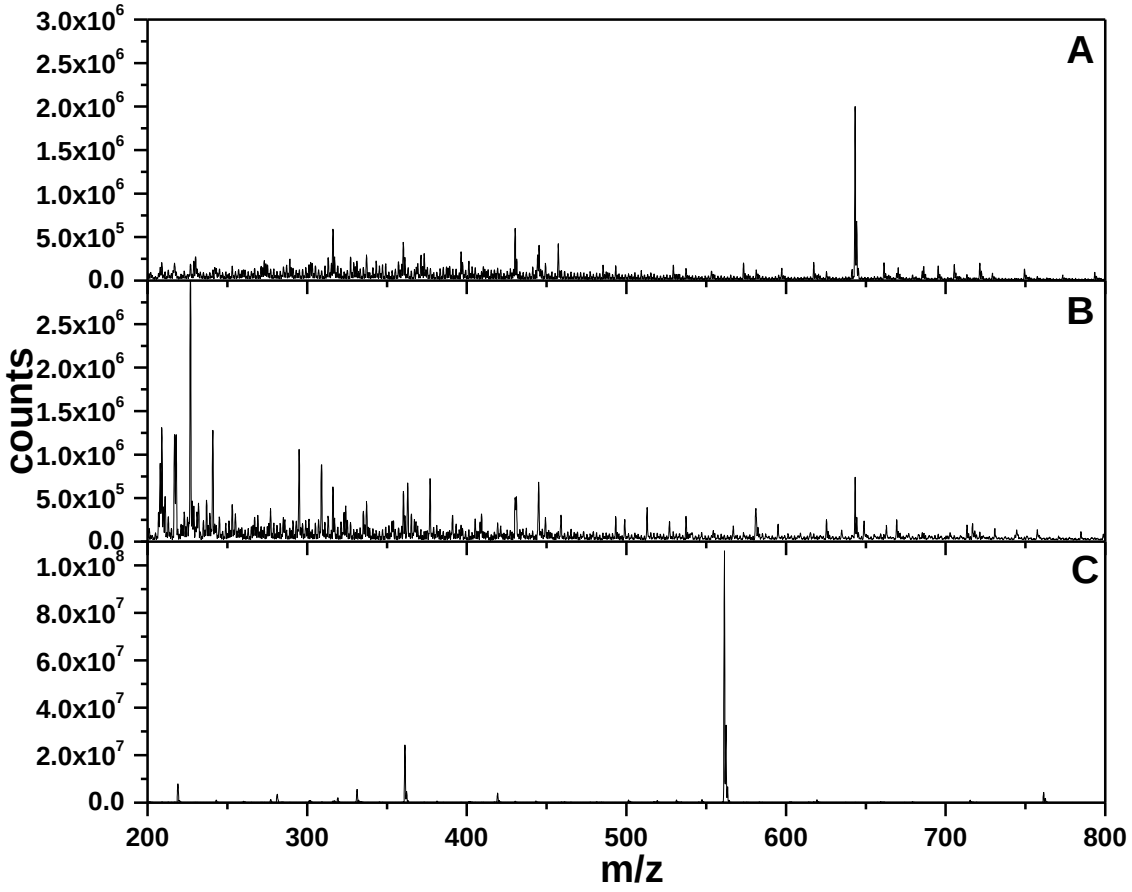

Figure 8-5. Mass spectra of: A) deionized water; B) 1 mM EDTA; and C) 1 mM DFOB in positive ion mode with 2 % acetic acid.

Characterization of ETDA by MS has historically presented challenges due to its easy fragmentation, structural similarities to matrix background, rapid complexation to many metals, and small concentrations in natural samples. To overcome these issues, some studies have investigated the complexation of EDTA to metals prior to analysis (Baron and Hering, 1998; Chen et al., 2008) or as metal-EDTA complexes in natural samples (Collins et al., 2001; Knepper et al., 2005; Orera et al., 2010). Therefore, to assess if Fe(III)-ligand complexes may be easily detected by MS, $FeCl_3$ was added to all samples ran in positive mode (Figure 8-6). Similar peaks were observed in all three solutions before 500 m/z, with

no other clear peaks observed in the blank or with ETDA. However, with DFOB, a peak corresponding to $[M+Fe]^+$ was observed at 615 m/z.

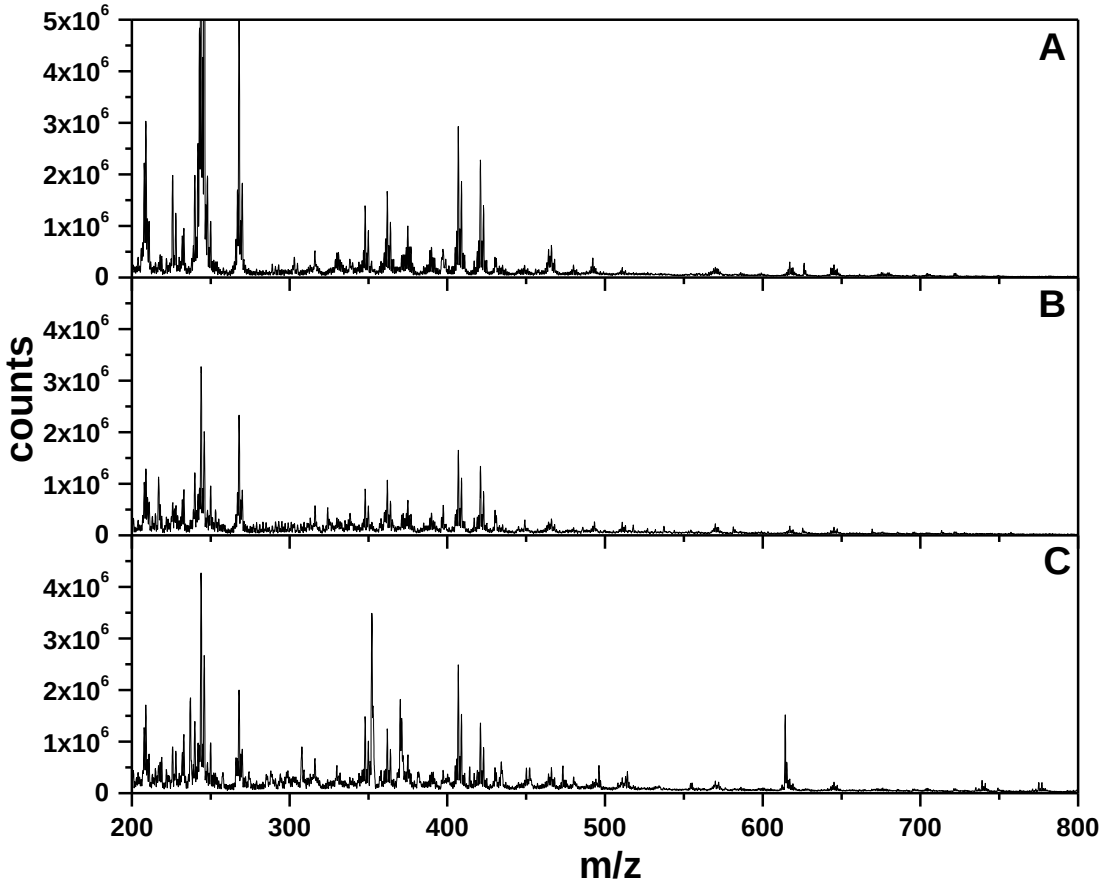

Figure 8-6. Mass spectra obtained after addition of $FeCl_3$ to samples of A) deionized water, B) 1 mM EDTA, and C) 1 mM DFOB in positive ion mode with 2 % acetic acid.

Although Fe(III)-DFOB resulted in a MS signal (Figure 8-6C), uncomplexed DFOB produced a much higher signal (Figure 8-5C). As no distinct peak was observed for EDTA in any of the conditions, it was determined that future work would focus only on hydrophobic ligands only. The results with Fe(III) indicated that complexation did not increase ionization in the positive ion mode with these ligands, and was not explored

further. Negative ion mode was not run on samples amended with $FeCl_3$ due to precipitation of Fe(III) oxides at basic pH; future work could investigate different forms of Fe(III) which may be more easily complexed by ligands without precipitation and result in higher ionization of Fe(III)-ligands. Whereas complexation by Fe(III) prior to ionization would not be suitable if LC is employed before ESI-MS analysis, investigation of Fe(III) complexation prior to ESI-MS may be promising.

8.4.5 Efficiency of the SPE Concentration Procedure with Model Fe(III)-Binding Ligands

To evaluate the efficiency of the SPE concentration procedure, riboflavin and DFOB were analyzed by ESI-MS after both SPE1 and SPE2 separations without IMAC, in both positive and negative ion modes (Figure 8-7). Standards were prepared in 1 M NaOH solutions so as to be similar to samples eluted by IMAC. After SPE1 separation of DFOB (Figure 8-7A), a peak corresponding to $[M+Na]^+$ was observed in the positive ion mode, whereas peaks for $[M-H]^-$ and $[M+Cl]^-$ were observed in the negative mode. After SPE2 separation (Figure 8-7B), clear peaks corresponding to $[M+2H]^{2+}$ and $[M+H]^+$ were observed in positive ion mode, however, the peak observed after SPE1 separation for $[M+Na]^+$ was no longer detected. The same peaks for $[M-H]^-$ and $[M+Cl]^-$ were observed in negative ion mode after SPE2 separation as observed after SPE1. Peaks corresponding to known adducts were not observed after SPE1 of riboflavin in either positive or negative ion mode (Figure 8-7C). However, after SPE2 (Figure 8-7D), a clear peak corresponding to $[M+Na]^+$ was observed in positive ion mode, along with two small peaks for for $[2M-Na]^{2+}$ and $[2M+K]^{2+}$. In negative ion mode, peaks corresponding to $[M-H]^-$, $[M+Cl]^-$, and $[M+HAc+H]^-$ were observed.

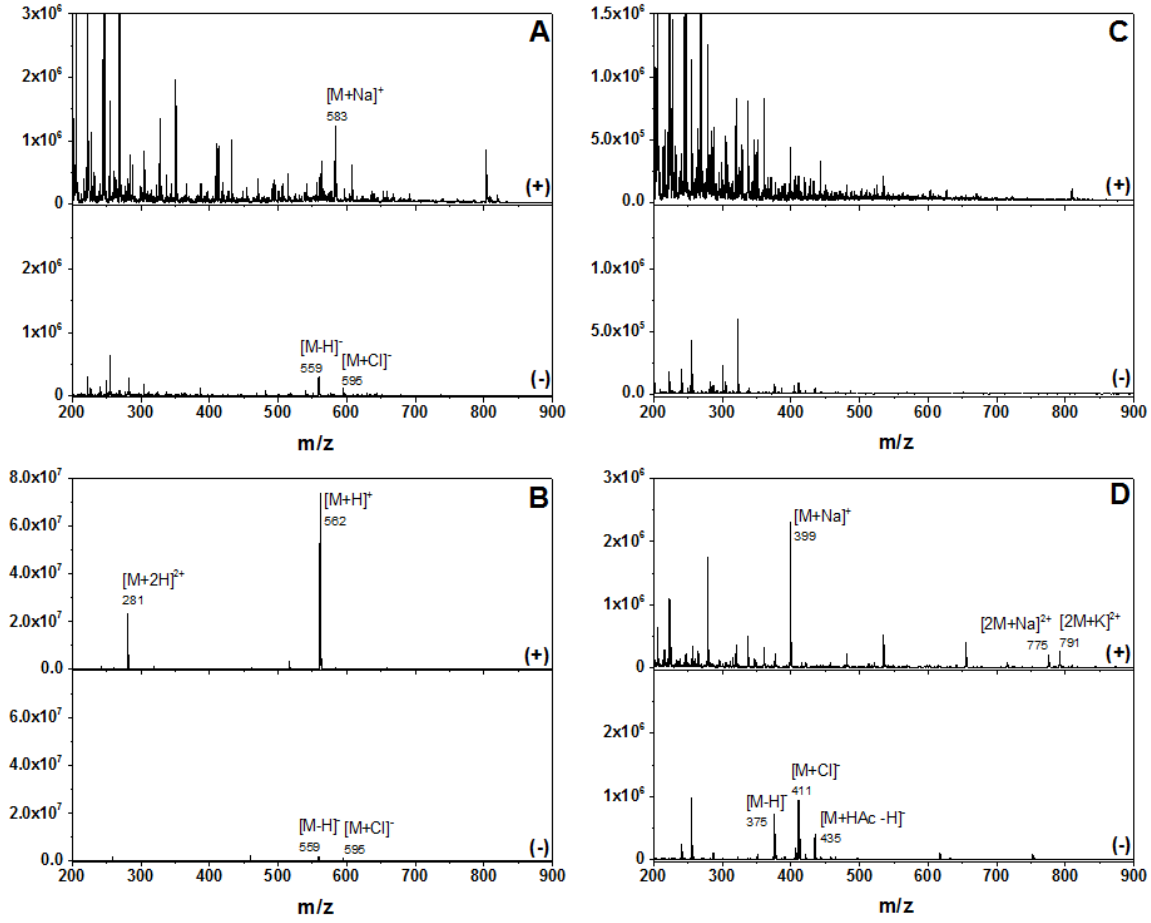

Figure 8-7. Mass spectra collected in both positive (+) and negative (-) mode from SPE-ESI-MS samples of 1 mM DFOB after: A) SPE1 and B) SPE2 sequential extraction, and 0.2 mM riboflavin after C) SPE1 and D) SPE2 sequential extraction.

Given that basic compounds should be retained in SPE1 while acidic compounds are expected to be retained better in SPE2, it is slightly surprising that DFOB was detected better in the SPE2 sample. Riboflavin was also more strongly retained in the SPE2 sample. Both species produce more intense peaks in positive mode as expected. In the current SPE scheme, sequential elution of SPE1 and SPE2 could slightly decrease the concentration of ligand reaching SPE2, therefore future work should focus on SPE2 only for these specific ligand types.

8.4.6 Combined IMAC-SPE-ESI-MS Separation, Preconcentration, and Analysis of Model Fe(III)-Binding Organic Ligands

Building on the experimental steps, riboflavin and DFOB were analyzed after IMAC-SPE-ESI-MS in the positive ion mode (Figure 8-8). The SPE1 step was skipped and only SPE2 was performed. Both species produced clear peaks in positive ion mode. Peaks were observed corresponding to $[M+H]^+$ and $[M+Na]^+$ for riboflavin (Figure 8-8A) and $[M+H]^+$ and $[M+Fe]^+$ for DFOB (Figure 8-8B). The results demonstrate the ability of the current IMAC-SPE procedure to isolate known Fe(III)-binding ligands. Detection of $[M+Fe]^+$ with DFOB suggests that some iron is still stripped from the Chelex resin during IMAC elution and its concentration has to be determined if LC is to be re-introduced into the experimental sequence.

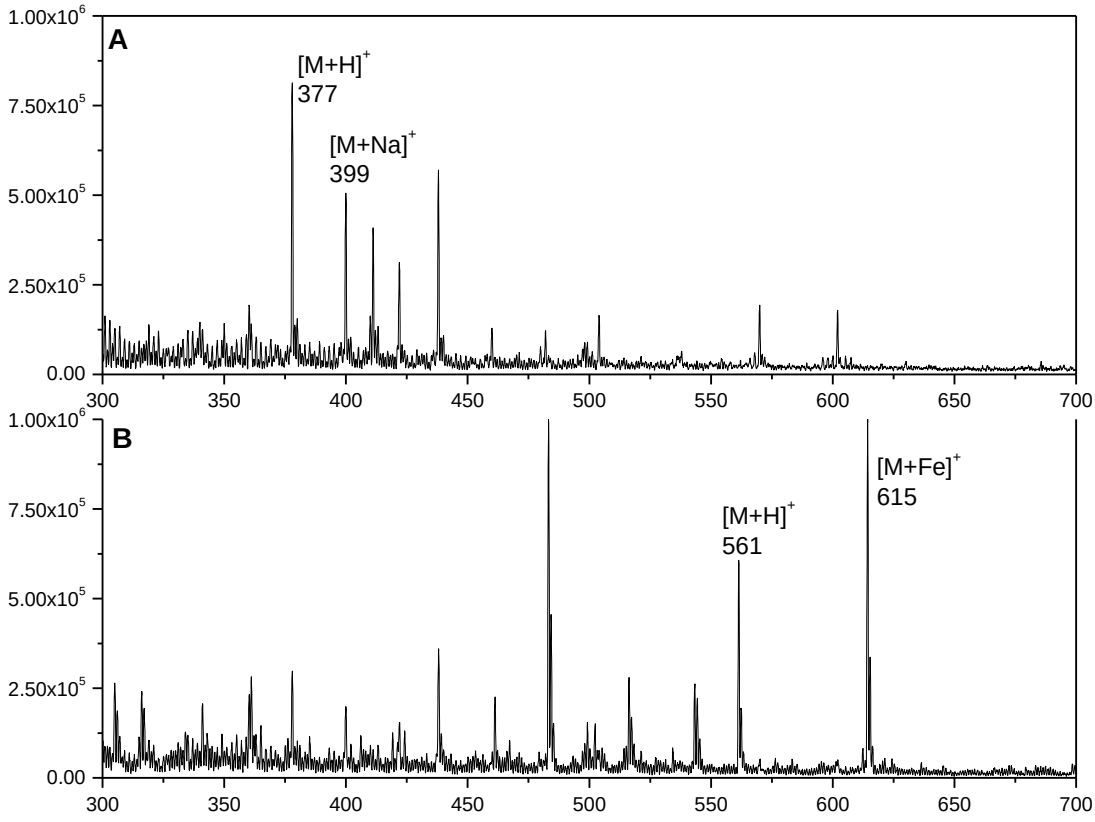

Figure 8-8. Mass spectra in the positive ion mode of 20 mL of: A) 0.2 mM Riboflavin; and B) 1 mM DFOB separated, preconcentrated, and analyzed by IMAC-SPE-ESI-MS.

Given that increased adsorption of organic ligands to Fe(III)-chelex is observed at decreased pH (Muszynska et al., 1992). It was suspected that decreasing the pH of the sample prior to concentration by IMAC would increase detection by MS. Therefore, samples of DFOB at initial pH of 2.6, 4, 6, and 7.6 were investigated by ESI-MS (Figure 8-9). Large peaks corresponding to $[M+H]^+$ were observed in all samples in the positive ion mode. The largest peak was observed from the sample at initial pH 6, but there was no clear trend with pH. Clear peaks were also observed at 462, 484, and 516 m/z although

they do not correspond to known adducts. As no obvious benefit was found from decreasing sample pH prior to IMAC, the pH of future samples was unaltered.

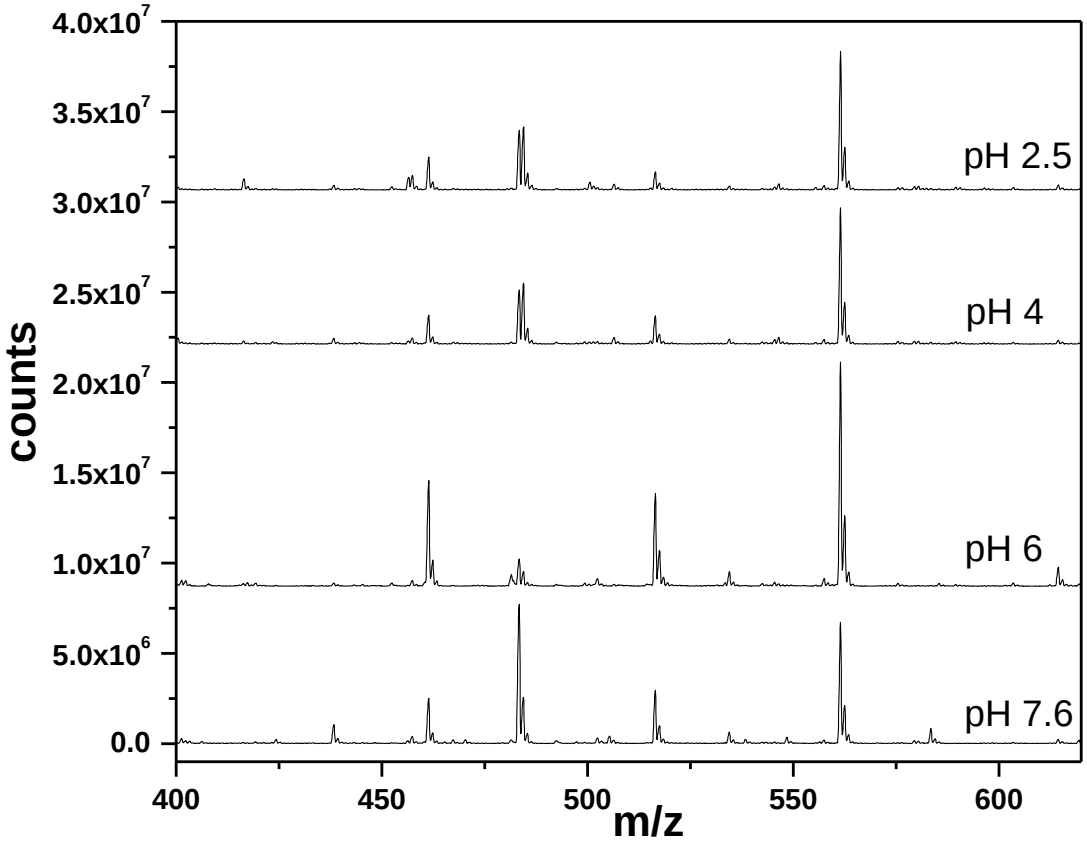

Figure 8-9. Mass spectra in the positive ion mode of 20 mL 1 mM DFOB adjusted to different initial pH values and separated, preconcentrated, and analyzed by IMAC-SPE-ESI-MS.

8.4.7 Retention of Microbially-Produced Fe(III)-Binding Ligands on the IMAC Column and IMAC-SPE-ESI-MS Analysis of the Supernatant of Shewanella Cultures

Voltammetric analysis of *S. oneidensis* MR-1 anaerobic incubations in the presence of 2L-ferrihydrite demonstrated production of electrochemical peaks corresponding to Fe^{2+} and organic-Fe(III) complexes (**Figure 8-10**), and concentrations mirrored results of previous incubations (Figure 8-11). Indeed, org-Fe(III) has been previously detected during DIR (Beckler et al., 2015; Fennessey et al., 2010; Jones et al., 2010; Nevin and Lovley, 2002; Taillefert et al., 2007a) as organic ligands may non-reductively solubilize solid Fe(III), allowing Fe(III) to be brought into the cell prior to reduction.

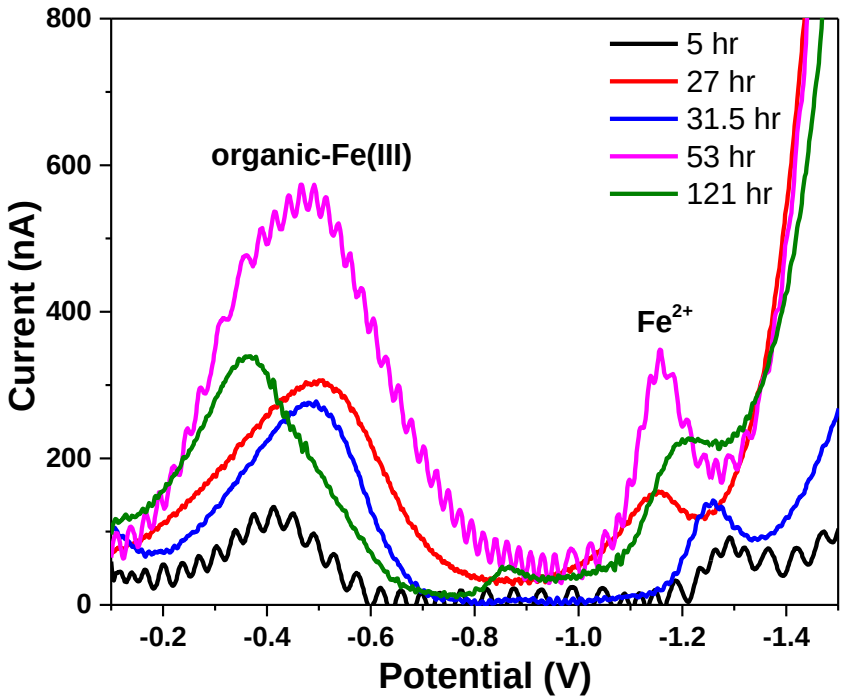

Figure 8-10. Voltammetric scans showing peaks corresponding to organic-Fe(III) complexes and Fe^{2+} produced over time in anaerobic incubations of *S. oneidensis* MR-1 on 2L-ferrihydrite.

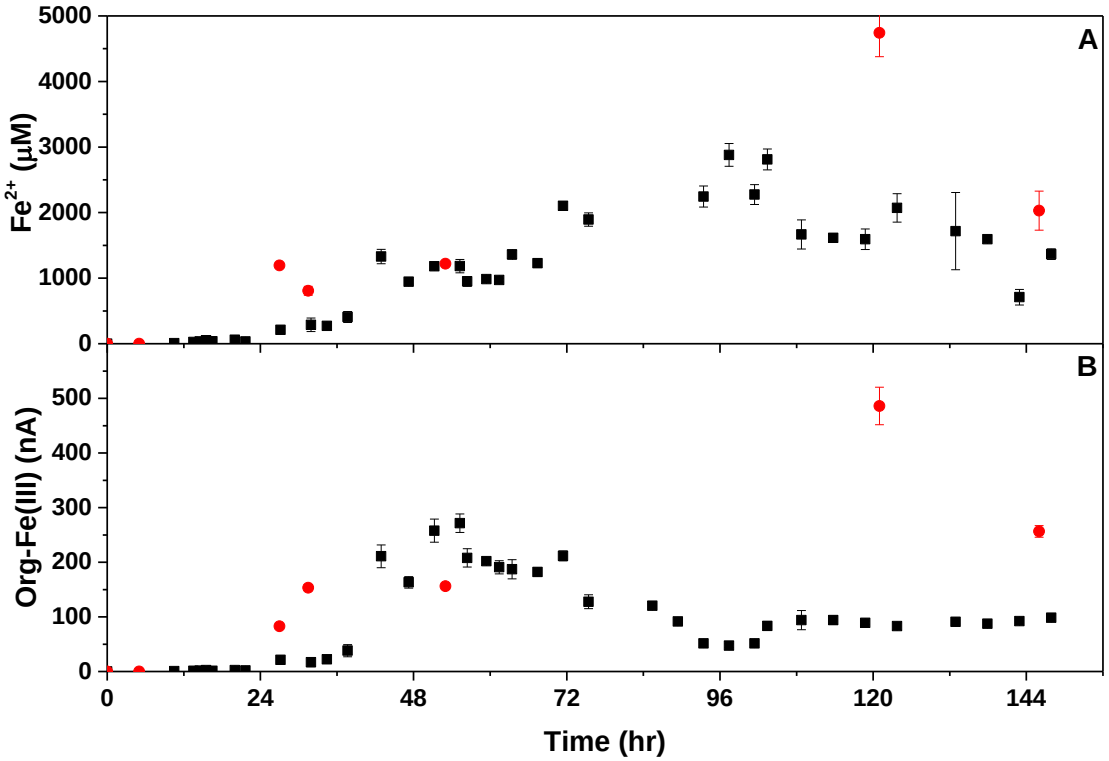

Figure 8-11. Electrochemical detection of A) dissolved Fe^{2+} and B) organic-Fe(III) during incubation of *S. oneidensis* MR-1 with 40 mM 2L-ferrihydrite in modified M1 medium used for IMAC (red circles) compared to a previous replicate incubation conducted with in situ voltammetric analysis (Chapter 5) (black squares).

Besides mass spectrometry, a variety of other methods exist to investigate IMAC efficiency. Absorbance around 254 nm has been used to assess IMAC retention of nucleotides (Dobrowolska et al., 1991), humic acids (Burba et al., 2000), siderophores (Simionato et al., 2010), and Cu-binding ligands (Ross et al., 2003). Siderophores have also been detected at 450 nm using an Fe(III) addition assay (Braich and Codd, 2008; Carson et al., 1992; Dilworth et al., 1998; Soe and Codd, 2014).

To investigate the ability of spectrophotometric methods to evaluate Fe(III)-IMAC, 90 mL each of 0.1 mM DFOB, filtered supernatant collected from incubations of *S. oneidensis* MR-1 with ferrihydrite after 27 hours (corresponding to 1.19 ± 0.04 mM Fe^{2+}

and 83 ± 1 nA organic-Fe(III) determined electrochemically) and modified M1 medium as a blank were passed through separate IMAC columns and eluted with 20 ml of a 0.5 M NaOH solution. Eluates from the IMAC column were collected from both the 90 mL sample and the 20 mL of 0.5 M NaOH eluent (Figure 8-12). In all three samples, the pH of the eluate from the loaded sample (1-90 mL) gradually increased due to interactions with the IMAC column, then rapidly increased to around pH 13.55 during elution with NaOH (cumulative 90-110 mL) (Figure 8-12A). The slight dip in pH in the DFOB and MR-1 samples during elution with NaOH could be due to the loss of hydroxyl ions during exchange with Fe(III)-ligands bound to the IMAC column, which was not observed with the M1 blank. Absorbance at 254 and 450 nm of the loaded sample eluate (1-90 mL) suggested that some organic fractions of both the M1 and MR-1 samples were not retained on the column while the DFOB sample was efficiently retained (Figure 8-12B,C). Increased absorbance of the M1 sample compared to the MR-1 sample could be due to the electron donor lactate and possibly its oxidized by-products which are partially consumed and produced microbially in the MR-1 sample but not in the original medium. Upon elution with NaOH, (90-110 mL) the absorbance at both 254 and 450 nm rapidly increased in all three samples after a small phase lag, then decreased suggesting that the ligands absorbed to the IMAC column had been eluted completely within the first 15 mL of NaOH. Increase in absorbance during NaOH elution was not expected for the M1 blank sample. However, at both 254 and 450 nm, the maximum absorbance of the M1 sample was observed in the fraction collected at 95.5 mL, while maximum absorbance for the MR-1 and DFOB samples were observed slightly later in the 98.5 mL fraction. This finding along with the pH variations in the first 5.5 ml of NaOH elution could indicate difference in the binding

ligand concentration and composition between the two samples (DFOB and MR-1) expected to contain Fe(III)-binding ligands and the blank (M1) which was not expected to include such ligands. The differences in absorbance at 450 nm before and after the Fe(III) addition assay indicated that Fe(III)-binding ligands were eluted by NaOH from all three samples (Figure 8-12D), however future work should investigate the effect of pH on the Fe(III) addition assay. Together, these results demonstrate the ability of the IMAC column to retain organic ligands, and for these ligands to be released from the column with increased pH by NaOH elution. Although the composition of the ligands cannot be determined from these measurements, measuring pH and absorbances at 254 and 450 nm provides an easy and cost effective method that validates the IMAC efficiency.

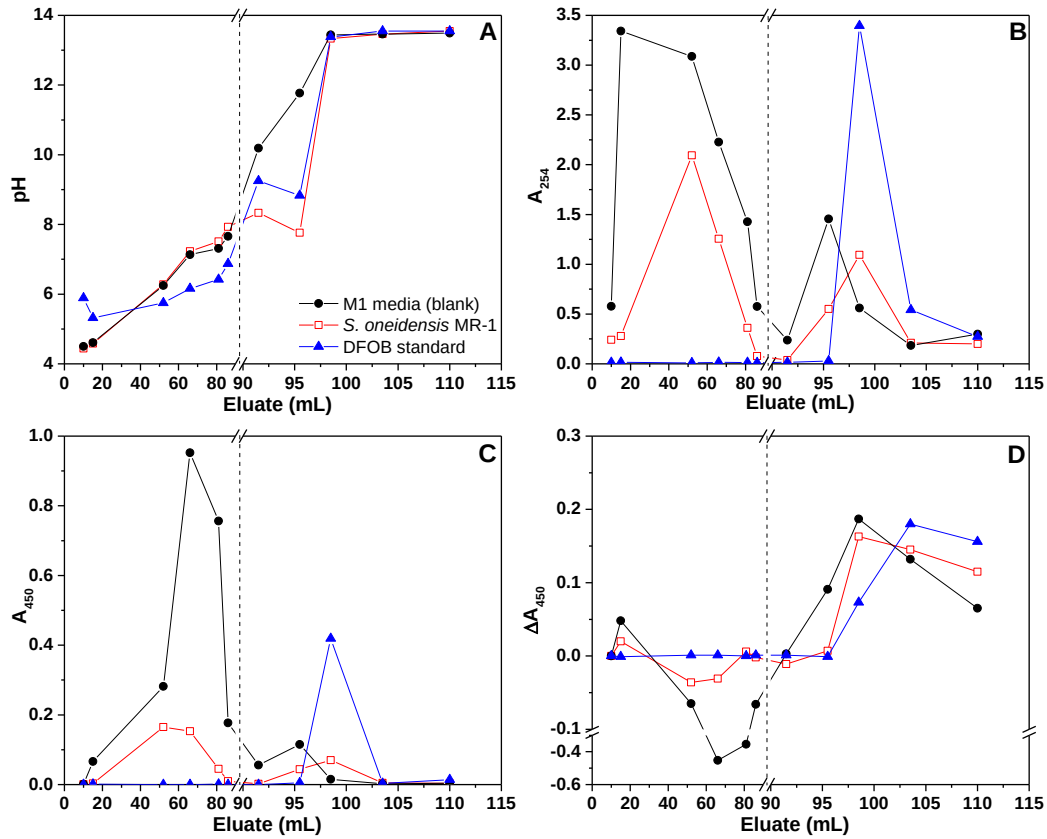

Figure 8-12. Chemical analysis of fractions collected during IMAC loading of 90 ml samples and elution with 20 ml of 0.5 M NaOH: A) pH; B) absorbance at 254 nm; C) absorbance at 450 nm; and D) difference in absorbance at 450 nm before and after the Fe(III) addition assay. The dash line represents the point before which the sample was loaded and after which the sample was eluted with NaOH.

To further investigate the slight differences observed between the original M1 medium and medium after 27 hours incubation of *S. oneidensis* MR-1 observed by pH and absorbance, 50 mL of samples were analyzed by IMAC-SPE-ESI-MS (Figure 8-13). However, unfortunately no distinct peaks were observed in the sample taken from the incubation that were not also observed in the M1 medium blank.

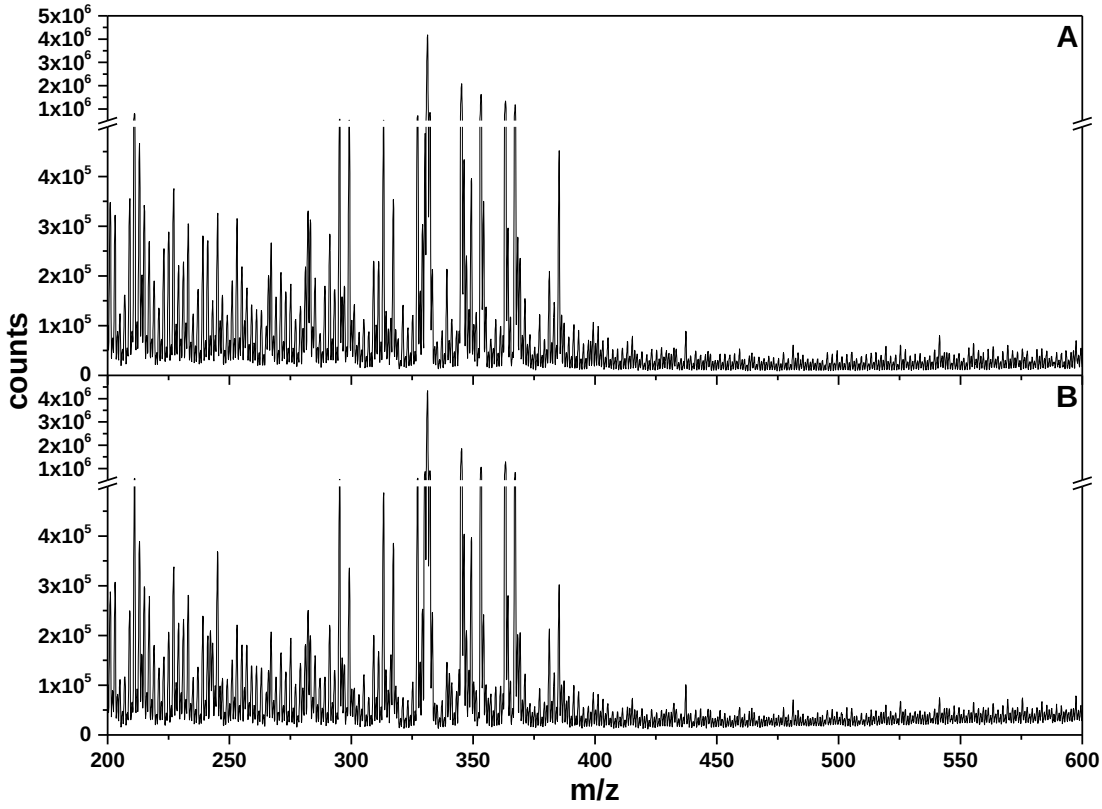

Figure 8-13. IMAC-SPE-ESI-MS positive ion mass spectra of: A) M1 medium; and B) filtered supernatant collected after 27 hours from incubations of *S. oneidensis* MR-1 with 40 mM ferrihydrite in modified M1 medium.

8.4.8 IMAC-SPE-ESI-MS Separation and Analysis of Marine Sediment Pore Waters

Pore waters were collected from St. 6B at a water depth of 150 m on the upper-slope of the continental margin off Cape Lookout (Chapter 6) to determine whether the IMAC-SPE-ESI-MS procedure could be applied to identify Fe(III)-binding organic ligands from natural samples. Both Fe^{2+} and organic-Fe(III) complexes were detected electrochemically throughout the top 12 cm of the sediment column (Figure 8-14), although concentrations were relatively low compared to other sites on the continental margin off Cape Lookout (Chapter 6) and similar continental slope sediments investigated previously (Beckler et al.,

2016; Taillefert et al., 2017). Pore waters were collected from three sections across the sediment core, representing three different horizons: surficial sediment without organic-Fe(III) complexes (1-6 cm), mid-sediment depths that include low concentrations of organic-Fe(III) complexes (9-16 cm), and the deepest section of the sediment core which was not geochemically analyzed but could be sulfidic (30-38 cm). Finally, a 0.54 M NaCl solution was used as a blank. From each section 20 mL of pore waters were collected and, along with 20 mL of the blank, were amended with 2.5 mL of 0.2 mM riboflavin as an internal standard before IMAC-SPE-ESI-MS analysis.

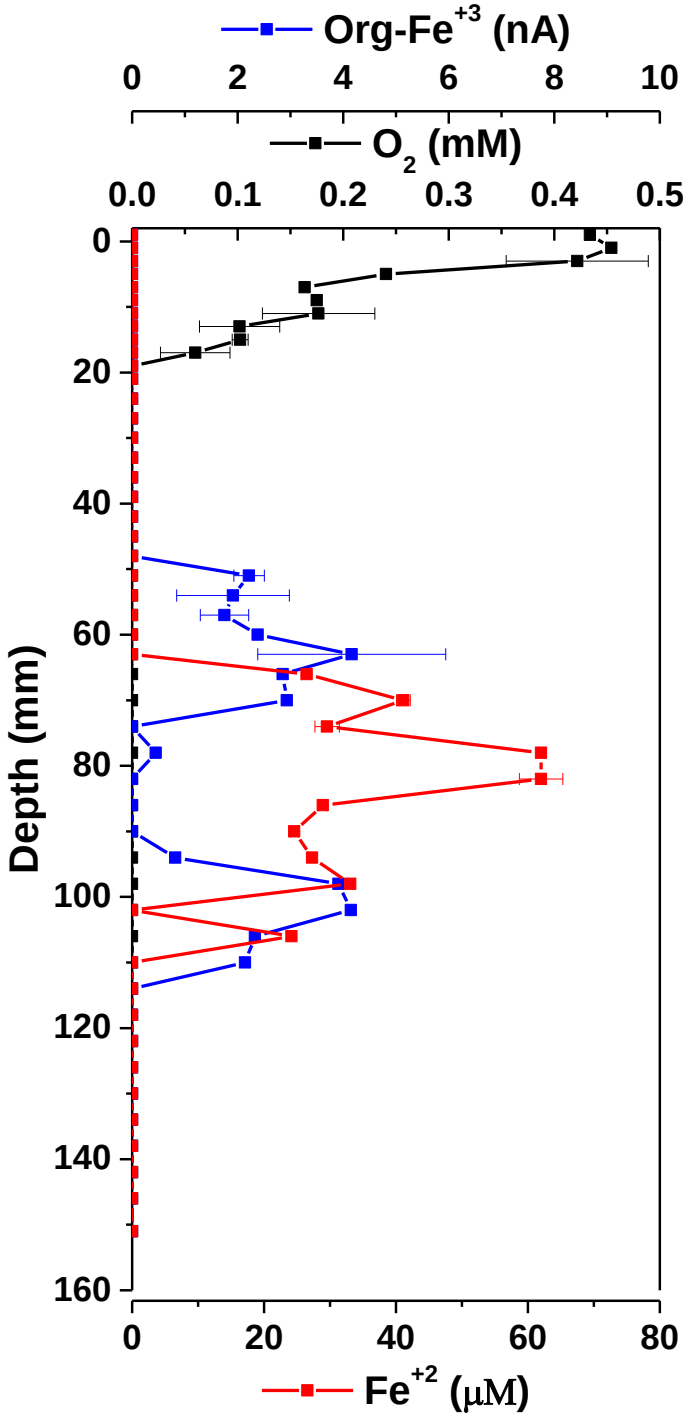

Figure 8-14. Depth profile of the main redox species determined electrochemically from St. 6B off Cape Lookout (more details in Chapter 6). Dissolved sulfides, FeS_{aq}, or Mn^{2+} were not detected in the pore waters.

MS peaks were observed at 331 and 353 m/z in the positive ion mode in all four samples (Figure 8-15). Peaks were also detected at 279 and 289 m/z in the pore water samples but not the blank, and decreased with sediment depth. Large peaks at 211 and 215 m/z were detected in all pore water samples, and a large peak at 214 m/z was also detected in pore waters from 9-16 cm depths, which was the section with the most iron measured in the depth profiles (Figure 8-14). Although peaks were observed in the NaCl blank at 437, 481, and 525, they were not observed in the pore water samples, and peaks were mostly below detection after 360 m/z. Although two small peaks were observed at 377 and 189 (not shown) m/z corresponding to riboflavin $[M+H]^+$ and $[M+2H]^{2+}$ in all samples, the concentration appears to be too small to act as a sufficient internal standard. Future analysis of samples using MS-MS could provide further information about the composition of peaks observed in the pore waters. Future work should also be done on natural samples with increased concentrations of dissolved iron, such as marsh sediments, as the low concentrations or iron found in continental shelf sediments suggests that the concentrations of organic ligands may be low.

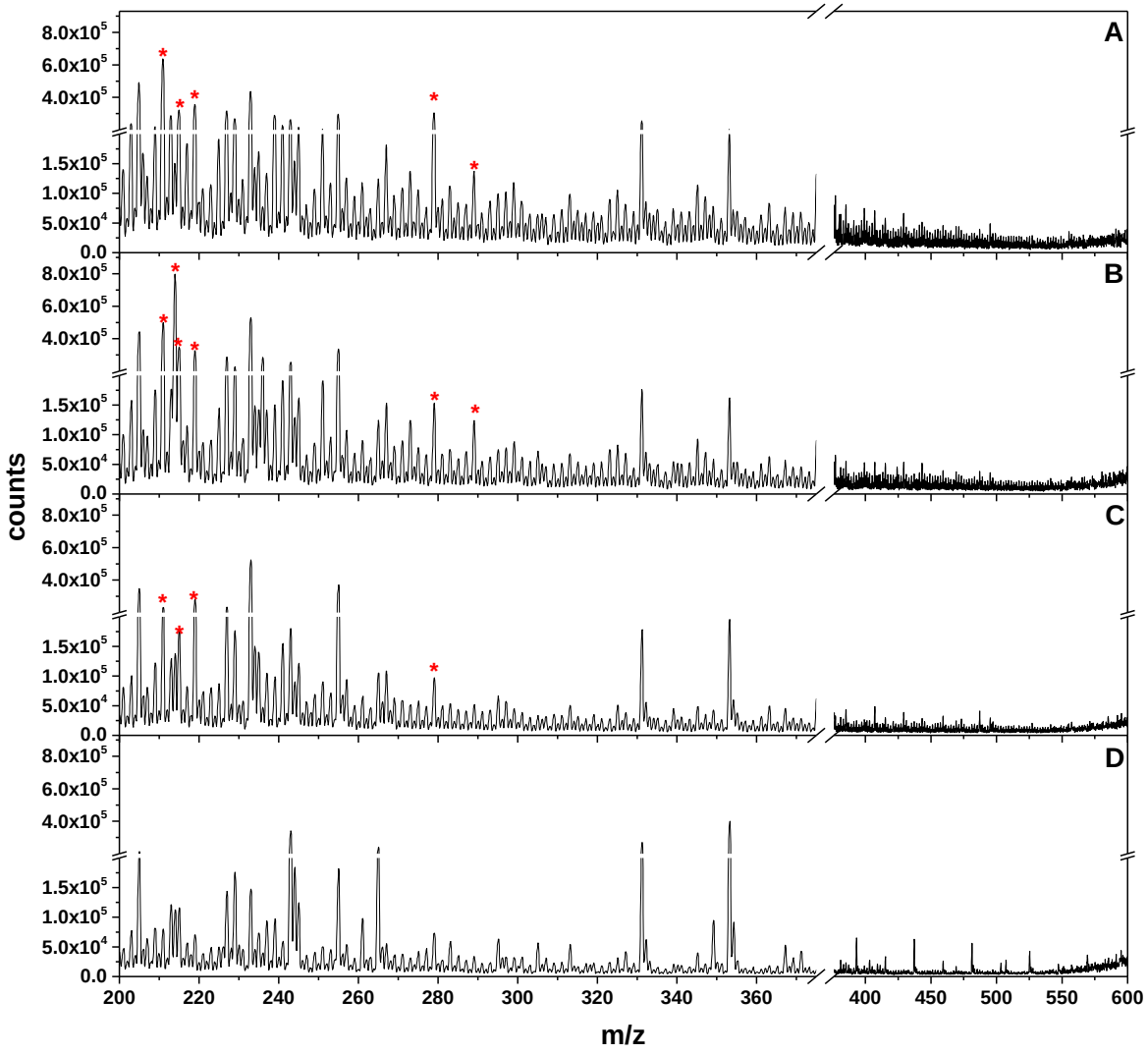

Figure 8-15. Mass spectrometry results from IMAC-SPE-ESI-MS in the positive mode of pore waters extracted from sediment depths: A) 1-6 cm; B) 9-16; and C) 30-38 cm from St. 6B off Cape Lookout, NC compared to: D) 0.54 mM NaCl to represent a blank. Red stars demark peaks observed in pore water samples but not the blank.

8.5 Conclusion

An immobilized metal affinity chromatography (IMAC) procedure was developed to isolate and identify the natural ligands involved in the solubilization of Fe(III) oxides. The method was optimized with model hydrophobic iron binding ligands riboflavin and desferroxamine-B through IMAC coupled with solid phase extraction (SPE), reverse phase liquid chromatography (LC), and electrospray ionization mass spectrometry (ESI-MS). Polar iron binding ligands such as citrate and EDTA required normal phase LC with a hydrophilic interaction (HILIC) column and were generally more difficult to observe by ESI-MS, although all complexes were confirmed in both positive and negative ion mode. SPE of riboflavin and DFOB was increased after acidification (SPE2) rather than directly after elution from the IMAC column (SPE1) with increased ionization observed in positive ion mode. Both riboflavin and DFOB were detected after IMAC-SPE2-ESI-MS with no clear dependence on the initial sample pH. Analysis of pH from fractions collected after IMAC alone indicated Fe(III)-binding ligands produced during *S. oneidensis* MR-1 incubations with ferrihydrite were absent in blank M1 medium. Unfortunatly, no distinct peaks differences were observed from IMAC-SPE2-ESI-MS of M1 medium and *S. oneidensis* incubation supernatant, potentially due to the early incubation sampling time. Distinct peaks were observed after IMAC-SPE2-ESI-MS of marine pore waters at different sediment depths, however m/z could not be accurately corresponded to known compounds.

CHAPTER 9. CONCLUSIONS

Despite the potential impact of the dissimilatory reduction of Fe(III) and Mn(IV) oxides on the biogeochemical transformation of carbon, nitrogen, sulfur, and phosphorus as well as the immobilization or degradation of both inorganic and organic contaminants, the microbial mechanism of metal reduction remains under debate as the organism must transfer electrons to a solid electron acceptor, a unique physiological problem in microbiology. In this dissertation, the ability for thiols to act as electron shuttles during dissimilatory reduction of Fe(III) and Mn(IV/III) oxides was investigated in both well-defined conditions either abiotically or with pure cultures of an iron-reducing microorganism and in a variety of freshwater and marine sediments.

In Chapter 3 and 4, in-depth investigation of the chemical reduction of ferrihydrite and δ-MnO_2 by four common low molecular weight thiols (cysteamine, cysteine, homocysteine, reduced glutathione) at environmentally relevant concentrations and pH demonstrated that thiols structure complexity is inversely proportional to reduction rate, but directly related to reaction extent, indicating that surface complexes play a significant role in the ability of thiols to reduce metal oxides. Kinetic modeling confirmed the reaction mechanism between thiols and Fe(III). Similar trends were observed between thiols with Mn(III,IV) oxides albeit at much higher rates, and a transient intermediate sulfur surface species was observed for the first time during the reaction. This transient intermediate provides support for a mechanism involving two successive one-electron transfer steps with formation of transient Mn(III) surface sites. In addition, the surface area-normalized reactivity of aged δ-MnO_2 decreased as a result of its structural transformation to

cryptomelane but remained higher than that of manganite, suggesting that Mn(III) formed as transient surface intermediate promotes the reduction of Mn(IV) oxides relative to manganite. This study demonstrates the importance of correlating mineral structure and reactivity when dealing with the redox properties of Mn(IV) oxides and extends the potential for thiols commonly found in sedimentary environments to be utilized as electron shuttles during dissimilatory Mn(III,IV) reduction.

In Chapter 5, the presence of thiols in a variety of freshwater and marine sediments was determined and compared to the biogeochemical transformation of iron and sulfur in these environments. Detection of cysteine, glutathione, cysteamine, and 3-MPA in all these sediments demonstrated that the distribution of these species is widespread. Significant correlations between cysteine, glutathione, and possibly cysteamine with Fe^{2+} and org-Fe(III) complexes in sediments not exposed to sulfate reduction suggested that these thiols may be involved in the dissimilatory reduction of Fe(III) oxides. Indeed, the ability of the model metal-reducing bacteria *Shewanella* MR-1 to reduce cystine and produce endogenous thiols during the reduction of Fe(III) oxides was confirmed, and the endogenous production of cysteine, glutathione, and cysteamine during incubations of *Shewanella* MR-1 was evidenced and linked to the production of org-Fe(III) complexes generated as intermediate in dissimilatory iron reduction to destabilize Fe(III) from Fe(III) oxides. These findings represent the first to demonstrate relationship between the electron shuttling and Fe(III)-solubilization bacterial mechanisms in *Shewanella* and suggest that bacterially-produced thiols may not only reduce org-Fe(III) complexes but also be involved in signaling the cells for endogenous production of the Fe(III)-binding ligands. Finally, sediment slurry incubations provided additional evidence that glutathione and cysteine are

microbially produced during DIR and function as electron shuttles in natural environments. In addition to demonstrate that cysteine and glutathione could represent good proxies of dissimilatory iron reduction in sediments, these sediment incubations also highlighted the good correlation between 3-MPA and $\sum H_2S$ or FeS_{aq} production, suggesting that 3-MPA could be a good proxy of sulfate reduction in marine sediments.

Reduction of Fe(III) oxides in marine sediments may have important implications in chemical oceanography as it may allow dissolved iron to diffuse across the sediment water interface and the benthic iron flux may stimulate primary productivity in iron-limited surface waters. As the abiotic reduction of Fe(III) oxides by dissolved sulfide produced during sulfate reduction may immobilize iron in sulfur minerals and thus suppress the iron flux, it is important determine in what biogeochemical conditions the dissolved iron flux from the sediment is promoted or suppressed. In Chapter 6, the benthic flux and speciation iron along a transect across the continental margin off Cape Lookout, North Carolina was determined to investigate the potential for passive continental margin sediments without large upwelling events or riverine input to provide dissolved iron to the ocean. High diffusive fluxes of both dissolved Fe^{2+} and org-Fe(III) complexes on the mid-slope and increased depth-integrated rates of dissolved Fe^{2+} and Fe(III) determined from sediment incubations demonstrate that these sediments act as a depocenter for terrigenous material and organic matter and may just represent as important sources of iron to the oceans as shelf sediments, aerosols, rivers, or hydrothermal vents. The production of dissolved Fe(III) was likely regulated by a combination of aerobic oxidation in the presence of natural organic ligands near the sediment-water interface, DIR deep in the sediments, or chemical oxidation of Fe(II) complexed to natural organic ligands across the sediment column.

Although the diffusive flux of iron may be controlled by sulfate reduction, which reduces and immobilize iron rapidly, sulfate reduction did not appear to significantly affect the iron flux from mid-slope sediments. Extrapolation of the sedimentary flux from the Cape Lookout mid-slope depocenter to the global ocean indicated that this iron flux rival global estimates of iron inputs derived from aerosols, rivers, and hydrothermal vents. These findings demonstrated that passive margins that are generally overlooked in global estimates generate a significant flux of iron to the overlying waters.

In contrast to the North Carolina continental margin, the sediments of the Rhône River prodelta receive large riverine inputs of organic and inorganic particles that result in intense anaerobic respiration and the complete removal of sulfate from pore waters in the proximal domain. In Chapter 7, benthic respiration, alkalinity and DIC fluxes were quantified in the Rhône River prodelta using benthic landers and pore water profiles. The intensity of sulfate reduction in the proximal domain resulted in the precipitation of iron sulfide and carbonate minerals which removed iron, sulfide, and DIC from the pore waters. As the reduced metabolites of organic matter mineralization were buried in the solid phase, less alkalinity was consumed by the reoxidation of HS^- and Fe^{2+} in the oxic layers of these sediments, and the flux of dissolved iron from the sediment was suppressed and replaced by a significant flux of alkalinity to the bottom waters. The strongest alkalinity and DIC fluxes were detected in the vicinity of the river mouth and were much stronger than fluxes of dissolved oxygen, indicating the decoupling of oxic and anoxic biogeochemical processes. Although sulfate reduction dominated the proximal and prodelta domains, evidence for dissimilatory reduction of Fe(III) oxides was observed in the depth profiles, suggesting that anaerobic processes in the Rhône River prodelta are dynamic and

potentially controlled by pulsed sediment accumulations. The intensity of the alkalinity and DIC fluxes decreased offshore as the sedimentation rate and the relative importance of anaerobic mineralization pathways compared to aerobic processes decreased. In these conditions the more classical coupling between aerobic and anaerobic process occurs, lowering the benthic alkalinity fluxes. Overall, these findings suggested that sediments exposed to large riverine inputs of inorganic and organic material prevent the flux of dissolved iron to the overlying waters but provide a source of alkalinity that may help buffer the acidification of coastal waters.

Finally, the composition of organic-Fe(III) detected in both natural sediments and pure culture incubations throughout this thesis remain unknown. To determine the composition of natural Fe(III)-binding organic ligands and potentially differentiate between the abiotic and microbial formation of these complexes, an immobilized metal affinity chromatography (IMAC) procedure was developed in Chapter 8 to isolate and identify the natural ligands involved in the solubilization of Fe(III) oxides. The method was optimized with model hydrophobic iron binding ligands riboflavin and desferroxamine-B through IMAC coupled with solid phase extraction (SPE), reverse phase liquid chromatography (LC), and electrospray ionization mass spectrometry (ESI-MS). Although polar iron-binding ligands such as citrate and EDTA required normal phase LC with a hydrophilic interaction (HILIC) column and were generally more difficult to observe though ESI-MS, all standard ligands were confirmed in both positive and negative mode. Isolation of these model iron binding ligands by this procedure demonstrates its potential for the extraction of natural iron-binding ligands from marine pore waters.

9.1 Recommendations for Future Research

This work has investigated the potential use of both thiols and organic-Fe(III) to identify dissimilatory iron reduction in natural sediments, however many questions about these species remain unanswered. The microbial mechanism of thiol production and disulfide reduction is not completely understood, and microbiology work following Seng K. Wee (2013) and Rebecca Copper (2015) should be continued. Endogenous production of thiols has been observed during dissimilatory iron reduction by *S. oneidensis* MR-1, however pure culture incubations with alternate terminal electron accpetors such as O_2, NO_3^-, Mn(III,IV), or fumarate have yet to be analysed for thiols. Given the rapid reduction of Mn(III,IV) oxides by thiols, it seems likely that microorganisms could cycle thiols to increase rates of Mn(III,IV) reduction. This process could be investigated with amendments of thiols and disulfides to incubations of *S. oneidensis* MR-1 with Mn(III,IV) oxides. In both pure cultures and natural sediments, it is not certain that disulfides are homogeneous, and cysteine-homocysteine pairs could exist as well as cysteine-cysteine pairs. Currently, it is difficult to account for mixed disulfide compounds. Understanding the abiotic relationship between thiols would provide more insight into the suite of thiols produced during dissimilatory iron reduction. Interestingly, the reaction between specific thiols and homogeneous disulfides has yet to be studied.

To determine the composition of organic-Fe(III), isolation and identification of Fe(III)-binding ligands in both natural samples and incubations of model Fe(III)-reducing microbes with IMAC-SPE-ESI-MS should be pursued. Many options for SPE cartridges are available and could potentially prove better for the concentration of organic ligands than the HLB cartridges used in this dissertation. Future work should continue the use of

spectrophotometric methods to investigate IMAC efficiency and provide information about the isolated ligands. For example, previous studies have investigated Fe(III)-IMAC separation by detecting amino acids, peptides, and proteins by the ninhydrin assay, protein concentrations by the Bradford assay, and total phosphate by persulfate digestion (Machida et al., 2007; Muszynska et al., 1986; Muszynska et al., 1992). Natural samples from locations with increased anaerobic respiration should be investigated rather than pore waters from passive continental margins. Additionally, samples over the entire course of *S. oneidensis* MR-1 incubations with Fe(III) should be analyzed. Eventually, MS-MS could be utilized to determine additional information about isolated ligands.

Detection of trace Fe^{2+} during benthic chamber incubations may provide insight into the source of iron to the open ocean. The method optimized in this dissertation and performed on the R/V Savannah to detect Fe^{2+} in bethic chamber incubations in the Gulf of Mexico in 2017 could be greatly improved to allow easy and consistent measurements. Redesign of the chemoluminescence detector could allow for better exclusion of light, which produces a response at the detector and greatly decreases sensitivity. More importantly, a serpentine flow cell should be designed and connected with a high velocity and high pressure pump system. Consistent equal mixing of reagent and samples is extremely difficult in a low pressure system, and this issue with the current set-up remains critical. Additional tests should be completed with the sulfite reducing agent for analysis of total iron, and benthic chamber samples from past cruises could be analyzed to check the method. Finally, adaptation of the luminol detector for direct attachment to the benthic chamber on deep sea landers could provide *in situ* detection of Fe^{2+} production. As samples may be exposed to oxic conditions over the ~ 24 hour deployments, *in situ* detection would

decrease the risk of sample oxidation prior to analysis. Detection of Fe^{2+} by luminol could be easily attached to current *in situ* HPLC systems as analysis does not require any derivation steps, the luminol reagent can be easily prepared beforehand, the detector is small and requires little energy, and the housing on the benthic lander would block any external light from impacting the detector.

Finally, after conducting numerous sediment incubations it has become clear that comparison between systems with and without molybdate addition provides important information about the dominant respiration processes occurring. Future sediment incubations should be sure to include molybdate treatments. Addition of paraformaldehyde should also be investigated as an alternate to heat killing sediment.

APPENDIX A. SUPPLEMENTAL INFORMATION FOR CHAPTER 4

Mn K-edge XAS data were collected on manganite and cryptomelane standards, as well as fresh and aged birnessite samples. Solid suspensions were vacuum filtered through 0.2 μm polycarbonate membranes and mounted in an acrylic sample holder covered with Kapton tape. Samples were stored at -20 °C and thawed prior to analysis. XAS data were collected at Beamline 4-1 of the Stanford Synchrotron Radiation Lightsource (SSRL; Menlo Park, CA) using Si(220) monochromator and Beamlines 5-BM-D at the Advanced Photon Source (APS; Argonne National Laboratory, Lemont, IL) using Si(111) monochromators, all with 40% detuning to avoid higher order harmonics. Energy calibration used Mn foil. XAS data were collected in both transmission and fluorescence mode using a Lytle detector (Beamlines 4-1 at SSRL) or a vortex detector (Beamline 5-BM-D at APS). Both XANES (X-ray absorption near edge structure) and EXAFS (extended X-ray absorption fine structure) data were collected. Two to six scans were collected and averaged. Analysis of the Mn XANES spectra for each sample showed no photo-reduction of samples under X-ray beam. XAS data analysis was performed using the programs SIXPACK (Webb, 2005) and Ifeffit (Ravel and Newville, 2005). Linear combination fitting of the EXAFS data was conducted using fresh δ-MnO_2, triclinic birnessite, and manganite as end members. Fitting results with lowest residual (R factor) was used.

Calculated rate constants were normalized to the BET specific surface area (SSA) by dividing by (MnO_2 (g/L) x MnO_2 SSA (m^2/g) (Table A 1).

Table A 1 Linear combination fitting results of Mn EXAFS data using fresh birnessite, triclinic birnessite, and cryptomelane as end members.

Sample	Fresh δ-MnO_2	Triclinic birnessite	Cryptomelane	R factor
δMnO_2_2m	0.505 (0.082)	0.087 (0.047)	0.408 (0.116)	0.00848
δMnO_2_2.5yr			1	0.03681
δMnO_2_6yr			1	0.03213

Table A 2 BET specific surface area (SSA) of different age δ-MnO_2 and manganite along with the pseudo-first order rate constants and pseudo-first order rate constants normalized to SSA for their reaction with cysteine, n.a means data not available.

Sample	Label	SSA (m^2/g)	Rate constant (min^{-1})	Rate constant normalized to SSA ($m\ min^{-1}$)
Fresh δ-MnO_2	Fresh δ-MnO_2	191.7	16.56	9.94×10^{-5}
δ-MnO_2 aged for 1 month	δMnO_2_1m	107.4	2.62 ± 0.07	$2.80 \pm 0.1 \times 10^{-5}$
δ-MnO_2 aged for 2 month	δMnO_2_2m	60.1	1.06 ± 0.18	$2.03 \pm 0.4 \times 10^{-5}$
δ-MnO_2 aged for 3 month	δMnO_2_3m	43.9	0.69 ± 0.05	$1.81 \pm 0.1 \times 10^{-5}$
δ-MnO_2 aged for 1.5 year	δMnO_2_1.5yr	n.a	0.52 ± 0.09	
δ-MnO_2 aged for 2.5 year	δMnO_2_2.5yr	41.3	0.36 ± 0.09	$9.97 \pm 2.5 \times 10^{-6}$
δ-MnO_2 aged for 6 year	δMnO_2_6yr	58.2	0.22 ± 0.04	$4.33 \pm 0.9 \times 10^{-6}$
Manganite	Manganite	31.7	0.08 ± 0.01	$3.01 \pm 0.5 \times 10^{-6}$

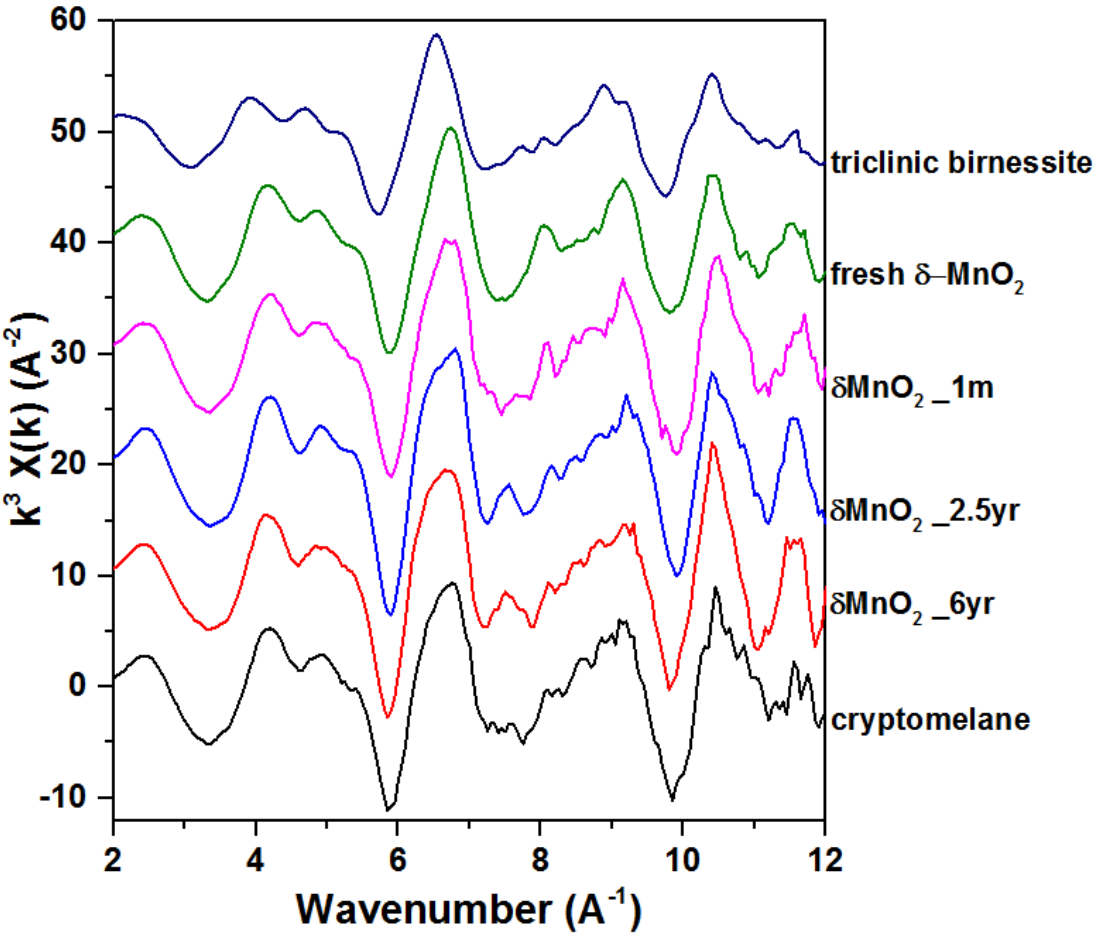

Figure A 1 k^3-weighted Mn K-edge extended X-ray absorption fine structure (EXAFS) data of fresh and aged δ-MnO_2, cryptomelane, and triclinic birnessite.

APPENDIX B. SUPPLEMENTAL INFORMATION FOR CHAPTER 6

B.1 Sulfide Flux Calculations

The flux of total sulfide is dependent on both H_2S and HS^-, while S^{2-} should be negligible at this pH range. To confirm that use of the HS^- molecular diffusion coefficient is acceptable for use with ΣH_2S concentrations determined electrochemically when pH values were not available at all core depths, three cores were compared using each method. The average minimum pH measured for all cores was 7.7 ± 0.3, which is much higher than the pKa_1 of H_2S (6.8), therefor in most cases $HS^- >> H_2S$ minimizing differences further. The flux of ΣH_2S ($F_{\Sigma H_2S}$) was determined from the electrochemically determined ΣH_2S concentrations using Eq. 6-1 with Eq. 6-2 values for HS^- used. Based on the pH and pKa_1 of sulfide, the concentrations of HS^- and H_2S were also determined from the measured ΣH_2S concentrations. The flux of HS^- (F_{HS^-}) was determined using Eq. 6-1 and 6-2 while the combined flux of HS^- and H_2S was calculated as $F_{H_2S+HS^-} = F_{H_2S} + F_{HS^-}$. The flux of H_2S (F_{H_2S}) was determined from Eq. 6-1 with the molecular diffusion coefficient determined following:

$$D^0_{H_2S} = \left((4.72x10^{-9}) \frac{T}{\mu V_b^{0.6}} \right) \quad \text{(A1)}$$

For three sediment cores, the flux of sulfide can be seen to be within error for all cases expect for the 2015 Core 10 (Figure B 1), however this core had the lowest measured pH values (7.03), and would therefore expect to have a larger ratio of H_2S. The minimum pH values observed in 2015 Core 11 was 7.62 and in 2016 core 13 was 7.45. As all other cores

have higher pH, and the methods are within error, the use of the HS^- molecular diffusion coefficient equation is determined to be acceptable for use with measured ΣH_2S concentrations when pH values are not available.

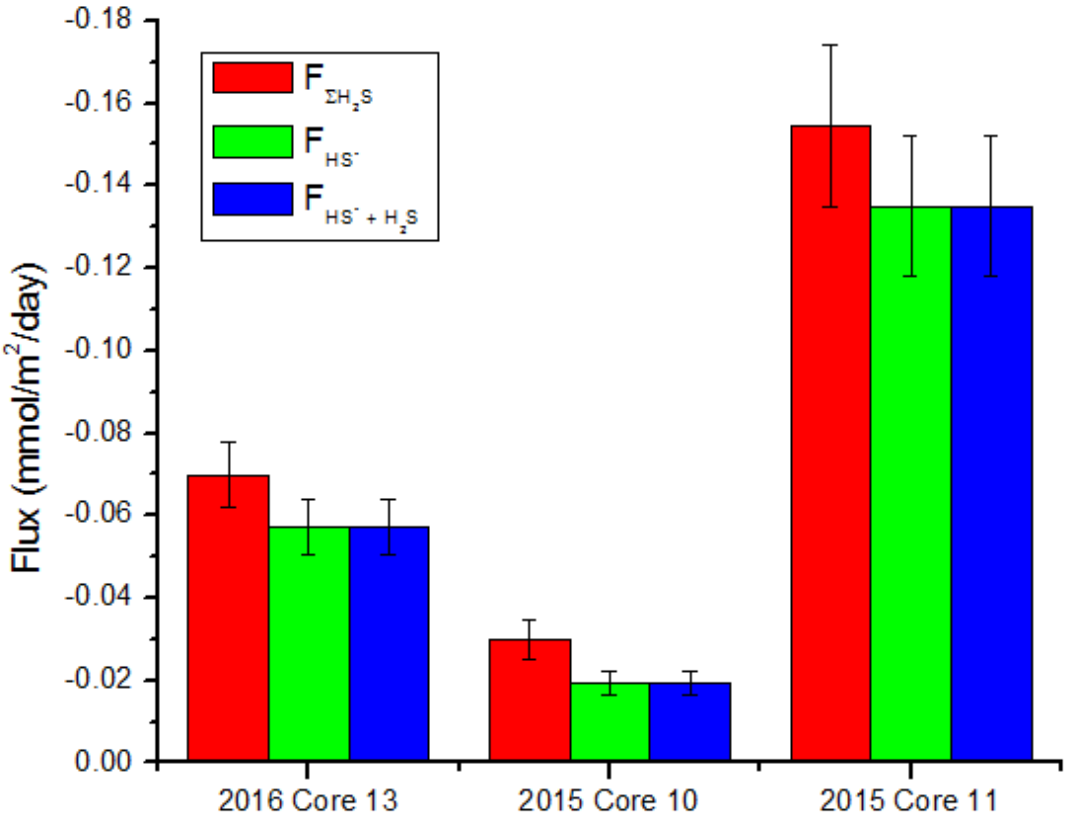

Figure B 1 Diffusive fluxes of sulfide determined by three different methods for three sediment cores.

B.2 Sediment Incubation Zones

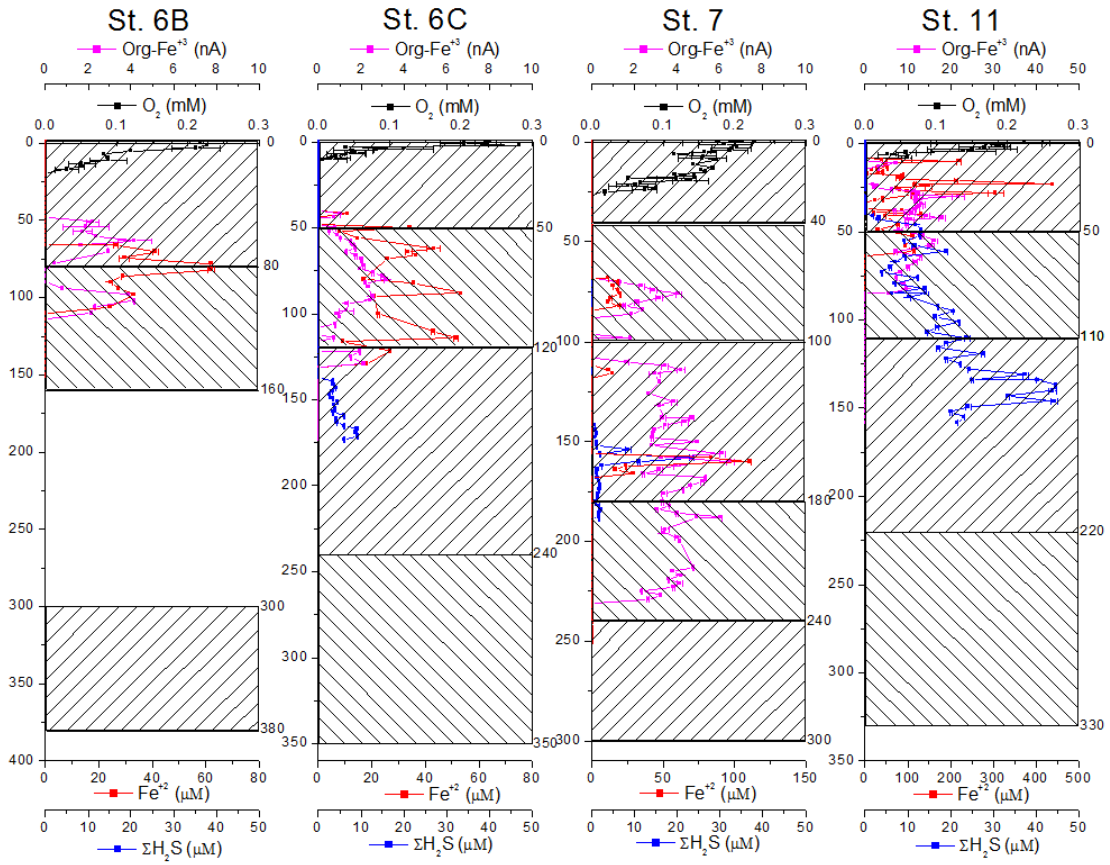

Figure B 2 Depth profiles of dissolved O_2, Fe^{2+}, organic-Fe^{3+}, and $\sum H_2S$ concentrations measured electrochemically for sediment cores used for incubations. Hatched sections were homogenized for separate incubations.

REFERENCES

Aizenshtat, Z., Krein, E.B., Vairavamurthy, M.A. and Goldstein, T.P., 1995. Role of Sulfur in the Transformations of Sedimentary Organic Matter: A Mechanistic Overview, Geochemical Transformations of Sedimentary Sulfur. ACS Symposium Series. American Chemical Society, pp. 16-37.

Al-Farawati, R. and Van Den Berg, C.M.G., 2001. Thiols in coastal waters of the western North Sea and English Channel. Environmental Science & Technology, 35(10): 1902-1911.

Aller, R.C., 1998. Mobile deltaic and continental shelf muds as suboxic, fluidized bed reactors. Marine Chemistry, 61(3): 143-155.

Aller, R.C., Blair, N.E. and Brunskill, G.J., 2008. Early diagenetic cycling, incineration, and burial of sedimentary organic carbon in the central Gulf of Papua (Papua New Guinea). Journal of Geophysical Research: Earth Surface, 113(F1).

Aller, R.C., Mackin, J.E. and Cox, R.T., 1986. Diagenesis of Fe and S in Amazon inner shelf muds: apparent dominance of Fe reduction and implications for the genesis of ironstones. Continental Shelf Research, 6(1): 263-289.

Alperin, M.J. et al., 1999. Benthic fluxes and porewater concentration profiles of dissolved organic carbon in sediments from the North Carolina continental slope. Geochimica Et Cosmochimica Acta, 63(3-4): 427-448.

Alperin, M.J., Suayah, I.B., Benninger, L.K. and Martens, C.S., 2002. Modern organic carbon burial fluxes, recent sedimentation rates, and particle mixing rates from the upper continental slope near Cape Hatteras, North Carolina (USA). Deep Sea Research Part II: Topical Studies in Oceanography, 49(20): 4645-4665.

Altaf, M. and Jaganyi, D., 2014. Kinetics of the Degradation of l-Cysteine at Freshly Prepared Nano-sized MnO2 Surfaces in the Absence and Presence of TX-100. Journal of Solution Chemistry, 43(2): 269-282.

Amante, C. and Eakins, B.W., 2009. ETOPO1 1 Arc-Minute Global Relief Model: Procedures, Data Sources and Analysis. NOAA Technical Memorandum NESDIS NGDC-24., National Geophysical Data Center, NOAA.

Amirbahman, A., Sigg, L. and vonGunten, U., 1997. Reductive dissolution of Fe(III) (hydr)oxides by cysteine: Kinetics and mechanism. Journal of Colloid and Interface Science, 194(1): 194-206.

Amstaetter, K., Borch, T. and Kappler, A., 2012. Influence of humic acid imposed changes of ferrihydrite aggregation on microbial Fe(III) reduction. Geochimica et Cosmochimica Acta, 85: 326-341.

Anderson, R.F., Rowe, G.T., Kemp, P.F., Trumbores, S. and Biscaye, P.E., 1994. Carbon budget for the mid-slope depocenter of the Middle Atlantic Bight. Deep Sea Research Part II: Topical Studies in Oceanography, 41(2): 669-703.

Anderson, T.F. and Pratt, L.M., 1995. Isotopic Evidence for the Origin of Organic Sulfur and Elemental Sulfur in Marine Sediments, Geochemical Transformations of Sedimentary Sulfur. ACS Symposium Series. American Chemical Society, pp. 378-396.

Andersson, A.J. and Mackenzie, F.T., 2012. Revisiting four scientific debates in ocean acidification research. Biogeosciences, 9(3): 893-905.

Andrabi, S.M.Z. and Khan, Z., 2007. Reactivity of some sulphur- and non-sulphur-containing amino acids towards water soluble colloidal MnO2. A kinetic study. Colloid and Polymer Science, 285(4): 389-396.

Anschutz, P., Dedieu, K., Desmazes, F. and Chaillou, G., 2005. Speciation, oxidation state, and reactivity of particulate manganese in marine sediments. Chemical Geology, 218(3-4): 265-279.

Anschutz, P., Zhong, S.J., Sundby, B., Mucci, A. and Gobeil, C., 1998. Burial efficiency of phosphorus and the geochemistry of iron in continental margin sediments. Limnology and Oceanography, 43(1): 53-64.

Atzei, D., Ferri, T., Sadun, C., Sangiorgio, P. and Caminiti, R., 2001. Structural characterization of complexes between iminodiacetate blocked on styrene-divinylbenzene matrix (Chelex 100 resin) and Fe(III), Cr(III), and Zn(II) in solid phase by energy-dispersive X-ray diffraction. Journal of the American Chemical Society, 123(11): 2552-2558.

Bae, S. and Lee, W., 2013. Biotransformation of lepidocrocite in the presence of quinones and flavins. Geochimica et Cosmochimica Acta, 114: 144-155.

Banat, I.M. and Nedwell, D.B., 1984. Inhibition of sulfate reduction in anoxic marine sediment by group-VI anions. Estuarine Coastal and Shelf Science, 18(3): 361-366.

Banerjee, D. and Nesbitt, H.W., 1999. Oxidation of aqueous Cr(III) at birnessite surfaces: Constraints on reaction mechanism. Geochimica Et Cosmochimica Acta, 63(11-12): 1671-1687.

Banerjee, D. and Nesbitt, H.W., 2000. XPS study of reductive dissolution of birnessite by H2SeO3 with constraints on reaction mechanism. American Mineralogist, 85(5-6): 817-825.

Bargar, J.R. et al., 2009. Structural characterization of terrestrial microbial Mn oxides from Pinal Creek, AZ. Geochimica et Cosmochimica Acta, 73(4): 889-910.

Bargar, J.R. et al., 2005. Biotic and abiotic products of Mn (II) oxidation by spores of the marine Bacillus sp. strain SG-1. American Mineralogist, 90(1): 143-154.

Baron, D. and Hering, J.G., 1998. Analysis of metal-EDTA complexes by electrospray mass spectrometry. Journal of Environmental Quality, 27(4): 844-850.

Barrett, J.R., 1965. Subsurface currents off Cape Hatteras. Deep Sea Research and Oceanographic Abstracts, 12(2): 173-184.

Bauer, J.E. et al., 2013. The changing carbon cycle of the coastal ocean. Nature, 504: 61.

Beckler, J.S., 2014. The biogeochemical source and role of soluble organic-Fe(III) complexes in continental margin sediments, Georgia Institute of Technology.

Beckler, J.S., Jones, M.E. and Taillefert, M., 2015. The origin, composition, and reactivity of dissolved iron(III) complexes in coastal organic- and iron-rich sediments. Geochimica et Cosmochimica Acta, 152: 72-88.

Beckler, J.S., Kiriazis, N., Rabouille, C., Stewart, F.J. and Taillefert, M., 2016. Importance of microbial iron reduction in deep sediments of river-dominated continental-margins. Marine Chemistry, 178: 22-34.

Beckler, J.S., Nuzzio, D.B. and Taillefert, M., 2014. Development of single-step liquid chromatography methods with ultraviolet detection for the measurement of inorganic anions in marine waters. Limnology and Oceanography-Methods, 12: 563-576.

Behrenfeld, M.J. and Kolber, Z.S., 1999. Widespread iron limitation of phytoplankton in the South Pacific Ocean. Science, 283(5403): 840-843.

Ben-Yaakov, S., 1973. pH Buffering of pore water of recent anoxic marine sediments. Limnology and Oceanography, 18(1): 86-94.

Bennett, S.A. et al., 2008. The distribution and stabilisation of dissolved Fe in deep-sea hydrothermal plumes. Earth and Planetary Science Letters, 270(3): 157-167.

Berelson, W. et al., 2003. A time series of benthic flux measurements from Monterey Bay, CA. Continental Shelf Research, 23(5): 457-481.

Berner, R., 1970. Sedimentary pyrite formation. A. Science, 268: 1-23.

Berner, R.A., 1980. Early Diagenesis: A Theoretical Approach, Princeton University Press.

Berner, R.A. and Raiswell, R., 1983. Burial of organic carbon and pyrite sulfur in sediments over phanerozoic time: a new theory. Geochimica et Cosmochimica Acta, 47(5): 855-862.

Bhatia, M.P. et al., 2013. Greenland meltwater as a significant and potentially bioavailable source of iron to the ocean. Nature Geoscience, 6(4): 274-278.

Bianchi, T.S. and Allison, M.A., 2009. Large-river delta-front estuaries as natural "recorders" of global environmental change. Proceedings of the National Academy of Sciences, 106(20): 8085-8092.

Bianchi, T.S. et al., 2010. The science of hypoxia in the Northern Gulf of Mexico: A review. Science of the Total Environment, 408: 1471-1484.

Bilinski, H., Giovanoli, R., Usui, A. and Hanžel, D., 2002. Characterization of Mn oxides in cemented streambed crusts from Pinal Creek, Arizona, U.S.A., and in hot-spring deposits from Yuno-Taki Falls, Hokkaido, Japan. American Mineralogist, 87(4): 580-591.

Biscaye, P.E., Anderson, R.F. and Deck, B.L., 1988. Fluxes of particles and constituents to the eastern United States continental slope and rise: SEEP—I. Continental Shelf Research, 8(5): 855-904.

Bjerrum, J., 1958. Stability Constants. Chemical Society, London.

Blair, N.E., Plaia, G.R., Boehme, S.E., DeMaster, D.J. and Levin, L.A., 1994. The remineralization of organic carbon on the North Carolina continental slope. Deep Sea Research Part II: Topical Studies in Oceanography, 41(4): 755-766.

Blake, J.A. et al., 1987. Study of Biological Processes on the U.S. South Atlantic Slope and Rise. Phase 2. Final Report, U.S. Department of the Interior, Minerals Management Service, Washington, DC.

Blake, J.A. et al., 1985. Study of Biological Processes on the U.S. South Atlantic Slope and Rise. Phase 1. Benthic Characterization Study. Final Report, U.S. Department of the Interior, Minerals Management Service, Washington, DC.

Bond, D.R. and Lovley, D.R., 2005. Evidence for involvement of an electron shuttle in electricity generation by Geothrix fermentans. Applied and Environmental Microbiology, 71(4): 2186-2189.

Borch, T. et al., 2010. Biogeochemical Redox Processes and their Impact on Contaminant Dynamics. Environmental Science & Technology, 44(1): 15-23.

Borowki, W., Pau, C. and Ussler, W., 1996. Marine pore-water sulfate profiles indicate in situ methane flux from underlying gas hydrate. Geology, 24(7): 655-658.

Boudreau, B.P., 1997. Diagenetic Models and Their Implementation: Modeling Transport and Reactions in Aquatic Sediments. Springer-Verlag.

Boyle, E.A., Edmond, J.M. and Sholkovitz, E.R., 1977. Mechanism of iron removal in estuaries. Geochimica Et Cosmochimica Acta, 41(9): 1313-1324.

Braich, N. and Codd, R., 2008. Immobilised metal affinity chromatography for the capture of hydroxamate-containing siderophores and other Fe(III)-binding metabolites directly from bacterial culture supernatants. Analyst, 133(7): 877-880.

Brendel, P.J. and Luther, G.W., 1995. Development of a gold amalgam voltammetric miroelectrode for the determination of dissolved Fe, Mn, O2, and S(-II) in porewater of marine and fresh-water sediments. Environmental Science & Technology, 29(3): 751-761.

Brenner, H., Braeckman, U., Le Guitton, M. and Meysman, F.J.R., 2016. The impact of sedimentary alkalinity release on the water column CO2 system in the North Sea. Biogeosciences, 13(3): 841-863.

Bricker, O., 1965. Some stability relations in system MN-O2-H2O at 25 degrees and 1 atmosphere total pressure. American Mineralogist, 50(9): 1296-&.

Briseno, A.L., Mannsfeld, S.C.B., Jenekhe, S.A., Bao, Z. and Xia, Y., 2008. Introducing organic nanowire transistors. Materials Today, 11(4): 38-47.

Bristow, G. and Taillefert, M., 2008. VOLTINT: A Matlabg (R)-based program for semi-automated processing of geochemical data acquired by voltammetry. Computers & Geosciences, 34(2): 153-162.

Brittain, T., Blackmore, R., Greenwood, C. and Thomson, A.J., 1992. Bacterial nitrite-reducing enzymes. Eur J Biochem, 209(3): 793-802.

Broecker, W.S. and Peng, T.-H., 1974. Gas exchange rates between air and sea. Tellus, 26(1-2): 21-35.

Bruland, K.W., Rue, E.L. and Smith, G.J., 2001. Iron and macronutrients in California coastal upwelling regimes: Implications for diatom blooms. Limnology and Oceanography, 46(7): 1661-1674.

Bruland, K.W., Rue, E.L., Smith, G.J. and DiTullio, G.R., 2005. Iron, macronutrients and diatom blooms in the Peru upwelling regime: brown and blue waters of Peru. Marine Chemistry, 93(2-4): 81-103.

Buck, K.N., Lohan, M.C., Berger, C.J.M. and Bruland, K.W., 2007. Dissolved iron speciation in two distinct river plumes and an estuary: Implications for riverine iron supply. Limnology and Oceanography, 52(2): 843-855.

Buffle, J., 1988. Complexation Reaction sin Aqueous Systems: An Analytical Approach. Wiley & Sons, New York, NY.

Bull, D.C. and Taillefert, M., 2001. Seasonal and topographic variations in porewaters of a southeastern USA salt marsh as revealed by voltammetric profilingdagger. Geochem Trans, 2(1): 104.

Bura-Nakic, E., Viollier, E., Jezequel, D., Thiam, A. and Ciglenecki, I., 2009. Reduced sulfur and iron species in anoxic water column of meromictic crater Lake Pavin (Massif Central, France). Chemical Geology, 266(3-4): 311-317.

Burba, P., Jakubowski, B., Kuckuk, R., Kullmer, K. and Heumann, K.G., 2000. Characterization of aquatic humic substances and their metal complexes by immobilized metal-chelate affinity chromatography on iron(III)-loaded ion exchangers. Fresenius Journal of Analytical Chemistry, 368(7): 689-696.

Burdige, D.J., 2011. Estuarine and Coastal Sediments - Coupled Biogeochemical Cycling. Treatise on Esturarine and Coastal Science, 5:279–316.

Burdige, D.J., Alperin, M.J., Homstead, J. and Martens, C.S., 1992a. The Role of Benthic Fluxes of Dissolved Organic Carbon in Oceanic and Sedimentary Carbon Cycling. Geophysical Research Letters, 19(18): 1851-1854.

Burdige, D.J., Dhakar, S.P. and Nealson, K.H., 1992b. Effects of manganese oxide mineralogy on microbial and chemical manganese reduction. Geomicrobiology Journal, 10(1): 27-48.

Burdige, D.J. and Komada, T., 2011. Anaerobic oxidation of methane and the stoichiometry of remineralization processes in continental margin sediments. Limnology and Oceanography, 56(5): 1781-1796.

Burdige, D.J. and Nealson, K.H., 1986. Chemical and microbial studies of sulfide-mediated manganese reduction. Geomicrobiology Journal, 4(4): 361-387.

Burgos, W.D. et al., 2003. Reaction-based modeling of quinone-mediated bacterial iron(III) reduction. Geochimica et Cosmochimica Acta, 67(15): 2735-2748.

Burns, J.M., Craig, P.S., Shaw, T.J. and Ferry, J.L., 2010. Multivariate Examination of Fe(II)/Fe(III) Cycling and Consequent Hydroxyl Radical Generation. Environmental Science & Technology, 44(19): 7226-7231.

Cai, W.-J. and Reimers, C.E., 1993. The development of pH and pCO2 microelectrodes for studying the carbonate chemistry of pore waters near the sediment-water interface. Limnology and Oceanography, 38(8): 1762-1773.

Cai, W.J., 2011. Estuarine and coastal ocean carbon paradox: CO2 sinks or sites of terrestrial carbon incineration? Ann Rev Mar Sci, 3: 123-45.

Canfield, D.E., 1989. Sulfate reduction and oxic respiration in marine sediments: implications for organic carbon preservation in euxinic environments. Deep Sea Res A, 36(1): 121-38.

Canfield, D.E. et al., 1993a. Pathways of organic carbon oxidation in three continental margin sediments. Marine Geology, 113(1): 27-40.

Canfield, D.E., Thamdrup, B. and Hansen, J.W., 1993b. The anaerobic degradation of organic matter in Danish coastal sediments: iron reduction, manganese reduction, and sulfate reduction. Geochim Cosmochim Acta, 57(16): 3867-83.

Cao, P. and Stults, J.T., 1999. Phosphopeptide analysis by on-line immobilized metal-ion affinity chromatography-capillary electrophoresis-electrospray ionization mass spectrometry. Journal of Chromatography A, 853(1-2): 225-235.

Capet, A., Meysman, F.J.R., Akoumianaki, I., Soetaert, K. and Grégoire, M., 2016. Integrating sediment biogeochemistry into 3D oceanic models: A study of benthic-pelagic coupling in the Black Sea. Ocean Modelling, 101: 83-100.

Carey, E. and Taillefert, M., 2005. The role of soluble Fe(III) in the cycling of iron and sulfur in coastal marine sediments. Limnology and Oceanography, 50(4): 1129-1141.

Carman, R. and Rahm, L., 1997. Early diagenesis and chemical characteristics of interstitial water and sediments in the deep deposition bottoms of the Baltic proper. Journal of Sea Research, 37(1-2): 25-47.

Carpenter, R., 1987. Has man altered the cycling of nutrients and organic C on the Washington continental shelf and slope? Deep Sea Research Part A. Oceanographic Research Papers, 34(5): 881-896.

Carson, K.C., Holliday, S., Glenn, A.R. and Dilworth, M.J., 1992. Siderophore and organic-acid production in root nodule bacteria. Archives of Microbiology, 157(3): 264-271.

Cathalot, C. et al., 2010. Temporal variability of carbon recycling in coastal sediments influenced by rivers: assessing the impact of flood inputs in the Rhône River prodelta. . Biogeosciences, 7: 1187–1205.

Cathalot, C. et al., 2013. The fate of river organic carbon in coastal areas: A study in the Rhône River delta using multiple isotopic (δ 13 C, Δ 14 C) and organic tracers. Geochimica et Cosmochimica Acta, 118: 33–55.

Cerame-Vivas, M.J. and Gray, I.E., 1966. The Distributional Pattern of Benthic Invertebrates of the Continental Shelf off North Carolina. Ecology, 47(2): 260-270.

Chapman, C.S., Capodaglio, G., Turetta, C. and van den Berg, C.M.G., 2009. Benthic fluxes of copper, complexing ligands and thiol compounds in shallow lagoon waters. Marine Environmental Research, 67(1): 17-24.

Charmasson, S., Radakovitch, O., Arnaud, M., Bouisset, P. and Pruchon, A.-S., 1998. Long-core profiles of 137Cs, 134Cs, 60Co and 210Pb in sediment near the Rhône River (Northwestern Mediterranean Sea). Estuaries, 21(3): 367-378.

Chase, Z. et al., 2005. Manganese and iron distributions off central California influenced by upwelling and shelf width. Marine Chemistry, 95(3): 235-254.

Chen, C.-T.A. and Borges, A.V., 2009. Reconciling opposing views on carbon cycling in the coastal ocean: Continental shelves as sinks and near-shore ecosystems as sources of atmospheric CO2. Deep Sea Research Part II: Topical Studies in Oceanography, 56(8): 578-590.

Chen, M., Wang, W.X. and Guo, L., 2004. Phase partitioning and solubility of iron in natural seawater controlled by dissolved organic matter. Global Biogeochemical Cycles, 18(4).

Chen, Z.L., Sun, Q., Xi, Y.F. and Owens, G., 2008. Speciation of metal-EDTA complexes by flow injection analysis with electrospray ionization mass spectrometry and ion chromatography with inductively coupled plasma mass spectrometry. Journal of Separation Science, 31(21): 3796-3802.

Chow, S.S. and Taillefert, M., 2009. Effect of arsenic concentration on microbial iron reduction and arsenic speciation in an iron-rich freshwater sediment. Geochimica et Cosmochimica Acta., 73: 6008-6021.

Clayton, T.D. and Byrne, R.H., 1993. Spectrophotometric seawater pH measurements: total hydrogen ion concentration scale calibration of m-cresol purple and at-sea results. Deep Sea Research Part I: Oceanographic Research Papers, 40(10): 2115-2129.

Coale, K.H. et al., 1996. A massive phytoplankton bloom induced by an ecosystem-scale iron fertilization experiment in the equatorial Pacific Ocean. Nature, 383(6600): 495-501.

Coates, J.D., Cole, K.A., Chakraborty, R., O'Connor, S.M. and Achenbach, L.A., 2002. Diversity and ubiquity of bacteria capable of utilizing humic substances as electron donors for anaerobic respiration. Appl Environ Microbiol, 68(5): 2445-52.

Coates, J.D. et al., 1998. Recovery of humic-reducing bacteria from a diversity of environments. Appl Environ Microbiol, 64(4): 1504-9.

Coates, J.D., Woodward, J., Allen, J., Philp, P. and Lovley, D.R., 1997. Anaerobic degradation of polycyclic aromatic hydrocarbons and alkanes in petroleum-

contaminated marine harbor sediments. Applied and Environmental Microbiology, 63(9): 3589-3593.

Collins, R.N., Onisko, B.C., McLaughlin, M.J. and Merrington, G., 2001. Determination of metal-EDTA complexes in soil solution and plant xylem by ion chromatography-electrospray mass spectrometry. Environmental Science & Technology, 35(12): 2589-2593.

Cooper, R.E., 2015. Bacterial Iron and Manganese Reduction Driven by Organic Sulfur Electron Shuttles, Georgia Institute of Technology, Atlanta, GA.

Cooper, R.E., Goff, J.L., Reed, B.C., Sekar, R. and DiChristina, T.J., 2016. Breathing Iron: Molecular Mechanism of Microbial Iron Reduction by Shewanella oneidensis, Manual of Environmental Microbiology, Fourth Edition. American Society of Microbiology.

Cornel, P.K., Summers, R.S. and Roberts, P.V., 1986. Diffusion of humic-acid in dilute aqueous-solution. Journal of Colloid and Interface Science, 110(1): 149-164.

Cossarini, G., Lazzari, P. and Solidoro, C., 2015. Spatiotemporal variability of alkalinity in the Mediterranean Sea. Biogeosciences, 12(6): 1647-1658.

Csanady, G.T., 1990. Physical basis of coastal productivity: The SEEP and MASAR experiments. Eos, Transactions American Geophysical Union, 71(36): 1060-1065.

Csanady, G.T. and Hamilton, P., 1988. Circulation of slopewater. Continental Shelf Research, 8(5): 565-624.

Cui, H., Liu, F., Feng, X., Tan, W. and Wang, M.K., 2010. Aging promotes todorokite formation from layered manganese oxide at near-surface conditions. Journal of soils and sediments, 10(8): 1540-1547.

Dale, A.W. et al., 2015. A revised global estimate of dissolved iron fluxes from marine sediments. Global Biogeochemical Cycles, 29(5): 691-707.

Davison, W., 1991. The solubility of iron sulfides in synthetic and natural-waters at ambient temperature. Aquatic Sciences, 53(4): 309-329.

Davison, W., 1993. Iron and manganese in lakes. Earth-Science Reviews, 34(2): 119-163.

Davison, W., Buffle, J. and DeVitre, R., 1998. Voltammetric characterization of a dissolved iron sulphide species by laboratory and field studies. Analytica Chimica Acta, 377(2-3): 193-203

Davison, W., Buffle, J. and Devitre, R., 1988. Interpretations of speciation measurements - a case-study - direct polarographic determination of O2, FE(II), MN(II), S(-II) and related species in anoxic waters. Pure and Applied Chemistry, 60(10): 1535-1548.

Dawson, R.C.M., 1959. Data for Biochemical Research. Clarendon Press, Oxford.

de Baar, H. et al., 1990. On iron limitation of the Southern Ocean: Experimental observations in the Weddell and Scotia Sea, 65, 105-122 pp.

Deguzman, R.N. et al., 1994. Sythesis and characterization of ocathedral molecular-sieves (OMS-2) having the hollandite structure. Chemistry of Materials, 6(6): 815-821.

DeMaster, D.J., Pope, R.H., Levin, L.A. and Blair, N.E., 1994. Biological mixing intensity and rates of organic carbon accumulation in North Carolina slope sediments. Deep Sea Research Part II: Topical Studies in Oceanography, 41(4): 735-753.

DeMaster, D.J. et al., 2002. Deposition of bomb 14C in continental slope sediments of the Mid-Atlantic Bight: assessing organic matter sources and burial rates. Deep Sea Research Part II: Topical Studies in Oceanography, 49(20): 4667-4685.

Devereux, R., Lehrter, J.C., Beddik Jr., D.L., Yates, D.F. and Jarvis, B.M., 2015. Manganese, iron, and sulfur cycling in Louisiana continental shelf sediments. . Continental Shelf Research, 99: 46-56.

Diaz, R.J., Cutter, G.R. and Rhoads, D.C., 1994. The importance of bioturbation to continental slope sediment structure and benthic processes off Cape Hatteras, North Carolina. Deep Sea Research Part II: Topical Studies in Oceanography, 41(4): 719-734.

DiChristina, T.J., Fredrickson, J.K. and Zachara, J.M., 2005. Enzymology of electron transport: Energy generation with geochemical consequences. Molecular Geomicrobiology, 59: 27-52.

DiChristina, T.J., Moore, C.M. and Haller, C.A., 2002. Dissimilatory Fe(III) and Mn(IV) reduction by Shewanella putrefaciens requires ferE, a homolog of the pulE (gspE) type II protein secretion gene. Journal of Bacteriology, 184(1): 142-151.

Dickson, A.G., 1981. An exact definition of total alkalinity and a procedure for the estimation of alkalinity and total inorganic carbon from titration data. Deep Sea Research Part A. Oceanographic Research Papers, 28(6): 609-623.

Dickson, A.G., 1993. pH buffers for sea water media based on the total hydrogen ion concentration scale. Deep Sea Research Part I: Oceanographic Research Papers, 40(1): 107-118.

Dickson, A.G., Sabine, C.L., and Christian, J.R., 2007. Guide to Best Practices for Ocean CO_2 Measurements., volume 3. PISCES Special Publication.

Dilworth, M.J., Carson, K.C., Giles, R.G.F., Byrne, L.T. and Glenn, A.R., 1998. Rhizobium leguminosarum bv. viciae produces a novel cyclic trihydroxamate siderophore, vicibactin. Microbiology, 144(3): 781-791.

Dobrowolska, G., Muszynska, G. and Porath, J., 1991. Model studies on iron(III) ion affinity-chromatography interactions of immobilized metal-ions with nucleotides. Journal of Chromatography, 541(1-2): 333-339.

Doong, R.A. and Schink, B., 2002. Cysteine-mediated reductive dissolution of poorly crystalline iron(III) oxides by Geobacter sulfurreducens. Environmental Science & Technology, 36(13): 2939-2945.

Dryden, C.L., Gordon, A.S. and Donat, J.R., 2007. Seasonal survey of copper-complexing ligands and thiol compounds in a heavily utilized, urban estuary: Elizabeth River, Virginia. Marine Chemistry, 103(3-4): 276-288.

Edsall, J.T. and Wyman, J., 1958. Biophysical chemistry. Thermodynamics, electrostatics, and the biological significance of the properties of matter. Biophysical chemistry. Thermodynamics, electrostatics, and the biological significance of the properties of matter, Vol. I. xv+699p. Illus. pp.

Eitel, E.M. and Taillefert, M., 2017. Mechanistic investigation of Fe(III) oxide reduction by low molecular weight organic sulfur species. Geochimica Et Cosmochimica Acta, 215: 173-188.

El-Naggar, M.Y. et al., 2010. Electrical transport along bacterial nanowires from Shewanella oneidensis MR-1. Proceedings of the National Academy of Sciences of the United States of America, 107(42): 18127-18131.

Elrod, V.A., Berelson, W.M., Coale, K.H. and Johnson, K.S., 2004. The flux of iron from continental shelf sediments: A missing source for global budgets. Geophysical Research Letters, 31(12).

Elzinga, E.J., 2011. Reductive transformation of birnessite by aqueous Mn (II). Environmental science & technology, 45(15): 6366-6372.

Emerson, S. et al., 1982. Environmental oxidation rate of manganese(II) - bacterial catalysis. Geochimica et Cosmochimica Acta, 46(6): 1073-1079.

Emmenegger, L., King, D.W., Sigg, L. and Sulzberger, B., 1998. Oxidation Kinetics of Fe(II) in a Eutrophic Swiss Lake. Environmental Science & Technology, 32(19): 2990-2996.

Esch, M.E.S., Shull, D.H., Devol, A.H. and Moran, S.B., 2013. Regional patterns of bioturbation and iron and manganese reduction in the sediments of the southeastern Bering Sea. Deep-Sea Research Part Ii-Topical Studies in Oceanography, 94: 80-94.

Estournel, C., Kondrachoff, V., Marsaleix, P. and Vehil, R., 1997. The plume of the Rhone: numerical simulation and remote sensing. Continental Shelf Research, 17(8): 899-924.

Falkowski, P.G., Barber, R.T. and Smetacek, V., 1998. Biogeochemical controls and feedbacks on ocean primary production. Science, 281(5374): 200-206.

Faria, G.L., Reis, E.L., Jannotti, N. and Araújo, F.G.S., 2013. Chemical, physical and typological characterization of main brazilian manganese lump ores. Latin American applied research, 43: 17-22.

Feng, X.H., Zhai, L.M., Tan, W.F., Liu, F. and He, J.Z., 2007. Adsorption and redox reactions of heavy metals on synthesized Mn oxide minerals. Environmental Pollution, 147(2): 366-373.

Feng, X.H. et al., 2010. Formation of nano-crystalline todorokite from biogenic Mn oxides. Geochimica et Cosmochimica Acta, 74(11): 3232-3245.

Fennessey, C.M., Jones, M.E., Taillefert, M. and DiChristina, T.J., 2010. Siderophores Are Not Involved in Fe(III) Solubilization during Anaerobic Fe(III) Respiration by Shewanella oneidensis MR-1. Applied and Environmental Microbiology, 76(8): 2425-2432.

Ferdelman, T.G., Church, T.M. and Luther, G.W., 1991. Sulfur enrichment of humic substances in a Delaware salt-marsh sediment core. Geochimica Et Cosmochimica Acta, 55(4): 979-988.

Fitzwater, S.E. et al., 2003. Iron, nutrient and phytoplankton biomass relationships in upwelled waters of the California coastal system. Continental Shelf Research, 23(16): 1523-1544.

Flynn, T.M., O'Loughlin, E.J., Mishra, B., DiChristina, T.J. and Kemner, K.M., 2014. Sulfur-mediated electron shuttling during bacterial iron reduction. Science, 344(6187): 1039-42.

Friedl, G., Dinkel, C. and Wehrli, B., 1998. Benthic fluxes of nutrients in the northwestern Black Sea. Marine Chemistry, 62(1): 77-88.

Friedrich, J. et al., 2002. Benthic Nutrient Cycling and Diagenetic Pathways in the North-western Black Sea. Estuarine, Coastal and Shelf Science, 54(3): 369-383.

Froelich, P.N. et al., 1979. Early oxidation of organic-matter in pelagic sediments of the eastern equatorial atlantic - suboxic diagenesis. Geochimica et Cosmochimica Acta, 43(7): 1075-1090.

Fung, I.Y. et al., 2000. Iron supply and demand in the upper ocean. Global Biogeochemical Cycles, 14(1): 281-295.

Gaillard, J.-F., Pauwels, H., and Michard, G. (1989). Chemical diagenesis in coastal marine sediments. Oceanologica Acta, 12(3):173–187.

Garrels, R.M. and Lerman, A., 1984. Coupling of the sedimentary sulfur and carbon cycles - an improved model. American Journal of Science, 284(9): 989-1007.

Garrels, R.M. and Thompson, M.E., 1960. Oxidation of pyrite by iron sulfate solutions. American Journal of Science, 258: 57-67.

Gerringa, L.J.A. et al., 2007. Kinetic study reveals weak Fe-binding ligand, which affects the solubility of Fe in the Scheldt estuary. Marine Chemistry, 103(1): 30-45.

Giovanelli, J., 1987. Sulfur Amino-Acids of Plants - An Overview. Methods in Enzymology, 143: 419-426.

Gledhill, M. and Buck, K.N., 2012. The organic complexation of iron in the marine environment: a review. Front Microbiol, 3: 69.

Gledhill, M. and Van Den Berg, C.M.G., 1994. Determination of complexation of iron(III) with organic complexing ligands in seawater using cathodic stripping voltammetry. Marine Chemistry, 47(1): 41-54.

Glud, R.N., 2008. Oxygen dynamics of marine sediments. Marine Biology Research, 4(4): 243-289.

Gorby, Y.A. et al., 2006. Electrically conductive bacterial nanowires produced by Shewanella oneidensis strain MR-1 and other microorganisms. Proceedings of the National Academy of Sciences of the United States of America, 103(30): 11358-11363.

Got, H. and Aloisi, J.C., 1990. The Holocene sedimentation on the Gulf of Lions margin: a quantitative approach. Continental Shelf Research, 10(9): 841-855.

Hall, P.J. and Aller, R.C., 1992. Rapid, small-volume, flow injection analysis for SCO2, and NH4+ in marine and freshwaters. Limnology and Oceanography, 37(5): 1113-1119.

Hansard, S.P. and Landing, W.M., 2009. Determination of iron(II) in acidified seawater samples by luminol chemiluminescence. Limnology and Oceanography: Methods, 7(3): 222-234.

Hansel, C.M., Benner, S.G. and Fendorf, S., 2005. Competing Fe(II)-induced mineralization pathways of ferrihydrite. Environmental Science & Technology, 39(18): 7147-7153.

Hansel, C.M. et al., 2003. Secondary mineralization pathways induced by dissimilatory iron reduction of ferrihydrite under advective flow. Geochimica Et Cosmochimica Acta, 67(16): 2977-2992.

Harris, P.T., Macmillan-Lawler, M., Rupp, J. and Baker, E.K., 2014. Geomorphology of the oceans. Marine Geology, 352: 4-24.

Hartnett, H.E., Keil, R.G., Hedges, J.I. and Devol, A.H., 1998. Influence of oxygen exposure time on organic carbon preservation in continental margin sediments. Nature, 391: 572.

Hedges, J.I. and Keil, R.G., 1995. Sedimentary organic matter preservation: an assessment and speculative synthesis. Marine Chemistry, 49(2): 81-115.

Hedges, J.I., Keil, R.G. and Benner, R., 1997. What happens to terrestrial organic matter in the ocean? . Org. Geochem. , 27: 195-212.

Heip, C.H.R. et al., 1995. Production and consumption of biological particles in temperate tidal estuaries. Oceanography and Marine Biology: an annual review. Vol. 33: 1-149.

Heitnerwirguin, C. and Markovits, G., 1963. Kinetics of ion exchange in chelating resin bio-chelex 100 .1. Exchange of alkaline earth ions. Journal of Physical Chemistry, 67(11): 2263-&.

Henneke, E., Luther, G.W. and Delange, G.J., 1991. Determination of inorganic sulfur speciation with polarographic techniques - some preliminary results for recent hypersaline anoxic sediments. Marine Geology, 100(1-4): 115-123.

Henrichs, S.M. and Reeburgh, W.S., 1987. Anaerobic Mineralization of Marine Sediment Organic-Matter - Rates adn the Role of Anaerobic Processes in the Oceanic Carbon Economy. Geomicrobiology Journal, 5(3-4): 191-237.

Herszage, J., Afonso, M.D. and Luther, G.W., 2003. Oxidation of cysteine and glutathione by soluble polymeric MnO(2). Environmental Science & Technology, 37(15): 3332-3338.

Hinkle, M.A., Flynn, E.D. and Catalano, J.G., 2016. Structural response of phyllomanganates to wet aging and aqueous Mn (II). Geochimica et Cosmochimica Acta, 192: 220-234.

Holmes, L.D. and Schiller, M.R., 1997. Immobilized iron(III) metal affinity chromatography for the separation of phosphorylated macromolecules: Ligands and applications. Journal of Liquid Chromatography & Related Technologies, 20(1): 123-142.

Honjo, S., Francois, R., Manganini, S., Dymond, J. and Collier, R., 2000. Particle fluxes to the interior of the Southern Ocean in the Western Pacific sector along 170 degrees W. Deep-Sea Research Part Ii-Topical Studies in Oceanography, 47(15-16): 3521-3548.

Hu, X. and Cai, W.-J., 2011. An assessment of ocean margin anaerobic processes on oceanic alkalinity budget. Global Biogeochemical Cycles, 25(3).

Hu, H., Mylon, S.E. and Benoit, G., 2006. Distribution of the thiols glutathione and 3-mercaptopropionic acid in Connecticut lakes. Limnology and Oceanography, 51(6): 2763-2774.

Huang, N., Siegel, M.M., Kruppa, G.H. and Laukien, F.H., 1999. Automation of a Fourier transform ion cyclotron resonance mass spectrometer for acquisition, analysis, and e-mailing of high-resolution exact-mass electrospray ionization mass spectral data. Journal of the American Society for Mass Spectrometry, 10(11): 1166-1173.

Huettel, M., Ziebis, W., Forster, S. and Luther, G.W., 1998. Advective transport affecting metal and nutrient distributions and interfacial fluxes in permeable sediments. Geochimica Et Cosmochimica Acta, 62(4): 613-631.

Hunter, K. and W. BoydA, P., 2007. Iron-binding ligands and their role in the ocean biogeochemistry of iron, 4.

Hutchins, D.A. and Bruland, K.W., 1998. Iron-limited diatom growth and Si : N uptake ratios in a coastal upwelling regime. Nature, 393(6685): 561-564.

Hutchins, D.A., DiTullio, G.R., Zhang, Y. and Bruland, K.W., 1998. An iron limitation mosaic in the California upwelling regime. Limnology and Oceanography, 43(6): 1037-1054.

Ingledew, W.J. and Poole, R.K., 1984. The respiratory chains of Escherichia coli. Microbiological Reviews, 48(3): 222-271.

Inman, M.P., Beattie, J.K., Jones, D.R. and Baldwin, D.S., 2001. Abiotic hydrolysis of the detergent builder tripolyphosphate by hydrous manganese dioxide. Water Research, 35(8): 1987-1993.

Isokawa, M., Funatsu, T. and Tsunoda, M., 2013. Fast and simultaneous analysis of biothiols by high-performance liquid chromatography with fluorescence detection under hydrophilic interaction chromatography conditions. Analyst, 138(13): 3802-3808.

Jacobson, M.E., 1994. Chemical and biological mobilization of Fe(III) in marsh sediments. Biogeochemistry, 25(1): 41-60.

Jahnke, R.A., 2010. A Global synthesis. In Carbon and Nutrient Fluxes in Continental Margins, pages 597–615. K.-K. Liu, L. Atkinson, R. Quinones, L. Talaue-McManus (eds), Berlin.

Jahnke, R.A. and Christiansen, M.B., 1989. A free-vehicle benthic chamber instrument for sea floor studies. Deep Sea Research Part A. Oceanographic Research Papers, 36(4): 625-637.

Jahnke, R.A. and Jahnke, D.B., 2000. Rates of C, N, P and Si recycling and denitrification at the US Mid-Atlantic continental slope depocenter. Deep-Sea Research Part I-Oceanographic Research Papers, 47(8): 1405-1428.

Jameson, R.F., Linert, W., Tschinkowitz, A. and Gutmann, V., 1988. Anaerobic Oxidation of Cysteine to Cystine by Iron(III) .1. The Reaction in Acidic Solution. Journal of the Chemical Society-Dalton Transactions(4): 943-946.

Janowitz, G.S. and Pietrafesa, L.J., 1980. A Model and Observations of Time-Dependent Upwelling over the Mid-Shelf and Slope. Journal of Physical Oceanography, 10(10): 1574-1583.

Jenne, E.A., 1968. Controls on Mn, Fe, Co, Ni, Cu, and Zn Concentrations in Soils and Water: the Significant Role of Hydrous Mn and Fe Oxides, Trace Inorganics In Water. Advances in Chemistry. AMERICAN CHEMICAL SOCIETY, pp. 337-387.

Jiang, J. and Kappler, A., 2008. Kinetics of Microbial and Chemical Reduction of Humic Substances: Implications for Electron Shuttling. Environmental Science & Technology, 42(10): 3563-3569.

Jickells, T., Spokes, L., 2001. Atmospheric iron inputs to the oceans. In: D. Turner, Hunter, K. (Editor), Biogeochemistry of Iron in Seawater. Wiley, New York.

Jickells, T.D. et al., 2005. Global iron connections between desert dust, ocean biogeochemistry, and climate. Science, 308(5718): 67-71.

Jin, Q.S. and Bethke, C.M., 2002. Kinetics of Electron Transfer through the Respiratory Chain. Biophysical Journal, 83(4): 1797-1808.

Jin, W. and Chen, H., 2000. A new method of determination of diffusion coefficients using capillary zone electrophoresis (peak-height method). Chromatographia, 52(1): 17-21.

Jocelyn, P.C., 1967. Standard Redox Potential of Cystiene-Cystine from Thio-Disulphide Exchange Reaction with Glutathione and Lipoic Acid. European Journal of Biochemistry, 2(3): 327-&.

Johnson, K.S. et al., 2001. The annual cycle of iron and the biological response in central California coastal waters. Geophysical Research Letters, 28(7): 1247-1250.

Johnson, K.S., Chavez, F.P. and Friederich, G.E., 1999. Continental-shelf sediment as a primary source of iron for coastal phytoplankton. Nature, 398(6729): 697-700.

Johnson, K.S., Gordon, R.M. and Coale, K.H., 1997. What controls dissolved iron concentrations in the world ocean? Marine Chemistry, 57(3-4): 137-161.

Johnson, T.C., 1989. Hydrography and sedimentation on the continental slope and rise off North and South Carolina., North Carolina Coastal Oceanography Symposium. National Undersea Research Program 89-2, pp. 151-172.

Jones, J.G., Gardener, S. and Simon, B.M., 1983. Bacterial Reduction of Ferric Iron in a Stratified Eutrophic Lake. Journal of General Microbiology, 129(JAN): 131-139.

Jones, M.E., Beckler, J.S. and Taillefert, M., 2011. The flux of soluble organic-iron(III) complexes from sediments represents a source of stable iron(III) to estuarine waters and to the continental shelf. Limnology and Oceanography, 56(5): 1811-1823.

Jones, M.E., Fennessey, C.M., DiChristina, T.J. and Taillefert, M., 2010. Shewanella oneidensis MR-1 mutants selected for their inability to produce soluble organic-Fe(III) complexes are unable to respire Fe(III) as anaerobic electron acceptor. Environmental Microbiology, 12(4): 938-950.

Jorgensen, B.B., 1982. Mineralization of organic-matter in the sea bed - the role of sulfate reduction. Nature, 296(5858): 643-645.

Jørgensen, B.B. and Kasten, S., 2006. Sulfur Cycling and Methane Oxidation. In: H.D. Schulz and M. Zabel (Editors), Marine Geochemistry. Springer Berlin Heidelberg, Berlin, Heidelberg, pp. 271-309.

Jourabchi, P., Van Cappellen, P., and Regnier, P., 2005. Quantitative interpretation of pH distributions in aquatic sediments: A reaction-transport modeling approach. American Journal of Science, 305(9):919–956.

Kaden, J., Galushko, A.S. and Schink, B., 2002. Cysteine-mediated electron transfer in syntrophic acetate oxidation by cocultures of Geobacter sulfurreducens and Wolinella succinogenes. Archives of Microbiology, 178(1): 53-58.

Kalinowski, B.E., Liermann, L.J., Givens, S. and Brantley, S.L., 2000. Rates of bacteria-promoted solubilization of Fe from minerals: a review of problems and approaches. Chemical Geology, 169(3): 357-370.

Kappler, A., Benz, M., Schink, B. and Brune, A., 2004. Electron shuttling via humic acids in microbial iron(III) reduction in a freshwater sediment. FEMS Microbiol Ecol, 47(1): 85-92.

Kappler, A. and Bryce, C., 2017. Cryptic biogeochemical cycles: unravelling hidden redox reactions. Environmental Microbiology, 19(3): 842-846.

Kavaklı, P.A., Kavaklı, C. and Güven, O., 2014. Preparation and characterization of Fe(III)-loaded iminodiacetic acid modified GMA grafted nonwoven fabric adsorbent for anion adsorption. Radiation Physics and Chemistry, 94: 105-110.

Kawakami, S.K. and Achterberg, E.P., 2012. Particulate Thiol Peptides Along a Salinity Gradient of a Metal-Contaminated Estuary. Estuaries and Coasts, 35(2): 658-664.

Kemp, P.F., 1994. Microbial carbon utilization on the continental shelf and slope during the SEEP-II experiment. Deep Sea Research Part II: Topical Studies in Oceanography, 41(2): 563-581.

Kemp, W.M., Sampou, P.A., Garber, J., Tuttle, J. and Boynton, W.R., 1992. Seasonal depletion of oxygen from bottom waters of Chesapeake Bay: roles of benthic and planktonic respiration and physical exchange processes. Marine Ecology Progress Series, 85(1-2): 137-152.

Kessick, M.A. and Morgan, J.J., 1975. Mechanism of autoxidation of manganese in aqueous solution. Environmental Science & Technology, 9(2): 157-159.

Kiene, R.P., 1991. Evidence for the biological turnover of thiols in anoxic marine sediments. Biogeochemistry, 13(2): 117-135.

Kiene, R.P., Malloy, K.D. and Taylor, B.F., 1990. Sulfur-Containing Amino-Acids as Precursors of Thiols in Anoxic Coastal Sediments. Applied and Environmental Microbiology, 56(1): 156-161.

Kiene, R.P. and Taylor, B.F., 1988a. Biotransformations of Organosulfur Compounds in Sediments via 3-Mercaptopropionate. Nature, 332(6160): 148-150.

Kiene, R.P. and Taylor, B.F., 1988b. Demethylation of dimethylsulfoniopropionate and production of thiols in anoxic marine sediments. Appl Environ Microbiol, 54(9): 2208-12.

King, D.W., Lounsbury, H.A. and Millero, F.J., 1995. Rates and Mechanism of Fe(II) Oxidation at Nanomolar Total Iron Concentrations. Environmental Science & Technology, 29(3): 818-824.

King, G.M., 1988. Patterns of sulfate reduction and the sulfur cycle in a South Carolina salt marsh1,2. Limnology and Oceanography, 33(3): 376-390.

Kiontke, A., Oliveira-Birkmeier, A., Opitz, A. and Birkemeyer, C., 2016. Electrospray Ionization Efficiency Is Dependent on Different Molecular Descriptors with Respect to Solvent pH and Instrumental Configuration. Plos One, 11(12).

Klüpfel, L., Piepenbrock, A., Kappler, A. and Sander, M., 2014. Humic substances as fully regenerable electron acceptors in recurrently anoxic environments. Nature Geoscience, 7: 195.

Knepper, T.P., Werner, A. and Bogenschutz, G., 2005. Determination of synthetic chelating agents in surface and waste water by ion chromatography-mass spectrometry. Journal of Chromatography A, 1085(2): 240-246.

Kolber, Z.S. et al., 1994. Iron Limitation of Phytoplanton Photosynthesis in teh Equatorial Pacific Ocean. Nature, 371(6493): 145-149.

Komada, T. et al., 2016. Organic matter cycling across the sulfate-methane transition zone of the Santa Barbara Basin, California Borderland. Geochimica et Cosmochimica Acta, 176: 259-278.

Koretsky, C.M. et al., 2003. Seasonal oscillation in microbial iron and sulfate reduction in saltmarsh sediments. Biogeochemistry, 64: 179-203.

Kostka, J.E. et al., 2002. The rates and pathways of carbon oxidation in bioturbated saltmarsh sediments. Limnology and Oceanography, 47(1): 230-240.

Kostka, J.E. and Luther, G.W., 1994. Partitioning and speciation of solid phase iron in saltmarsh sediments. Geochimica et Cosmochimica Acta, 58(7): 1701-1710.

Kostka, J.E., Luther, G.W. and Nealson, K.H., 1995. Chemical and biological reduciton of Mn(III)-pyrophosphate complexes - potential importance of dissolved Mn(III) as an environmental oxidant. Geochimica Et Cosmochimica Acta, 59(5): 885-894.

Kostka, J.E. and Nealson, K.H., 1995. Dissolution and Reduction of Magnetite by Bacteria. Environmental Science & Technology, 29(10): 2535-2540.

Krumins, V., Gehlen, M., Arndt, S., Van Cappellen, P. and Regnier, P., 2013. Dissolved inorganic carbon and alkalinity fluxes from coastal marine sediments: model estimates for different shelf environments and sensitivity to global change. Biogeosciences, 10(1): 371-398.

Lam, P.J. and Bishop, J.K.B., 2008. The continental margin is a key source of iron to the HNLC North Pacific Ocean. Geophysical Research Letters, 35(7).

Lam, P.J. et al., 2006. Wintertime phytoplankton bloom in the subarctic Pacific supported by continental margin iron. Global Biogeochemical Cycles, 20(1).

Lansard, B., Rabouille, C., Denis, L. and Grenz, C., 2008. In situ oxygen uptake rates by coastal sediments under the influence of the Rhone River (NW Mediterranean Sea). Continental Shelf Research, 28: 1501-1510.

Lansard, B., Rabouille, C., Denis, L. and Grenz, C., 2009. Benthic remineralization at the land–ocean interface: A case study of the Rhône River (NW Mediterranean Sea). Estuarine, Coastal and Shelf Science, 81(4): 544–554.

Lanson, B. et al., 2002. Structure of heavy-metal sorbed birnessite: Part 1. Results from X-ray diffraction. American Mineralogist, 87(11-12): 1631-1645.

Lanson, B., Drits, V.A., Silvester, E. and Manceau, A., 2000. Structure of H-exchanged hexagonal birnessite and its mechanism of formation from Na-rich monoclinic buserite at low pH. American Mineralogist, 85(5-6): 826-838.

Latta, D.E., Gorski, C.A. and Scherer, M.M., 2012. Influence of Fe2+-catalysed iron oxide recrystallization on metal cycling. Biochemical Society Transactions, 40: 1191-1197.

Le Gall, A.-C. and van den Berg, C.M.G., 1993. Cathodic stripping voltammetry of glutathione in natural waters. Analyst, 118(11): 1411-1415.

Le Gall, C.A. and Van Den Berg, C.M.G., 1998. Folic acid and glutathione in the water column of the North East Atlantic. Deep Sea Research Part I: Oceanographic Research Papers, 45(11): 1903-1918.

Leal, M.F.C. and Van den Berg, C.M.G., 1998. Evidence for strong copper(I) complexation by organic ligands in seawater. Aquatic Geochemistry, 4(1): 49-75.

Learman, D., Voelker, B., Vazquez-Rodriguez, A. and Hansel, C., 2011a. Formation of manganese oxides by bacterially generated superoxide. Nature Geoscience, 4(2): 95-98.

Learman, D.R. et al., 2011b. Coupled biotic–abiotic Mn(II) oxidation pathway mediates the formation and structural evolution of biogenic Mn oxides. Geochimica et Cosmochimica Acta, 75(20): 6048-6063.

Lefkowitz, J.P. and Elzinga, E.J., 2015. Impacts of Aqueous Mn(II) on the Sorption of Zn(II) by Hexagonal Birnessite. Environmental Science & Technology, 49(8): 4886-4893.

Lefkowitz, J.P., Rouff, A.A. and Elzinga, E.J., 2013. Influence of pH on the reductive transformation of birnessite by aqueous Mn (II). Environmental science & technology, 47(18): 10364-10371.

Legall, A.C. and Van Den Berg, C.M.G., 1993. Cathodic Stripping of Voltammetry of Glutathione in Natural-Waters. Analyst, 118(11): 1411-1415.

Lehrter, J.C., Beddick, D.L., Devereux, R., Yates, D.F. and Murrell, M.C., 2012. Sediment-water fluxes of dissolved inorganic carbon, O2, nutrients, and N2 from the hypoxic region of the Louisiana continental shelf. Biogeochemistry, 109(1): 233-252.

Li, Y.-F., Zhu, S.-C. and Liu, Z.-P., 2016. Reaction network of layer-to-tunnel transition of MnO2. Journal of the American Chemical Society, 138(16): 5371-5379.

Li, Y.-H. and Gregory, S., 1974. Diffusion of ions in sea water and in deep-sea sediments. Geochimica et Cosmochimica Acta, 38(5): 703-714.

Li, Y., Agrawal, A., Sakon, J. and Beitle, R.R., 2001. Characterization of metal affinity of green fluorescent protein and its purification through salt promoted, immobilized metal affinity chromatography. Journal of Chromatography A, 909(2): 183-190.

Liang, L., McCarthy, J.F., Jolley, L.W., McNabb, J.A. and Mehlhorn, T.L., 1993. Iron dynamics: Transformation of Fe(II)/Fe(III) during injection of natural organic matter in a sandy aquifer. Geochimica et Cosmochimica Acta, 57(9): 1987-1999.

Lide, D.R., 2003. Handbook of Chemistry and Physics. In: D.R. Lide (Editor). Taylor & Francis.

Lin, H., Szeinbaum, N.H., DiChristina, T.J. and Taillefert, M., 2012. Microbial Mn(IV) reduction requires an initial one-electron reductive solubilization step. Geochimica Et Cosmochimica Acta, 99: 179-192.

Liu, D., Dong, H., Zhao, L. and Wang, H., 2014. Smectite Reduction by Shewanella Species as Facilitated by Cystine and Cysteine. Geomicrobiology Journal, 31(1): 53-63.

Liu, X.W. and Millero, F.J., 2002. The solubility of iron in seawater. Marine Chemistry, 77(1): 43-54.

Lohan, M.C. and Bruland, K.W., 2008. Elevated Fe(II) and Dissolved Fe in Hypoxic Shelf Waters off Oregon and Washington: An Enhanced Source of Iron to Coastal Upwelling Regimes. Environmental Science & Technology, 42(17): 6462-6468.

Lonergan, D.J. et al., 1996. Phylogenetic analysis of dissimilatory Fe(III)-reducing bacteria. Journal of Bacteriology, 178(8): 2402-2408.

Lovley, D.R., 1991. Dissimilatory Fe(III) and Mn(IV) Reduction. Microbiological Reviews, 55(2): 259-287.

Lovley, D.R., 2008. Extracellular electron transfer: wires, capacitors, iron lungs, and more. Geobiology, 6(3): 225-231.

Lovley, D.R. et al., 1989. Oxidation of aromatic contaminants coupled to microbial iron reduction. Nature, 339(6222): 297-300.

Lovley, D.R., Coates, J.D., Blunt-Harris, E.L., Phillips, E.J.P. and Woodward, J.C., 1996. Humic substances as electron acceptors for microbial respiration. Nature, 382: 445.

Lovley, D.R., Holmes, D.E. and Nevin, K.P., 2004. Dissimilatory Fe(III) and Mn(IV) reduction. In: R.K. Poole (Editor), Advances in Microbial Physiology, Vol. 49. Advances in Microbial Physiology. Academic Press Ltd-Elsevier Science Ltd, London, pp. 219-286.

Lowe, K.L., DiChristina, T.J., Roychoudhury, A.N. and Van Cappellen, P., 2000. Microbiological and Geochemical Characterization of Microbial Fe(III) Reduction in Salt Marsh Sediments. Geomicrobiology Journal, 17(2): 163-178.

Lu, A.H. and Li, Y., 2015. Reactivity of Natural Mn Oxide Cryptomelane. In: X. Feng, W. Li, M. Zhu and D.L. Sparks (Editors), Advances in the Environmental Biogeochemistry of Manganese Oxides. ACS Symposium Series, pp. 89-106.

Luijten, M.L. et al., 2004. Anaerobic reduction and oxidation of quinone moieties and the reduction of oxidized metals by halorespiring and related organisms. FEMS Microbiol Ecol, 49(1): 145-50.

Luther, G.W., 1990. The frontier-molecular-orbital theory approach in geotechnical processes. In: W. Stumm (Editor), Aquatic Chemical Kinetics. John Wiley & Sons, New York, pp. 173.

Luther, G.W., 2005. Manganese(II) oxidation and Mn(IV) reduction in the environment - Two one-electron transfer steps versus a single two-electron step. Geomicrobiology Journal, 22(3-4): 195-203.

Luther, G.W., Church, T.M. and Powell, D., 1991. Sulfur speciation and sulfide oxidation in the water column of the Black Sea. Deep Sea Research Part A. Oceanographic Research Papers, 38: S1121-S1137.

Luther, G.W., Church, T.M., Scudlark, J.R. and Cosman, M., 1986. Inorganic and Organic Sulfur Cycling in Salt-Marsh Pore Waters. Science, 232(4751): 746-749.

Luther, G.W. and Ferdelman, T.G., 1993. Voltammetric characterization of iron(II) sulfide complexes in laboratory solutions and in marine waters and porewaters. Environmental Science & Technology, 27(6): 1154-1163.

Luther, G.W. et al., 2008. Use of voltammetric solid-state (micro)electrodes for studying biogeochemical processes: Laboratory measurements to real time measurements with an in situ electrochemical analyzer (ISEA). Marine Chemistry, 108(3-4): 221-235.

Luther, G.W., Kostka, J.E., Church, T.M., Sulzberger, B. and Stumm, W., 1992. Seasonal iron cycling in the salt-marsh sedimentary environment - the importance of ligand complexes with Fe(II) and Fe(III) in the dissolution of Fe(III) minerals and pyrite respectively. Marine Chemistry, 40(1-2): 81-103.

Luther, G.W., Shellenbarger, P.A. and Brendel, P.J., 1996. Dissolved organic Fe(III) and Fe(II) complexes in salt marsh porewaters. Geochimica et Cosmochimica Acta, 60(6): 951-960.

Luther, G.W., Sundby, B., Lewis, B.L., Brendel, P.J. and Silverberg, N., 1997. Interactions of manganese with the nitrogen cycle: Alternative pathways to dinitrogen. Geochimica Et Cosmochimica Acta, 61(19): 4043-4052.

Ma, S. et al., 2008. Solid-state Au/Hg microelectrode for the investigation of Fe and Mn cycling in a freshwater wetland: Implications for methane production. . Electroanalysis, 20: 233-239.

MacCrehan, W. and Shea, D., 1995. Temporal relationship of thiols to inorganic sulfur compounds in anoxic Chesapeake Bay sediment porewater. In: M.A. Vairavamurthy and M.A.A. Schoonen (Editors), Geochemical Transformations of Sedimentary Sulfur. Acs Symposium Series, pp. 294-310.

Machida, M. et al., 2007. Purification of phosphoproteins by immobilized metal affinity chromatography and its application to phosphoproteome analysis. Febs j, 274(6): 1576-87.

Macrellis, H.M., Trick, C.G., Rue, E.L., Smith, G. and Bruland, K.W., 2001. Collection and detection of natural iron-binding ligands from seawater. Marine Chemistry, 76(3): 175-187.

Madison, A.S., Tebo, B.M., Mucci, A., Sundby, B. and Luther, G.W., III, 2013. Abundant Porewater Mn(III) Is a Major Component of the Sedimentary Redox System. Science, 341(6148): 875-878.

Mandernack, K.W., Post, J. and Tebo, B.M., 1995. Manganese mineral formation by bacterial spores of the marine Bacillus, strain SG-1: evidence for the direct oxidation of Mn (II) to Mn (IV). Geochimica et Cosmochimica Acta, 59(21): 4393-4408.

Marie, L., Pernet-Coudrier, B., Waeles, M. and Riso, R., 2016. Seasonal variation and mixing behaviour of glutathione, thioacetamide and fulvic acids in a temperate macrotidal estuary (Aulne, NW France), 184.

Marinelli, R.L., Jahnke, R.A., Craven, D.B., Nelson, J.R. and Eckman, J.E., 1998. Sediment nutrient dynamics on the South Atlantic Bight continental shelf. Limnology and Oceanography, 43(6): 1305-1320.

Marsili, E. et al., 2008. Shewanella secretes flavins that mediate extracellular electron transfer. Proceedings of the National Academy of Sciences, 105(10): 3968-3973.

Martin, J.H., 1990. Glacial-interglacial CO2 change: the iron hypothesis. Paleoceanography, 5(1): 1-13.

Martin, J.H. and Fitzwater, S.E., 1988. Iron-deficiency limits phytoplankton growth in the northeast pacific subarctic. Nature, 331(6154): 341-343.

Martin, J.M. and Meybeck, M., 1979. Elemental mass-balance of material carried by major world rivers. Marine Chemistry, 7(3): 173-206.

Matrai, P.A. and Vetter, R.D., 1988a. Particulate Thiols in Coastal Waters - The Effect of Light and Nutrients on their Plankton Production. Limnology and Oceanography, 33(4): 624-631.

Matrai, P.A. and Vetter, R.D., 1988b. Particulate thiols in coastal waters - the effect of light and nutrients on their planktonic production. Limnology and Oceanography, 33(4): 624-631.

Matsuura, T. et al., 2008. Coadsorption of Trivalent Metal Ions and Anions on Strongly Acidic Cation-Exchange Resins by Bridge Bonding. Analytical Chemistry, 80(24): 9666-9671.

McCormack, P., Worsfold, P.J. and Gledhill, M., 2003. Separation and Detection of Siderophores Produced by Marine Bacterioplankton Using High-Performance Liquid Chromatography with Electrospray Ionization Mass Spectrometry. Analytical Chemistry, 75(11): 2647-2652.

McGregor, B., 1984. Resolution: A key to better understanding continental slope and rise processes. U.S. Atlantic Continental Margin. Ocean Technology Conference, Paper 4722, 16th Annual OTC: 111-118.

McKee, B.A., Aller, R.C., Allison, M.A., Bianchi, T.S. and Kineke, G.C., 2004. Transport and transformation of dissolved and particulate materials on continental margins influenced by major rivers: Benthic boundary layer and seabed processes. . Continental Shelf Research, 24: 899-926.

Meier, T. and Issels, R.D., 1995. Promotion of Cyst(e)ine Uptake. Biothiols, Pt B, 252: 103-112.

Meiggs, D. and Taillefert, M., 2011. The effect of riverine discharge on biogeochemical processes in estuarine sediments. Limnology and Oceanography, 56(5): 1797-1810.

Meister, A. and Anderson, M.E., 1983. Glutathione. Annual Review of Biochemistry, 52: 711-760.

Mellor, C.A. and Paull, C.K., 1994. Sea beam bathymetry of the Manteo 467 lease block off Cape Hatteras, North Carolina. Deep Sea Research Part II: Topical Studies in Oceanography, 41(4): 711-718.

Miller, S.L. and Schlesinger, G., 1993. Prebiotic Synthesis of Vitamin Coenzymes.1. Cysteamine and 2-Mercatoethansulfonic Acid (Coenzyme-M). Journal of Molecular Evolution, 36(4): 302-307.

Millero, F.J., 1998. Solubility of Fe(III) in seawater. Earth and Planetary Science Letters, 154(1): 323-329.

Millero, F.J., Yao, W. and Aicher, J., 1995. The speciation of Fe(II) and Fe(III) in natural waters. Marine Chemistry, 50(1): 21-39.

Milliman, J.D., 1994. Organic matter content in U.S. Atlantic continental slope sediments: Decoupling the grain-size factor. Deep Sea Research Part II: Topical Studies in Oceanography, 41(4): 797-808.

Milliman, J.D., Pilkey, O.H. and Ross, D.A., 1972. Sediments of the Continental Margin off the Eastern United States. GSA Bulletin, 83(5): 1315-1334.

Miralles, J., Radakovitch, O. and Aloisi, J.C., 2005. 210Pb sedimentation rates from the Northwestern Mediterranean margin. Marine Geology, 216(3): 155-167.

Mitsch, W.J. and Gosselink, J.G., 1993. Wetlands, 2ed. International Thompson Publishing, New York.

Moore, J.K., Doney, S.C., Glover, D.M. and Fung, I.Y., 2002. Iron cycling and nutrient-limitation patterns in surface waters of the World Ocean. Deep-Sea Research Part Ii-Topical Studies in Oceanography, 49(1-3): 463-507.

Moore, J.K., Doney, S.C. and Lindsay, K., 2004. Upper ocean ecosystem dynamics and iron cycling in a global three-dimensional model. Global Biogeochemical Cycles, 18(4).

Moore, T.E., Ellis, M. and Selwood, P.W., 1950. Solid Oxides and Hydroxides of Manganese1. Journal of the American Chemical Society, 72(2): 856-866.

Mopper, K. and Taylor, B.F., 1986. Biogeochemical cycling of sulfur - thiols in coastal marine sediments Acs Symposium Series, 305: 324-339.

Morgan, J.J., 2000. Manganese in natural waters and earth's crust: Its availability to organisms. In: A. Sigel and H. Sigel (Editors), Metal Ions in Biological Systems, Vol 37: Manganese and Its Role in Biological Processes. Metal Ions in Biological Systems, pp. 1-34.

Morrison, K.D., Bristow, T.F. and Kennedy, M.J., 2013. The reduction of structural iron in ferruginous smectite via the amino acid cysteine: Implications for an electron shuttling compound. Geochimica Et Cosmochimica Acta, 106: 152-163.

Mucci, A. et al., 2000. The fate of carbon in continental shelf sediments of eastern Canada: a case study. Deep Sea Research Part II: Topical Studies in Oceanography, 47(3): 733-760.

Muglia, J., Somes, C.J., Nickelsen, L. and Schmittner, A., 2017. Combined Effects of Atmospheric and Seafloor Iron Fluxes to the Glacial Ocean. Paleoceanography, 32(11): 1204-1218.

Muller-Karger, F.E. et al., 2005. The importance of continental margins in the global carbon cycle. Geophysical Research Letters, 32(1).

Murphy, J. and Riley, J.P., 1962. A modified single solution method for determination of phosphate in natural water. Analytica Chimica Acta, 26(1): 31-&.

Murray, J.W., 1974. Surface chemistry of hydrous manganese-dioxide. Journal of Colloid and Interface Science, 46(3): 357-371.

Murray, J.W. and Kuivila, K.M., 1990. Organic matter diagenesis in the northeast Pacific: transition from aerobic red clay to suboxic hemipelagic sediments. Deep Sea Research Part A. Oceanographic Research Papers, 37(1): 59-80.

Muszynska, G., Andersson, L. and Porath, J., 1986. Selective adsorption of phosphoproteins on gel-immobilized ferric chelate. Biochemistry, 25(22): 6850-6853.

Muszynska, G., Dobrowolska, G., Medin, A., Ekman, P. and Porath, J.O., 1992. Model studies of iron(III) ion affinity-chromatography .2. interaction of immobilized iron(III) ions with phosphorylated amino-acids, peptides and proteins. Journal of Chromatography, 604(1): 19-28.

Myers, C.R. and Myers, J.M., 2002. MtrB is required for proper incorporation of the cytochromes OmcA and OmcB into the outer membrane of Shewanella putrefaciens MR-1. Applied and Environmental Microbiology, 68(11): 5585-5594.

Myers, C.R. and Nealson, K.H., 1988. Bacterial manganese reduction and growth with manganese oxide as the sole electron-acceptor. Science, 240(4857): 1319-1321.

Nakayama, N. et al., 2016. Size fractionation of nanoparticulate metal sulfides in oxic water of Lake Teganuma, Japan. Geochemical Journal, 50(3): 281-286.

Nealson, K.H., Tebo, B.M. and Rosson, R.A., 1988. Occurrence and Mechanisms of Microbial Oxidation of Manganese. In: A.I. Laskin (Editor), Advances in Applied Microbiology. Academic Press, pp. 279-318.

Nelson, Y.M. and Lion, L.W., 2003. Formation of Biogenic Manganese Oxides and Their Influence on the Scavenging of Toxic Trace Elements, Geochemical and Hydrological Reactivity of Heavy Metals in Soils. CRC Press.

Neretin, L.N., Pohl, C., Jost, G., Leipe, T. and Pollehne, F., 2003. Manganese cycling in the Gotland Deep, Baltic Sea. Marine Chemistry, 82(3-4): 125-143.

Nesbitt, H.W., Canning, G.W. and Bancroft, G.M., 1998. XPS study of reductive dissolution of 7 angstrom-birnessite by H3AsO3, with constraints on reaction mechanism. Geochimica Et Cosmochimica Acta, 62(12): 2097-2110.

Nevin, K.P. and Lovley, D.R., 2002. Mechanisms for accessing insoluble Fe(III) oxide during dissimilatory Fe(III) reduction by Geothrix fermentans. Appl Environ Microbiol, 68(5): 2294-9.

Nico, P.S. and Zasoski, R.J., 2000. Importance of Mn(III) Availability on the Rate of Cr(III) Oxidation on δ-MnO2. Environmental Science & Technology, 34(16): 3363-3367.

Niewöhner, C., Hensen, C., Kasten, S., Zabel, M. and Schulz, H.D., 1998. Deep Sulfate Reduction Completely Mediated by Anaerobic Methane Oxidation in Sediments of

the Upwelling Area off Namibia. Geochimica et Cosmochimica Acta, 62(3): 455-464.

Noffke, A. et al., 2012. Benthic iron and phosphorus fluxes across the Peruvian oxygen minimum zone. Limnology and Oceanography, 57(3): 851-867.

Nuzzio, D.B., Taillefert, M. and Luther, G.W., 2000. Application of in situ electroanalytical techniques to aquatic and sediment systems. Abstracts of Papers of the American Chemical Society, 220: U317-U317.

O'Loughlin, E.J., 2008. Effects of electron transfer mediators on the bioreduction of lepidocrocite (gamma-FeOOH) by Shewanella putrefaciens CN32. Environmental Science & Technology, 42(18): 6876-6882.

O'Sullivan, D.W., Hanson, A.K. and Kester, D.R., 1995. Stopped flow luminol chemiluminescence determination of Fe(II) and reducible iron in seawater at subnanomolar levels. Marine Chemistry, 49(1): 65-77.

Oldham, V.E., Owings, S.M., Jones, M.R., Tebo, B.M. and Luther, G.W., 2015. Evidence for the presence of strong Mn(III)-binding ligands in the water column of the Chesapeake Bay. Marine Chemistry, 171: 58-66.

Orera, I., Orduna, J., Abadia, J. and Alvarez-Fernandez, A., 2010. Electrospray ionization collision-induced dissociation mass spectrometry: a tool to characterize synthetic polyaminocarboxylate ferric chelates used as fertilizers. Rapid Communications in Mass Spectrometry, 24(1): 109-119.

Orr, W.L., 1986. Kerogen/asphaltene/sulfur relationships in sulfur-rich Monterey oils. Organic Geochemistry, 10(1): 499-516.

Oscarson, D.W., Huang, P.M., Defosse, C. and Herbillon, A., 1981. Oxidative power of Mn(IV) and Fe(III) oxides with respect to As(III) in terrestrial and aquatic environments. Nature, 291(5810): 50-51.

Osteryoung, J.G. and Osteryoung, R.A., 1985. Square wave voltammetry. Analytical Chemistry, 57(1): 101-110.

Ostwald, J., 1992. Genesis and paragenesis of the tetravalent manganese oxides of the australian continent. Economic Geology and the Bulletin of the Society of Economic Geologists, 87(5): 1237-1252.

Parc, S., Nahon, D., Tardy, Y. and Vieillard, P., 1989. Estimated solubility products and fields of stability for cryptomelane, nsutite, birnessite, and lithiophorite based on natural lateritic weathering sequences. American Mineralogist, 74(3-4): 466-475.

Park, S.-G. and Butcher, D.J., 2010. Investigation of the interaction between arsenic species and thiols via electrospray ionization tandem mass spectrometry. Microchemical Journal, 95(1): 57-66.

Pastor, L. et al., 2011. Modeling biogeochemical processes in sediments from the Rhone River prodelta area (NW Mediterranean Sea). Biogeosciences, 8: 1351-1366.

Peck, H.D., Jr. and LeGall, J., 1982. Biochemistry of dissimilatory sulphate reduction. Philos Trans R Soc Lond B Biol Sci, 298(1093): 443-66.

Pedersen, T.F., Shimmield, G.B. and N.B, P., 1992. Lack of enhanced preservation of organic matter in sediments under the oxygen minimum on the Oman Margin. Geochimica et Cosmochimica Acta, 56(1): 545-551.

Perdue, E.M., Beck, K.C. and Helmut Reuter, J., 1976. Organic complexes of iron and aluminium in natural waters. Nature, 260: 418.

Peri-Okonny, U., 2001. Effects of eluent pH and different types of acidic modifiers on the retention and electrospray ionization efficiency of basic analytes in LC-ESI-MS, Seton Hall University, South Orange, NJ.

Periat, A., Krull, I.S. and Guillarme, D., 2015. Applications of hydrophilic interaction chromatography to amino acids, peptides, and proteins. Journal of Separation Science, 38(3): 357-367.

Peterson, B.J. and Howarth, R.W., 1987. Sulfur, carbon, and nitrogen isotopes used to trace organic matter flow in the salt-marsh estuaries of Sapelo Island, Georgia. Limnol. Oceanogr., 32: 1195-1213.

Pietrafesa, L.J., Janowitz, G.S. and Wittman, P.A., 1985. Physical Oceanographic Processes in the Carolina Capes, Oceanography of the Southeastern U.S. Continental Shelf. American Geophysical Union, pp. 23-32.

Pomeroy, L.R. and Wiegert, R.G., 1981. The ecology of a salt marsh. Springer-Verlag, New-York.

Popenoe, P., 1980. Single-channel seismic-reflection profiles collected on the northern Blake Plateau, 29 September to 19 October 1978., U.S. Geol. Surv. Open-File Rep. 80-1256:4.

Popenoe, P., Coward, E.L. and Cashman, K.V., 1982. A regional assessment of potential environmental hazards to and limitations on petroleum development of the Southeastern United States Atlantic continental shelf, slope, and rise, offshore North Carolina. 82-136.

Post, J.E., 1999. Manganese oxide minerals: Crystal structures and economic and environmental significance. Proceedings of the National Academy of Sciences of the United States of America, 96(7): 3447-3454.

Postma, D. and Appelo, C.A.J., 2000. Reduction of Mn-oxides by ferrous iron in a flow system: Column experiment and reactive transport modeling. Geochimica Et Cosmochimica Acta, 64(7): 1237-1247.

Poulton, S.W. and Raiswell, R., 2002. The low-temperature geochemical cycle of iron: From continental fluxes to marine sediment deposition. American Journal of Science, 302(9): 774-805.

Pozzato, L. et al., 2017. Origin of remineralized organic matter in sediments from the Rhone River prodelta (NW Mediterranean) traced by Δ 14 C and δ 13 C signatures of pore water DIC. . Progress in Oceanography.

Pratt, R.M., 1966. The Gulf Stream as a graded river. . Limnology and Oceanography(11): 60-67.

Premuzic, E.T., Benkovitz, C.M., Gaffney, J.S. and Walsh, J.J., 1982. The nature and distribution of organic matter in the surface sediments of world oceans and seas. Organic Geochemistry, 4(2): 63-77.

Pyzik, A.J. and Sommer, S.E., 1981. Sedimentary Iron Monosulfides - Kinetics and Mechanism of Formation. Geochimica Et Cosmochimica Acta, 45(5): 687-698.

Rabouille, C. et al., 2003. Oxygen demand in coastal marine sediments: comparing in situ microelectrodes and laboratory core incubations. Journal of Experimental Marine Biology and Ecology, 285-286: 49-69.

Radakovitch, O., Cherry, R.D. and Heussner, S., 1999. 210Pb and 210Po: tracers of particle transfer on the Rhône continental margin (NW Mediterranean). Deep Sea Research Part I: Oceanographic Research Papers, 46(9): 1539-1563.

Raiswell, R., Benning, L.G., Tranter, M. and Tulaczyk, S., 2008. Bioavailable iron in the Southern Ocean: the significance of the iceberg conveyor belt. Geochemical Transactions, 9.

Raiswell, R. et al., 2006. Contributions from glacially derived sediment to the global iron (oxyhydr)oxide cycle: Implications for iron delivery to the oceans. Geochimica Et Cosmochimica Acta, 70(11): 2765-2780.

Rassmann, J., Lansard, B., Pozzato, L. and Rabouille, C., 2016. Carbonate chemistry in sediment porewaters of the Rhône River delta driven by early diagenesis (northwestern Mediterranean). Biogeosciences, 13: 5379-5394.

Ravel, B. and Newville, M., 2005. ATHENA, ARTEMIS, HEPHAESTUS: data analysis for X-ray absorption spectroscopy using IFEFFIT. Journal of Synchrotron Radiation, 12: 537-541.

Reguera, G. et al., 2005. Extracellular electron transfer via microbial nanowires. Nature, 435: 1098.

Remucal, C.K. and Ginder-Vogel, M., 2014. A critical review of the reactivity of manganese oxides with organic contaminants. Environ Sci Process Impacts, 16(6): 1247-66.

Rhoads, D.C. and Hecker, B., 1994. Processes on the continental slope off North Carolina with special reference to the Cape Hatteras region. Deep Sea Research Part II: Topical Studies in Oceanography, 41(4): 965-980.

Richardson, P.L., 1977. On the crossover between the Gulf Stream and the Western Boundary Undercurrent. Deep Sea Research, 24(2): 139-159.

Richter, K., Schicklberger, M. and Gescher, J., 2012. Dissimilatory reduction of extracellular electron acceptors in anaerobic respiration. Appl Environ Microbiol, 78(4): 913-21.

Rickard, D., 1989. Experimental concentration-time curves for the iron(II) sulfide precipitation process in aqueous-solutions and their interpretation. Chemical Geology, 78(3-4): 315-324.

Rickard, D., 1995. Kinetics of FeS precipitation .1. competing reaction mechanisms. Geochimica Et Cosmochimica Acta, 59(21): 4367-4379.

Rickard, D., 1997. Kinetics of pyrite formation by the H2S oxidation of iron (II) monosulfide in aqueous solutions between 25 and 125 degrees C: The rate equation. Geochimica Et Cosmochimica Acta, 61(1): 115-134.

Rickard, D. and Luther, G.W., 2007. Chemistry of iron sulfides. Chemical Reviews, 107(2): 514-562.

Roden, E.E. et al., 2010. Extracellular electron transfer through microbial reduction of solid-phase humic substances. Nature Geoscience, 3: 417.

Roden, E.E., Sobolev, D., Glazer, B. and Luther, G.W., 2004. Potential for Microscale Bacterial Fe Redox Cycling at the Aerobic-Anaerobic Interface. Geomicrobiology Journal, 21(6): 379-391.

Roden, E.E. and Zachara, J.M., 1996. Microbial reduction of crystalline iron(III) oxides: Influence of oxide surface area and potential for cell growth. Environmental Science & Technology, 30(5): 1618-1628.

Rose, A.L. and Waite, T.D., 2001. Chemiluminescence of Luminol in the Presence of Iron(II) and Oxygen: Oxidation Mechanism and Implications for Its Analytical Use. Analytical Chemistry, 73(24): 5909-5920.

Ross, A.R.S., Ikonomou, M.G. and Orians, K.J., 2000. Characterization of dissolved tannins and their metal-ion complexes by electrospray ionization mass spectrometry. Analytica Chimica Acta, 411(1-2): 91-102.

Ross, A.R.S., Ikonomou, M.G. and Orians, K.J., 2003. Characterization of copper-complexing ligands in seawater using immobilized copper(Il)-ion affinity chromatography and electrospray ionization mass spectrometry. Marine Chemistry, 83(1-2): 47-58.

Roussiez, V., Aloisi, J.-C., Monaco, A. and Ludwig, W., 2005. Early muddy deposits along the Gulf of Lions shoreline: A key for a better understanding of land-to-sea transfer of sediments and associated pollutant fluxes. Marine Geology, 222-223: 345-358.

Rowe, G.T., Boland, G.S., Phoel, W.C., Anderson, R.F. and Biscaye, P.E., 1994. Deep-sea floor respiration as an indication of lateral input of biogenic detritus from continental margins. Deep Sea Research Part II: Topical Studies in Oceanography, 41(2): 657-668.

Rowe, G.T., Kaegi, M.E.C., Morse, J.W., Boland, G.S. and Escobar Briones, E.G., 2002. Sediment community metabolism associated with continental shelf hypoxia, Northern Gulf of Mexico. Estuaries, 25(6): 1097-1106.

Rowe, G.T. and Menzies, R.J., 1968. Deep bottom currents off the coast of North Carolina. Deep Sea Research and Oceanographic Abstracts, 15(6): 711-719.

Rozan, T.F. et al., 2002. Iron-sulfur-phosphorus cycling in the sediments of a shallow coastal bay: Implications for sediment nutrient release and benthic macroalgal blooms. Limnology and Oceanography, 47(5): 1346-1354.

Rue, E.L. and Bruland, K.W., 1995. Complexation of iron(III) by natural organic-ligands in the central north pacific as determined by a new competitive ligand equilibration adsorptive cathodic stripping voltammetric method. Marine Chemistry, 50(1-4): 117-138.

Rue, E.L. and Bruland, K.W., 1997. The role of organic complexation on ambient iron chemistry in the equatorial Pacific Ocean and the response of a mesoscale iron addition experiment. Limnology and Oceanography, 42(5): 901-910.

Salamon, C.W., Jameson, R.F. and Linert, W., 2004. Anaerobic oxidation of cysteine to cystine by manganese(III) in aqueous acetic acid. Inorganica Chimica Acta, 357(1): 41-50.

Samczynski, Z., 2006. Ion exchange behavior of selected elements on Chelex 100 resin. Solvent Extraction and Ion Exchange, 24(5): 781-794.

Sanchiz, J., Esparza, P., Dominguez, S., Brito, F. and Mederos, A., 1999. Solution studies of complexes of iron(III) with iminodiacetic, alkyl-substituted iminodiacetic and nitrilotriacetic acids by potentiometry and cyclic voltammetry. Inorganica Chimica Acta, 291(1-2): 158-165.

Sarradin, P.-M. and Caprais, J.-C., 1996. Analysis of dissolved gases by headspace sampling gas chromatography with column and detector switching. Preliminary results. Analytical Communications, 33(10): 371-373.

Schaff T., L.L., Blair N., Demaster D., Pope R., Boehme S., 1992. Spatial heterogeneity of benthos on the Carolina continental slope: large (100km)-scale variation. Marine Ecology Progress Series, 88(2-3): 143-160.

Schippers, A. and Jorgensen, B.B., 2001. Oxidation of pyrite and iron sulfide by manganese dioxide in marine sediments. Geochimica Et Cosmochimica Acta, 65(6): 915-922.

Schoonen, M.A.A. and Barnes, H.L., 1991. Reactions forming pyrite and marcasite from solution .1. nucleation of FeS2 below 100 degrees C. Geochimica Et Cosmochimica Acta, 55(6): 1495-1504.

Schwertmann, U. and Murad, E., 1983. Effect of pH on the formation of goethite and hematite from ferrihydrite. Clays and Clay Minerals, 31(4): 277-284.

Schwertmann, U., Stanjek, H. and Becher, H.H., 2004. Long-term in vitro transformation of 2-line ferrihydrite to goethite/hematite at 4, 10, 15 and 25 degrees C. Clay Minerals, 39(4): 433-438.

Schwertmann, U.C., R, 2000. Iron oxides in the laboratory: preperation and characterization. Wiley-VCH.

Scott, D.T., McKnight, D.M., Blunt-Harris, E.L., Kolesar, S.E. and Lovley, D.R., 1998. Quinone Moieties Act as Electron Acceptors in the Reduction of Humic Substances by Humics-Reducing Microorganisms. Environmental Science & Technology, 32(19): 2984-2989.

Seeberg-Elverfeldt, J., Schlüter, M., Feseker, T. and Kölling, M., 2005. Rhizon sampling of porewaters near the sediment-water interface of aquatic systems. Limnology and Oceanography: Methods, 3(8): 361-371.

Seidler, J. et al., 2011. Metal ion-mobilizing additives for comprehensive detection of femtomole amounts of phosphopeptides by reversed phase LC-MS. Amino Acids, 41(2): 311-320.

Sempéré, R., Charrière, B., Van Wambeke, F. and Cauwet, G., 2000. Carbon inputs of the Rhône River to the Mediterranean Sea: Biogeochemical implications. Global Biogeochemical Cycles, 14(2): 669-681.

Severmann, S., McManus, J., Berelson, W.M. and Hammond, D.E., 2010. The continental shelf benthic iron flux and its isotope composition. Geochimica et Cosmochimica Acta, 74(14): 3984-4004.

Shea, D. and MacCrehan, W.A., 1988. Role of biogenic thiols in the solubility of sulfide minerals. Science of The Total Environment, 73(1): 135-141.

Shindo, H. and Huang, P.M., 1984. Catalytic effects of manganese(IV), iron(III), aluminum, and silicon-oxides on the formation of phenolic polymers. Soil Science Society of America Journal, 48(4): 927-934.

Simionato, A.V.C., Silva-Stenico, M.E., Tsai, S.M. and Carrilho, E., 2010. Evidences of Siderophores Synthesis by Grapevine Xylella fastidiosa, Causal Agent of Pierce's

Disease, through Instrumental Approaches. Journal of the Brazilian Chemical Society, 21(4): 635-641.

Sisley, M.J. and Jordan, R.B., 1995. Kinetics and Equilibrium Studies of the Reactions of Cysteine and Penicillamine with Aqueous Iron(III). Inorganic Chemistry, 34(24): 6015-6023.

Skyring, G.W., 1987. SULFATE REDUCTION IN COASTAL ECOSYSTEMS. Geomicrobiology Journal, 5(3-4): 295-374.

Smith, K.L., Carlucci, A.F., Jahnke, R.A. and Craven, D.B., 1987. Organic carbon mineralization in the Santa Catalina Basin: benthic boundary layer metabolism. Deep Sea Research Part A. Oceanographic Research Papers, 34(2): 185-211.

Sobolev, D. and Roden, E.E., 2001. Suboxic deposition of ferric iron by bacteria in opposing gradients of Fe(II) and oxygen at circumneutral pH. Appl Environ Microbiol, 67(3): 1328-34.

Soe, C.Z. and Codd, R., 2014. Unsaturated Macrocyclic Dihydroxamic Acid Siderophores Produced by Shewanella putrefaciens Using Precursor-Directed Biosynthesis. Acs Chemical Biology, 9(4): 945-956.

Soetaert, K., Hofmann, A.F., Middelburg, J.J., Meysman, F.J.R. and Greenwood, J., 2007. The effect of biogeochemical processes on pH. Marine Chemistry, 105(1): 30-51.

Sorensen, J., 1988. Dimethylsulfide and Methane Thiol in Sediment Porewater of a Danish Estuary. Biogeochemistry, 6(3): 201-210.

Stankovich, M.T. and Bard, A.J., 1977. Electrochemistry of proteins and related substnaces 1. Cystine and cysteine at mercury-electrode. Journal of Electroanalytical Chemistry, 75(2): 487-505.

Stefánsson, U., Atkinson, L.P. and Bumpus, D.F., 1971. Hydrographic properties and circulation of the North Carolina shelf and slope waters. Deep Sea Research and Oceanographic Abstracts, 18(4): 383-420.

Stone, A.T., 1983. The Reduciton and Dissolution of Manganese(III) and (IV) Oxides by Organics, California Institute of Technology, Pasadena, CA.

Stookey, L.L., 1970. Ferrozine - A new spectrophotometric reagent for iron. Analytical Chemistry, 42(7): 779-&.

Stumm, W., 1992. Chemistry of of the solid-water interface: Processes at the mineral-water and particle-water interface in natural waters. John Wiley and Sons, Inc., New York.

Stumm, W. and Morgan, J., 1996. Aquatic Chemsitry: Chemical Equilibria and Rates in Natural Waters. Wiley Interscience, New York.

Tagliabue, A. et al., 2010. Hydrothermal contribution to the oceanic dissolved iron inventory. Nature Geoscience, 3: 252.

Taillefert, M. et al., 2007a. Shewanella putrefaciens produces an Fe(III)-solubilizing organic ligand during anaerobic respiration on insoluble Fe(III) oxides. Journal of Inorganic Biochemistry, 101(11-12): 1760-1767.

Taillefert, M. et al., 2017. Early diagenesis in the sediments of the Congo deep-sea fan dominated by massive terrigenous deposits: Part II - Iron-sulfur coupling. Deep-Sea Research Part Ii-Topical Studies in Oceanography, 142: 151-166.

Taillefert, M., Bono, A.B. and Luther, G.W., 2000a. Reactivity of Freshly Formed Fe(III) in Synthetic Solutions and (Pore)Waters: Voltammetric Evidence of an Aging Process. Environmental Science & Technology, 34(11): 2169-2177.

Taillefert, M., Hover, V.C., Rozan, T.F., Theberge, S.M. and Luther, G.W., 2002a. The influence of sulfides on soluble organic-Fe(III) in anoxic sediment porewaters. Estuaries, 25(6): 1088-1096.

Taillefert, M., Luther, G.W. and Nuzzio, D.B., 2000b. The application of electrochemical tools for in situ measurements in aquatic systems. Electroanalysis, 12(6): 401-412.

Taillefert, M., Neuhuber, S. and Bristow, G., 2007b. The effect of tidal forcing on biogeochemical processes in intertidal salt marsh sediments. Geochemical Transactions, 8(1): 6.

Taillefert, M. et al., 2002b. Seasonal Variations of Soluble Organic-Fe(III) in Sediment Porewaters as Revealed by Voltammetric Microelectrodes, Environmental Electrochemistry. ACS Symposium Series. American Chemical Society, pp. 247-264.

Tang, D.G., Wen, L.S. and Santschi, P.H., 2000. Analysis of biogenic thiols in natural water samples by high-performance liquid chromatographic separation and fluorescence detection with ammonium 7-fluorobenzo-2-oxa-1,3-diazole-4-sulfonate (SBD-F). Analytica Chimica Acta, 408(1-2): 299-307.

Tang, Y., Webb, S.M., Estes, E.R. and Hansel, C.M., 2014. Chromium (III) oxidation by biogenic manganese oxides with varying structural ripening. Environmental Science: Processes & Impacts, 16(9): 2127-2136.

Taylor, R., McKenzie, R. and Norrish, K., 1964. The mineralogy and chemistry of manganese in some Australian soils. Soil Research, 2(2): 235-248.

Teal, J.M., 1962. Energy-flow in salt-marsh ecosystem of Georgia. Ecology, 43(4): 614-&.

Tebo, B.M. et al., 2004. Biogenic manganese oxides: Properties and mechanisms of formation. Annual Review of Earth and Planetary Sciences, 32: 287-328.

Tebo, B.M., Ghiorse, W.C., Van Waasbergen, L.G., Siering, P.L. and Caspi, R., 1997. Bacterially mediated mineral formation : insights into manganese(II) oxidation from molecular genetic and biochemical studies. Rev. Mineral., 35: 225-266.

Tercier-Waeber, M.L. and Taillefert, M., 2008. Remote in situ voltammetric techniques to characterize the biogeochemical cycling of trace metals in aquatic systems. Journal of Environmental Monitoring, 10(1): 30-54.

Terry, J.M. et al., 2008. Chemiluminescence Detector with a Serpentine Flow Cell. Analytical Chemistry, 80(24): 9817-9821.

Thamdrup, B., Fossing, H. and Jorgensen, B.B., 1994. Manganese, Iron, and Sulfur Cycling in a Coastal Marine Sediment, Aarhus Bay, Denmark. Geochimica Et Cosmochimica Acta, 58(23): 5115-5129.

Theberge, S.M., Luther, G.W. and Farrenkopf, A.M., 1997. On the existence of free and metal complexed sulfide in the Arabian Sea and its oxygen minimum zone. Deep-Sea Research Part Ii-Topical Studies in Oceanography, 44(6-7): 1381-1390.

Thomas, C.J. et al., 2002. Organic carbon deposition on the North Carolina continental slope off Cape Hatteras (USA). Deep Sea Research Part II: Topical Studies in Oceanography, 49(20): 4687-4709.

Thomas, H. et al., 2009. Enhanced ocean carbon storage from anaerobic alkalinity generation in coastal sediments. Biogeosciences, 6(2): 267-274.

Tu, S., Racz, G.J. and Goh, T.B., 1994. Transformations of synthetic birnessite as affected by pH and manganese concentration. Clays and Clay Minerals, 42(3): 321-330.

Ullman, W.J. and Aller, R.C., 1982. Diffusion coefficients in nearshore marine sediments1. Limnology and Oceanography, 27(3): 552-556.

Urban, N.R., Ernst, K. and Bernasconi, S., 1999. Addition of sulfur to organic matter during early diagenesis of lake sediments. Geochimica Et Cosmochimica Acta, 63(6): 837-853.

Uygun, D.A., Uygun, M., Akgol, S. and Denizli, A., 2015. Reversible adsorption of catalase onto Fe3+ chelated poly(AAm-GMA)-IDA cryogels. Materials Science & Engineering C-Materials for Biological Applications, 50: 379-385.

Vairavamurthy, A. and Mopper, K., 1987. Geochemical Formation of Organosulfur Compounds (Thiols) by Addition of H2S to Sedimentary Organic-Matter. Nature, 329(6140): 623-625.

Vairavamurthy, M.A., Manowitz, B., Maletic, D. and Wolfe, H., 1997. Interactions of thiols with sedimentary particulate phase: studies of 3-mercaptopropionate in salt marsh sediments from Shelter Island, New York. Organic Geochemistry, 26(9-10): 577-585.

Vairavamurthy, M.A., Orr, W.L. and Manowitz, B., 1995. Geochemical Transformations of Sedimentary Sulfur: An Introduction, Geochemical Transformations of Sedimentary Sulfur. ACS Symposium Series. American Chemical Society, pp. 1-14.

Van Cappellen, P. and Wang, Y., 1996. Cycling of iron and manganese in surface sediments; a general theory for the coupled transport and reaction of carbon, oxygen, nitrogen, sulfur, iron, and manganese. American Journal of Science, 296(3): 197-243.

van de Velde, S. and Meysman, F.J.R., 2016. The Influence of Bioturbation on Iron and Sulphur Cycling in Marine Sediments: A Model Analysis. Aquatic Geochemistry, 22(5): 469-504.

van den Berg, C.M.G., 1995. Evidence for organic complexation of iron in seawater. Marine Chemistry, 50(1): 139-157.

van der Zee, C. and van Raaphorst, W., 2004. Manganese oxide reactivity in North Sea sediments. Journal of Sea Research, 52(2): 73-85.

van Dongen, B.E., Schouten, S. and Sinninghe Damsté, J.S., 2003. Sulfurization of Carbohydrates Results in a Sulfur-Rich, Unresolved Complex Mixture in Kerogen Pyrolysates. Energy & Fuels, 17(4): 1109-1118.

Vancleemput, O. and Baert, L., 1983. Nitrate Stability Influenced by Iron Compounds. Soil Biology & Biochemistry, 15(2): 137-140.

Vargas, M., Kashefi, K., Blunt-Harris, E.L. and Lovley, D.R., 1998. Microbiological evidence for Fe(III) reduction on early Earth. Nature, 395(6697): 65-67.

Villalobos, M., Toner, B., Bargar, J. and Sposito, G., 2003. Characterization of the manganese oxide produced by pseudomonas putida strain MnB1. Geochimica et Cosmochimica Acta, 67(14): 2649-2662.

von Gunten, U. and Schneider, W., 1991. Primary products of the oxygenation of iron(II) at an oxic—anoxic boundary: Nucleation, aggregation, and aging. Journal of Colloid and Interface Science, 145(1): 127-139.

Walsh, J.J., 1989. How much shelf production reaches the deep sea? In: W.H. Berger, V. Smetacek and G. Wefer (Editors), Productivity of the Ocean: Present and Past. Wiley, Dahlem Konferenzen, pp. 175-191.

Walsh, J.J., Biscaye, P.E. and Csanady, G.T., 1988. The 1983–1984 shelf edge exchange processes (SEEP)—I experiment: hypotheses and highlights. Continental Shelf Research, 8(5): 435-456.

Walsh, J.J. et al., 1985. Organic storage of CO2 on the continental slope off the mid-Atlantic bight, the southeastern Bering Sea, and the Peru coast. Deep Sea Research Part A. Oceanographic Research Papers, 32(7): 853-883.

Walsh, M.J. and Ahner, B.A., 2013. Determination of stability constants of Cu(I), Cd(II) & Zn(II) complexes with thiols using fluorescent probes. Journal of Inorganic Biochemistry, 128: 112-123.

Wang, Z.M. et al., 2008. Kinetics of Reduction of Fe(III) Complexes by Outer Membrane Cytochromes MtrC and OmcA of Shewanella oneidensis MR-1. Applied and Environmental Microbiology, 74(21): 6746-6755.

Weaver, R.M. and Hochella, M.F., 2003. The reactivity of seven Mn-oxides with Cr-aq(3+): A comparative analysis of a complex, aq environmentally important redox reaction. American Mineralogist, 88(11-12): 2016-2027.

Webb, S., Tebo, B. and Bargar, J., 2005. Structural characterization of biogenic Mn oxides produced in seawater by the marine Bacillus sp. strain SG-1. American Mineralogist, 90(8-9): 1342-1357.

Webb, S.M., 2005. SIXpack: a graphical user interface for XAS analysis using IFEFFIT. Physica Scripta, T115: 1011-1014.

Wee, S.K., 2013. Novel Pathway for Microbial Fe(III) Reduction: Electron Shuttling Through Naturally Occuring Thiols, Georgia Institute of Biology.

White, D.J., Noll, M.R. and Makarewicz, J.C., 2008. Does Manganese Influence Phosphorus Cycling under Suboxic Lake Water Conditions? Journal of Great Lakes Research, 34(4): 571-580.

Winter, D., Seidler, J., Ziv, Y., Shiloh, Y. and Lehmann, W.D., 2009. Citrate Boosts the Performance of Phosphopeptide Analysis by UPLC-ESI-MS/MS. Journal of Proteome Research, 8(1): 418-424.

Wolf, M., Kappler, A., Jiang, J. and Meckenstock, R.U., 2009. Effects of Humic Substances and Quinones at Low Concentrations on Ferrihydrite Reduction by Geobacter metallireducens. Environmental Science & Technology, 43(15): 5679-5685.

Wolf-Gladrow, D.A., Zeebe, R.E., Klaas, C., Körtzinger, A. and Dickson, A.G., 2007. Total alkalinity: The explicit conservative expression and its application to biogeochemical processes. Marine Chemistry, 106(1): 287-300.

Wu, J., Boyle, E., Sunda, W. and Wen, L.-S., 2001. Soluble and Colloidal Iron in the Oligotrophic North Atlantic and North Pacific. Science, 293(5531): 847-849.

Wu, J.F. and Luther, G.W., 1994. Size-fractionated iron concentrations in the water column of the western north-atlantic ocean. Limnology and Oceanography, 39(5): 1119-1129.

Zhang, J., Wang, F., House, J.D. and Page, B., 2004. Thiols in wetland interstitial waters and their role in mercury and methylmercury speciation. Limnology and Oceanography, 49(6): 2276-2286.

Zhao, H. et al., 2016. Redox Reactions between Mn (II) and Hexagonal Birnessite Change its Layer Symmetry. Environmental science & technology.

Zhu, M., Ginder-Vogel, M., Parikh, S.J., Feng, X.-H. and Sparks, D.L., 2010. Cation effects on the layer structure of biogenic Mn-oxides. Environmental science & technology, 44(12): 4465-4471.

Zhu, M., Paul, K.W., Kubicki, J.D. and Sparks, D.L., 2009. Quantum Chemical Study of Arsenic (III, V) Adsorption on Mn-Oxides: Implications for Arsenic(III) Oxidation. Environmental Science & Technology, 43(17): 6655-6661.

Zinder, B., Furrer, G. and Stumm, W., 1986. The coordination chemistry of weathering: II. Dissolution of Fe(III) oxides. Geochimica et Cosmochimica Acta, 50(9): 1861-1869.